Radio Study of Galactic Supernova Remnants and the Interstellar Medium

A Thesis submitted for the degree of

Doctor of Philosophy

(in PHYSICS)

to the

UNIVERSITY OF PUNE

by

SANJAY BHATNAGAR

National Centre for Radio Astrophysics
Tata Institute of Fundamental Research
Pune - 411 007

July 2001

Contents

List of Figures

List of Tables

Acknowledgments

It has been a long trek - at least longer than what I imagined it would be. On the trek, I am fortunate to have come in touch with a variety of people. Some of them have become close at a personal level too. This is an attempt to convey to the reader, my appreciation for these people who directly or indirectly affected the course of this trek.

Apart from the usual stuff, I was taught by Prof. H. S. Mani, at IIT Kanpur, that ”research is not just another profession, it is a way of life”. I also remember Prof. A.P.Shukla who, in his inimitable way, sparked in his students a desire for learning. I owe my presence in the National Centre for Radio Astrophysics (NCRA) to Prof. Mani, and to Prof. Shukla for making learning interesting, and motivating me into the pursuit of research. I express my deep respectful thanks to them.

Once at NCRA, stepping into that ”way of life”, the fascination of thinking big while keeping one’s feet firmly on ground came with Prof. Govind Swarup, and others at the NCRA. Prof. Swarup’s description, sometimes past midnight, of the design of some mechanical structure (which, I later realized was the GMRT antenna), how to do quick arithmetic (where I was made to play the role akin to that of temporary register of a computer CPU), his introducing me to Fourier Transforms, Aperture Synthesis, and Radio Astronomy in general are the first few steps into that ”way of life” I fondly remember. His later demand that I be able to give quick answers to questions that he ”might throw at me while passing by in the corridors” helped me in many ways. His enthusiasm is even now a source of inspiration. Over the years I have interacted with him a lot. He became the source of guidance, consultations and advice and sometimes even a sink for my outbursts due to problems in personal and professional life. I am all the more thankful to him for this, and hope to continue this relationship in future.

For my thesis, I slowly gravitated towards A. Pramesh Rao probably because of his approach to work and his style of thinking and his scientific interests. He gradually became my unofficial guide at NCRA. During the early stages of the GMRT (and to some extent even now), I learnt from him the tricks of the trade, and thoroughly enjoyed that phase of my thesis and GMRT debugging and I am very thankful to him for that. All along he encouraged me to be independent. Partly because of this, I was able to do large parts of my work independently. Even for work where he was not directly involved or interested, he was and continues to remain an excellent person to bounce off ideas - and I sometimes even receive healthy criticism with equanimity.

Another scientist from whom I learnt a good deal is T.J.Cornwell. The time I spent working with him was very satisfying in terms of work in hand, and in future, as well as in terms of learning directly from someone whose work I admire a lot. I could not pursue that line of work due to limitations of my domestic and professional problems. I may have disappointed him there. However, I continue to find in him a very understanding, supportive and inspiring senior colleague. Tim - my heartfelt thanks to you for everything. I look forward to working together again sometime. The possibility to finally go forward from where we left gives an inviting and positive hue to the future.

I am very grateful to D.J.Saikia (a.k.a. Sykes) for agreeing to become my Official Guide. Besides reading my thesis and providing useful comments/criticisms and contributing his all important signatures to my thesis, his contribution in the role of a more experienced friend and well-wisher was a great support. I remember long sessions where he would patiently listen to my diatribe that I would pour out. His counsel at various points of time, his assistance, and discussions were of great help. His legendary wholehearted laughter (which often reached me in my office with minimal attenuation) and his one-liner punch-lines kept the environment cheerful (though I must add that he is now trying to extort something useful out of me as a "fee" for his signatures!). Sykes, I am indeed grateful to you for all you have done.

Interaction with Rajaram Nityananda towards the concluding stages of my work, started with what was to become Chapter 7 of my thesis. It has been a very rewarding and fruitful experience. Working with him has been sheer joy, and I hope to do more fruitful work with him in future. I continue to learn from his very broad spectrum of interests. I am grateful to him for his indulgence in often going out of his way to help me out in facing problems on various fronts of life.

I also spent sometime working with K.R. Anantharamaiah of the Raman Research Institute, Bangalore and it was such a pleasure. Although, finally, that work did not go into my thesis, I hope to pursue that line of work with him in the near future. He and Namir Kassim of the Naval Research Labs. became the target for bouncing off many of my ideas.

Thank you both for tolerating and helping me.

I wish to also thank S. Ananthkrishnan, Gopal-Krishna, C.R. Subrahmanya, V.K. Kulkarni, M. Vivekananda, and K. Subramaniya, for all the help, cheer and fun they brought in life.

Many thanks to my friend Prem Kumar, who helped at various stages with some drawings, and in printing and binding the thesis.

My close friends Sulekha and Goutam Chattopadhyay contributed towards this effort in ways I find difficult to describe - in any case I wish not to attract severe penalties they would impose on expressing formal ”thanks”. Nonetheless, I would say this much – without my family and them I would not have made it. I also found an excellent companion in Divya Oberoi (”Div”) and Jaishree Oberoi. At Pune, I fondly remember long sessions of discussions on just any thing under the Sun, interspersed with generous helpings of aaloo-paranthas at their home adding spice to our discussions.

Rajiv Singh (RK), Ajit Kulkarni, V.M. Tatke (Maharaj), Ramana Athreya, Nissim Kanekar, Sanjay Upreti, Niraj Upadyay, Ajith Kumar (Ajithum), Hemant Lohkhande - all with their own inimitable and unique personalities, helped eliminate drudgery from work and life in general. Late night strolls, tea/coffee/milk sessions (and lately, sessions of Nissim’s own invention of “Turmeric milk”, in the inviting company of potential new members of this gang) followed by “profound” discussions, hikes in the Sahyadris (particularly the Bhimashankar hike), catching snakes in the NCRA campus and photographing them from distances otherwise considered unsafe, and the music sessions were the activities with all these friends which helped me keep tempo of work and made life enjoyable. My thanks to all of them.

I also wish to thank the entire GMRT staff without whose cooperation and help this work would not have been possible. My special thanks to all the telescope operators (Anirudh, Mangesh, Sanjay, Manisha, Manish, Jayprakash and Jitendra) for all help during observations and keeping the GMRT control room environs cheerful (though again I must remind Mangesh that my investment in the music CD that I contributed to the GMRT Control Room did not give the expected dividends).

I enjoy a very special relationship with my youngest Chacha/Chachi - Mr. Anand Shankar / Ms. Mamta Shankar. I find in them a friend, an elder, a patient listener, concerned counselor/critic and a determined well-wisher who invariably make me feel comfortable and stable in life. Also my brothers-in-law and sisters were great sources of inspiration. My special thanks to them all for all they have done.

I always had, and to some extent still have, faith in the basic goodness of all humans and in the beauty of human relationships. During this trek, I came close to some people whose approach to life and relationships however leaves a nagging doubt in the mind. I am sure that what nature does to us must be handled with care, humility, compassion and love - but sometimes people, even in normal circumstances, can become completely insensitive and prefer going for easier solutions in life. I do not know if some of such people have contributed towards this work - positively or negatively. But I will remember them all - some of them even fondly - for a long time.

I am truly amazed by the patience and determination to constantly show the brighter side of life that my family, particularly my parents showed. Past few years have by far been the roughest patch in life I have walked and I have no doubt that without their patience and faith in me, I would have gone down that slippery path which I had begun to walk. There was nothing to look forward on that path, certainly not a thesis. I dedicate my thesis to them and I hope I have made them happier.

I would like to thank the NCSA Astronomy Digital Image Library (ADIL) for providing some of the images used for the purpose of illustration in this thesis.

The NASA's Astrophysics Data System was extensively used during the course of this work for locating data, other references available on the web and for building the bibliography database for this thesis.

Most of the work which required computers was done using computers running the GNU/Linux operating system. The software I used was almost entirely from the Open Source movement and I am convinced that without the excellent work of all those GNUians out there, my life would have been more difficult. I wish to thank all those anonymous contributors to the Open Source movement and hope to become part of it by contributing something substantial someday.

Declaration

CERTIFIED that the work incorporated in this thesis entitled "**Study of Galactic Supernova Remnants and Interstellar Medium at low frequencies**" submitted by **Sanjay Bhatnagar** was carried out by the candidate under my supervision. Such material as has been obtained from other sources has been duly acknowledged in the thesis.

Place : Pune	Prof. D. J. Saikia
July , 2001	Thesis Supervisor

Abstract

This dissertation presents a study of Galactic Supernova Remnants (SNRs), using the newly available Giant Metrewave Radio Telescope (GMRT) at a frequency of 327 MHz. Extensive debugging and calibration of the telescope parameters was required before the above could be carried out; this is also presented here.

Towards the end of their evolution, stars with masses greater than about $8M_{\odot}$ explode, producing one of the most energetic observable events in the Galaxy. These explosions of massive stars are referred to as Supernovae (SNe). The shock wave traveling outwards, initially interacts with the circumstellar material of the progenitor star, giving the initial radiation detected in the x-ray, optical and radio bands. After crossing the circumstellar envelope, it continues to interact with the interstellar medium (ISM), sweeping up ISM material, and producing objects with extended emission; these are identified as Supernova Remnants (SNRs). When the mass of material swept up by this expanding blast wave becomes much greater than the ejected mass and the age of the SNR is comparable to the radiative cooling time, the shock wave decelerates, increasing the compression ratios by a large amount and setting up instabilities. Re-accelerated electrons in a thin shell, moving in the presence of a compressed (and hence amplified) magnetic field, produce non-thermal (synchrotron) radiation with a negative spectral index α ($S \propto \nu^{\alpha}$) which can be detected for up to $\sim$ few $\times 10^4$ years.

The circumstellar environment of the progenitor star and the properties of the local ISM produce varied SNR morphologies. Morphological studies of a large number of SNRs have allowed their classification into various categories essentially based on the radio morphology. About 80% of the known SNRs show a shell-type morphology. Other morphologies include flat spectrum filled-center (or 'crab-like'), composite, barrel-shaped, and bi-annular.

Galactic objects have usually been identified as candidate SNRs based on morphological evidence and the lack of thermal emission (excess over the expected synchrotron

emission at high frequencies). Extended emission with no associated thermal component, and showing one of the typical SNR morphologies, would be considered to be a good candidate SNR. However, reliable deciphering of the morphology requires observations with angular resolution several times higher than the extent of the emission. Further, morphological evidence alone is often insufficient for an unambiguous identification of Galactic objects as SNRs. Detection of a negative spectral index, which indicates the presence of non-thermal emission, is also used in combination with morphological evidence to identify SNRs. This, of course, requires multi-frequency observations, especially at low frequencies, to provide clear evidence of the presence or absence of an SNR. Morphology and non-thermal emission are thus the primary signatures used for the identification of SNRs in the galaxy.

Apart from providing the crucial primary morphological signature for the identification of SNRs, high resolution observations of such objects also provide valuable information about the ISM. Morphology of a given class of SNRs is believed to be the result of a similar circumstellar and ISM environment. Detailed morphological studies of SNRs therefore provide information about the local ISM and the progenitor star. With SNRs distributed all over the Galaxy, such studies provide information about the large scale distribution and structure of the ISM. Angular resolutions better than ~ 1 arcmin are often necessary to decipher the morphology of typical SNRs and a spatially separate SNRs from other sources of extended emission in the Galaxy, as well as to study their interaction with the ISM, .

Measurements of continuum radio spectra also provide other valuable information about SNRs. The shape of the continuum spectrum (and the spectral index) is also an indirect measure of the spectrum of relativistic electron energies. Simple Fermi shock acceleration theory predicts a spectral index of -0.5. While this is consistent with the spectral indices of many shell-type SNRs, substantially higher values of the spectral index have also been seen in a few SNRs (it should be noted that reliable measurements of spectral index exist only for a small number of SNRs). Models invoking self-consistent non-linear shock models of first-order Fermi acceleration can account for higher values of spectral index, but require reliable determination of the shape of the spectrum, particularly at low radio frequencies. However, for about 35% of the SNRs in current SNR catalogues, the spectral index is poorly determined or, in some cases, completely unknown. The quality of the low frequency observations in the past has also been poor due to the lower resolutions and sensitivities of various low frequency telescopes up to the present time.

To meet the dual requirements of high resolution and sensitivity for extended non-thermal emission, many Galactic plane observations have, till recently, been done using single dish telescopes at $2-5$ GHz with a resolution of $2-4$ arcmin. However, at a resolution of a several arcmin, these observations are insufficient for detailed morphological studies of the SNRs. Single dish observations at these high frequencies also suffer from the problem of confusing extended thermal emission, abundantly present in the Galaxy. High resolution observations of SNRs at a number of frequencies below ~ 1 GHz, to reliably determine the spectrum and morphology, are therefore crucial for correct identification and morphological studies, as well as for studies of the effects of the interaction with the ISM and radiation mechanism in the SNR shells.

This dissertation contains work done towards a low frequency study of Galactic SNRs using the GMRT at a frequency of 327 MHz. The sensitivity of the GMRT to large angular scales with high resolution offers a crucial advantage in mapping the Galactic plane where the emission field is usually very complex. These features of the GMRT were exploited to study a sample of nine fields containing new candidate Galactic SNRs in the southern part of the Galactic plane at 327 MHz. This sample of fields was chosen from recent surveys done using the Molonglo Synthesis Telescope (MOST) at 843 MHz and the Parkes 64-m dish at 2.4 GHz (note that the two surveys had no overlapping fields of view). The RMS noise of these survey observations was typically ~ 20 mJy/beam. Further, many of these fields are in complicated regions with strong extended emission from other sources. Substantial thermal emission at these high frequencies as well as confusing emission from nearby strong sources severely limited the image fidelity. Finally, with information available only at single frequencies for most of the objects in this sample, their identification has remained inconclusive until the present work.

Full synthesis GMRT observations were carried out at 327 MHz for this sample of fields. These observations constitute the most sensitive and highest resolution images of these fields. Our observations confirmed most of these candidates as SNRs. Six fields show well resolved shell-type and two fields show barrel-shaped objects with non-thermal emission. IRAS 60–μm images of all these fields were also examined to look for any associated thermal emission. In one of the fields designated as $\mathrm{G}004.2+0.0$, significant thermal emission was detected. Radio flux density at 327 MHz is consistent with a flat spectrum source suggesting that it may be a compact thermal source.

Apart from the target SNRs in the fields, images of all the nine fields provide useful

information about many other objects in the field of view. The 327 MHz images, each with a field of view of $\sim 1.4°$, reveal a number of compact as well as extended sources of emission. Flux densities of the compact sources were measured at 327 MHz from the GMRT images and at 1420 MHz from the literature. The extended emission in one of the fields coincides with the location of previously identified as Ultra Compact HII (UC H II) regions. Recently, extended emission has been detected around many UC H II and the extended emission seen in this image may have the same origin. However, the true nature of the extended emission and the mechanism to sustain extended emission at such large scales to such low frequencies is not yet well understood. Similarly, the linear structure seen in another field is not clear. Such linear structures have been reported earlier as well. High resolution observations at other frequencies will be necessary for further study and to determine the nature of such objects.

Another compact source, G$003.6 - 0.1$, classified as an HII region from earlier higher frequency observations, showed significant structure and emission at 327 MHz. The GMRT observations reveal a shell-type morphology. Images at 5 GHz (from data acquired from the VLA archives) and 1.4 GHz (from the literature), at comparable resolution, provide resolved images of this object at these frequencies; two compact sources can be identified in these images, with extended emission around them. The spectrum of the extended emission is found to be non-thermal while emission from a strong compact source in the region shows a thermal signature. The current data on these components suggest that one of the components may be a radio star with a spectral index of ~ 0.5. The cometary morphology of the extended emission is similar to that seen in high resolution images of a number of UC H IIregions.

HI absorption profiles against Galactic objects provide information about the intervening ISM. These can be used to estimate distances to the objects using models for the distribution and velocity of the Galactic ISM. HI distance estimates for three morphologically distinct components in the above field were obtained from GMRT 1420 MHz HI absorption observations against these components.

The usefulness of observations such as the ones presented in this dissertation and future directions of research in this area are also discussed. This dissertation is expected to be the first step in a longer term campaign for a Galactic plane survey at a number of GMRT frequency bands. Such a survey will be very useful in the identification of new SNRs. Current SNR catalogues are known to be incomplete for small sized SNRs. Such a survey will separate thermal and non-thermal radiation effectively and allow the identi-

fication of compact, SNRs in the Galaxy.

The GMRT has only recently come to a stage where enough antennas are available in the interferometric mode to attempt the imaging of extended sources. A substantial fraction of the work done for this dissertation involved the debugging and calibration of the telescope, to enable the observations discussed above to be carried out. Further, large amounts of software were required to be written, both to carry out debugging activity as well as to enable flagging and calibration of telescope data in a semi-automated fashion. This aspect of the thesis work is discussed below.

Monitoring the data quality, the health of the system using the complex visibility function measured by an interferometer like the GMRT, identifying sources of data corruption, general debugging of the instrument, etc. all require sophisticated and efficient software for data analysis, browsing, and display. Extensive software was developed for this purpose in the form of general purpose object oriented libraries as well as programs for on-line and off-line data processing and display.

This GMRT data analysis software system was developed with the longer term goal of providing a software environment which could be used by other users of the telescope, as well for developing new data analysis and calibration techniques. A general purpose user interface library was also developed to make the application programs user-friendly. Using these libraries, programs for data editing, semi-automatic data flagging, on-line monitoring of the data, computation for antenna-based complex gains, amplitude and phase calibration, etc. were also developed. All this software was extensively used during the course of this dissertation. These libraries and programs have also been used by other researchers in the group, both to develop new software as well as for data analysis purposes.

For the purpose of imaging, it is necessary to measure the precise location of the antennas on the ground to an accuracy of a fraction of the wavelength. Further, one must also measure the time delay suffered by the signals from various antennas. The software discussed in the preceding paragraph was extensively used for the calibration of various instrumental parameters, including antenna positions and time delays. These measurements were used in a program for off-line phasing in the initial stages of this work and are now used for the on-line phasing of the telescope.

The complex visibility function, V, depends on a number of telescope parameters like the system temperature, sensitivity, antenna fixed delays, antenna positions, etc. During debugging, it was frequently required to view this data in various representations (e.g., Cartesian versus polar representation of complex numbers). Since the complex visibilities are a function of a multitude of parameters, and different debugging purposes require viewing V with respect to various quantities, it was necessary to develop a compact macro language parser to extract and display the data in a flexible and programmable manner.

Inteferometry at low frequencies poses new challenges in data calibration and analysis, which are interesting in their own right. Mapping here requires the use of different (and computationally intensive algorithms), compared to those used for mapping at higher frequencies. These algorithms are discussed in detail in this dissertation. Further, the volume of data for a typical GMRT observation is exceedingly large with varied sources of data corruption. Manual identification and flagging of bad data is therefore tedious, time consuming and fraught with human errors. During the course of this dissertation, procedures were evolved for the editing, calibration and mapping of low frequency data. New algorithms were developed to identify and flag bad data in a semi-automatic fashion. These algorithms were extensively used for the data analysis, substantially reducing the time required for data editing, as well as improving the quality of the edited data used for mapping purposes. These procedures and algorithms for the analysis of GMRT data, for the purpose of continuum imaging studies, are also discussed in this dissertation.

Algorithms for phase calibration, available in standard data reduction packages, are very sensitive to the presence of severely corrupted data. The problem of computation of antenna-based complex gains was formulated using complex calculus and the algorithm implemented as a general purpose program. This allowed insights into the working of this algorithm, and enabled devising of the variants which are robust in the presence of bad data. This was done by (1) automatically eliminating out-lying points, (2) doing two passes to eliminate dead/bad antennas. This algorithm was also used to identify and flag corrupted data in a semi-automatic fashion. It was extensively used for measuring antenna pointing offsets, on-line monitoring of the instrumental phase, closure errors in the telescope, as well as for antenna position and time delay calibration.

Techniques used to minimize polarization leakage in the system have not yet been realized for the GMRT. This leakage is a significant source of noise at 150 MHz and also contributes noise at all other bands, albeit at a lower level. An algorithm was developed to measure the leakage using *only* the co-polar visibilities currently produced by the GMRT correlator. This work also enabled us to understand the various sources of non-antenna based errors; this technique can now be used for better calibration of GMRT data.

New and robust algorithms for automatic data editing and better calibration are necessary for the analysis of data from any large scale observational project at low frequencies (such as the suggested multi-frequency Galactic plane survey). New software for on-line data monitoring and display as well as for generating flagging information during observations is also required to improve the data quality. Further, algorithms and associated software are also crucially necessary to detect RFI and possibly eliminate RFI affected data. Possibilities of future research in these directions is also discussed in this dissertation.

Chapter 1

Introduction

Towards the end of their evolution, stars with masses greater than about $8M_{\odot}$ explode, producing one of the most energetic observable events in our Galaxy and external galaxies. The generally accepted sequence of events leading to this outcome is as follows. A star is said to have formed when a self-gravitating cloud of gas (mostly hydrogen) collapses under its own gravity to densities and temperatures at which, hydrogen burning begins. Under the action of gravity, the centre gets denser and hotter resulting into a well defined series of nuclear reactions. These reactions, starting from hydrogen burning and going all the way to the formation of iron, start at the centre and feed on the products of earlier reactions, which continue to occur further out. With time, a series of concentric shells are formed around the core, consisting of various elements produced in the these reactions. This model is usually referred to as the "onion-skin model" with a core of iron surrounded by shells of lighter elements with the outer most shell consisting of hydrogen (and possibly some He, Ne, O, N and C). Simulations show that, depending upon the initial masses, some stars complete the full sequence of nuclear reactions while for others this sequence is interrupted (Trimble 1982; Woosley & Weaver 1986, and references therein). Single stars with initial masses greater than about $8M_{\odot}$, explode producing Type II supernovae (SNe) which are characterized by the presence of hydrogen lines in their spectra and are usually found in the spiral arms for spiral galaxies. Type I SNe on the other hand are produced due to a white dwarf reaching the critical mass due to accretion from a companion star in a binary system. These SNe are devoid of hydrogen lines in their spectra and occur in all types of galaxies. The star is completely disrupted in the case of Type I SNe and no compact core remains (Woosley & Weaver 1986). The central part of the iron core in Type II SNe, however, is compressed to nuclear densities and is left behind as a spinning degenerate neutron star, which is, in some cases, detected as a pulsar. After the core collapse, the rest of the material which is still in-falling, rebounds (since the neutron core cannot be further compressed) creating a powerful shock wave which ploughs though the the outer layers of the star and finally emerges out of the circumstellar material. The core collapse releases 10^{53} erg of gravitational energy in the form of neutrinos which, along with the blast wave, couple with the outer layers and eject them at high speeds. The explosion in both types of SNe releases $\sim 10^{51}$ erg of kinetic energy, which produces a shock wave travelling outwards. The cores of massive stars with initial masses in the range of $18 - 30M_{\odot}$ can also first explode as SNe and then collapse into low mass black holes (Brown & Bethe 1994). In such an event, a heavy star collapses into a black hole without returning matter to the galaxy. The empirical value of $\Delta Y/\Delta Z$ (the relative helium to metal enrichment) implies a maximum mass of the star, after which the nucleosynthesis must cut off (i.e., stars more massive than this limit cannot contribute higher metals to the galaxy). This maximum mass limit derived from the value of $\Delta Y/\Delta Z$ and that derived from the computation by Brown & Bethe (1994) are in good agreement.

The interaction of the above shock wave with the in-falling circumstellar material produces the initial radiation, which announces the onset of the explosive event to observers on Earth. The shape of the initial optical light curve and the spectra at the peak of optical emission can be used to differentiate between the Type I and Type II SNe (Weiler & Sramek 1988). Type-I SNe are characterized by the absence of hydrogen lines in their peak optical spectra while Type-II exhibit hydrogen lines in their spectra. Based on further finer details of the light curve, SNe are further sub-divided into Type Ia, Ib, II-L (linear) and II-P (plateau). However, initial radio emission has been detected from Type-Ia SNe. The optical light curve of Type II-L decreases monotonically in intensity after reaching a peak value while that of Type II-P, on the other hand goes through a flat plateau before starting to decay further. The peak absolute blue magnitude of Type Ia SNe has been found to be remarkably constant for different events; these can hence be used as ideal standard candles in the universe. Hubble constant can therefore be derived from the observations of extragalactic Type Ia SNe light curves. It is this property of Type Ia SNe which is responsible for the currently thriving industry of Supernova Cosmology (Branch 1998, and references therein).

Typically, radio emission is first detected at higher frequencies, and later, at successively lower frequencies due to changes in the optical depth for external free-free absorp-

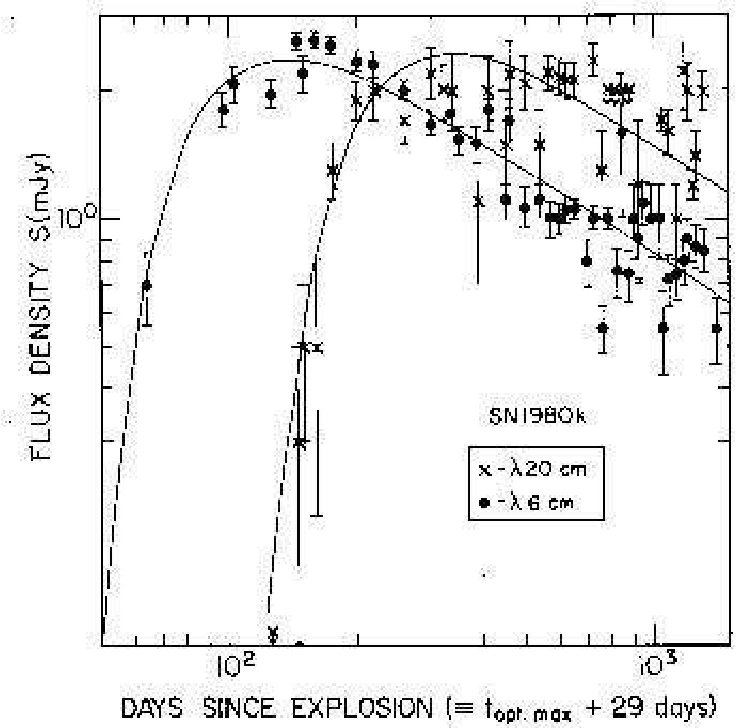

Figure 1.1: Initial radio light curves at 6 and 20 cm of a Type II-L SNe SN1980k taken from Weiler et al. (1986). Such light curves are thought to be typical of the class. The data points marked by crosses and filled circles are measured flux densities while the solid curves are the best fit theoretical curves. Emission at 6 cm starts and peaks earlier than at 20 cm. The emission initially increases rapidly, reaches a maximum value and then monotonically decays at both the frequencies.

tion (Weiler et al. 1986). A typical example of radio light curve for a Type II-L SN is shown in Fig. 1.1. The shape and spectral behavior of this initial radio light curve is thought to be typical of the class. Radio emission is detected significantly after the optical light is detected. The spectral index α ($S_\nu \propto \nu^\alpha$) evolves from a value of ~ 1 to a relatively constant value of ~ -0.7 when the emitting region becomes optically thin for radio photons (Fig. 1.2). Observations of SN1983N, a Type Ib SN, on the other hand, exhibited a far more rapid rise as well as decay in the flux density compared to that of Type II-L SN. This difference in the radio light curves of the two types have been interpreted as being due to significant differences between the environments of Type Ib and II-L SNe.

After the blast wave crosses the denser circumstellar envelope into the more tenuous interstellar medium (ISM), this initial radio emission ultimately dies down, over time scales of several weeks for Type I SNe to many years for Type II SNe. The evolution of the blast wave as it ploughs though the ISM can be roughly described in four distinct stages (Reynolds & Chevalier 1984). This interaction of the blast wave with the ISM, at much later times, produces sources of synchrotron emission in the sky, called Supernova Remnants (SNRs). SNRs are visible at radio bands (and at optical and X-ray bands in regions where the obscuration by the Galactic plane is relatively low) for up to $\sim 10^4 - 10^6$ years after the initial explosion. This dissertation is concerned with the observations of such Galactic SNRs at low radio frequencies.

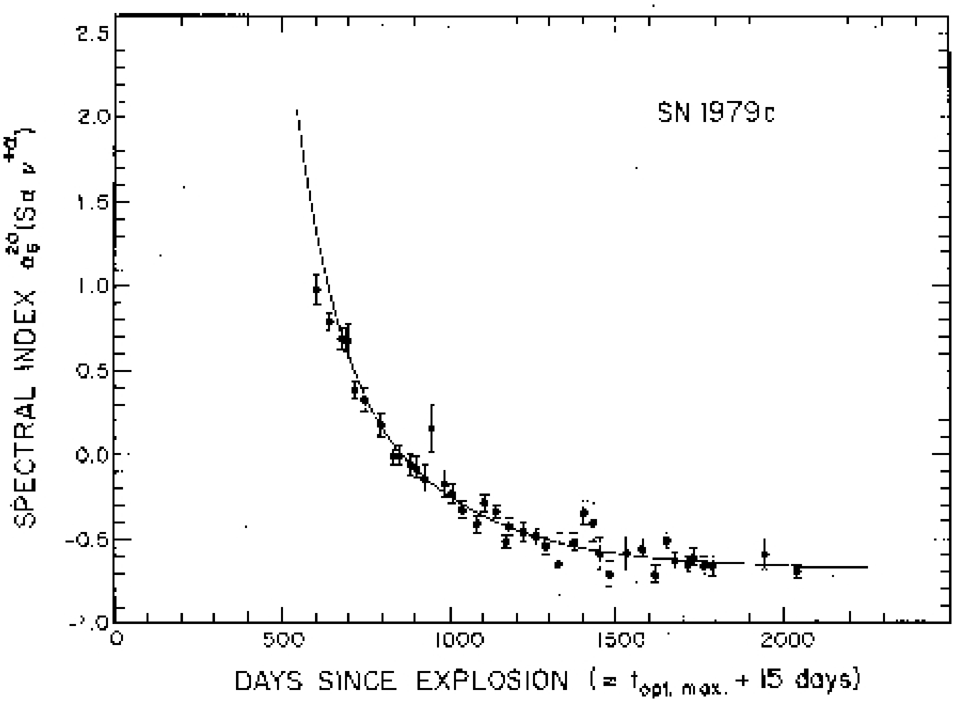

Figure 1.2: Spectral index evolution between 6 and 20 cm for a Type II-L SNe SN1979c taken from Weiler et al. (1986). The solid curve corresponds the best fit curve derived from the flux densities measured at these wavelengths.

1.1 Synchrotron Radiation

A relativistic electron moving at a velocity **v** in the presence of magnetic field of strength **B**, moves in a helical path around the field line, and consequently emits synchrotron radiation (Ginzburg & Syrovatskii 1969; Moffet 1975, and references therein). A brief description of the synchrotron emission mechanism and the results which follow is taken from Salter & Brown (1988). If the angle between the **v** and **B** vectors (the pitch angle) is θ

and the total energy of the electron is $E = \gamma mc^2$ where $\gamma = 1/(1 - v^2/c^2)^{1/2}$ is the Lorentz factor, the frequency of gyration around the field lines is given by

$$\nu_g = \frac{e\mathbf{B}_\perp}{2\pi\gamma mc} = \frac{\nu_\circ}{\gamma} \tag{1.1}$$

where $\mathbf{B}_\perp = \mathbf{B}\sin\theta$ is the component of the magnetic field perpendicular to the electron path and $\nu_\circ$ is the non-relativistic electron gyro-frequency. Due to relativistic effects, the radiation will be emitted in a narrow cone of half-angle of the order of $1/\gamma$. In general, a detector will detect pulses of radiation from such a system every time the the cone of emission crosses the detector's line of sight and the pulse shape will be defined by a cut across the cone of emission. The frequency of the pulses as seen by the detector will be the Doppler shifted gyration frequency given by

$$\nu'_g \sim \frac{\nu_g}{\sin^2\theta} \tag{1.2}$$

while the pulse width is

$$\Delta t \sim \frac{1}{2\pi\nu_g\gamma^3} \tag{1.3}$$

Since the width of the individual pulses will be narrow (at least for large values of γ), most of the emitted energy will be in harmonics of the fundamental frequency given by $(2\pi\Delta t)^{-1} \sim \nu_g\gamma^3$. For ultra-relativistic electron, these harmonics will be closely spaced and the resulting spectrum is essentially a continuum. The critical frequency at which the emission is maximum is given by

$$\nu_c = \frac{3}{2}\gamma^2\nu_\circ = 16.08 \times 10^6 \mathbf{B}_\perp E^2 \text{ MHz} \tag{1.4}$$

where E is the electron energy in GeV and $\mathbf{B}_\perp$ in gauss. The rate of loss of energy by the electron due to synchrotron radiation is given by

$$\frac{dE}{dt} = -119.7\mathbf{B}_\perp^2 E^2 \text{ GeV/yr} \tag{1.5}$$

This basic equation says that the most energetic electrons will lose energy at the fastest rate. With time, a high energy electron will lose energy and radiate for longer as a lower energy electron. For an ensemble of electrons with some initial energy distribution, with time time, more electrons will pile up at the lower energy end of the energy spectrum. This produces observable changes in the properties of the emission with time. This effect goes by the name of "ageing" in the literature.

For a homogeneous and isotropic ensemble of electrons with energy density distribution $N(E)dE$, the total intensity will be given by

$$I(\nu) = \int_0^\infty N(E)P(\nu)dE \tag{1.6}$$

where $P(\nu)$ is the spectrum of the electron with energy in the range between E and $E + dE$. For a power law energy spectrum given by $N(E)dE = N_\circ E^{-p}dE$ in a limited range $E_1 < E < E_2$, $I(\nu)$ is given by

$$I(\nu) = \frac{\sqrt{3}e^3 L}{8\pi mc^2}\left(\frac{3e}{4\pi m^3 c^5}\right)^{(p-1)/2} N_\circ \mathbf{B}_\perp^{(p+1)/2} \nu^{(1-p)/2} a(p) \tag{1.7}$$

where $a(p)$ is a slowly varying function of p and L is the spatial extent of the region with uniform magnetic field **B**. Clearly, for a power law distribution of initial energies, $I(\nu) \propto \nu^\alpha$ where α is the spectral index and is related to p as $\alpha = (1-p)/2$. p is usually greater than unity; a negative spectral index is thus observational evidence for synchrotron emission.

Emission from a single electron will clearly be elliptically polarized with the electric field vector perpendicular to the projected magnetic field vector. However, for an ensemble of electrons with a random distribution of pitch angles, the observed radiation will be partially linearly polarized with the degree of polarization in a uniform magnetic field given by

$$\Pi = \frac{p+1}{p+7/3} \tag{1.8}$$

Linear polarization and a negative spectral index are the two defining characteristics used to identify sources of synchrotron emission, although either is usually sufficient to identify the emission mechanism. Radiation can however be depolarized due to a variety of reasons ranging from random orientations of the magnetic field vectors within the resolution element of the telescope or thermal material along the line of sight to Faraday rotation in the Earth's ionosphere. Depolarization scales as λ^2 and consequently measurement of polarization at low frequencies is usually difficult. Hence, while detection of linearly polarized emission is a strong proof of synchrotron emission, a lack of it cannot rule it out. A negative spectral index is therefore frequently used as a signature of synchrotron radiation.

1.2 Galactic Supernova Remnants

A large number of SNRs are radio sources with only less than 30% visible in optical and X-ray bands. The lack of optical and X-ray radiation is primarily due to obscuration by the Galactic disk. Out of the 225 Galactic SNRs listed in the catalogue of Galactic SNRs (Green 2000), about 80% are of shell-type morphology (see Section 1.2.4) with a median size of ~ 30 arcmin. The emission is polarized (fractional polarization at $5-10\%$ level for the shell-type SNRs and much higher for filled centre SNRs) with a negative spectral index and is therefore believed to be synchrotron radiation. These gross observed radio properties of the radio emission from SNRs can be understood by modeling the shock wave as a spherical supersonic piston propagating in a uniform medium (the ISM) sweeping up the ISM mass as it moves. Its evolution is described as four distinct stages (Reynolds 1988, and references therein):

- Free expansion phase

  In this stage of the evolution, the ejected mass $M_\circ$ is much more than the mass swept-up by the shock front, i.e. $M_\circ \gg 4\pi R_s^3 \rho_1/3$ where R_s is the shock radius and ρ_1 the pre-shock density. The influence of the ISM on the dynamics of the ejecta in this stage is negligible and the initial properties of the explosion dominate the evolution. Consequently the blast wave freely expands into the medium.

- Sedov phase

  With time, the shock front sweeps up the ISM material and enters this phase when the swept-up ISM mass is comparable to that of the ejected mass. The shock is still strong and the pressure due to the swept-up mass is negligible. The expansion is essentially adiabatic (which is the other name this phase goes by) and the dynamical evolution is given by Sedov (1959) solution for the dynamics of a point explosion in a uniform medium. For a gas with the ratio of specific heats of 5/3, the shock radius and velocity (v_s) are given by

$$R_s = 1.17 \left(\frac{E_\circ}{\rho_1} \right)^{1/5} t^{2/5} \tag{1.9}$$

$$v_s = 0.4 R_s / t \tag{1.10}$$

where $E_\circ$ is the supernova energy. The ejecta begin to decelerate in this phase and a reverse shock develops which propagates into the ejecta, thus thermalizing it. The reverse shock propagating into the circumstellar material is thought to be responsible for the observed X-ray emission.

- Radiative phase

  Once the age of the remnant becomes comparable to the radiative cooling time scales near the shock, the blast wave enters the radiative phase. The deceleration becomes rapid and the shock compression becomes large. By this time, the dynamics and the resulting observed morphologies are significantly affected by the structure of the ISM, particularly the inhomogeneity of the ISM.

  The time at which this phase begins and the shock velocity at this time is given by

$$t = 3.5 \times 10^4 \left(\frac{E_\circ}{10^{51}\ \mathrm{erg}} \right) n_1^{-9/17}\ \mathrm{yr} \tag{1.11}$$

$$v = 230 n_1^{2/17} \left(\frac{E_\circ}{10^{51}\ \mathrm{erg}} \right)^{1/17}\ \mathrm{km\ s^{-1}} \tag{1.12}$$

  where n_1 is the pre-shock number density.

- Dissipative phase

  Once the expansion velocity of the shock decreases below the local sound speed, it dissipates and merges with the ISM on time scales of $10^5 - 10^6$ years.

This simple model of a shock wave propagating in a uniform medium, however, ignores a number of other effects such as dynamical effects of the magnetic field, pressure forces in the radiative phase and inhomogeneities in the ISM (Woltjer 1972). Hydrodynamic calculations show that SNe produce ejecta with a uniform density towards the outer parts while the inner parts (close to the star) have a steep density profile (like $\rho \propto r^{-7}$). A reasonable density profile for Type I SNe has a constant density ejecta for the inner four-sevenths of the mass, and the outer three-sevenths obeying $\rho \propto r^{-7}$. Numerical simulations for Type I SNe with such a density profile modified the evolution of the shock radius to $R_s \propto t^{4/7}$ when the Sedov phase is reached, which is closer to the observed value of the exponent (e.g. for Tycho and SN 1006).

1.2.1 Nonthermal Emission from SNRs

As mentioned earlier, radio emission from SNRs is believed to be synchrotron radiation which requires understanding of the origin of the relativistic electrons and magnetic field. Broadly, the central pulsar is thought to be the source of both these quantities for Crab-like SNRs (see Section 1.2.4), while, for shell-type SNRs, both come from the ambient ISM. The inferred magnetic fields in SNRs, measured from the rotation measure measurements of background radio sources, X-ray observations and Zeeman splitting of OH maser lines (Brogan et al. 2000), is however $\sim 2-3$ order of magnitude higher than the ambient magnetic field, requiring magnetic field amplification mechanisms as well. Although it is easy to imagine amplification of the frozen-in magnetic field in the SNR shells, the observed brightness of young shell-type SNRs is often more than can be explained by magnetic field amplification due to compression by the shock alone (although, magnetic field strengths measured for a few SNRs using the Zeeman splitting of OH (1720 MHz) lines are consistent with the hypothesis that ambient molecular cloud magnetic fields are compressed via the SNR shock to the observed values (Brogan et al. 2000)). The observationally deduced magnetic field for Cas A is far too high to be explained by magnetic field amplification by compression by a factor 4 compression. Similarly, the deduced magnetic field for the shell-type Kepler's SNR (Matsui et al. 1984) is too high to be produced by the amplification of the ambient field in the shock front. It is therefore believed that for shell-type SNRs, a combination of particle acceleration in the shock front (Bell 1978a,b) and magnetic field amplification as well as particle acceleration behind the shock (Gull 1973; Cowsik & Sarkar 1984) are responsible for the observed radio brightness. On the other hand, the observed properties and the evolution of Crab-type SNRs are believed to be dominated by rotational energy loss from the central pulsar (Reynolds & Chevalier 1984).

Two classes of electron acceleration mechanisms have been used: turbulent acceleration at the unstable contact discontinuity and acceleration in the shock front itself. The first mechanism uses "second-order Fermi acceleration" and explains the morphology and emission from SNRs like Cas A. The latter mechanism uses the more efficient "first-order Fermi acceleration". This has the added advantage that the inferred electron energy spectra is naturally a power law and explains the morphology and the spectra of typical shell-type SNRs (Reynolds & Ellison 1992). Mechanisms for magnetic field amplification are however far less well understood. Magnetic fields measured in a few SNRs are much too high to be explained by compression alone. Observed magnetic fields which are predominantly radial in young SNRs (Dickel & Milne 1976) also argue against the amplified field being the swept-up ambient field. Magnetic field amplification in the Rayleigh-Taylor instability due to the deceleration of the ejecta (Jun & Norman 1996a; Jun et al. 1996; Jun & Norman 1996b), is an attractive model, especially for clumpy ejecta and/or circulstellar medium in the sense that it can explain the mostly radial orientation of the magnetic field in the SNR shells. Their simulation also shows that such magnetic field amplification is dependent on the orientation of the field and can produce morphologies similar to those of "barrel-shaped" SNRs.

1.2.2 Continuum Radio Spectra

Although the details of the particle acceleration and magnetic field amplification mechanism are still not well understood, it is clear from the observed data that the radio emission from SNRs is synchrotron radiation. Radio emission from SNRs above ~ 100 MHz has a non-thermal spectrum (Equation 1.7) and significant linear polarization ($5-10\%$ for shell-type SNRs and up to 30% for filled centre SNRs). Both these gross properties are considered to be defining properties of synchrotron emission. Integrated continuum radio spectra are therefore the primary signatures used to identify SNRs. As is also obvious, SNRs also produce sources of extended emission. Radio SNRs are classified into roughly four categories (see Section 1.2.4) based on the radio morphology. Radio morphology also provides information about the SNR type, its interaction with the ambient ISM as well as with the ambient magnetic field (Dickel & Milne 1976). Candidate SNRs are therefore often identified from single frequency observations based on the morphological evidence. However, H II regions in the Galaxy also exhibit extended radio emission easily detected at higher frequencies and, in some cases even exhibit morphologies similar to those of SNRs. Identifications of SNRs based on a single high frequency observation are therefore unreliable; observations at at least two frequencies are therefore usually required for proper identification of extended radio sources, to get a handle on the spectral index. Non-detection of thermal infrared emission, and where possible, lack of radio recombination lines (RRLs) are also used as supporting evidences to distinguish synchrotron sources from sources of thermal emission. However, RRL observations in the Galaxy are usually at coarse resolution and have a patchy coverage of the Galactic plane. High frequency observations in the Galactic plane also suffer from contaminating thermal emission (see Section 1.2.3), which has a relatively flat spectrum above ~ 1 GHz. Below this frequency, typical thermal emission strongly turns over due to free-free absorption. Synchrotron emission on the other hand, has a negative spectral index for a large range of frequencies. As a result, the emission from SNRs is usually stronger at lower frequencies while the thermal emission is severely diminished. For these reasons, high resolution observations at low frequencies where the non-thermal emission is stronger than the thermal emission can identify SNRs unambiguously and also measure spatially resolved brightness variations. The latter provide crucial information about the interaction of the blast wave with the ISM as well about particle acceleration/magnetic field amplification.

The spectral index depends on the kinetic energy input mechanism (e.g. turbulence in the shells of shell-type SNRs and the central pulsar in Crab-type SNRs), localized particle acceleration mechanisms (e.g. interaction of the shock front with higher density ISM) and the properties of the intervening ISM (e.g. differential free-free absorption across SNRs). About 80% of the known Galactic SNRs are of shell-type (Green 2000) and exhibit a broad range of spectral indices ($-0.2 < \alpha < -0.8$) with a mean value of ~ -0.5. This implies a mean electron energy spectrum $\propto E^{-2}$, close to what is expected from theoretical models for acceleration in strong shocks. Implied electron energy spectra corresponding to the lower range of α are explained by attributing them to weaker shocks while those corresponding to the higher range require the inclusion of non-linear effects. Data also suggests a trend in the spectral index with the remnant age (i.e. with diameter). Smaller diameter SNRs, considered to be younger, have $\alpha < -0.5$ while older, larger diameter SNRs have flatter spectra. However it must also be kept in mind that the measured diameter is subject to (often large) errors in the distance estimate. Even if the distance is well known, the diameter of the SNR can be strongly influenced by the properties of the progenitor star and the local ISM and the inferred age may be quite different from the true age. Spectral indices for most SNRs have been obtained from measurements carried out with a variety of telescopes and techniques, resulting into uncertainties in flux density scales. As a result, the spectral indices are seldom known to accuracies better than ~ 0.1.

Measurements of spatial and/or temporal variations in the radio spectra of SNRs are probably the best way to study the nature of electron acceleration mechanisms. Spatial spectral variations provide information about the local dynamics and require spatially resolved observations at at least at two frequencies. High resolution observations are usually done using interferometric telescopes. However, the set of the spatial frequencies measured by such instruments with fixed physical separation between the antennas are a function of the observing frequency. As a result the spatial frequencies sampled at two different frequencies are in general different and dividing the two images at different frequencies to obtain spectral index maps produces artifacts. In telescopes like the Very Large Array (VLA) this problem is solved by scaling the array in proportion to the observing frequency, but for most other interferometric telescopes, this remains a problem. Observations with interferometric telescopes also suffer from missing larger scale emission which in turn result into differences in flux density base-level. Similarly, single dish observations also suffer from base-level problems due to very large scale background emission within the field of view of the telescope. To minimize the errors in the measurement of spectral index due to these effects, Anderson & Rudnick (1993) used the so called "T-T plot" to measure the local gradient in the maps at two frequencies. This method is insensitive to large scale base-level variations in the two maps and gives a more reliable spatially resolved spectral index measurement. They find a spatial variation from -0.7 to -0.4 across a few, hopefully representative, SNRs. More recently Katz-Stone et al. (2000a) used the method of spectral tomography to measure spectral variations within Tycho's SNR. They identified a number of filaments with spectral index different from that of the smoother background. The filaments in the outer rim show a trend such that brighter filaments have a flatter spectral index which could be due to the interaction of the blast wave with a inhomogeneous ambient medium or due to inhomogeneities in the magnetic field.

Absorption by the low density ionized medium

In their classic papers on the measurement of low-frequency continuum spectra of Galactic supernova remnants, Dulk & Slee (1975) reported spectral turnovers in several SNRs in the galactic plane at low frequencies. Such a turnover in the spectra of SNRs has since been confirmed by more extensive measurements at ~ 31 MHz (Kassim 1989). The spec-

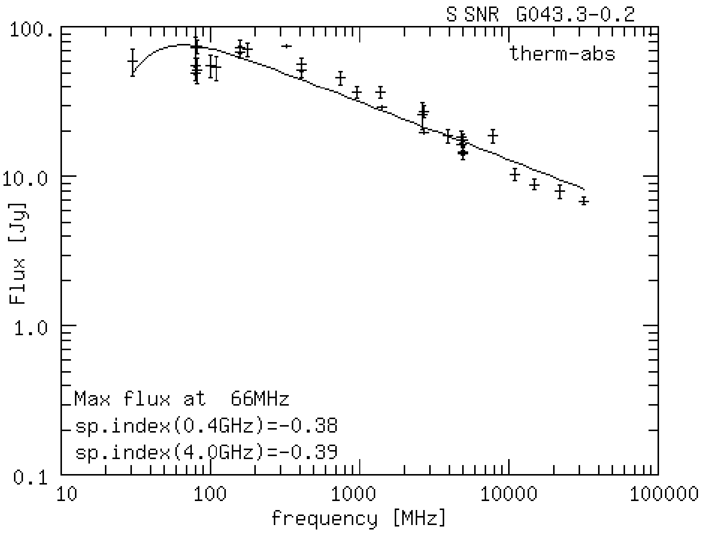

Figure 1.3: Plot showing a typical continuum spectra for Galactic SNRs. The spectral index at frequencies > 100 MHz is clearly non-thermal. Below this frequency, the flux density decreases due to free-free absorption in the intervening low density ISM.

tral index above ~ 100 MHz is negative and is typical of most SNRs (Fig.1.3[1]). The spectra however turns-over below this frequency due to absorption by low density ionized gas in the intervening ISM (Kassim 1989). The observed flux density at a frequency ν in the presence of absorbing foreground medium of free-free optical depth $\tau_{\nu_\circ}$ at a reference frequency $\nu_\circ$ can be written as

$$I(\nu) = I(\nu_\circ)\left(\frac{\nu}{\nu_\circ}\right)^{\alpha} e^{-\tau_{\nu_\circ}\left(\frac{\nu}{\nu_\circ}\right)^{-2.1}} \tag{1.13}$$

where $I(\nu)$ is in Jansky and the frequency ν is in MHz. $\tau_{\nu_\circ}$ is related to the emission measure EM(cm^{-6} pc^{-1}), and the electron temperature T_e(K) (Dulk & Slee 1975) by

$$\tau_\nu = 1.643 \times 10^5 a\left(T_e, \nu\right)\left(\nu^{-2.1}\right)\left(EM\ T_e^{-1.35}\right) \tag{1.14}$$

where $a(T_e, \nu)$ is the Gaunt factor, ~ 1 for the relevant range of T_e and ν. The emission measure EM is defined as

$$EM = \int_L n_e^2 dl \tag{1.15}$$

[1]Taken from the catalogue of Galactic SNR spectra compiled by S. A. Trushkin and available on the web from http://www.ratan.sao.ru/~cats

where n_e is the thermal electron density in cm^{-3} and the L is the path length to the source in parsec. With an estimate of the distance to an SNR and assuming that the spectral index is same at the range of frequencies under consideration, these equations can be used to estimate the properties of the absorbing gas, namely τ_ν and n_e. The absence of a low frequency turn over towards distant SNRs places severe constraints on the thermal electron density of any widely distributed ionized medium: $n_e \leq 0.26$ cm^{-3} for $T_e = 8000$ K and $n_e \leq 0.13$ cm^{-3} for $T_e = 3000$ K. If the absorbing gas is the warm ionized medium, the obtained parameters, using the optical depth derived from the study of low frequency spectral turn over and a path length of 100 pc are: $n_e \sim 2.9$ cm^{-3} for $T_e = 3000$ K and $n_e \sim 5.7$ cm^{-3} for $T_e = 8000$ K. The fact that some of the distant SNR do not show low frequency absorption while some of the closer ones do demonstrates that this medium is patchy and localized (Kassim 1989).

Evidence for the existence of a widespread low-density ionized component in the inner Galaxy has come from observations of radio recombination lines (RRLs) near 1400 MHz (Hart & Pedlar 1976; Lockman 1980; Heiles et al. 1996) and near 327 MHz (Anantharamaiah 1985b; Roshi & Anantharamaiah 2000). These RRLs have been detected at almost every observed position in the inner Galaxy (with $b = 0°$ and $|l| \leq 60°$) including those positions where there are no discrete radio continuum sources (i.e. blank regions). This is believed to be the extended H II region envelopes (EHEs) (Anantharamaiah 1985a). The parameters of the gas derived from the RRL observations are $T_e \sim 2000 - 8000$ K, $n_e \sim 0.5 - 10.0$ cm^{-3}, with a filling factor of $< 3\%$. Based on the statistics of spectral turnovers in a number of SNRs and the properties of the low-density envelopes derived using RRL data, Kassim (1989) has argued in favor of a connection between the RRL-gas and the free-free-absorbing gas towards SNRs. The optical depth towards a few SNRs inferred from the low frequency spectral turn over and that from RRL observations agree well with each other, lending support to this suggestion. On the theoretical front, McKee & Williams (1997) considered the luminosity function of OB associations in the Galaxy and found that about 65% of the ionizing photons emitted by O and B stars are absorbed outside the known HII regions. About 10% of these photons are needed to maintain the Warm Ionized Medium (WIM). The majority of the escaping photons can thus generate large HII envelopes. These HII envelopes are thus a reservoir of more than 50% of the ionizing photons emitted by all the O and B stars. An understanding of the properties of this ionized component is thus important in the galactic context. However the evidence remains circumstantial. The resolution of the low frequency RRL observations was too coarse to localize the source of RRL emission. High resolution RRL observation towards SNRs which do show spatially resolved low frequency absorption will provide a direct test for this. The Giant Meterwave Radio Telescope (GMRT) offers the right range of frequencies, resolution and sensitivity for these observations and is an ideal instrument for such a study.

1.2.3 Thermal emission

Apart from non-thermal emission, the Galactic plane, particularly at low Galactic latitudes, is also a sources of significant radio emission with a thermal spectrum. This emission is from H II regions and planetary nebulae in the Galaxy and is caused by the interaction between free charged particles, referred to as free-free or thermal *bremsstrahlung* emission.

The observed intensity from an emitting region of linear size L with a foreground radiation intensity of I_{fg} and background intensity of I_{bg} is given by

$$I = I_{bg}e^{-\tau} + \int_0^\tau \frac{j}{\kappa} e^{-t} dt + I_{fg} \tag{1.16}$$

where j and κ are the emission and absorption coefficients, and τ is the optical depth.

A charged particle moving in the electric field of another charged particle undergoes a change in its direction of motion. This change of direction requires acceleration and as a result the particle emits electromagnetic radiation. In a realistic situation, however, there is a distribution of particle velocities and the total radiation is determined by integrating the emission during one interaction over the velocity distribution. To compute this, it is assumed (1) that the electric field in which the particle is moving is effective only over a finite distance, (2) that the radiated energy is small compared to the kinetic energy of the moving particle (i.e. the encounter is adiabatic) and (3) the period of the emitted wave is small compared to the duration of the encounter. For a Maxwellian velocity distribution, $j(\nu)/\kappa(\nu) = B_\nu(T_e)$ where $B_\nu(T_e)$ is the Plank function. For $h\nu < kT_e$, this can be approximated by $B_\nu \approx 2kT_e/\lambda^2$ - the usual Rayleigh-Jeans approximation. For a source of homogeneous density and temperature with $I_{fg} = 0$, and using the Rayleigh-Jeans approximation, Equation 1.16 can be written as

$$I = I_{bg}e^{-\tau} + \frac{2kT_e\nu^2}{c^2}(1 - e^{-\tau}) \tag{1.17}$$

The flux density S at a frequency ν is defined as

$$S = \int_{source} I_\nu d\Omega \approx \frac{2k\nu^2}{c^2} \int T_{source} d\Omega \tag{1.18}$$

where Ω is the angular extent of the source and T_{source} is the source electron temperature. Equation 1.17 can then be transformed to an equation for the observed integrated flux density, assuming $I_{bg} = 0$, as

$$S_\nu = S(1 - e^{-\tau}) \tag{1.19}$$

In the high frequency, optically thin regime ($\tau \ll 1$), $S_\nu \approx S\tau$ and, since $\tau \propto \nu^{-2.1}$ and $S \propto \nu^2$, $S_\nu \propto \nu^{-0.1}$. Thus, the spectra at high frequencies is a weak function of the frequency. On the other hand, in the optically thick regime of low frequencies, $S_\nu = S \propto \nu^2$. Hence the spectral indices for radiation above and below the critical turnover frequency (typically $1 - 2$ GHz) are markedly different (-0.1 and 2 respectively, see Fig. 5.15).

From the point of view of radio study of SNRs, the important point to note is that thermal emission progressively diminishes at frequencies below ~ 1 GHz while the non-thermal emission progressively becomes stronger in this range of frequencies. Strong emission from H II regions has been observed all along the Galactic plane. High frequency observations close to or above this frequency are more sensitive to thermal emission and not well suited to the study of SNRs which emit non-thermal radiation at radio bands. On the other hand, at lower frequencies, thermal emission is diminished while non-thermal emission from SNRs progressively becomes stronger (see Fig. 5.15). Low frequency observations, where the contamination from thermal emission is minimized, are therefore more suited for the study of SNRs.

As mentioned above, angular resolution is important from the point of view of SNR identification and other detailed studies (particle acceleration, interaction with the local ISM, brightness variation as a function of galactic latitude, etc.). Since emission in the galactic plane occurs at all angular scales, it is also important that the observations be sensitive to large scale emission. To meet the requirement of high angular resolution with sensitivity to large scale emission, many observations of SNRs have been done at high frequencies either single dish instruments (Clark et al. 1975b,a; Duncan et al. 1997a,b) or using interferometric telescopes (Kesteven & Caswell 1987; Whiteoak & Green 1996; Gray 1994b,a). However the *uv-coverage* of these interferometric observations was not good resulting into severe artifacts in the images. Also, these observations often suffer from contamination by thermal emission, particularly for fields in the Galactic plane.

The GMRT, operating at 150, 233, 327, 610 and 1400 MHz provides frequency coverage where, typically, non-thermal emission is dominant. With a shortest physical antenna separation of ~ 100 m and largest separation of ~ 25 km, it also provides high angular resolution at these low frequencies (~ 20 arcsec to ~ 2 arcsec) while remaining sensitive to emission at large angular scales ($\sim 1^\circ$ to ~ 10 arcmin). With a large collecting area, GMRT offers many advantages for the study of Galactic non-thermal emission in general and SNRs in particular. High resolution multi-frequency mapping of the galactic plane will also make it possible to identify compact sources of non-thermal emission (possibly compact SNRs) which may be confused with compact thermal sources in high frequency observations.

1.2.4 Radio morphology

The gross morphology of SNRs is largely governed by (1) properties of the progenitor and the pre-supernova circumstellar environment and (2) properties of the local interstellar medium and magnetic field. Traditionally, Galactic SNRs are classified in four different categories namely (1) shell-type, (2) filled centre (or Crab-type), (3) composite and (4) barrel shaped. About 80% of the SNRs in the Galactic SNR catalogue compiled and maintained by Green (2000) exhibit what is referred to as the shell-type morphology. This is expected from the generic model of an isotropic blast wave ploughing though the ISM and producing a bubble of emission after it slows down, having gathered enough ISM mass at the shock front. In projection, the bubble appears as a ring or shell of emission. On the other hand Crab-type SNRs exhibit a nebula of flat spectrum emission and is believed to be powered by the central neutron star. Variations of these basic morphologies are produced either due to a difference in the progenitor or in the local interstellar environment. The observed properties of these classes of SNRs are also therefore characteristic of the class and are briefly described below.

- **Shell-type**

  As mentioned above, 80% of the known Galactic SNRs are of this type. Typical examples are Kepler's and Tycho's SNR, SN 1006 (Fig. 1.4). These SNRs are characterized by a ring of emission which is often incomplete. As the blast wave decelerates, it enters the radiative phase of its evolution. The contact discontinuity between the shock front and the shocked medium is unstable and produces a thin shell of turbulence. The turbulence in the shell is believed to be the source of particle acceleration within the shell and magnetic field amplification by turbulent mixing (Chevalier 1982). A reverse shock develops just behind the shell and moves into the out-flowing ejecta, heating it to sufficiently high temperatures to produce the observed X-ray emission (Chevalier & Fransson 1994).

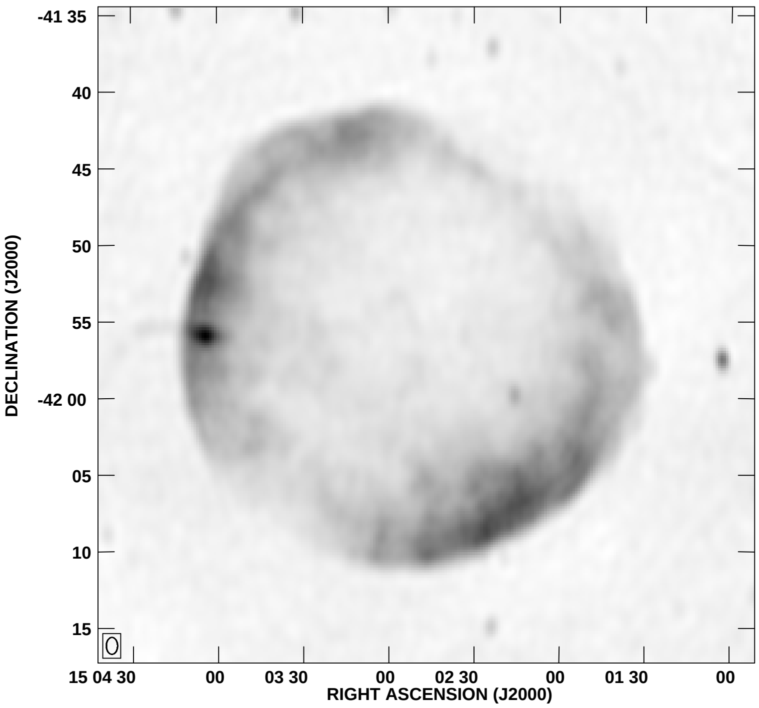

Figure 1.4: Image of a typical Galactic Shell-type SNR SN 1006 (courtesy of ADIL; image code `98.BG.01.07`). This 8-GHz image was made using the Molonglo Synthesis Radio Telescope (MOST). The brightened shell of emission with a weaker emission projected against the center is clearly seen.

The typical average spectral index α along the shell ranges from -0.7 to -0.3. In some of the sensitive images of shell-type SNRs, weak emission (from the bubble) is sometimes seen in projection, filling the interior of the ring. The spectral index of this emission and the ring is, however the same, indicating that this corresponds to the bubble of emission seen projected at the centre of the shell. Substantial variation in the brightness across the shell of emission is often seen and may be due to the inhomogeneity of the local ISM with which the shock front interacts. This also produces spectral index variations in some cases (Anderson & Rudnick 1993) indicating sites of enhanced particle acceleration or magnetic field amplification. The emission from the shell is linearly polarized at $5 - 15\%$ level and the inferred projected magnetic field is usually radial.

- **Filled centre/Crab-like/Plerionic**

  These types of SNRs are characterized by a flat spectrum plerionic emission ($\alpha \geq -0.3$) almost uniformly filling the emission region. Less than 10% of the known Galactic SNRs are of this type. Strong linear polarization up to 30% level has been observed from such SNRs. A typical example of this class of SNRs, not surprisingly, is the Crab SNR (Fig. 1.5) or 3C58. Reynolds & Chevalier (1984) modeled a plerion as a spherical, homogeneous bubble of relativistic particles and magnetic field inflated by a central neutron star amidst uniformly expanding supernova ejecta. The plerionic emission is believed to be driven by the rotational energy losses of the central neutron star, which is seen as a pulsar at the centre of the Crab nebula. The central neutron star is believed to be the source of the magnetic field as well as of the energy which accelerates the electron in the medium thereby maintaining the flat spectrum of the emission. With the advent of high resolution X-ray telescopes, many plerionic SNRs have been found to be strong X-ray sources where the X-ray emission comes from the central region.

  The blast wave should however produce a shell of emission outside such a nebula where it interacts with the ISM. The existence of a high-velocity, hydrogen-rich envelope corresponding to the initial blast wave is also required to account for the low total mass and kinetic energy of the observed nebula. No shell of emission has however been detected for such SNRs - at least not at radio frequencies. A deep search for the shell around the Crab nebula did not reveal any shell emission and this has been interpreted as being due to the blast wave expanding into a low density medium (Frail et al. 1995). The spectral index of the plerionic emission for the Crab nebula is ~ -0.26. If the shell is close to the edge of the nebula, it can be distinguished from the nebula by the change in the spectral index from this value to close to ~ -0.5, typical for shock accelerated shell emission. No evidence for a significant change in the spectral index was found by these authors. Similarly no such shell has been found in Hα and X-ray emission (Predehl & Schmitt 1995; Fesen et al. 1997). However, HST observations reveal a thin shell of [OIII] emission around the nebula

[2]The National Radio Astronomy Observatory is a facility of the National Science Foundation operated under cooperative agreement by Associated Universities, Inc.

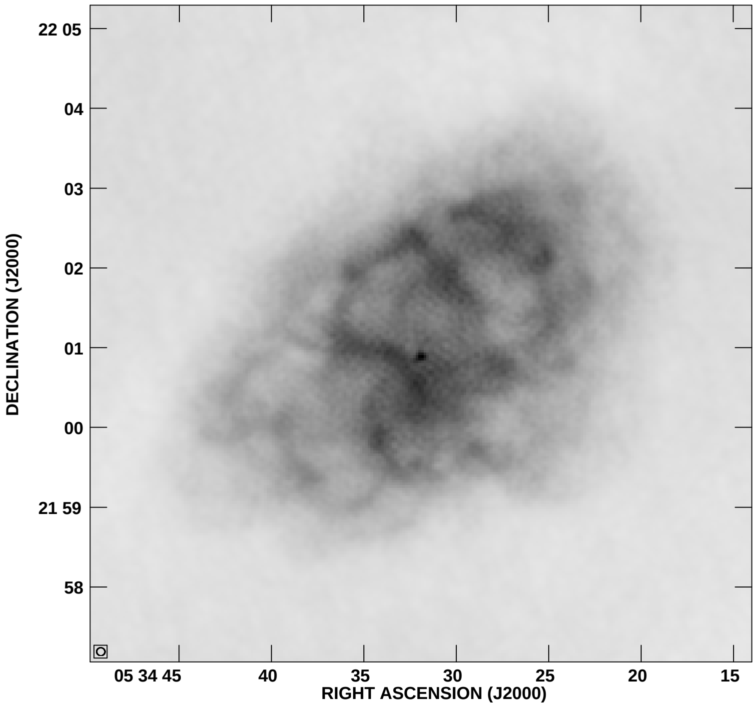

Figure 1.5: Image of a typical Galactic plerionic SNR - The Crab nebula (courtesy of ADIL; image code `95.RP.02.01`). This 327-MHz image was made using the VLA and is copyrighted by the NRAO[2](Observer: R.P.Perley). The compact source in the centre is the Crab pulsar.

(Sankrit & Hester 1997) which is interpreted as a cooling region behind a radiative shock propagating at ~ 150 km s^{-1} in a medium of density ~ 10 cm^{-3}. Ironically, the Crab SNR may then no more be of the "crab-type" but may be re-classified as of the composite class (see below).

Such shells have also not been detected for other plerionic SNRs. If the tenuous environment in which these SNRs are expanding is the reason for non-detection of the shell in radio continuum emission, it has been suggested that one must look for signs of interaction with the surrounding atomic or molecular gas (Jones et al. 1998). 21-cm neutral hydrogen observations of G074.9+1.2 (CTB87), which is a pulsar powered SNR with no outer shell, shows that this SNR lies within an expanding HI bubble (Wallace et al. 1997). The radio continuum emission also shows signs of flattening at a point of apparent contact between the HI bubble and the SNR, lending further support to this model. However evidence for a shell of emission around other plerionic SNRs like 3C58 remains elusive.

Compact radio quiet thermal X-ray sources within SNRs have also been found in a few remnants (Gotthelf et al. 1997; Gotthelf & Vasisht 1997; Vasisht & Gotthelf 1997). These compact objects may be radio quiet neutron stars in the SNRs and may thus explain the embarrassing lack of pulsar-SNR associations (Kaspi 1998) in the sense that a non-pulsar neutron star or radio-quiet pulsar may be associated with many SNRs. The recent discovery of X-ray pulsations from some of these compact sources (Vasisht et al. 2000; Gotthelf et al. 2000) lend support to the idea that for these compact objects are indeed the elusive radio quiet neutron stars which are thought to be produced by the explosion and hence associated with the SNRs.

- **Composite**

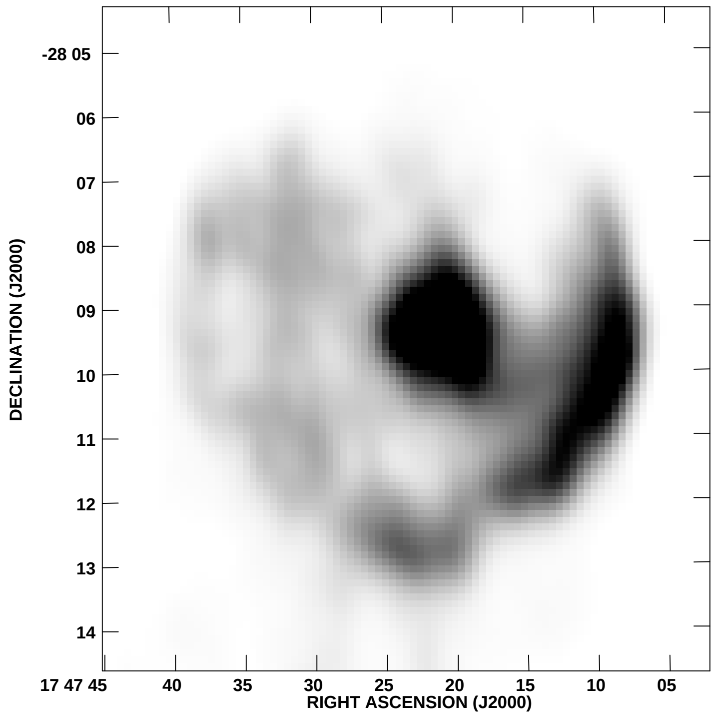

Figure 1.6: Image of a typical Galactic composite/mixed morphology SNR G000.9+0.1 taken from LaRosa et al. (2000). The shell and plerionic emission is clearly visible. The central compact source coincides with a compact thermal X-ray source.

This class of SNRs exhibit characteristics of both shell-type and plerionic SNRs (Fig. 1.6). These SNRs are characterized by flat spectrum emission from the central region with a steeper spectrum shell of emission. Typical examples of this class of SNRs are G000.9+0.1, CTB80, G326.3−1.8.

With high resolution imaging now possible in the X-ray band, this class has grown to include what are referred to as "centrally influenced" remnants; e.g. objects with shock powered radio shells with centrally enhanced X-ray emission. The X-ray radiation can be in the form of hard X-ray non-thermal emission from a compact nebula and/or extended soft thermal X-ray emission. Rho & Petre (1998) term SNRs with thermal X-ray emission inside hollow radio shells as "mixed morphology" SNRs. The X-ray emission is proposed to come from the evaporation of clouds (of pre-explosion origin) by the reflected and reverse shocks. Many of the thermal X-ray composite SNRs are interacting with molecular clouds (conclusions drawn from molecular line and OH maser observations, e.g. W44, 3C391, W28, IC443) (Frail et al. 1994; Claussen et al. 1997; Yusef-Zadeh et al. 1999; Frail & Mitchell 1998) and it has been suggested that this may be a generic property of the class.

- **Barrel shaped**

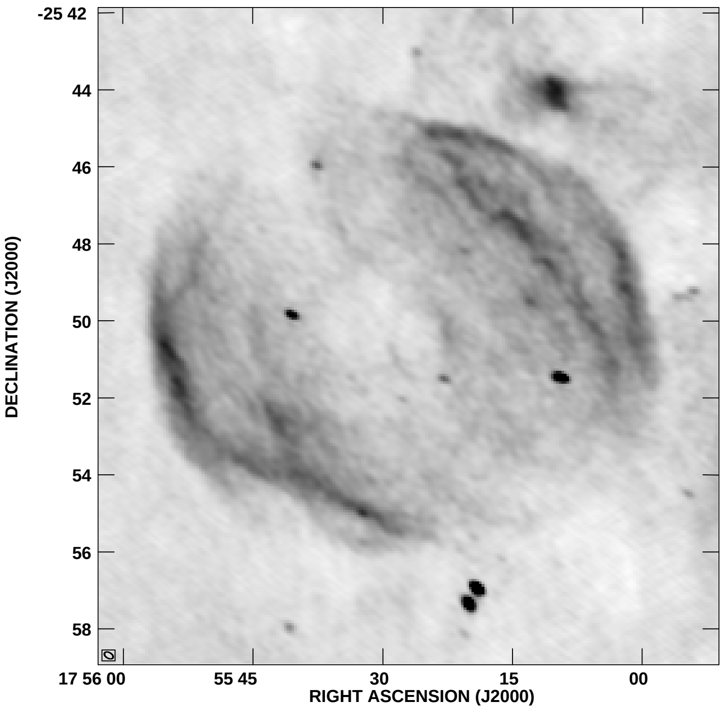

Figure 1.7: Image of a typical Galactic barrel-type G003.7−0.2 (Gaensler 1999) (image courtesy of ADIL; image code `98.BG.01.01`). This 1.4-GHz VLA image shows the double arc structure with an axis of symmetry running right through the middle of the two brightened arcs of emission.

These remnants are characterized by a clear axis of symmetry with lower emission along the axis in between two brighter limbs (Whiteoak & Gardner 1968; Kesteven & Caswell 1987; Caswell et al. 1989) (Fig. 1.7). Proposed explanations for such a morphology are either on the lines of "extrinsic" effects relating to the ambient ISM and magnetic field and "intrinsic" effects relating to the progenitor and its circumstellar medium. Such morphologies can be produced if the ejecta expands inside an elongated cavity (Bisnovatyi-Kogan et al. 1990). Alternatively, ejecta expanding in a uniform magnetic field will preferentially compress where the shock normal is perpendicular to the field lines producing enhanced emission where the magnetic field is more compressed (van der Laan 1962). On the other hand, such morphologies can be produced due to intrinsic reasons like toroidal distribution of ejecta (Bodenheimer & Woosley 1983) or due to initial high velocity of the progenitor (Rozyczka et al. 1993) or intrinsic preferentially polar outflows from the central compact object (Manchester & Durdin 1983; Willingale et al. 1996).

Analysis of highly resolved images of 17 barrel shaped SNRs done by Gaensler (1998) show evidence of a statistically significant tendency for the bilateral axes to be aligned with the Galactic plane. This is interpreted as lending support for the extrinsic effects being the dominant cause for the observed morphology - namely the alignment of the magnetic field with the Galactic plane.

1.2.5 Galactic distribution

Fig. 1.8 shows the distribution of the known Galactic SNRs as a function of Galactic longitude. Most of the known Galactic SNRs are in the 1st or the 4th quadrant. This bias towards the inner Galaxy is attributed to the fact that most of the star forming regions are in the Galactic arms which cover a larger fraction of the inner Galaxy. However, there appears to be a mild lack of SNRs in the 4th quadrant compared to the 1st quadrant which is most likely to be due to some selection effect, probably due to the use of different telescopes in these quadrants (Clark et al. 1975b; Altenhoff et al. 1979; Clark et al. 1975a; Kesteven & Caswell 1987; Gray 1994b,a; Whiteoak & Green 1996; Duncan et al. 1997a,b).

The incompleteness of the current Galactic SNR catalogue has been pointed out by Green (1991). He noted that the catalogue is incomplete in very large low surface brightness as well compact small sized young SNRs. Low surface brightness SNRs may be missed due to sensitivity limits of the observations. Higher frequency observations may also miss them because they are also inherently weaker at high frequencies. Such SNRs will also be missed in interferometric observations which are not sensitive to emission

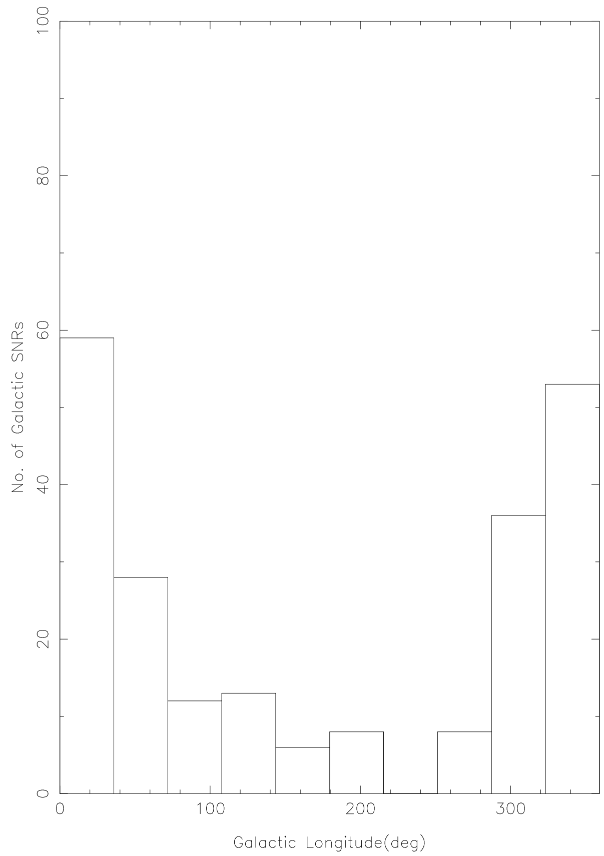

Figure 1.8: Distribution of known Galactic SNRs as a function of Galactic longitude. Most of the known SNRs are in the 1st and 4th quadrants. The number of SNRs in the 4th quadrant are however slightly less than that in the 1st quadrant. Significant lack of SNRs in the 3rd and 2nd quadrants is attributed to lack of star forming regions there.

at angular scales larger than a maximum value. Small sized compact SNRs may be missing because of confusion with compact source of thermal emission. Any statistical result based on the current SNR catalogue is therefore likely to be affected by these selection biases. This is reflected in about a factor of $2-3$ error in the distance estimates for SNRs using the statistically derived Σ-D relation. Green (1991) also argues that the proposed Σ-D-z relation is not statistically significant.

Statistical studies of a complete sample of Galactic SNRs can help answer many question about the remnants themselves, their parent supernovae, their relation to pulsars and their interactions with the ISM and the ambient magnetic field. Observations to remove, if possible, the above mentioned biases in current catalogues are therefore important from the point of view of Galactic SNR research.

1.3 Effects of the ISM on the observed properties of SNRs

Most of the emission from SNRs is due to the interaction of the blast wave with the material into which it expands (the circumstellar envelope or the ISM). Low frequency spectral turnover, pulsar dispersion measures, HI absorption and brightness variations across SNRs, in particular along the shells of the shell-type SNRs suggest that the environments into which SNR expand are non-uniform. This is, however, hardly surprising since the structure and energetics of the ISM is largely dominated by star forming regions and supernova explosions, both of which are localized compared to the extent of the Galaxy. These density variations in the ISM are in-turn also expected to shape the morphologies of the SNRs. Interaction of the blast wave with higher density regions will result in stronger deceleration resulting in higher turbulence. This produces larger particle acceleration and consequently stronger synchrotron emission in such regions of interaction. On the other hand, the ejecta will expand at a more rapid rate in a lower density region and may even become radio loud at comparatively later times when the swept-up mass is enough to decelerate the blast wave. These effects are believed to give rise to the blow-out (G312.4−0.4), one-sided (G338.1+0.4) or irregular morphologies. The expanding blast also interacts with the ambient magnetic field and amplifies it via turbulent amplification or by simple compression of the frozen-in fields. This interaction of the blast wave with the magnetic field is believed to be responsible for the barrel shaped SNRs and it has been suggested that many intrinsically barrel shaped SNRs may not appear to be so due to projection effects (Gaensler 1998).

Spatially resolved spectral index variations across SNRs trace changes in particle kinetic energies or magnetic field strengths or both. Both of these could also be due to the inhomogeneous nature of the medium into which the ejecta expands; reliable spatially resolved spectral index maps of SNRs thus give a handle on the scale of inhomogeneities in the ISM (Anderson & Rudnick 1993; Katz-Stone et al. 2000a). Spectral index changes across SNRs probe scales smaller than the size of the remnants. If the intrinsic properties of the SNRs can be independently established, spectral index changes between widely separated SNRs will probe scales of the order of the separation between the remnants.

It has been shown recently that the OH (1720 MHz) emission is associated with SNRs while the other OH maser transitions are associated with HII regions (Frail & Mitchell 1998). Both theoretical and observational evidence (Reach & Rho 1998, 1999; Frail & Mitchell 1998) suggests that the OH (1720 MHz) masers are associated with the C-type shocks and are collisionally pumped in molecular clouds at temperatures and densities of $50 - 125$ K and $10^5 - 10^6$ cm^{-3} respectively (Lockett et al. 1999, and references therein). OH masers at 1665, 1667 and 1612 MHz cannot be produced under these physical conditions and the absence of these lines along with the detection of OH (1720 MHz) emission favors this interpretation. The measurements of the post shock density and temperature for IC443 (van Dishoeck et al. 1993), W28, W44 and 3C391 (Frail & Mitchell 1998) are in excellent agreement with these theoretical predictions. A solution to the problem of producing OH, which is not directly formed by shocks, are proposed by Wardle et al. (1999). They suggest that the molecular cloud is irradiated by the X-rays produced by the hot gas in the interior of the SNR. This leads to photo-dissociation of the H_2O molecules, which is produced by the shock wave in copious amounts, behind the C-type shock resulting in the required enhancement of OH just behind the shock. Indeed, such maser emission has been found in SNRs whose morphologies have long been suspected to be shaped by their interaction with nearby molecular clouds (Frail et al. 1994; Claussen et al. 1997; Green et al. 1997). The fact that OH (1720 MHz) emission is possible for a very narrow range of physical parameters of the gas and other OH transitions in this range do not produce maser emission provides a powerful tool to probe the interaction of SNRs with molecular clouds. Detection of extended OH (1720 MHz) emission along with compact maser spots, tracing the radio continuum emission is suggestive of the maser emission tracing the extended region of such an interaction (Yusef-Zadeh et al. 1999).

1.4 Why low frequency?

As mentioned above, radio emission from SNRs is synchrotron radiation which has a non-thermal power law dependence on frequency with a negative spectral index α ($S \propto \nu^{\alpha}$). This makes the emission progressively stronger at lower frequencies (see Section 1.1). Thermal emission from typical HII regions, on the other hand has a flat spectrum above ≈ 1 GHz. Below this frequency the optical depth is much greater than 1 and the spectrum turns over with a spectral index of 2. Continuum spectra of Galactic objects at low frequencies are therefore frequently used to distinguish between thermal and non-thermal sources of emission (Kassim et al. 1989a; Kassim & Weiler 1990; Subrahmanyan & Goss 1995). Radio emission from SNRs is typically also extended, often with low surface brightness, with most of the remnants exhibiting easily identifiable morphologies. Detection of extended non-thermal emission in the Galaxy, with no thermal emission, has been the criterion used to identify Galactic sources as SNRs. Low frequency observations of SNRs also provide an added advantage in the sense that the surface brightness of typical SNRs increases at low frequencies, making it easier to detect and map them for detailed studies.

Interferometric telescopes are however insensitive to scales larger than those corresponding to the smallest projected baseline. Single dish telescopes, on the other hand, are sensitive to emission at all scales in the field. However, they provide the sensitivity and required resolution only at high frequencies. Many observations of SNRs till recently were therefore done using single dish instruments at high frequencies. However, apart from the contaminating thermal emission at these frequencies as well as inherently lower emission from SNRs, such observations are more prone to large scale confusing emission, which is abundantly present in the Galactic plane. The resolution of low frequency single dish observations is also not enough to resolve the extended emission.

Although high resolution interferometric observations of Galactic SNRs have been carried out, imaging at low frequencies using interferometers is also relatively tougher due to the problems arising from higher level of radio frequency interference (RFI), higher phase noise at low frequencies (due to various reasons ranging from cross talk to ionospheric phase corruption), non-co-planarity of arrays requiring much more complex software and higher computing power, etc. Hence, even interferometric observations have been typically done at frequencies > 1 GHz.

Sensitive low frequency observations which are also sensitive to extended emission are therefore most appropriate for SNR research. Aperture synthesis telescopes like the GMRT operating at relatively low frequencies are well suited for such observations.

1.5 Aperture synthesis at low frequencies

Low frequency aperture synthesis telescopes like the GMRT offer several unique advantages from the point of view of SNR research. The GMRT is best suited for SNR observations owing to its sensitivity, relatively high resolution as well as sensitivity to large scale emission at low frequencies. Observations done for this dissertation extensively used the GMRT which has only recently come to a stage where enough antennas are available in the interferometric mode to attempt the imaging of extended sources. Interferometry at low frequencies, however, poses new challenges in data calibration and analysis, which are interesting in their own right. A substantial fraction of the work done for this dissertation involved the debugging and calibration of the telescope, to enable the observations discussed above to be carried out. Further, large amounts of software were required to be written, both to carry out debugging activity as well as to enable flagging and calibration of telescope data in a semi-automated fashion. The origin of the problems in low frequency interferometry and the required on-line data monitoring and off-line data analysis are briefly described below.

1.5.1 Phase fluctuations

The plasma frequency of the ionosphere is ~ 12 MHz. The only cosmic radio emission reaching the surface of the earth is at frequency significantly higher than this value. However radio observations at a few 100 MHz are still severely affected by the ionosphere. The ionosphere is modeled as a thin (compared to the distance from the observing plane) slab of inhomogeneous plasma. A plane wave incident on the ionosphere filled with plasma blobs will emerge with the plasma fluctuations imprinted on the phase of the wavefront (Fig.1.9). The amplitude of this wave front will remain largely unchanged but the phase is no longer constant. The RMS phase fluctuations of the visibility phase induced due to the Earth's ionosphere can be written as (Cronyn 1972; Thompson et al. 1986, and references therein)

$$\Delta\phi = r_e \lambda a \Delta N_e \tag{1.20}$$

where λ is the wavelength, ΔN_e is the fluctuation in the electron number density, r_e is the classical electron radius and a is the characteristic size of the blobs. Low frequency observations are therefore more severely affected by temporal and spatial fluctuations in the ionospheric electron content. The diurnal and seasonal temporal fluctuations in the ionospheric electron content induced by the Sun and Solar activity directly affect the phase measured by low frequency interferometers, which, if not corrected, affects the sensitivity of the observations. Spatial fluctuations in ΔN_e are at scales ranging from several kilometers up to hundreds of kilometers. The wave front emerging out of such a phase screen can be thought of as composed of a number of plane waves traveling in slightly different directions. Decomposing this resultant wave into an angular spectrum of plane waves arriving from a variety of angles, one can define a full width of the angular spectrum, θ_s. This can be estimated by imagining that the blobs refract the incident wave by the amount $\pm\Delta\phi\lambda/2\pi$ over a distance a. Thus,

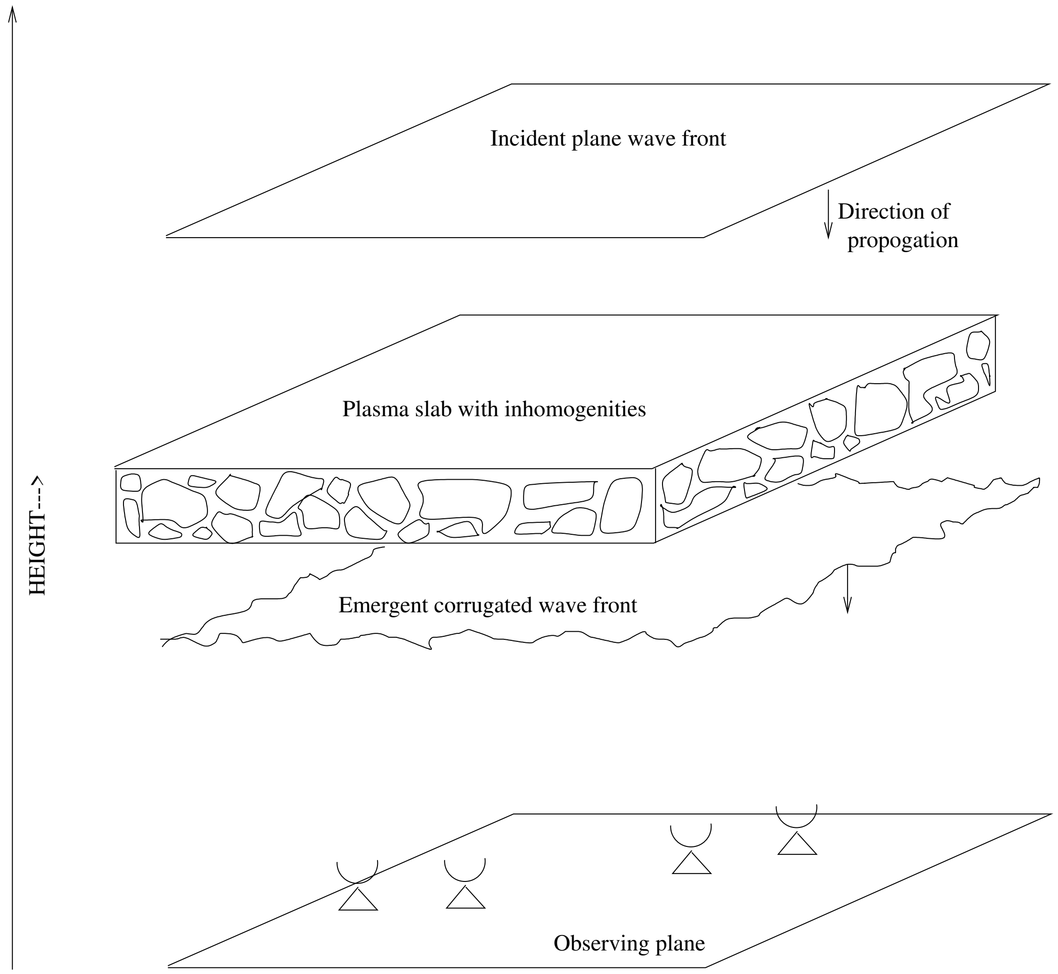

Figure 1.9: Schematic diagram showing the effect of the ionosphere. The incident plane wave above the ionosphere is shown with a constant phase. The ionosphere, modeled as a thin slab of inhomogeneous plasma, imprints the inhomogeneities on the phase of the emergent wave front. The emergent corrugated wave front is sampled at a various points on the observing plane by antennas separated in space.

$$\theta_s = \frac{1}{\pi} r_e \lambda^2 \Delta N_e \sqrt{L/a} \tag{1.21}$$

where L is the thickness of the ionospheric plasma screen. Let the correlation length of the ionospheric phase fluctuation be d. Phase corruption from two points in the ionosphere separated by more than this amount will be uncorrelated. Assume further that the joint probability distribution of these phases is Gaussian with a variance of $\Delta\phi^2$ and a normalized correlation function given by $\rho(d)$. For the sake of better understanding, let us also assume that

$$\rho(d) = e^{-d^2/2a^2} \tag{1.22}$$

It can then be shown that for $d \ll a$, the expectation value of the measured visibility V_m is given by

$$\langle V_m \rangle = V e^{-\Delta\phi^2 d^2/2a^2} \tag{1.23}$$

This limit samples the fluctuations in the phase due to fluctuations at length scales smaller than the typical blob size. Fluctuations at this scale induces small phase changes in the emerging wave front which can be treated as phase perturbations across the wavefront with the mean phase still preserved. Electron density fluctuations for $d > a$ induces large changes in the mean phase equivalent to a much larger spread in the angular spectrum. Consequently, $\langle V_m \rangle$ rapidly decreases for $d > a$.

The result of the these fluctuations is that a point source is broadened into a gaussian of diameter given by

$$\theta_s = \frac{\sqrt{2\ln 2}}{\pi} r_e \lambda^2 \Delta N_e \sqrt{L/a} \tag{1.24}$$

The final effect of phase fluctuations is therefore to effectively spread the power from a point source in the image (Cronyn 1972). If the intrinsic resolution of the telescope is smaller than θ_s, its resolution will be limited by the fluctuations in the phase and will be defined by θ_s. A more realistic treatment involves a power-law spectrum of phase fluctuations, similar to the Kolmogorov model for turbulence in a neutral medium. With such a power-law model for phase fluctuations, it can be shown that $\theta_s \propto \lambda^{2.2}$.

Ionospheric electron density also changes as a function of time due to diurnal and seasonal changes in the position of the Sun and also due to the activity on the Sun. Since the induced phase fluctuations scale with the wavelength, the effect of ionosphere is more severe at low frequencies. These phase errors need to be calibrated before the measured visibilities can be used for mapping. Long term (several tens of minutes) variations in the phase of an interferometer can be measured by periodic observation of a source of known structure, usually referred to as the phase calibrator, using the *self-cal* algorithm which decomposes the visibility phases into antenna based phases (Thompson & D'Addario 1982; Cornwell & Wilkinson 1981; Pearson & Readhead 1984). However for this, it is assumed that the variations in phase are small at angular scales smaller than the size of the primary beam of the antennas (iso-planatic case). At low frequencies, this assumption can break, at least for some fraction of time, and the derived phase corrections will not correct for the phase noise completely over the whole field. Schwab (1984) and Subrahmanya (1989) have described methods to relax the iso-planatic assumption. However, such algorithms have never been tried in real life or demonstrated to work well. This remains a potential problem, at least for high dynamic range imaging at low frequencies.

1.5.2 Non-coplanar baselines

The calibrated visibility function measured by an aperture synthesis telescope is given by[3]

$$V(u,v,w) = \iint I(l,m)P(l,m)e^{-2\pi\iota(ul+vm+w(\sqrt{1-l^2-m^2}))}\frac{dl\,dm}{\sqrt{1-l^2-m^2}} \tag{1.25}$$

where (u, v, w) are the projected co-ordinates of the antennas, l, m, and n are the direction cosines in the uvw co-ordinates system, $I(l, m)$ is the source brightness distribution (the image) and $P(l, m)$ is the far field antenna reception pattern (the primary beam).

For a small field of view ($l^2 + m^2 \ll 1$), V is related to the image by a 2D Fourier transform. However for $\theta_{PB}/\sqrt{\theta_r} > 0.1^{rad}$ where θ_{PB} and θ_r are the widths of the primary beam and the telescope resolution element, the image plane can no longer be expressed as a 2D Fourier transform of the visibility function (Cornwell & Perley 1999). The sky can no longer be approximated by a 2D plane and must be modeled as the surface of a

[3]The coefficient of w in the exponent for a fringe-stopped visibility (see Section 4.2) will be $(\sqrt{1-l^2-m^2}-1)$. This will effectively only shift the "image–volume" along the $n-$axis by one unit. Since this has no bearing on the problem of imaging with non-coplanar baselines, the -1 in the coefficient has been dropped from this equation.

sphere, referred to as the Celestial sphere. To continue to approximate Equation 1.25 as a 2D Fourier transform relation between the sky brightness distribution and the visibility will introduce severe distortions in the image away from the phase centre. The longest baseline for the GMRT at 327 MHz is ~ 25 km. Imaging with the GMRT at 327 MHz using baselines longer than $\sim 2-3$ km crosses the limit where the sky can be approximated, and a full 3D treatment of the problem is required to make distortion free images.

This problem can be handled by treating $\sqrt{1-l^2-m^2}$ as an independent co-ordinate. Re-writing Equation 1.25 as

$$V(u,v,w) = \iiint F(l,m,n) P(l,m) e^{-2\pi\iota(ul+vm+wn))} dl dm dn \tag{1.26}$$

a full 3D Fourier transform of V can then be used to make what is referred to as "image volume". I can be shown to be related to F as

$$F(l,m,n) = \frac{I(l,m)\delta(\sqrt{1-l^2-m^2}-n)}{\sqrt{1-l^2-m^2}} \tag{1.27}$$

where δ is the Dirac delta function. The 2D sky brightness distribution can be recovered from this image volume (Cornwell & Perley 1992). This method goes by the name of "3D inversion". Alternatively, the sky can be approximated as a set of 2D tangent planes. Images can be made for points close to the tangent points of these planes using the 2D approximation. These images can then be properly combined to recover the full primary beam image of the sky. This method goes by the name of "polyhedron imaging".

The Galactic plane at low frequencies exhibits complex emission all over the field of view. Hence, even if the source of interest is compact and close to the pointing centre, 2D imaging cannot be applied since the distortions of sources away from the pointing centre (which is assumed to be also the phase centre) will have unacceptable effects all over the image. It is therefore necessary to map the full field of view, even if the size of the source of interest is small compared to the primary beam. Polyhedron imaging is implemented in the Astronomical Image Processing System (`AIPS`) package and was extensively used for making full primary beam images this dissertation.

1.5.3 On-line and off-line data analysis

In these early days of the GMRT, apart from other sources of data corruption like radio frequency interference (RFI), ionospheric scintillation, etc., data was frequently corrupted due to the failure of various systems. Monitoring the data quality and the health of the system during the observations was therefore of paramount importance. Since there were many sources of data corruption and the manner in which they affected the data were varied, it is useful to develop techniques and software which can automatically identify as many of these problems as early on in the data analysis process as possible. Identifying sources of data corruption, general debugging of the instrument, etc. however require sophisticated and efficient software for data analysis, browsing, and display. Extensive software was developed for this purpose in the form of general purpose object oriented libraries as well as programs for on-line and off-line data processing and display.

The effort invested in software development is optimally used if the resultant software is easy to use at the user level and easy to extend at the programmer level. This is also almost necessary for software which is expected to be used by a relatively larger number of users. Development of a user interface which is easy to use as well designing the entire software such that it is easy to extend is therefore important. Also, a user interface which is not consistent with the functionality of the application programs to which it interfaces is unlikely to be useful. It is therefore desirable to develop a user interface which, as far as possible, automatically evolves with the application programs. The modern Object Oriented software design philosophy was adopted to achieve exactly this goal. Software designed in an Object oriented manner is highly modular and the modules are loosely coupled. The software is designed as set of "objects" which map closely to real-life objects in the problem being solved. Usually, these real-life objects do not change significantly over the software life time, but the coupling between various objects can drastically change. Such changes can be very easily incorporated in a big software system designed as set of objects. Apart from ease of maintenance, this also produces reliable software which is easy to debug.

A user interface, which becomes part of the compiled application programs (as against a user interface as an independent entity which loads and runs the applications programs) was developed in the form of a set of libraries. Such a user interface is referred to as an embedded user interface. Libraries which provide a high level, astronomically useful interface for manipulating the GMRT visibility database were also developed. Using these libraries, programs for data editing, semi-automatic data flagging, on-line monitoring of the data, computation for antenna-based complex gains, amplitude and phase calibration, etc. were also developed.

The visibility function V, depends on a number of telescope parameters like the system temperature (T^{sys}), antenna sensitivity, antenna fixed delays, antenna positions, etc. For debugging as well as for on-line data monitoring, it was frequently required to extract this data in various representations (e.g., Cartesian versus polar representation of complex numbers). Since the complex visibilities are a function of a multitude of parameters, and different debugging purposes require viewing V with respect to various quantities, it was necessary to develop a compact macro language parser to extract and display the data in a flexible and programmable manner. This macro language was implemented in the form of stand alone libraries as well as an application program which was extensively used for this dissertation.

The *self-cal* algorithm can be used to compute antenna based complex gains from the complex visibilities for a source of known structure. However, it is very sensitive to the presence of data from malfunctioning antennas or from a malfunctioning correlator. During the course of the observations, it was frequently the case that the data from a few antennas was unusable, at least for some fraction of the observing time. A large fraction of diagnosis of problems in the data/telescope is often done by examining the antenna based complex gains, which are computed using the self-cal algorithm which in turn required careful flagging of malfunctioning antennas/baselines. An algorithm was therefore implemented which was robust in such conditions and could identify bad baselines/antennas automatically. This was done by (1) automatically eliminating outlying points, (2) doing two passes to eliminate dead/bad antennas. This algorithm was also used to identify and flag corrupted data in a semi-automatic fashion.

1.5.4 Instrumental polarization leakage

Signals from the two orthogonally polarized feeds are brought to the base of the antenna via co-axial cables, which run physically close to each other. These signals are then brought to the a central location via optical fibers where they are converted to baseband signals. The two orthogonally polarized signals can leak in each other at various points in the signal path resulting into polarization impurity. To minimize this leakage, the technique of Walsh switching (Thompson et al. 1986, and references therein) is used wherein the two signals are multiplied by two orthogonal trains of square waves, called the Walsh functions. Later, before correlating the signals from different antennas, these Walsh switched signals are multiplied by the inverse Walsh functions to recover the original signals. Any leaked signal from one polarization channel to the other at time scales longer than the period of the Walsh functions then averages to zero.

The planned Walsh switching has not yet been implemented for the GMRT. In any case, polarization impurity introduced before the switching point will not be removed by Walsh switching. This leakage is a significant source of noise at 150 MHz and also contributes noise at all other bands, albeit at a lower level and manifests itself in the form of increased closure errors in the system (Rogers 1983). The current GMRT correlator computes only the *co-polar* visibilities (i.e. RR and LL visibilities only). Even with the planned extension of the correlator where the *cross-polar* visibilities (i.e. RL and LR visibilities) will also be computed, one can think of observations which will be done using the higher frequency resolution provided by the GMRT correlator in the non-polar mode. All such data will then be affected by errors related to this polarization impurity related errors. Rogers (1983) pointed out in the context of the VLBA, that polarization leakage causes closure errors even in nominally *co-polar* visibilities. Massi et al. (1997) have carried out a detailed study of this effect for the telescopes of the European VLBI Network (EVN). The polarization leakage in some of the EVN antennas corrupts the *co-polar* visibilities at a level visible as a reduction in the dynamic range of the maps (Massi & Aaron 1997a,b; Massi et al. 1998).

Non-polarimetric observations for imaging constitute a large fraction of observations done using interferometers where only the *co-polar* visibilities are recorded. The calibrators used for such observations are usually unpolarized. Since the above mentioned closure errors will affect such data adversely, a method to measure the polarization leakage using *only* the *co-polar* visibilites from an unpolarized calibrator to correct for these closure errors will be of use, particularly for high dynamic range imaging.

1.6 Organization of the thesis

Low frequency continuum spectra, radio morphology and, if possible polarization measurements are the key observables used to identify SNRs in the Galaxy. Spectra at frequencies greater than ~ 1 GHz suffer from contaminating thermal emission. Therefore, although higher angular resolution observations can be done at high frequencies, low frequency radio observations are more suited for SNR research. However with the lower resolutions and sensitivities at low frequencies, identification of the morphology, particularly in regions with complicated emission becomes difficult. High resolution sensitive observations at low radio frequencies therefore appears to be the optimal observation expected to yield rich dividends for various aspects of SNR research. This thesis reports the work done on these lines using the GMRT.

The main thrust of the thesis is the study of Galactic SNRs taking advantage of the high sensitivity and resolution of the GMRT which has recently become available for scientific usage. Since this work was done in the early stages of the GMRT, a large fraction of time was also spent in debugging the instrument and in developing extensive software for data browsing, display and off-line analysis. New algorithms and techniques were also developed which were useful, in particular for the GMRT, and, in general, for low frequency interferometry.

While debugging the GMRT, need for a sophisticated software for data browsing, display and analysis was felt early on. As a result, large amounts of software ($> 60\,000$ lines of code in `C++, C` and `FORTRAN`) was written with the goal of keeping it efficient and yet simple so that the turn around time between observations and results from data analysis is minimized. This software was also written in a modern object oriented fashion, with the hope that many more astronomers/engineers will find it useful to write useful application programs using the the underlying software libraries as well as to extend the software system.

The thesis is organized in the form of eight chapters and four appendices. The present chapter briefly describes the model for supernova explosions and introduces the theoretical concepts of radio synchrotron emission in Section 1.1. Particular emphasis is laid on the fact that low radio frequency observations for the purpose of identification of SNRs in the Galaxy provides a crucial advantage over high frequency observations. The various stages of the evolution of SNRs are described in Section 1.2. Proposed mechanisms to explain the observed non-thermal emission from SNRs are discussed in Section 1.2.1 and the information drawn from measured continuum spectra of SNRs is discussed in Section 1.2.2. At frequencies higher than ~ 1 GHz, thermal emission from HII regions in the Galaxy is strong and sometimes even dominant. The spectral signatures and nature of thermal emission in the presence of absorbing foreground medium are discussed in Section 1.2.3. Various observed radio morphologies, distribution of SNRs in the Galaxy and the effects of the ISM on the observed properties of SNRs are discussed in Sections 1.2.4, 1.2.5 and 1.3 respectively.

Chapter 2 describes the GMRT from an astronomical point of view. The underlying principle of aperture synthesis is discussed in Section 2.1, with emphasis on the problems related to imaging at low frequencies. Section 2.2 briefly describes the parabolic dishes and the geometry of the array. Section 2.3 describes the signal path from the antennas feeds till the digital back-end correlator while Section 2.4 describes the astronomically relevant parameters of the telescope. Most of the observations included in this dissertation were done when the GMRT hardware as well software was in a state of being debugged. Consequently, a large fraction of the time was spent in debugging activities, which required understanding the details of the hardware - particularly of the GMRT FX-type correlator. The GMRT correlator hardware and associated software is described in some detail in Section 2.5. Section 2.5.1 describes the algorithm used for accurate time stamping of the data in the data acquisition software. Precise location of the antennas on the ground as well as the fixed instrumental delay suffered by the signal from individual antennas before reaching the correlator are two important parameters of an aperture synthesis telescope. Before imaging could be attempted, these measurements were made for the GMRT. Details of the baseline and antenna fixed delay calibration and its results are described in Section 2.6.

Chapter 3 very briefly describes the design and implementation of the GMRT off-line data analysis software system, which was extensively used during the course of this work. Section 3.1 discusses the need for the development of such a software system. Section 3.2 describes the philosophy behind the design of this software system consisting of a set of generic libraries and a number of application programs. Data manipulation libraries are described briefly in Section 3.3 while the user interface system and a few selected application programs, most extensively used during the course of this work, are described in Sections 3.4 and 3.5 respectively.

Chapter 4 describes the 325-MHz GMRT observations of a sample of candidate SNR fields. Section 4.1 describes the parameters of these observations. Mapping in the Galactic plane at 325-MHz with the GMRT requires mapping of the entire field of view which in turn requires use of specialized imaging and deconvolution algorithms. Section 4.2 discusses the techniques used from imaging at low frequencies, which were used for mapping the GMRT data. Section 4.3 describes the observational procedure used for these observations including the use of off-line data analysis software for on-line monitoring of the system health and the data quality. The details of data analysis and calibration are described in Section 4.4. Section 4.5 discusses the details related to inversion of the visibility data and deconvolution of the images. Finally, Section 4.6 presents the full primary beam 325-MHz images of all the fields. Most of the SNRs studied in this dissertation are large in angular size (typically > 7 arcmin). Although these GMRT observations could provide typical resolution of ~ 20 arcsec for these southern fields, the maps presented here are typically at arcmin resolution. The reason for this is two fold: (1) since many of the SNRs had low surface brightness, lower resolution maps show the morphology more clearly (2) large scale emission tend to "break-up" at the highest resolution due to a combination of problems of deconvolution of large sources as well as phase noise that could not be calibrated. For a few fields, where the angular size of the sources of interest was of the order of arcmin, high resolution images were used.

Full primary beam maps of almost all the fields at 325-MHz exhibit a number of sources of compact as well extended emission, particularly in the Galactic plane. The primary goal of these observations was the low frequency study of Galactic SNRs in the fields - many of which were not confirmed SNRs. Chapter 5 goes on to discuss the SNRs in these fields. Section 5.1 discusses the difference between low and high frequency observations of Galactic SNRs to bring forth the advantages offered by deep high resolution observations at low frequency. Section 5.2 then discusses the individual candidate SNRs in the fields. Some of the fields also contained other previously identified SNRs. For a few of them, these 325-MHz observations are the first observations at this frequency; in fact, these are also the first high resolution observations at this frequency for all these sources. These results are described and discussed in Section 5.3. Finally, Section 5.4 discusses these results in a broader perspective of Galactic SNR research.

Other sources in the field are discussed in Chapter 6. Section 6.1 briefly discusses the nature of other dominant sources of radio emission and Section 6.2 presents a list of point sources in the fields along with their measured flux densities at 325-MHz and, where possible, at 1400 MHz. Section 6.3 discusses the sources of extended emission in these fields, which are not SNRs. These high resolution observations at relatively low frequency are the first ever observations of these objects and the somewhat unexpected significant extended emission seen at this frequency is interesting from the point of view of better understanding of these sources (usually classified as "thermal"). Section 6.5 concludes the chapter with a summary of the results from these observations.

A technique for the computation of polarization leakage using only the *co-polar* visibilities is described in Chapter 7. Section 7.2 describes the motivation which led to the development of this technique. Section 7.3 mathematically describes the algorithm and also presents the results of the simulations done to test it. Section 7.4 presents the results of the tests done with real data acquired in a controlled experiment and the interpretation of the results in terms of the magnitude of the polarization leakage for various antennas. The Poincaré sphere is a convenient and possibly more intuitive representation of the polarization state of radiation. Interpretation of these results on the Poincaré sphere and the equivalence of the polarization leakage induced phase closure errors and the Pancharatanam phase is discussed in Section 7.5. Since only *co-polar* visibilities are used for the computation of polarization leakage, the solutions are not unique, but still provide useful information about the polarization properties of the antennas. This is discussed in Section 7.6.

Chapter 8 gives consolidated conclusions and results from this work. Section 8.1 describes the major results from the testing and debugging of the GMRT and the software developed for the purpose. Section 8.2 discusses the astronomical results from the observations of the candidate SNRs done for this dissertation. Section 8.3 discusses the inferences about other sources in the fields based on these low frequency observations. Section 8.4 proposes the future directions of research in the fields of Galactic SNRs, compact/Ultra compact H II regions as well as in the field of developing data analysis techniques for radio interferometry at low frequencies and related software development.

Details of the user interface for the off-line software is included as Appendix A. A flexible mechanism was developed to allow easy extraction for any type of data from the GMRT visibility database. This was implemented in the form of a macro language; and the parser and complier for this language is implemented as a stand alone library and used in the program `xtract`. Details of all this work are included as Appendix B. A flexible antenna and baseline naming convention is uniformly used in all off-line application programs. This convention is described in Appendix C. Finally, Appendix D presents the formulation of the problem of computation of antenna based complex gains from the measured complex visibilities. The iterative equations are derived using complex calculus and the interpretation of these equations for better understanding of the algorithm is also presented.

Chapter 2

The Giant Meterwave Radio Telescope

The Giant Meterwave Radio Telescope (GMRT) (Swarup et al. 1991), located 70 km North of Pune at a latitude of $19°05'\ N$ and a longitude of $74°03'\ E$, is a connected element aperture synthesis radio telescope. It is optimized to run at meter wavelengths and currently operates at the 150, 233, 327, 610 and 1420-MHz bands. In addition to this, there are plans to put the 50 MHz feeds on few antennas to test the data quality since the major limitation is expected to come from Radio Frequency Interference (RFI) and ionospheric phase contamination. The 233 and 610 MHz feeds are co-axial which will ultimately allow simultaneous observations at these frequencies. This chapter describes the GMRT from an astronomical point of view, with emphasis on the 327-MHz band.

2.1 Principles of aperture synthesis

An aperture synthesis telescope, like the GMRT, consists of a number of antennas located on the ground and the resolution of such a telescope is proportional to the maximum projected separation between the antennas. The locations of the antennas are usually specified in the Earth-centred XYZ co-ordinate system. The Earth centred XYZ frame is related to the xyz location of the antennas on the ground by

$$\begin{bmatrix} X \\ Y \\ Z \end{bmatrix} = \begin{bmatrix} -\sin\mathcal{L} & \cos\mathcal{L} & 0 \\ 0 & 0 & 0 \\ \sin\mathcal{L} & \cos\mathcal{L} & 0 \end{bmatrix} \begin{bmatrix} x \\ y \\ z \end{bmatrix} \tag{2.1}$$

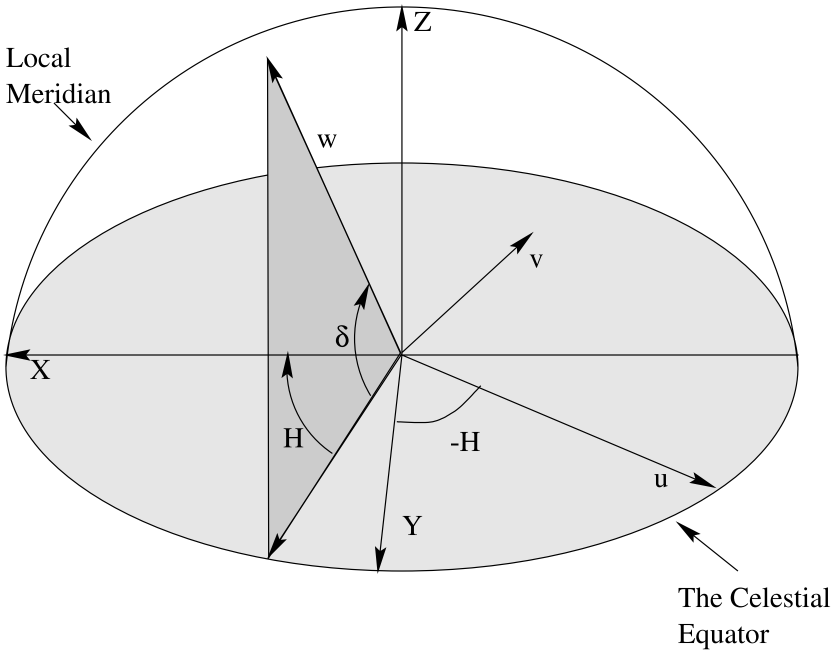

Figure 2.1: The right handed Cartesian co-ordinate system in which antenna positions are described is shown in the figure by the X,Y and Z-axis. The X and Y are in the plane parallel to earth's equator with X-axis in the local meridian plane and Y-axis towards the east. The Z-axis points towards the north celestial pole (NCP). The w-axis of the uvw co-ordinate system, points towards the phase centre of the array at hour-angle H and declination δ. In terms of H and δ, X,Y and Z are measured towards ($H = 0, \delta = 0$), ($H = -6^h, \delta = 0$) and ($\delta = 90°$). The uv-plane is parallel to the tangent plane at the phase centre on the celestial sphere and rotates with the rotation of the Earth.

where $\mathcal{L}$ is the nominal latitude of the telescope site. The x-axis points towards the geographical east, y-axis towards the north and z-axis towards the local zenith.

However, for the purpose of imaging, only the relative separation between the antennas is important. This separation between the antennas is usually referred to as the *baseline* and is measured in units of the wavelength λ of the incident radiation. For the purpose of the theory of synthesis imaging, the antenna positions are specified in the so called uvw frame. The geometric relationship between this XYZ frame and the uvw frame is shown in Fig. 2.1 and the co-ordinate transformation is given by

$$\begin{bmatrix} u \\ v \\ w \end{bmatrix} = \begin{bmatrix} \sin H & \cos H & 0 \\ -\sin\delta\cos H & \sin\delta\sin H & \cos\delta \\ \cos\delta\cos H & -\cos\delta\sin H & \sin\delta \end{bmatrix} \begin{bmatrix} X \\ Y \\ Z \end{bmatrix} \tag{2.2}$$

where H is the Hour Angle and δ the declination of the source.

The geometric relation between the observing plane represented by the uv-plane and the sky plane represented by the lm-plane is shown in Fig. 2.2. The lm-plane in the sky is parallel to the plane in which measurements are made (the uv-plane) and the separation between them is denoted by R. The w-axis points towards the origin of the lmn frame given by ($l = 0$,$m = 0$) and is parallel to the n-axis. The treatment of the theory of synthesis imaging given below follows that of Thompson et al. (1986) and Clark (1999).

Let $E(\vec{s}, \vec{b}_1, t)$ represent the electric field produced by an infinitesimal element in the sky in the direction $\vec{s}$ at point $\vec{b}_1$ in the uvw frame (Fig. 2.2). The total electric field $e(\vec{b}_1, t)$ measured at this point will be an integral of the signals from all the radiation elements and is given by

$$e(\vec{b}_1, t) = \int_P E(\vec{s}, \vec{b}_1, t) d\vec{s} \tag{2.3}$$

$\vec{b}_1$ is the vector denoting the point **1** in the uvw frame. Let R_1 be the distance between point $\vec{b}_1$ and the point in the source plane towards the direction given by the vector $\vec{s}_1$. $E(\vec{s}_1, \vec{b}_1, t)$ can then be written as

$$E(\vec{s}_1, \vec{b}_1, t) = \frac{\xi(\vec{s}_1, t - \tau_1)}{R_1} e^{-2\pi\iota\nu(t-\tau_1)} \tag{2.4}$$

where ξ is the complex amplitude of the radiation at the source, ν is the frequency of the radiation, $\tau_1 = R_1/c$ and c is the speed of light. τ_1 represents the propagation delay for the radiation of complex amplitude ξ to travel the distance R_1.

The *source coherence function*, defined as

$$\begin{aligned} \Gamma(\vec{s}_1, \vec{s}_2, \tau) &= \lim_{T\to\infty} \frac{1}{2T} \int_{-T}^{T} \xi(\vec{s}_1, t)\xi^\star(\vec{s}_2, t - \tau) dt \\ &= \langle \xi(\vec{s}_1, t)\xi^\star(\vec{s}_2, t - \tau) \rangle \end{aligned} \tag{2.5}$$

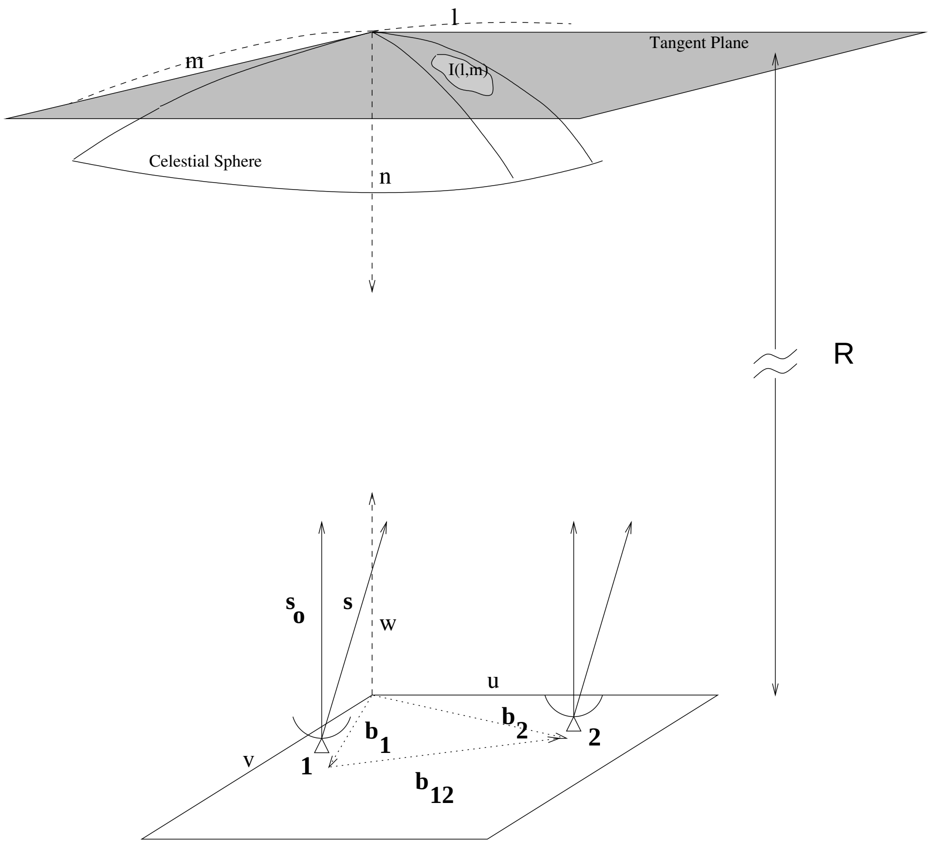

Figure 2.2: Figure showing the orientation of source co-ordinate reference frame and the observing plane. The 2D approximation of the Celestial sphere is shown as the tangent plane at the origin of the sky co-ordinate system.

is a measure of the coherence between radiation from two points on the source given by the directions $\vec{s}_1$ and $\vec{s}_2$ respectively. For a spatially incoherent source, radiation from two points on the source will be uncorrelated. For such a source, $\Gamma(\vec{s}_1, \vec{s}_2, \tau) = \delta(\vec{s}_1 - \vec{s}_2)$ and equation 2.5 can be written as

$$\Gamma(\vec{s}, \tau) = \langle \xi(\vec{s}, t)\xi^{\star}(\vec{s}, t - \tau)\rangle \tag{2.6}$$

This is the auto-correlation function of the radiation from the source $\Gamma(\vec{s}, 0)$ is a measure of the average surface brightness of the radiation from the source.

The *mutual coherence function*, measured at two points $\vec{b}_1$ and $\vec{b}_2$ on the observing plane is defined as

$$\begin{aligned}\gamma(\vec{b}_1, \vec{b}_2, \tau) &= \lim_{T\to\infty} \frac{1}{2T} \int\limits_{-T}^{T} e(\vec{b}_1, t) e^\star(\vec{b}_2, t - \tau) dt \\ &= \langle e(\vec{b}_1, t) e^\star(\vec{b}_2, t - \tau)\rangle\end{aligned} \tag{2.7}$$

Using Equations 2.3 and 2.4 and the equivalent equations for the point $\vec{b}_2$, the above equation can be written as

$$\begin{aligned}\gamma(\vec{b}_1, \vec{b}_2, 0) &= \int \langle E(\vec{s}, \vec{b}_1, t) E^\star(\vec{s}, \vec{b}_2, t)\rangle d\vec{s} \\ &= \int \langle \xi(\vec{s}, t - \tau_1) \xi^\star(\vec{s}, t - \tau_2)\rangle e^{-2\pi\iota\nu(\tau_2 - \tau_1)} \frac{d\vec{s}}{R_1 R_2} \\ &= \int \langle \xi(\vec{s}, t) \xi^\star(\vec{s}, t - \tau_t)\rangle e^{-2\pi\iota\nu\tau_t} \frac{d\vec{s}}{R_1 R_2}\end{aligned} \tag{2.8}$$

where $\tau_t = \tau_2 - \tau_1 = (R_2 - R_1)/c$ is the relative delay between the signals measured at the points $\vec{b}_1$ and $\vec{b}_2$ respectively.

In the above equation, the dependence on $\vec{b}_1$ and $\vec{b}_2$ is implicitly via τ_t. For a plane wavefront from a direction $\vec{s}$ in the sky, $\tau_t = \vec{b}_{12} \cdot \vec{s}/c$ where $\vec{b}_{12}$ is the vector separating the two antennas. It is therefore clear that γ depends only on the relative separation between the antenna positions given by $\vec{b}_1$ and $\vec{b}_2$ and can be written as

$$\gamma(\vec{b}_1, \vec{b}_2, 0) = \gamma(\vec{b}_1 - \vec{b}_2, 0) = \gamma(\vec{b}_{12}, 0) \tag{2.9}$$

The components of $\vec{b}_{12}$ will be given by (u_{12}, v_{12}, w_{12})=$(u_2 - u_1, v_2 - v_1, w_2 - w_1)$. Using direction cosines of $\vec{s}$ as the (l, m, n) co-ordinates of a point in the sky, we get

$$\tau_t = \frac{\vec{b}_{12} \cdot \vec{s}}{c} = \frac{u_{12} l + v_{12} m + w_{12} n}{c} \tag{2.10}$$

Let the antenna located at point $\vec{b}_1$ track a direction given by the unit vector $\vec{s}$ in the sky. Due to the separation between the antennas on the ground, to track the same point in the sky, a second antenna located at point $\vec{b}_2$ will need to point in a slightly different direction given by $\vec{s}_2$. The angle between $\vec{s}$ and $\vec{s}_2$ is given by $\tan^{-1}(|\vec{b}_2 - \vec{b}_1|/R)$. This difference in the pointing directions results in an extra relative delay between the signal arriving at the two antennas from a point in the sky. As a result, one of the antennas samples a slightly delayed version of the wave front. If, however, $R \gg |\vec{b}_2 - \vec{b}_1|/\lambda$ where λ is the wavelength of the radiation, the same wavefront will be sampled by the two antennas ($\tan^{-1}(|\vec{b}_2 - \vec{b}_1|/R) \approx 0$). This corresponds to the usual plane wavefront approximation. This approximation is used in the rest of the treatment.

In the limit of the plane wave front approximation, the denominator in Equation 2.8 can be adequately represented by R^2 and $d\vec{s}/R^2 = dldm/\sqrt{1-l^2-m^2}$. The phase of the *mutual coherence function* in Equation 2.7, for a spatially incoherent source, therefore, depends only on the relative separation between the points of measurement in the far field of the radiation.

Let $\vec{s}_\circ$ represent the unit vector along the w-axis pointing towards ($l = 0, m = 0$). The components of $\vec{s}_\circ$ in the uvw frame will be (0,0,1). The relative delay between the signals received at the two antennas from a point source in this direction will be $\tau_g = \vec{s}_\circ \cdot \vec{b}_{12}/c = w_{12}/c$. Treating $\vec{s}_\circ$ as the reference direction towards the origin of the source co-ordinate system, the instantaneous phase of $\gamma(\vec{b}_{12})$ can be measured with respect to this direction, without losing any information about the sky brightness distribution. This can be done by rotating the phase of γ by $-2\pi\nu w_{12}/c$. The point in the sky in the direction $\vec{s}_\circ$ is referred to as the *phase centre* and τ_g is referred to as the *geometrical delay*. The *Phase centre* direction defines the origin of the source co-ordinate system. Since $\vec{s}_\circ$ is an arbitrary vector, the *phase centre* can be chosen at any convenient point in the sky. Usually, this is coincident with the antenna pointing centre.

The visibility phase for a point source at the *phase centre*, after correcting for the *geometrical phase* is equal to zero. With this correction, the visibility is said to be 'phased' for the *phase centre*. An interferometer phased for this reference direction will remain phased for all points on the surface of a sphere of unit radius passing through the point ($l = 0, m = 0$), centred at ($u = 0, v = 0$) and described by the equation $l^2 + m^2 + n^2 = 1$. Under ideal conditions (i.e., with no other source of phase errors), any residual phase would be due to the relative separation between the *phase centre* and a source of emission located on such a sphere. In that sense, the visibility phase from a 'phased' interferometer provides information about the distribution of the sky brightness, *relative to the phase centre*. Moving one of the antennas to the origin of the uvw frame, the (u_{12}, v_{12}, w_{12}) co-ordinates are just the co-ordinates of the other antenna and the subscript '12' can be dropped from Equation 2.10.

The length of time for which a signal remains coherent is given by the inverse of the bandwidth $\Delta\nu$. After correcting for the *geometrical delay*, the relative delay between the signals is $\tau_c = \tau_t - \tau_g$. Replacing τ_t by τ_c in Equation 2.8 corresponds to the geometrical delay corrected version of this equation. If $\tau_c \ll \Delta\nu^{-1}$, two versions of a time series displaced with respect to each other in time by τ_c will remain coherent. In the limit of the validity of the assumption that $\tau_c \ll \Delta\nu^{-1}$, $\langle \xi(\vec{s},t)\xi^\star(\vec{s},t-\tau_c)\rangle$ in Equation 2.8 can be replaced by $\langle \xi(\vec{s},t)\xi^\star(\vec{s},t)\rangle = \langle|\xi(\vec{s})|^2\rangle$. This is the same as the source auto-correlation function at zero lag, $\Gamma(\vec{s},0)$ (Equation 2.6) and is equal to the two dimensional source surface brightness, denoted by $I(l,m)$

Therefore, under the approximation that:

- the observing plane is in the far field of the radiation ($R \gg |\vec{b}_2 - \vec{b}_1|/\lambda$)
- the total delay between the signals received at the two points on the observing plane is much less than the signal coherence time ($\tau \ll \Delta\nu^{-1}$)

using the relation between l,m,n in Equation 2.10 and the above mentioned phase rotation, Equation 2.8 can be re-written as

$$\gamma(u,v,w) = \iint I(l,m)e^{-2\pi\iota\left(ul+vm+w\left(\sqrt{1-l^2-m^2}-1\right)\right)}\frac{dldm}{\sqrt{1-l^2-m^2}} \tag{2.11}$$

where u, v and w are now the co-ordinates in the uvw frame measured in units of the wavelength. γ is usually referred to as the *visibility function* and denoted by $V(u,v,w)$.

The integrals in the above equation are over the entire sky (limits of the integral from -1 to 1). However, the antenna primary beam limits the part of the sky from which the antenna can receive radiation to $\sim \lambda/D$, where D is the diameter of a circular aperture. Assuming that the response close to the centre of the primary beam is ≈ 1, with an additional approximation that the field of view is small ($l^2+m^2 \ll 1$), Equation 2.11 can be written as

$$\gamma(u,v) = \iint I(l,m)e^{-2\pi\iota(ul+vm)}dldm \tag{2.12}$$

This is a 2D Fourier transform relation between the *mutual coherence function* (*visibility*) and the source surface brightness. This statement is referred to as the *van Cittert-Zernike theorem* (Born & Wolf 1959 [and later eds]; Thompson et al. 1986) and forms the basis of imaging with interferometric radio telescopes.

The source surface brightness $I(l,m)$ is described in the lm-plane while u and v are the equivalent conjugate variables in Fourier space. u and v can therefore be interpreted as the spatial frequencies and the *visibility function* as the spatial frequency spectrum of the source surface brightness distribution. Synthesis radio telescopes like the GMRT measure the *visibility function* at several points in the uvw frame using an array of N antennas which instantaneously produce $N(N-1)/2$ pairs of interferometers. Due to the rotation of the earth, the projected separations between the antennas change as the antennas track a source in the sky. Over time, each antenna pair therefore measures the visibility at several points in the uvw frame. As a result, over time, the array of antennas partially covers the uvw volume, up to a maximum projected antenna separation of B_{max} corresponding to a spatial resolution of $1/B_{max}$. Also, an interferometric array does not measure V for baselines smaller than a minimum value. Just as the maximum baseline length for which V is measured corresponds to the highest spatial resolution the telescope can provide, the smallest baseline for which V is measured corresponds to largest angular scale that can be represented reliably in the final image. Hence, an interferometric observation will be insensitive to scales larger than $1/B_{min}$; this problem of missing short spacing measurements is referred to as the problem of "missing short spacing". When imaging extended objects in the sky, like the ones imaged for this dissertation, the shortest spacing for which a reliable measurement exist has for reaching implications – missing short spacings result in missing extended emission in the image.

If $\gamma(u,v)$ is completely sampled, at least at the Nyquist rate, it can be inverse Fourier transformed to recover the source brightness distribution $I(l,m)$. With a finite number of antennas located at discrete locations on the ground, the *visibility function* is sampled at a discreet set of points. The observed visibility can, therefore, be thought of as the true visibility, multiplied by the sampling function given by

$$S(u,v) = \delta(u - u(t), v - v(t)) \tag{2.13}$$

where $(u(t), v(t))$ represents the points sampled at time t. Using the convolution theorem for Fourier transform (Bracewell 1986 [and later eds]), it can be shown that the function I, recovered by the inverse Fourier transform of $S(u,v)\gamma(u,v)$, will be convolved by the inverse Fourier transform of S. The inverse Fourier transform of S, denoted by B, is usually referred to as the *dirty beam* or the *point spread function* or the *telescope transfer function*. $I^d = I \star B$ is referred to as the *dirty map*, where '$\star$' represents the convolution operator. I is recovered from I^d using non-linear deconvolution techniques (Högbom 1974; Clark 1980; Cornwell & Evans 1985).

The approximation that $l^2 + m^2 \ll 1$ breaks down at low frequencies and Equation 2.11 accurately described the measured *visibility function*. However, this is *not* a

Fourier transform relation. Techniques used to recover I in such cases are described in Chapter 4.

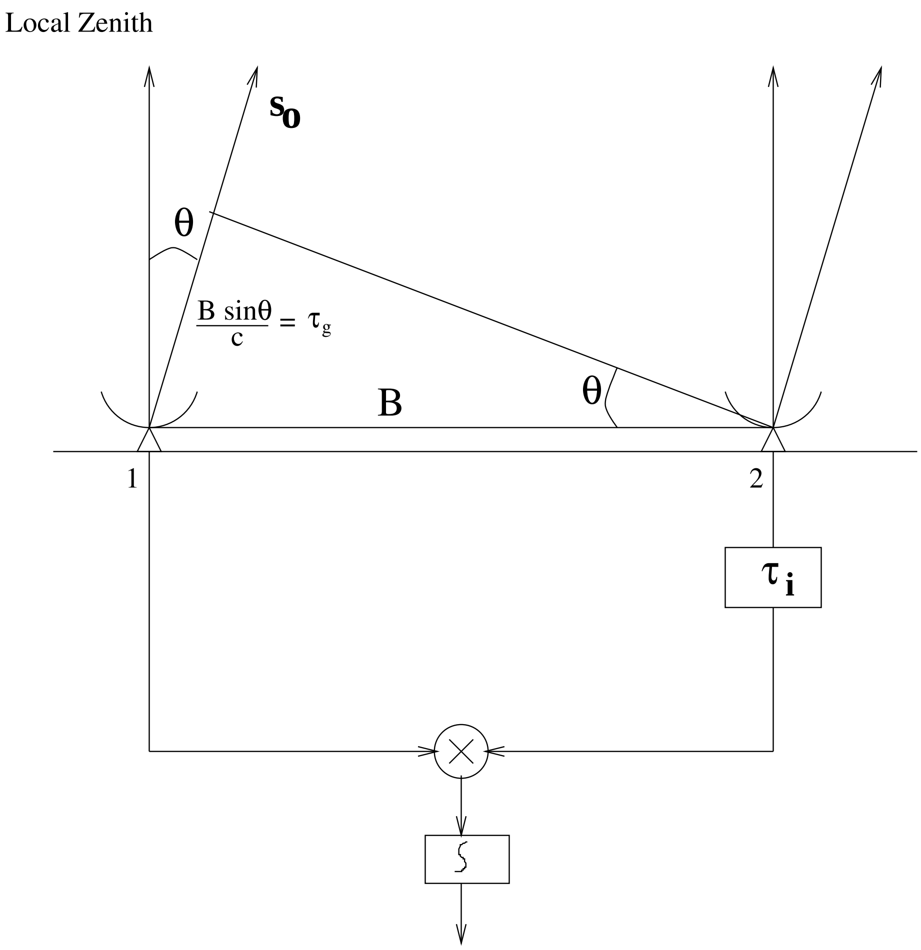

Figure 2.3: Figure shows a simplified one dimensional block diagram of a two element interferometer. A compensating delay τ_i is introduced in the path of one of the signals. The two signals are then multiplied and integrated to measure the *mutual coherence* between the signals from the two antennas.

2.1.1 Interferometry in practice

In practice, γ is measured by a number of two element interferometers, one of which is shown in Fig. 2.3. The signal from antenna **1** lags behind the signal from the antenna **2** by a phase equal to $2\pi\frac{b_{12}\cdot\vec{s_o}}{c}$ where $\vec{s_o}$ is the reference unit vector mentioned in the previous section. Under the plane wave approximation, the signals from the two antennas can be written as

$$\begin{aligned} S_1 &= e_1 + \epsilon_1 \\ S_2 &= e_2 + \epsilon_2 = e_1 e^{2\pi \frac{b_{12} \cdot \vec{s_o}}{c}} + \epsilon_2 \end{aligned} \tag{2.14}$$

where ϵ_1 and ϵ_2 are independent additive random noises from the two antennas. These signals are multiplied and the product averaged in the complex correlator to form the visibilities as

$$\begin{aligned} V(u,v,w) &= \langle S_1 \cdot S_2^{\star} \rangle \\ &= \langle e_1 \cdot e_2^{\star} \rangle + \langle e_1 \cdot \epsilon_2^{\star} \rangle + \langle e_2 \cdot \epsilon_1^{\star} \rangle + \langle \epsilon_1 \cdot \epsilon_2^{\star} \rangle \end{aligned} \tag{2.15}$$

Since ϵ_1 and ϵ_2 are independent zero mean gaussian random variables, the last three terms will reduce to zero.

The response of the interferometer to a point source of flux density I, located at the *phase centre* ($l = 0, m = 0$) is therefore

$$V(u,v,w) = Ie^{2\pi\iota \frac{b_{12} \cdot \vec{s_o}}{c}} = Ie^{2\pi\iota w} = Ie^{2\pi\iota\nu\tau_g} \tag{2.16}$$

where τ_g is the *geometrical delay* mentioned earlier. It is equal to the time delay due to the extra path length (equal to the projected separation between the antennas along $\vec{s_o}$) which the radiation has to travel to reach one of the antennas. With reference to Fig. 2.3, $\nu\tau_g = \frac{D}{\lambda}\sin(\theta) = w_\lambda$ where $D = |\vec{b}_{12}|$ and w_λ is the instantaneous component of the separation between the antennas along the w-axis measured in units of the wavelength of the incident radiation. Equation 2.16 can therefore be rewritten as

$$V(u,v,w) = I(l,m)\left[\cos(2\pi\frac{D}{\lambda}\sin(\theta(t))) + \iota\sin(2\pi\frac{D}{\lambda}\sin(\theta(t)))\right] \tag{2.17}$$

Antennas receive radiation from a finite part of the sky, defined by the antenna primary beam. For an extended source, within the antenna primary beam, $V(u,v,w)$ will be an integral over the source (integral over l and m;Equation 2.12) and can be thought of as a superposition of plane waves from the individual infinitesimal elements constituting the extended source given by Equation 2.17.

As the interferometer tracks the source in the sky, the projected separation and hence the *geometrical delay* changes with time. θ changes slowly going from $-\theta_{max}$ to θ_{max} when the antennas track a source from rise to set over several hours. θ_{max} depends on the declination of the source and the minimum elevation limits of the antennas. Over short intervals of time, θ changes almost linearly with time. The interferometer response to a point source (the real and imaginary parts) therefore varies quasi-sinusoidally over short periods of time with a frequency proportional to the separation between the antennas. This quasi-sinusoidal variation of the interferometer output, due to the changing *geometrical delay*, is referred to as the *fringe pattern*. The amplitude of this fringe pattern is directly proportional to the power emitted by the source in the sky. The phase of these fringes also changes sinusoidally with time with a period of 24 hours. The phase of this *fringe pattern* due to the *geometrical delay* however carries no astronomically useful information about the sky (it only carries information about the direction in the sky being tracked). In practice therefore, the *geometrical delay* is continuously compensated by introducing a time variable compensating delay τ_i in the signal from one of the antennas. This operations is referred to as *delay tracking*. The radio-frequency (RF) signals from the antenna feeds, centred at a frequency ν°_{RF}, are converted to an intermediate frequency band centred at ν°_{IF} to be transported to the correlator (in the case of GMRT, over optical fiber cables). The path length for the signals from the antenna to the correlator introduces a time invariant *fixed delay* τ_{Fix} suffered by the signals at ν_{IF}. The compensating delay τ_i must therefore compensate for τ_{Fix} as well.

For the GMRT, the compensating delay $\tau_i = \tau_g + \tau_{Fix}$ is applied to the signals at baseband frequencies in the correlator. However, the signals suffer the delays τ_g and τ_{Fix} at the RF and IF frequencies respectively. Delay compensation at the baseband therefore leaves a residual phase given by

$$\begin{aligned}\frac{\Delta\phi}{2\pi} &= [\tau_g \nu^\circ_{RF} + \tau_{Fix}\nu^\circ_{IF}] + [(\tau_g + \tau_{Fix} - \tau_{Int})\,\nu_i] \\ &\equiv \frac{\Delta\phi^\circ}{2\pi} + \frac{\Delta\phi_i}{2\pi}\end{aligned} \tag{2.18}$$

where ν_i is the centre frequency of the i^{th} frequency channel and τ_{Int} is the time delay, applied in the correlator *Delay/DPC* system (see 2.5.2 for details). This delay compensated signal is fed to the *FFT* section of the correlator to be split into a number of frequency channels. $\Delta\phi^\circ$ is applied at the very first stage of the FFT butterfly network in the *FFT* section. The remaining phase gradient, denoted by $\Delta\phi_i$, is applied as a phase gradient in the last stage of the *FFT* network.

Effectively, the phase of the visibilities is rotated by $\Delta\phi$, equivalent to the residual delay due to the differences in the RF, IF and base band frequencies. The phase of the visibility for a point source located at the phase centre is thus reduced to zero at all times. This final rotation of the fringe phase is referred to as *fringe stopping* or *fringe rotation.*

Note that the total phase applied to the visibilities via *delay tracking* and *fringe rotation* is equal to $2\pi w$ and this effectively phases the interferometer for a point in the sky (the phase centre). Application of this total phase is achieved in the GMRT correlator in two stages, as explained in Section 2.5.2.

The response of the interferometer is integrated over the signal bandwidth as seen by the multiplier in the correlator. If $H(\nu)$ represents the voltage response of the antennas as seen by the multiplier, the effect of a finite bandwidth is to modulate the output of the interferometer by the Fourier transform of H. If the receiver has a flat response for a range of frequencies $\nu_o \pm \Delta\nu$, the output V, for a source of unit flux density, will be given by

$$V(u,v,w) = \frac{\sin(\pi\Delta\nu\tau)}{\pi\Delta\nu\tau} e^{2\pi\nu_o\tau} \tag{2.19}$$

where $\tau = \tau_g - \tau_i - \tau_{Fix}$ is the total residual relative time delay between the signals from the two antennas after delay compensation. The Fourier transform of H is referred to as the *fringe washing* function. Since H is a band limited function, the fringe washing function is finite for a limited range of τ and defines the coherence time of the fringe pattern, which is $1/\Delta\nu$ for the above example. The total relative residual delay between the two signals before multiplication, therefore, must be $\ll 1/\Delta\nu$ for the signals from the two antennas to remain coherent when they arrive at the multiplier. Large departures of τ from this value would result in decoherence of the signals, resulting in reduction of the amplitude of the interferometer output. Therefore, in practice, knowledge of both the instantaneous geometric delay *and* the fixed delay is important.

w is the relative antenna separation along the w-axis. As is clear from Equation 2.2, the geometrical delay involves the measurement of the relative (X, Y, Z) co-ordinates of different antennas. It is therefore important to measure the relative antenna co-ordinates as well as the fixed delays for phasing the array (reducing the fringe phase to zero for the phase centre). The procedure used for measuring the relative antenna co-ordinates (referred to as *baseline calibration*) and *fixed delays* (referred to as *fixed delay calibration*) for the GMRT is described in Sections 2.6.1 and 2.6.2 respectively.

As mentioned earlier, $V(u, v, w)$ is measured for several values of u, v and w by tracking the source in the sky for several hours, during which the projected baseline of a single interferometer changes with time. In practice, a number of antennas are used and the output of all the $N(N-1)/2$ interferometer pairs made by an array of N antennas provide instantaneous measurements at several values of u, v and w. The instantaneous set of points measured in the uvw frame by an array of antennas is referred to as the *snapshot uv-coverage*. As the array tracks a source in the sky, each interferometer generates a track in the *uv-plane*, dramatically increasing the *uv-coverage* of the array. The set of u, v, w points, measured by an array of antennas over several hours of source tracking, is referred to as the *full synthesis uv-coverage*. The shape and density of the *uv-coverage* of the array determines the telescope transfer function and the geometry of the array is usually optimized to maximize the *uv-coverage* (Mathur 1969). The configuration of the 30-antenna GMRT array and resulting *uv-coverage* are described in Section 2.2.

2.2 The Array

The GMRT antennas are fully steerable parabolic dishes each of 45m diameter each with an Alt-azimuth mount. A turret at the prime focus of the antenna is supported by a quadripod and holds a sealed metallic cube which houses the broadband low noise amplifier (LNA), RF filters, the polarizer and the RF switch for swapping the polarization channels for each RF band (see Section 2.3). The feeds for 150, 327, 233/610, and 1420 MHz are mounted on the four faces of the turret which can be rotated to bring the desired feed in focus using the *feed positioning system* (FPS). The feed bandwidths and the range of frequencies covered by the various feeds are listed in Table 2.1. The feed bandwidths correspond to a Standing wave ratio of ≤ 2. The 233-MHz feed has the smallest bandwidth while the cross-polar characteristic of the 150-MHz feed is the worst. The measured cross-polar power at 327 and 610 MHz bands is ~ -42 and ~ -47 dB respectively while that for the 150-MHz feed is ~ -22 dB. The value away from the centre of the radiation pattern is ~ -22 dB for 327 and 610 MHz bands while that for the 150-MHz feed is ~ -20 dB (see Sankar (2000) for more details). Since the GMRT is predominantly a low frequency instrument, the reflecting surface of the antennas is a light weight wire mesh. The wire mesh is held in place by a network of steel ropes, creating patches of flat surfaces which approximate a parabola. This design is referred to as the *Stretched Mesh Attached to Rope Trusses* design or the SMART design (Swarup et al. 1991). Three sizes of wire mesh are used, going from smallest sized mesh (10 mm) in the inner region of the parabola to the largest size (20 mm) towards the edge to produce a tapered illumination pattern which reduces the side-lobe levels of the antenna radiation pattern. Mesh of different sizes each covers one third of the total surface area. The reflecting surface for each antenna was measured by theodolite, to determine the surface accuracy compared to an ideal parabola. An RMS deviation of 8, 9 and 14 mm from an ideal parabola was measured for the three regions of the surface (Sankar 2000).

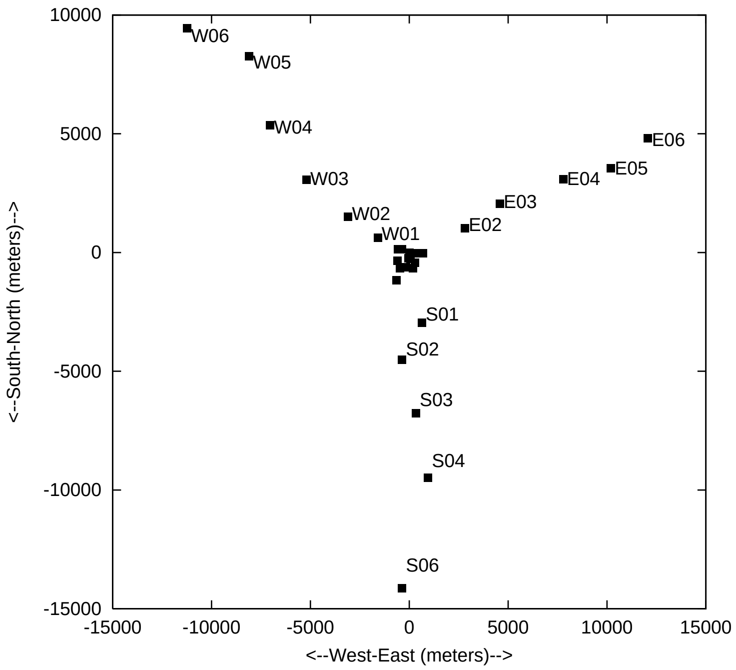

Figure 2.4: The location of the GMRT antennas. The three arms of the 'Y' shaped array are each ≈ 14 km long.

The GMRT is composed of 30 such antennas. The antennas are located in a roughly 'Y' shaped geometry (Mathur 1969), as shown in Fig. 2.4. Fourteen antennas are located randomly in a region of size ≈ 1 km$\times 1$ km, referred to as the *Central Square* (see Fig. 2.5). These antennas provide the short spacing coverage of the uv-plane, which is essential for mapping large scale structures. The rest of the antennas are located in ~ 14 km long Western-, Eastern-, and Southern-arms. The Eastern- and Southern-arms each have 5 antennas, roughly along a straight line, while the Western-arm has 6 antennas. This arrangement of antennas was designed to maximize the telescope sensitivity to large scale emission as well as to provide high resolution. The shortest spacing of ~ 60 m in the *Central Square* is provided by the antennas C05, C06 and C09 while the largest spacing of ~ 25 km is provided by the *arm* antennas. The *Central Square* antennas together provide a uv-coverage up to 1 km. The uv-coverage for a full 12^h synthesis observation using the full array is shown in Fig. 2.6. The uv-coverage due to *Central Square* antennas alone, for

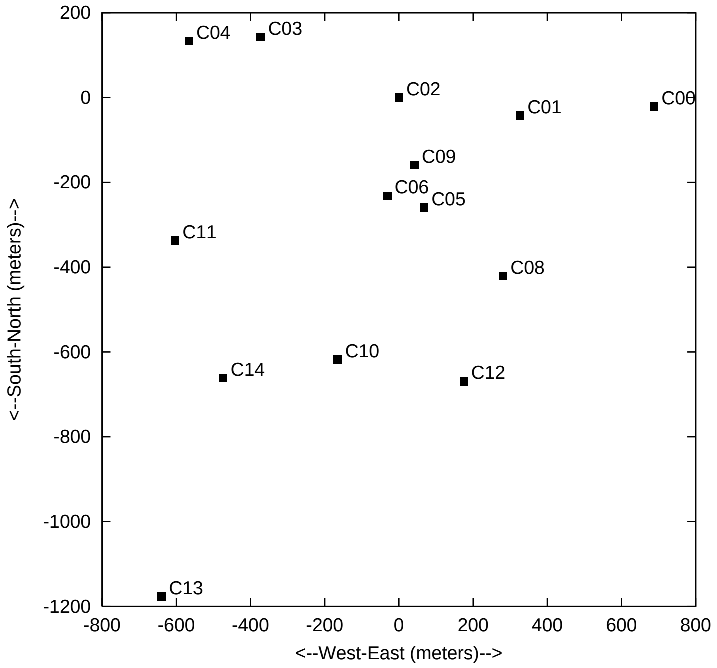

Figure 2.5: The location of only the *Central Square* GMRT antennas.

a full 12^h synthesis at a few declinations is shown in Fig. 2.7.

2.3 Signal flow

A detailed description and analysis of the analog signal flow for the GMRT has been described elsewhere (Praveen Kumar & Srinivas 1996; Praveen Kumar 2000). This section briefly describes the aspects of the GMRT analog receivers which are relevant from the point of view of astronomical observations.

The GMRT operates at the 150, 233, 327, 610 and L-band extending from $1000 - 1450$ MHz. The L-band is split into four sub-bands centred at 1060, 1170, 1280 and 1390 MHz with a bandwidth of 120 MHz while the bandwidth at other bands is ~ 40 MHz. Fig. 2.8 shows a simplified schematic diagram, with the major components of the GMRT receiver. The L-band feeds measure two orthogonal linear polarizations while the feeds at all other bands measure circular polarizations. The 233 and 610 MHz feeds are co-axial feeds. The front-end low noise amplifiers have been designed to either receive two polarization signals from a single feed or the same polarization signal from two different feeds. This, for the case of 233/610 MHz feeds, allows simultaneous single polarization observations at these bands. An RF switch after the front-end box allows swapping of the

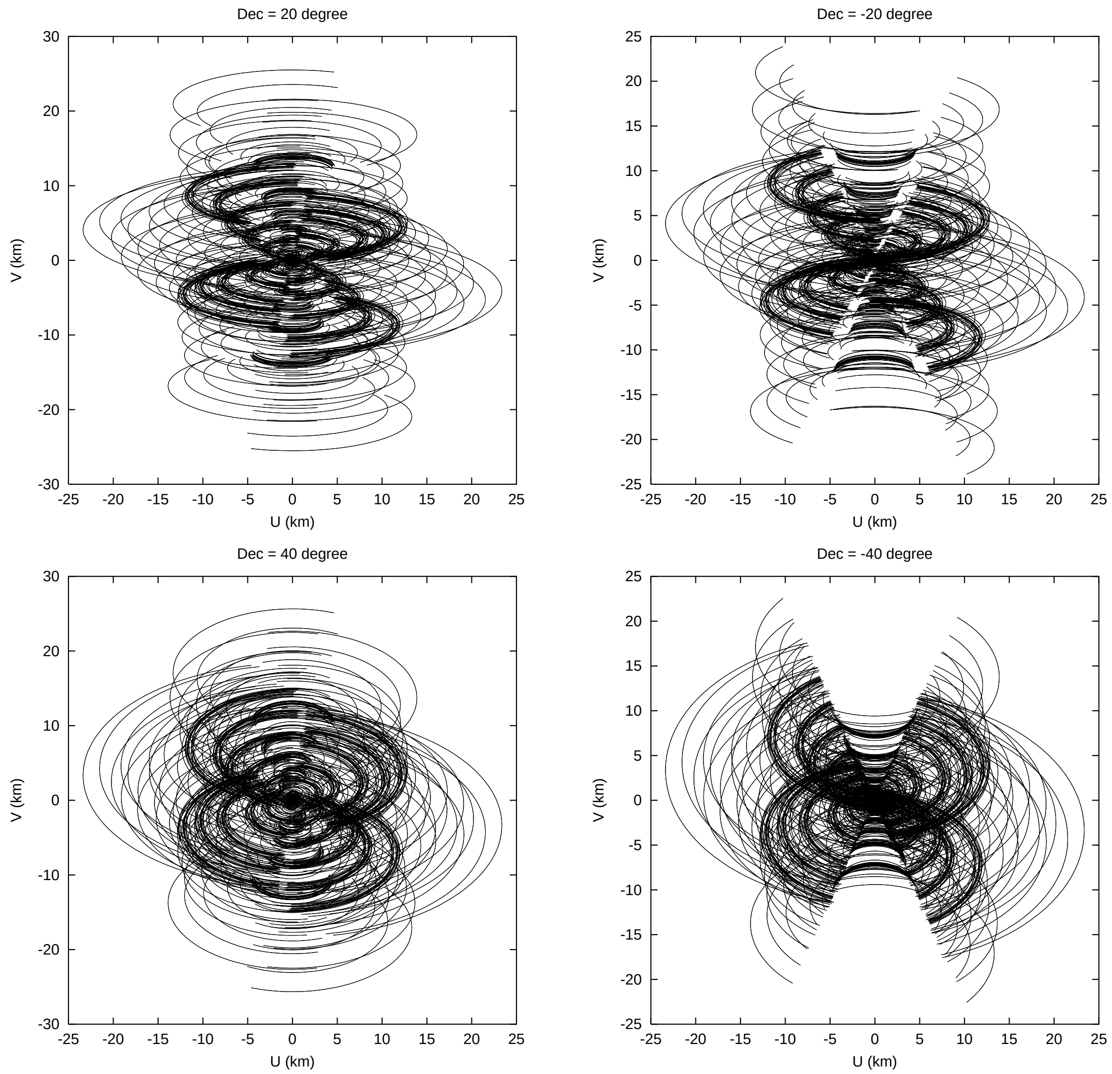

Figure 2.6: Full synthesis uv-coverage of the full GMRT array at declinations of 20°, -20°, 40° and -40° respectively.

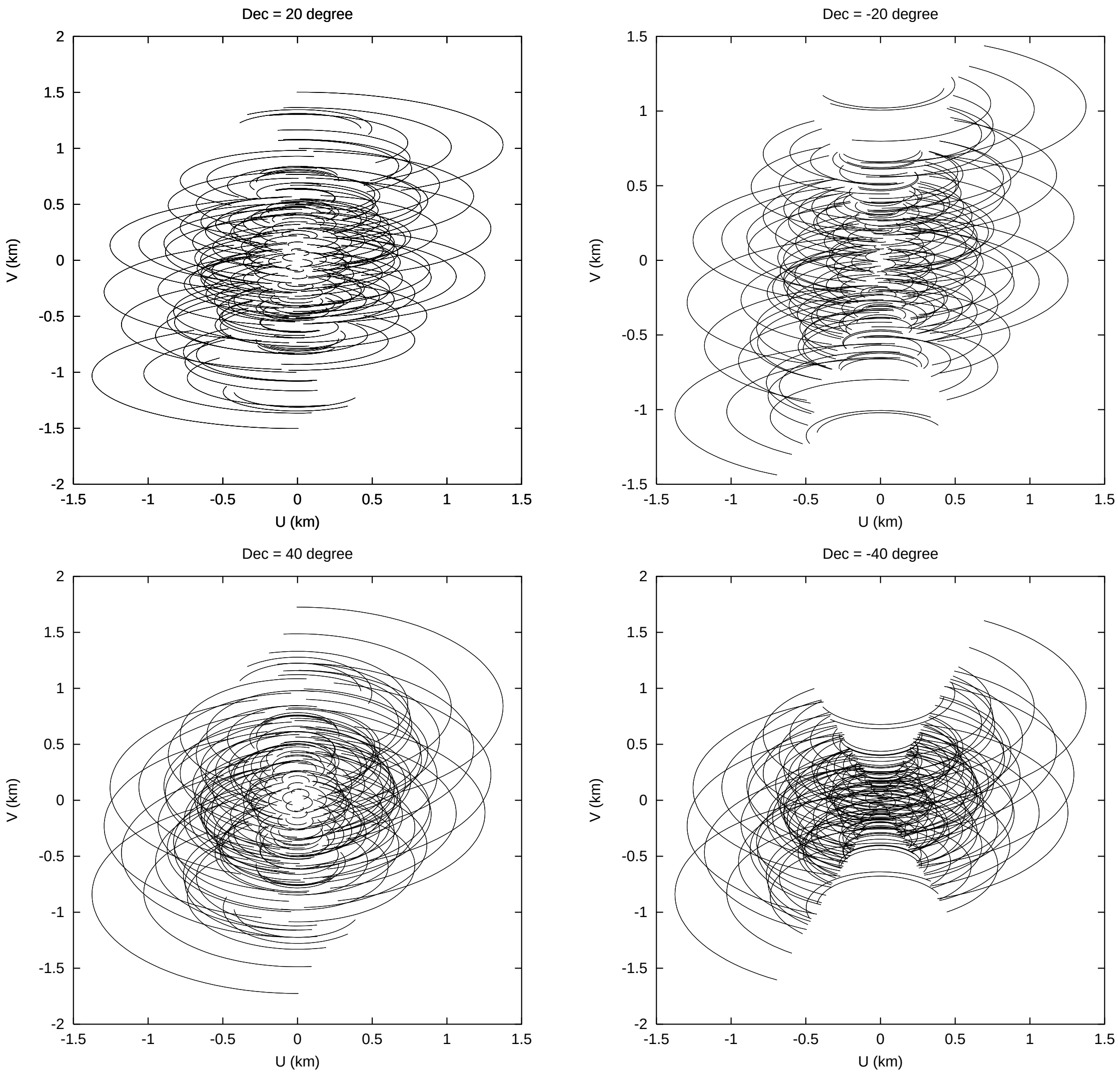

Figure 2.7: Full synthesis uv-coverage of the GMRT *Central Square* at declinations of $20°$, $-20°$, $40°$ and $-40°$ respectively.

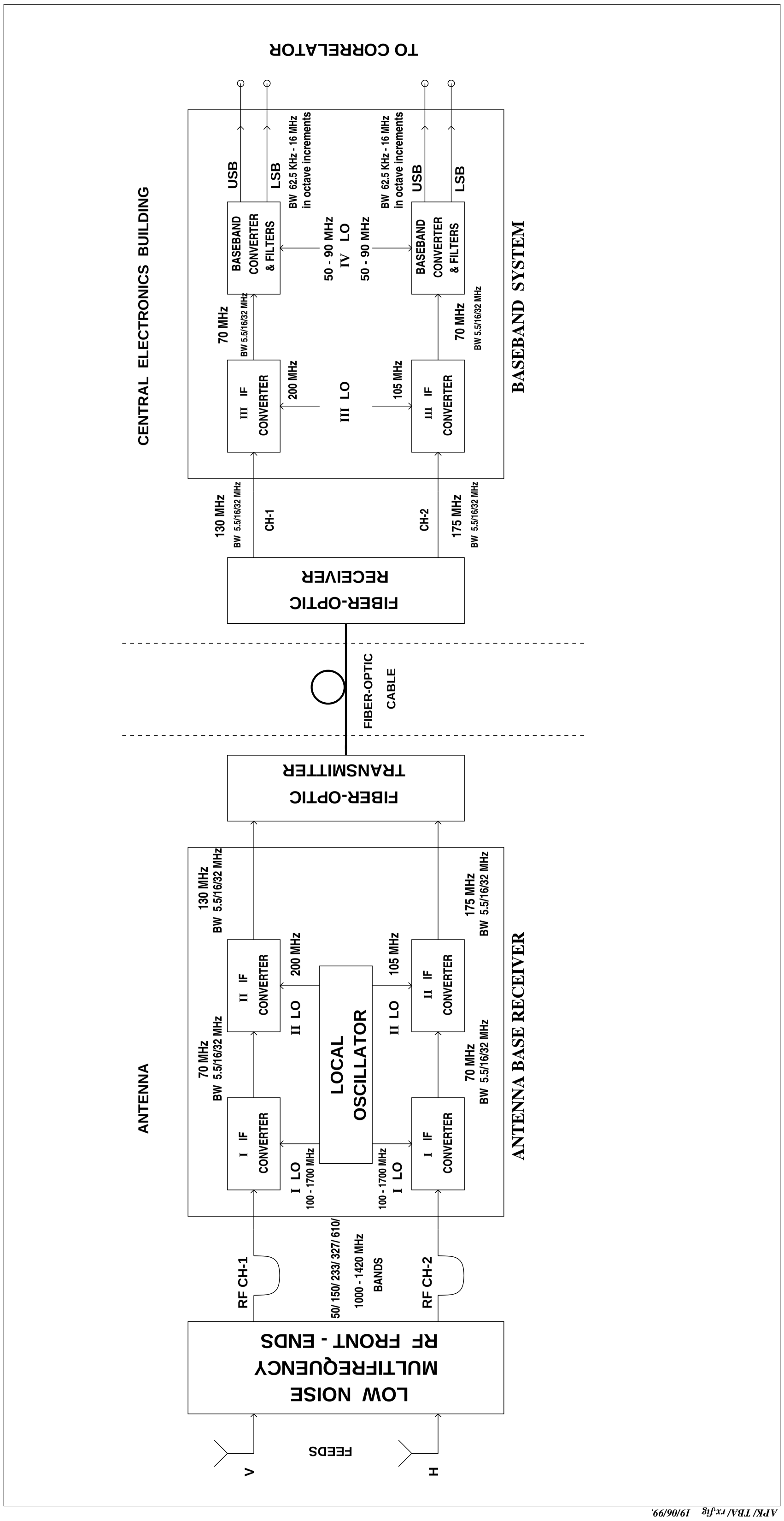

Figure 2.8: Block diagram showing the GMRT receiver system. The diagram is taken from Praveen Kumar (2000).

Table 2.1: Table of GMRT feeds and corresponding bandwidths for standing wave ratios of ≤ 2. The 233 and 610 MHz feeds are co-axial feeds.

Nominal Centre Freq. (MHz)	Feed Bandwidth (MHz)	Freq. Range (MHz)	Reliable Range (MHz)
150	130	$117 - 247$	$150 - 158?$
233	12	$228 - 240$	$232 - 238$
327	138	$286 - 424$	$315 - 335$
610	127	$580 - 707$	$590 - 630$
1420	580	$1000 - 1580$	$1000 - 1450$

two polarizations signals. Solar attenuators of 14, 30 and 44 dB are also available. Four calibrated noise sources, named *Low, Medium, High* and *Extra-high cal* can be used to calibrate the receiver system. However, the planned periodic injection of calibrated noise has not yet been implemented. The Front-end electronics also has the facility for Walsh switching of the two polarization channels using orthogonal Walsh functions to minimize polarization leakage. However this is also not yet operational at the GMRT.

The RF band is first converted to an IF band centred at 70 MHz using what is referred to as the *First LO* (First Local Oscillator). Here, bandwidths of 5.5, 16 or the full RF bandwidths can be selected. The two IF signals corresponding to the two polarizations are then converted to 130 and 175 MHz with a maximum bandwidth of 32 MHz using the *Second LO*. These signals are then transported over optical fibers to the Central Electronics Building (CEB). Variable attenuators in the range of $0 - 30$ dB, which can be varied in steps of 2 dB are available separately for the two IF signals. An automatic level controller (ALC) at the output of the IF can be bypassed if required (e.g. for observations requiring measurement of variations at high time resolution). At the CEB, the 130- and 175-MHz signals, recovered from the output of the optical fibers, are fed to the Base Band system for conversion to base-band signals. These signals are first converted to 70 MHz band and then split into *Upper-* and *Lower-Sidebands* using the tunable *Fourth LO*. This LO can be tuned between $50 - 90$ MHz in steps of 100 Hz. At the base band, bandwidths of the 62.5, 125, 250, 500 KHz or 1, 2, 4, 8, 16 MHz can be selected. Another ALC is provided at the output of the baseband. Signal levels are kept at 0 dBm by this ALC before being fed to the correlator (see Section 2.5). This ALC also can, however, be bypassed.

For the purpose of astronomical observations, settings of the attenuators and the *First* and *Fourth LO*s are important. The combination of these two LOs determine the exact RF frequency used for observations.

2.4 Telescope parameters

The output of the individual antennas is a random signal composed of the signals from the source of interest in the sky, the sky background emission and the thermal noise generated by the various electronic components through which the signal flows. The output of the antennas and the receiver is usually expressed in terms of the temperature of a blackbody which will emit equivalent power. The *system temperature* (T^{sys}) of an antenna at a particular frequency, is equivalent to the total power from the antenna when it points towards a blank sky. The power received by an antenna due to the celestial source alone is represented by the *antenna temperature* (T^a).

The normalized visibility amplitude from antennas 1 and 2 is given by

$$|V_{12}| = \sqrt{\frac{T_1^a T_2^a}{(T_1^{sys} + T_1^a)(T_2^{sys} + T_2^a)}} \tag{2.20}$$

where $T^{sys} = T^r + T^{bg} + T^{spill}$, T^r is the receiver temperature, T^{bg} is the temperature of the sky background emission, and T^{spill} is antenna spill-over temperature. An unpolarized point source of flux density S (in units of $W\mathrm{m}^{-2}\mathrm{Hz}^{-1}$) will result in $T^a = A_e S/2k = \eta S$ where A_e is the effective collecting area of the antenna, k is the Boltzman's constant and η is the *antenna sensitivity*. For identical antennas and for the range of S where $T^a \ll T^{sys}$, $|V_{12}| \approx T^a/T^{sys} \propto S$. T^r, T^{sys} and η are therefore important telescope parameters, which together determine the sensitivity of the telescope.

These and other astronomically relevant parameters of the GMRT are listed in Table 2.2[1]. Fifth column is listed the angular resolution for both *Central Square* and full array.

2.5 The GMRT correlator

The prototype 4 and 8 antenna correlator, all of the initial design and most of the implementation of the final 30 antenna single sideband correlator currently in use and

[1] Initial measurements of T^{sys} and sensitivity at 327 MHz were done by me and others. Later, these measurements were done by A.P.Rao, N.G.Kantharia and others and also by various users from the Raman Research Institute, Bangalore for L-band. The method used is described in Section D.2

Table 2.2: Table of GMRT system parameters

Band (MHz)	T^{sys} (K)	Sensitivity (K/Jy)	Field of view HPBW/1^{st} Null	Resolution C.Sq./Full	Max. angular scale[a](arcmin)
150	450	0.35	$2^\circ.6/3^\circ.1$	$7'/17''$	60
233	180	0.30	$1^\circ.6/2^\circ.0$	$4'/11''$	44
327	100	0.35	$1^\circ.2/1^\circ.4$	$3'/8''$	32
610	90	0.30	$38'/46'$	$1'.7/4''$	17
1420[b]	70	0.25	$25'/30'$	$43''/2''$	8

[a]Computed for a reliable data up to $\sim 100\lambda$
[b]Effective antenna diameter is ~ 33 m due to leakage from the mesh

which was used for the observations for this dissertation were designed and built by the team consisting of C.R.Subramanya, A.Dutta, V.M.Tatke, A.Dikshit, R.K.Malik, U.Puranik, M.Burse and others. Further development for the second sideband correlator and maintenance is now done by Y.Gupta, M.Burse, S.Sirothia, C.P.Kanade, K.H.Dahimiwal, I.Halagalli and others, with contributions from A.Roshi. This section describes aspects of the GMRT correlator relevant from the point of view of astronomical observations. A more detailed description of the current correlator hardware design is given by Tatke (1998). The correlator control and data acquisition software for potentially multiple sub-array mode of operation was designed and implemented by R.K.Singh and C.R.Subrahmanya. A detailed description of the current correlator control and data acquisition software is given by Singh (2000). The sub-array mode of operation is described by Chengalur (2000).

2.5.1 Overview

The GMRT back-end for interferometric observations is an FX-type digital correlator. The block diagram in Fig. 2.9 shows the various stages of the correlator. The first stage of this correlator consists of a set of four samplers per antenna - one for each of the two IFs per side-band of the antenna. Each antenna produces two IFs which can carry either the two orthogonal polarization signals or the same polarization from two different RF bands (as in the case of $233/610$ MHz dual frequency feed). The analog to digital converter (ADC) of the samplers converts the input analog signal to 8-bit unsigned numbers. These 8-bit samples are converted to 6-bit unsigned numbers before being fed to the next stage of the correlator, referred to as the *Delay and Data Preparation Cards*, or the

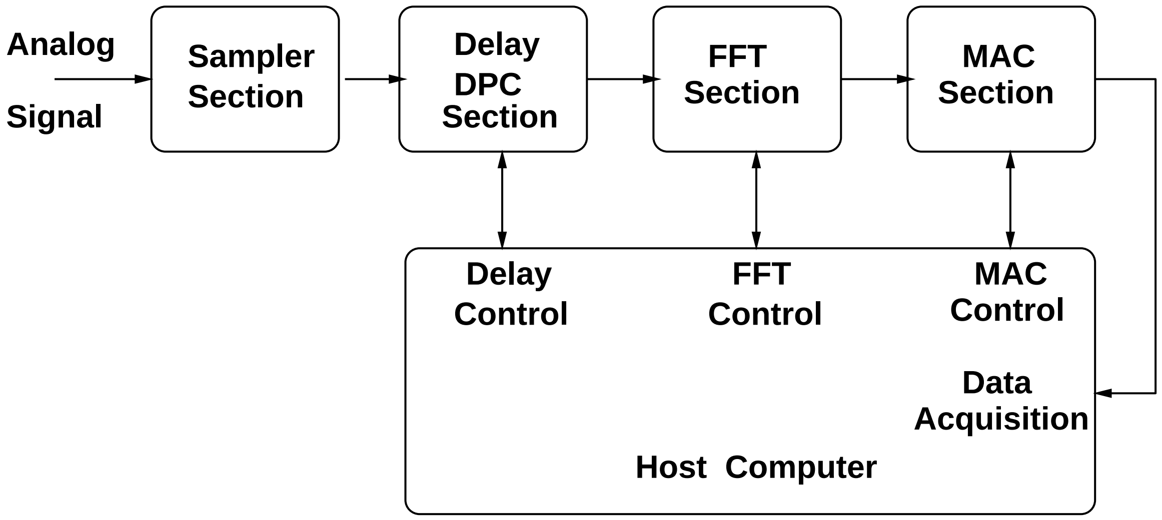

Figure 2.9: Schematic diagram of a single correlator pipeline. Signals from each antenna pass through independent pipelines consisting of the Sampler, Delay/DPC, and the FFT sections. Signals from two independent pipelines are multiplied in the MAC section. The output of the MAC section is fed to the DAS card on the Host computer. The Host computer also controls the Delay/DPC, FFT and MAC hardware.

Delay/DPC system. These samples are further converted to 4-bit signed numbers in the *Delay/DPC* system (see the section on Samplers below), before being fed to the next stage of the correlator. This conversion from 8-bit to 4-bit samples is required since the VLBA FFT chips used in the correlator work with 4-bit signed numbers. Part of the *compensating delay* equivalent to integral units of correlator clock is applied in the *Delay/DPC* stage. Any residual delay (corresponding to a fraction of the correlator clock) is applied as a phase ramp across the band, after the signals have been Fourier transformed (see Section 2.5.2). The *Delay/DPC* stage is followed by the Fast Fourier Transform or the *FFT* stage which performs a 512-point FFT corresponding to 256 point complex spectra (the other 256 points being the complex conjugate spectra). The output complex numbers are represented in *4,4,4-bit* format consisting of two 4-bit numbers for the mantissa of the real and imaginary parts and a common 4-bit exponent.

The correlation between signals from two antennas with the same polarization is referred to as the *co-polar* visibilities. This correlation is done by multiplying the antenna signals and averaging the result in the correlator. The output of the *FFT* stage is therefore fed to the *Multiplier and Accumulation (MAC)* stage of the correlator. Each *MAC* chip accepts 4 input data streams – 2 IFs from the two antennas. However each MAC can only handle a total of 256 channels per antenna. Therefore, either the number of channels per IF must be reduced from 256 to 128 or, only one IF with all the 256 channels must be fed to the *MAC*. This reduction of 256 channels for each IF to 128 channels to produce the *co-polar* visibilities is done by averaging two adjacent frequency channels. However, the GMRT correlator can also be used with a resolution of 256 frequency channels by sacrificing one of the polarization signals from the antennas.

The *MAC* output format consists of two 15-bit mantissa for real and imaginary parts and a common 6-bit exponent (this format is referred to as *15,15,6-bit format*). The accumulators in the *MAC* stage provide the *Short Term Accumulation (STA)*. Each *STA* cycle corresponds to 512 correlator clock cycles, required for reading the 512 points into the *FFT* section plus 4 clock cycles required to set-up the FFT cards before it can perform an FFT. Thus, each FFT cycle requires 516 correlator clock cycles. The correlator runs on an *effective* clock of 32 MHz and the *STA* accumulates the data for 4096 FFT cycles. Thus, the *STA* corresponds to an integration of $(512 + 4) * 4096/(32MHz) = 66$ ms of time. (Strictly speaking, the samplers run on a 32 MHz clock. This is the shortest time resolution that the GMRT correlator can provide. The *Delay/DPC* system reads the input data at the rate of 32 MHz but output data rate is 32.125 MHz. The rest of the correlator operates at 32.125 MHz to effectively take care of the dead time corresponding to the 4 clock cycles required for *FFT* setup).

The data rates corresponding to a *STA* time interval is large (8 MBytes/sec) and difficult to sustain for any data recording system. The *STA* data therefore needs to be integrated further to reduce the data rate by accumulating in the *Long Term Accumulation (LTA)* stage of the correlator. This stage has not yet been implemented in the hardware and therefore, the *STA* stage has been set to integrate for 8192 FFT cycles corresponding to a minimum integration time of 132 ms. This brings down the data rates to 4 MBytes/sec and the data is further integrated in the software for an integration time than can be set by the user to produce the final *LTA* data. The output of the *STA* stage is the final product of the correlator and is produced in the form of three data streams from the three *MAC* racks per sideband.

All the three *MAC* output streams are fed to the *Data Acquisition System (DAS)*, via a 16-bit bus. The *DAS* consists of a dual CPU PC running under the `GNU/Linux` Operating System (OS) with a data acquisition card on its PCI bus. The *STA* data from all *MAC*s is acquired on this card at the rate of 4 MBytes/sec consisting of all the 256 channels (256 frequency channels with only one polarization, or 128 channels with both polarizations).

The software device driver (which runs in the kernel space of the OS) and the supporting program (running in the user space of the OS) convert the input complex numbers from the correlator representation to the IEEE floating point representation. The software LTA is done at this stage for a time interval set by the user and the data rate further reduced. Through a series of network software, this data is transfered to another machine over the fast Ethernet to be recorded on the disk in what is referred to as the *LTA*-format (Singh (2000)). The last stage in the chain of software also provide facilities for further integration in time and frequency and for defining sub-arrays, etc. (the usage of the sub-array mode of the software is described by Chengalur (2000)).

Samplers

The analog-to-digital converter (ADC) used in the GMRT samplers is an 8-bit flash ADC (Tatke 1998). The input to these samplers is the band limited gaussian random noise from the antennas, converted to base-band (BB) (corresponding to a frequency range of 0 to 16 MHz). The output power of the baseband system is proportional to the antenna temperature which is a function of the sky temperature. The sky temperature, can vary by as much as a factor of $4-5$ between the Galactic plane and away from it. However, the samplers are designed to sample a fixed range of input signal. The BB output signals are therefore maintained at 0 dbm by the Automatic Level Controller (ALC) before being fed to the samplers. This corresponds to a peak-to-peak variation of ± 1 V spanning the input random signal up to the six sigma level. In order to preserve the statistical properties of the input, the 2^8 comparator voltage levels (in the ADC) must be optimally set such that the samplers neither saturate when the input voltage deviates by six sigma from the mean, nor sample the weaker signals too coarsely (corresponding to much smaller deviations from the mean). As of now, the 2^8 voltage levels corresponding to 8-bit sampling are uniformly distributed across this range of voltage, corresponding to a voltage resolution of 7.8 mV (provisions however exist for a more sophisticated scheme to distribute the levels across the range of input signal). However, before being fed to the next stage of the correlator (namely the Delay/DPC stage), the 8-bits samples are converted to 6-bit samples by dropping the 2 least significant bits (LSB) of the samples. Effectively, this corresponds to 2^6 levels covering the full range of ± 1 V, with a resolution of 31.25 mV, but which *still* sample the full range of the input signal up to six sigma, although at a coarser resolution. These 6-bit samples are unsigned. Inside the Delay/DPC system these samples are further converted to 4-bit signed values via a look-up table. The look-up table is made such that the 2^4 levels are again uniformly distributed for the entire range of the input signal (in this case, the 6-bit samples). Hence, effectively, the input signal with 6-bit resolution is further sampled at a coarser resolution of 4-bits without statistically altering the signal.

For the purpose of astronomical observations, this entire operation of converting the 8-bit unsigned samples to 4-bit signed samples can be ignored and the GMRT samplers can be treated as an *effective* 4-bit samplers.

Long Term Accumulation (LTA) and time keeping

This section describes the mechanisms used in the correlator data acquisition software for deriving accurate time information. This is essentially a description of the work done by Singh (2000).

The input data to the DAS is averaged for a length of time set by the user to produce the long term accumulated (LTA) data. This interval is typically set to $10 - 20$ sec. The LTA operation is currently done in the software and may be moved to hardware in future (if required).

As mentioned earlier, a synthesis radio telescope like the GMRT utilizes the earth rotation to synthesize an effective large aperture. To keep the array instantaneously phased, the time varying *geometrical delay* must be continually compensated. The phasing of the array is therefore a time critical operation requiring accurate time keeping. Accurate time information is also required for proper pointing of the antennas and tracking of an astronomical source. Stamping of astronomical data with accurate time is therefore very important.

Absolute time for the GMRT is kept using the real time clock (RTC) of the GMRT correlator control computer. This clock is synchronized with the GPS time using a GPS receiver. The GPS and correlator system clocks are used to remove any time jumps and/or slow drifts of this real time computer clock as described below. This time stamping of the visibility data in the GMRT correlator/data acquisition achieves an accuracy of $\sim 100\,\mu$sec.

The correlator provides a synchronization pulse to the DAS to indicate the start of each *STA* cycle via an *STA interrupt*. This information is also supplied to the DAS via one of the bits of the data bus, referred to as the data synchronization bit. The DAS software uses this information to (1) do a consistency check (2) determine the start of the *STA* data in a stream of continuous data flowing on the data bus from the MAC. The DAS card also receives an interrupt signal at the start of each minute from the GPS receiver. The *interrupt handler* (the software which does time critical operations when a hardware interrupt is received) for both these interrupts (STA and GPS interrupts) reads the PC time from the PC RTC at each interrupt and maintains a list of corresponding PC time stamps. The list of PC time stamps recorded at each GPS interrupt is then examined for a constant difference of 1 minute. A continuous series is selected such that the time difference between successive samples is accurate to 100 μsec. This series of PC time stamps is referred to as a series of "good" GPS-interrupted time stamps. This series is used to set up a linear equation between the GPS time and the PC time. Since GPS time can be easily converted to the local time standard (Indian Standard Time or IST), this equation essentially converts the PC time to accurate IST time. This equation provides a first order calibration of the PC time, and takes care of any short glitch in the PC time (which can happen due to variety of reasons including overloading of the PC bus). Similarly, the PC time is recorded at each *STA interrupt*. This list of *STA*-interrupted PC time stamps is also examined and a continuous series selected such that the time difference between successive PC time stamps is equal to one *STA* cycle, to an accuracy of 100 μsec. This series of "good" PC time stamps is used to set up a linear relation between the PC time and *STA* time. The PC time to IST time equation is then used to convert the *STA* time to IST time, and is also used to tag each *STA* data block with a sequence number.

The three sources of timing information to the DAS (1) the *STA* interrupts (2) the GPS interrupts, and (3) the data synchronization bit, all provide time information with respect to the PC RTC. In the above scheme, on a short time scale, unless all these three sources produce drifts and/or glitches, time stamping of the data will remain accurate to 100 μsec. Since all these are independently running clocks, the probability of all three producing error at the same time is very low and it has been shown that the above time stamping scheme is quite robust to short time scale glitches and time drifts.

To account for slow drifts in the PC time, an attempt is made to set up a new linear equation between the *STA* sequence number and PC time after every 16 *STA* cycles. The new relation is not accepted unless it matches with the previous one within 100 μsec. Similarly, a new relation is set up between GPS and PC time at each GPS interrupt.

On a longer time scale, an error can occur due to some catastrophic error in either of these sources (e.g. the interrupts not arriving at the PC due to hardware failures). If the DAS software cannot set up the new equations for more than a threshold time interval, it is assumed that an irrecoverable error has occurred rendering the current equations invalid. In such a case, the DAS sets up fresh equations and the data between such an event and the time interval required to set up valid equations is unreliable and is flagged. In practice, however, such events are very infrequent.

However, a slow drift in the PC RTC, with respect to which *all* three sources of timing information are measured, can produce a drift in the final IST time stamps in the data. Data blocks are expected to arrive at the DAS at a pre-determined constant rate. Data blocks themselves therefore can be effectively used as yet another clock, which is independent of the PC time. Any drift of the PC clock will show up as a *consistent* shift in the equations between the GPS and PC time and between STA and PC time with respect to the arrival of the data blocks. Hence, any consistent error in the arrival of the data blocks measured with respect to the IST time, derived from the two linear equations, will indicate a drift in the PC time. This fact is used to monitor a slow drift in the PC time over the time scale of setting up new equations.

The PC time is also synchronized to the minute pulse from the GPS. Errors in the PC RTC *less* than half a minute can therefore be corrected and PC clock synchronized to the GPS clock. However if the PC RTC is in error by more than half a minute, this synchronization will result into minimum of 1 min in the PC RTC. It is therefore important to set the PC RTC to *within* $1/2$ min of the GPS time.

2.5.2 Delay compensation

As mentioned earlier, the *compensating delay* (equal to $\tau_g + \tau_{Fix}$; see Section 2.1.1, page 51) which needs to be applied to one of the antennas of an interferometer is applied in the GMRT correlator in two stages. A delay equivalent to an integral multiple of the correlator clock (τ_{Int}) is applied in the *Delay/DPC* section of the correlator. The input data stream is copied into a dual port RAM at the location given by the write-counter. Data is read simultaneously from this RAM from the location given by the read-counter. The offset between the read- and the write-counters for this RAM is maintained such that the read-counter lags behind the write-counter. Since the output samples are read with a time delay (equal to the difference between the counters multiplied by the correlator clock cycle), the output data stream corresponds to the input data stream with a time delay. The time delay, however, can only be in multiples of the correlator clock cycle. The residual delay, corresponding to a fraction of the correlator clock cycle is applied in the *fractional sample time correction* or *FSTC* operation. The last stage of the FFT butterfly network provides a facility to apply a channel dependent phase. The frequency channel dependent time varying, phase corresponding to this residual delay, represented by τ_{FSTC}, is applied as a linear phase gradient across the band as

$$\tau_{FSTC}(t) = \frac{1}{2\pi}\left.\frac{d\phi}{d\nu}\right|_t \tag{2.21}$$

Note that τ_{FSTC} includes the residual delay due to delay resolution in the Delay/DPC system of the correlator plus the channel dependent residual delay of Equation 2.18.

The output of the *FFT* stage of the correlator is a set of 256 independent complex numbers. These complex numbers are represented by three 4-bit numbers; one each for the mantissa of real and imaginary parts and one for a common exponent. The complex gains, applicable at the last stage of the FFT butterfly network, are represented by 5 bits each for the real and imaginary parts but has no exponent bit. Thus the channel dependent phase gradient for the *FSTC* is also limited to a 5-bit representation.

The *FFT* stage of the correlator performs a real-time Fourier transform of the input signal effectively splitting the input bandwidth of $\Delta\nu$ into 128 frequency channels, each of width $\Delta\nu/128$ (the *FFT* stage of the correlator can be treated as a set of 128 filter banks). The time series from each of the 128 frequency channels from an antenna, are then multiplied with the corresponding channels from all other antennas, before being integrated in the *MAC* section of the correlator. The effective input bandwidth, as seen by the multiplier is therefore $\Delta\nu/128$. For the GMRT, the maximum value of $\Delta\nu$ is 16 MHz corresponding to a maximum channel width of 125 KHz, giving a *fringe washing function* of width ~ 8 μsec. Therefore, for the GMRT correlator, the residual delay must remain less than a fraction of this width (typically less then few micro seconds).

2.5.3 Imaging modes

In the final double sideband correlator, in the continuum, non-polar mode, the correlator can be used to record the two *co-polar* visibilities (the nominal RR and LL correlations) per antenna with a full bandwidth of 32 MHz (both sidebands). In the current single sideband correlator only one sideband of 16 MHz can be processed. In the full polar mode, which will be available with the dual sideband correlator, the cross polar visibilities (namely RL and LR) cal also be recorded. Since the correlator can handle only 256 channels per antenna at the MAC stage, the cross polar mode can be used with only one of the sidebands with a maximum bandwidth of 16 MHz.

The GMRT correlator naturally produces spectral visibilities with a maximum of 256 channels across the entire observing band, if only one polarization is used, or with 128 channels, if both polarizations are used. For normal continuum observations, the 128 channels across a 16 MHz band provide a channel resolution of 125 kHz. For observations where bandwidth smearing is not important (and in the absence of RFI), these channels can be collapsed on-line to produce continuum visibilities. At lower frequencies where primary beams are large, bandwidth smearing can be important for sources away from the phase centre. Also, at frequencies below 610 MHz, intermittent RFI is always a possibility. To reduce bandwidth smearing and to detect and flag narrow band RFI-contaminated data, all the 128 channels are usually recorded. Provision for frequency averaging before recording does however exist and can be used where RFI and bandwidth smearing problems are not perceived to be serious.

For spectral line observations, channel resolution can be increased by controlling the sampling rate of the input signal. The sampling rate can be changed between 32 MHz and 0.125 MHz in steps of two. This corresponds to an effective bandwidth between 16 MHz and 0.25 MHz with a frequency resolution between 125 kHz and ~ 1.95 kHz respectively.

2.6 Baseline and fixed delay calibration

A synthesis radio telescope measures the two-dimensional spatial frequency spectrum of the source structure. Instantaneous projected separations between the elements of the interferometer in the *uvw-frame* determine the spatial frequency being sampled by the antenna pairs. The projected separation between the antennas, given by w, gives rise to the *geometrical delay* which needs to be compensated by *delay tracking* before the signals are multiplied. The value of w is given by

$$w = [X_{ij}\cos(H) - Y_{ij}\sin(H)]\cos(\delta) + Z_{ij}\sin(\delta) \tag{2.22}$$

where (X_{ij}, Y_{ij}, Z_{ij})=$(X_i - X_j, Y_i - Y_j, Z_i - Z_j)$. The *geometrical delay* is therefore a function of the *relative* antenna positions. Precise measurement of the relative locations of the antennas is hence important for phasing the array, which is necessary for imaging with such a telescope.

The radio frequency (RF) signals from the two orthogonal feeds of the antenna are converted to two separate intermediate frequencies (IF) and brought to the Central Electronics building (CEB) for correlation via the optical fiber cables. The *fixed delay* suffered by the signals from each antenna varies from antenna to antenna since the physical length of the optical fibers to various antennas differ. This *fixed delay* is largely constant, showing small and slow variations due to changing ground temperature. Since the optical fiber cables are dispersive, any *relative fixed delay* between antenna pairs results in a time invariant phase ramp across the band in the visibility data. This phase ramp must also be removed or calibrated before averaging the channels to produce the continuum visibilities or before being used for imaging.

The following two sections describe the methodology used and results of baseline and fixed delay calibration.

2.6.1 Baseline calibration

Historically, the GMRT antenna positions were first determined using theodolite measurements. These were refined using P-band observations following the procedure laid down by Bhatnagar & Rao (1996). Later, dual frequency GPS measurements (Kulkarni 1997) were done to independently determine the antenna co-ordinates.

The GPS measurements provided the antenna co-ordinates relative to the reference GPS antenna, to a quoted accuracy of ~ 2 cm. However, monitoring the phase as a function of hour angle at 327 MHz indicated errors in excess of few meters for some antennas. These GPS co-ordinates were then further refined using P-band observations of celestial sources. Antenna based phases were determined using the GMRT off-line program `rantsol` (Bhatnagar 1999) from a continuous (~ 7 hours) tracking of `3C48` at 327 MHz. The antenna based phases were modeled as a function of hour angle to measure the relative antenna co-ordinates (see below and Bhatnagar & Rao (1996)). The set of co-ordinates from these measurements were accurate to ~ 1 m for the arm antennas and ~ 0.1 m for the central square antennas. The phase variations at 327 MHz due to other factors (~ 30 arcsec error in antenna pointing which was later corrected, ionospheric contributions, etc.) did not allow determination of X and Y to better accuracies. The Z co-ordinate could not be calibrated at 327 MHz since not enough 327-MHz calibrators could be found which could cover a large declination range but were close enough in hour angle. The proximity of calibrators in hour angle for Z calibrations was necessary to eliminate any unwanted scatter in the phase as a function of declination due to residual errors in the X and Y co-ordinates (see page 73).

These co-ordinates were then further refined using L-band observations (Chengalur & Bhatnagar 2001). Since the residual phase is proportional to the projected baseline length measured in units of the wavelength of the incident radiation, L-band is the best frequency to determine the residual co-ordinate errors in the antenna positions. For this purpose, VLA L-band calibrators `0217+738` and `1125+261` were tracked for several hours at 1280 MHz to compute the antenna based phases. Corrections of $0.5-1$ m, consistent with the residual co-ordinate errors from the 327-MHz measurements, were found for a few antennas. The final co-ordinates for the *Central Square* antennas are now known to an accuracy of $\approx\ 0.05$ m. The residual phases for arm antennas correspond to position errors of $0.02-0.36$ m. These errors do not repeat from day-to-day and are also different for different sources indicating that the residual phases are probably not due to antenna position errors.

The procedure used

Assuming no errors in the antenna pointing ($\Delta H\ =\ \Delta\delta\ =\ 0$), the antenna based phase for an antenna with a position error of $(\Delta X,\Delta Y,\Delta Z)$ with respect to a reference antenna located at the origin ($(X,Y,Z)=(0,0,0)$), as a function of the hour angle and declination is given by

$$\phi=2\pi\frac{\nu^o_{RF}}{c}\left[\Delta X\cos(\delta)\cos(H)-\Delta Y\cos(\delta)\sin(H)+\Delta Z\sin(\delta)\right]+2\pi\tau_{Fix}\nu_{IF} \tag{2.23}$$

where ν^o_{RF} is the frequency of the centre of the RF band, H is the Hour Angle, δ is the declination of the phase center, τ_{Fix} is the fixed delay suffered by the signal at the IF frequency ν_{IF} and c is the speed of light. The orientation of the X, Y, and Z axis is shown in Fig. 2.1.

As can be seen from Equation 2.23, an error in Z will contribute a constant phase for a fixed value of δ. It is therefore necessary to observe a number of sources at different declinations to distinguish between the phase contributed by the terms involving ΔZ and τ_{Fix} (both of which are independent of H).

The terms involving ΔX and ΔY in Equation 2.23 have a sinusoidal dependence on H. Hence, by tracking a point source for several hours (to get coverage in H while keeping δ constant), the left hand side of the above equation can be modeled as

$$\phi=C+A\sin(\frac{2\pi}{24.0}H+2\pi\psi) \tag{2.24}$$

where C is a constant and H is in unit of hours. Equating this to the RHS of Equation 2.23 the expressions for ΔX and ΔY (in meters) can be written as

Table 2.3: List of antenna measured antenna co-ordinates and fixed delays. All positions and fixed delays are measured with respect to antenna C02. Currently, same fixed delays are set for both the IF signals from an antenna. With the new version of $Delay/DPC$ system (currently under development), the fixed delays for the two IFs will need to be calibrated separately.

Ant. No.	Name	X(m)	Y(m)	Z(m)	Fixed delay(m)
00	C00	6.95	687.88	-20.04	-497.89
01	C01	13.24	326.43	-40.35	179.15
02	C02	0.00	0.00	0.00	588.10
03	C03	-51.10	-372.72	133.59	480.47
04	C04	-51.08	-565.94	123.43	80.98
05	C05	79.09	67.82	-246.59	84.89
06	C06	71.23	-31.44	-220.58	-177.43
07	C08	130.77	280.67	-400.33	-463.19
08	C09	48.56	41.92	-151.65	259.30
09	C10	191.32	-164.88	-587.49	-442.73
10	C11	102.42	-603.28	-321.56	-284.13
11	C12	209.28	174.85	-635.54	-1044.71
12	C13	368.58	-639.53	-1117.92	-1347.68
13	C14	207.30	-473.71	-628.63	-423.23
14	E02	-348.04	2814.55	953.67	-3877.18
15	E03	-707.58	4576.00	1932.46	-7742.26
16	E04	-1037.11	7780.69	2903.29	-13748.08
17	E05	-1177.37	10200.00	3343.20	-20440.99
18	E06	-1571.32	12073.46	4543.13	-25151.18
19	S01	942.99	633.92	-2805.93	-5486.16
20	S02	1452.85	-367.30	-4279.16	-9232.06
21	S03	2184.54	333.03	-6404.96	-13826.41
22	S04	3072.86	947.68	-8979.50	-18670.27
23	S06	4592.71	-369.04	-13382.48	-27847.16
24	W01	-201.50	-1591.94	591.32	-1336.69
25	W02	-482.67	-3099.41	1419.39	-4642.84
26	W03	-992.01	-5199.90	2899.11	-9608.61
27	W04	-1734.55	-7039.03	5067.53	-15280.83
28	W05	-2706.09	-8103.13	7817.14	-21583.03
29	W06	-3102.11	-11245.60	8916.26	-29257.26

$$\Delta X = \frac{A\sin(\psi)c}{\cos(\delta)2\pi\nu^o_{RF}} \tag{2.25}$$

$$\Delta Y = \frac{A\cos(\psi)c}{\cos(\delta)2\pi\nu^o_{RF}} \tag{2.26}$$

A and ψ can be measured by fitting Equation 2.24 to the antenna based phases, with A, C and ψ as the parameters of the fit. Equations 2.25 and 2.26 then gives the antenna position errors along the X- and Y-axis. ϕ, which is the antenna based phase computed with respect to the reference antenna located at the origin, was computed as a function of Hour Angle using the program `rantsol`. Equation 2.24 was then fitted to the phases from individual antennas to derive the values of C, A and ψ and Equations 2.25 and 2.26 used to derive the corrections for the X and Y co-ordinates of the antennas.

Table 2.4: List of L-band VLA calibrators used for ΔZ calibration

Source	RA (J2000)	Dec (J2000)	Flux density (Jy)
$0828-375$	$08^h28^m04^s.8$	$-37^\circ31'06''.3$	2.9
$0735-175$	$07^h35^m45^s.8$	$-17^\circ35'48''.4$	2.6
$0820-129$	$08^h20^m57^s.5$	$-12^\circ58'59''.2$	1.5
$0725-009$	$07^h25^m50^s.7$	$-00^\circ54'56''.5$	2.4
$0739+016$	$07^h39^m18^s.0$	$01^\circ37'04''.6$	1.8
$0825+031$	$08^h25^m50^s.3$	$03^\circ09'24''.5$	1.1
$0745+101$	$07^h45^m33^s.1$	$10^\circ11'12''.7$	3.3
$0738+177$	$07^h38^m07^s.4$	$17^\circ42'19''.0$	2.2
$0842+185$	$08^h42^m05^s.1$	$18^\circ35'41''.0$	1.4
$0741+312$	$07^h41^m10^s.7$	$31^\circ12'00''.2$	2.0
$0713+438$	$07^h13^m38^s.2$	$43^\circ49'17''.0$	2.2

The ΔZ correction requires observation of point sources at various declinations. A set of VLA L-Band calibrators with L-band flux densities > 1 Jy and covering a declination range of $\approx \pm 40^\circ$ were used to measure ΔZ. Since the observations of each of these calibrators were separated in time, any residual error in the X and Y co-ordinates would reflect in the data as an undesirable spread of the phases as a function of declination. To minimize the effects due to residual errors in X and Y co-ordinates, these calibrators were chosen to be within $\sim 1^h$ of each other in Right Ascension. The Z co-ordinate can then be found by fitting $\Delta Z \sin(\delta)$ to the antenna based phase as a function of declination. The final antenna co-ordinates, measured using this procedure, are tabulated in Table 2.3. The list of calibrators used for this purpose is given in Table 2.4. A typical phase variation as a function of declination, before and after correcting for the Z co-ordinate, is shown in Fig. 2.10. The variation of phase as a function of HA derived from $\sim 5h$ long observation of 3C286 (28 Jy at 327 MHz), for a representative set of *Central Square* and arm antennas is shown in Figs. 2.11 and 2.12 respectively. The source of the short term drifts of $\approx 5-10^\circ$ is likely to be the ionosphere. Phase variations over similar time scales and magnitude have been seen at the VLA and have been, to some extent, corrected using GPS based measurements of the variation in the ionospheric total electron content (Erickson et al. 2001).

The estimated accuracy of the antenna co-ordinates, derived from the variations in the phase as a function of hour angle and declination is ~ 5 cm. This will produce a maximum phase variation of $\sim 0^\circ.2$ per degree in declination and $\sim 5^\circ$ per hour in hour-angle at 1420 MHz due to errors in the antenna co-ordinates. Thus, observations of a calibrator located 20° away in the sky from the target source every half-an-hour, would result in a phase error of a few degrees when the antenna based complex gains derived from the calibrator scans are transferred to the data on the target source. These figures will be scaled down by a factor of ~ 4 at 327 MHz. At this level, phases of many antennas drift in an unsystematic manner and constitute the source of dominant phase errors. The residual phase errors due to errors in the antenna co-ordinates after fringe stopping are therefore negligible.

2.6.2 Fixed delay calibration

The *geometrical delay* τ_g is suffered by radiation at the RF frequency ν_{RF} while the dominant *fixed delay* is suffered at the IF frequency ν_{IF}. The *compensating delay* is applied at the base-band (BB) frequency ν_{BB} at the correlator. The total time delay applied at the correlator, (τ_{corr}) is therefore related to τ_g and τ_{Fix} as

$$\tau_g(\nu^o_{RF} + \nu_i) + \tau_{Fix}(\nu^o_{IF} + \nu_i) = \tau_{corr}(\nu^o_{BB} + \nu_i) \tag{2.27}$$

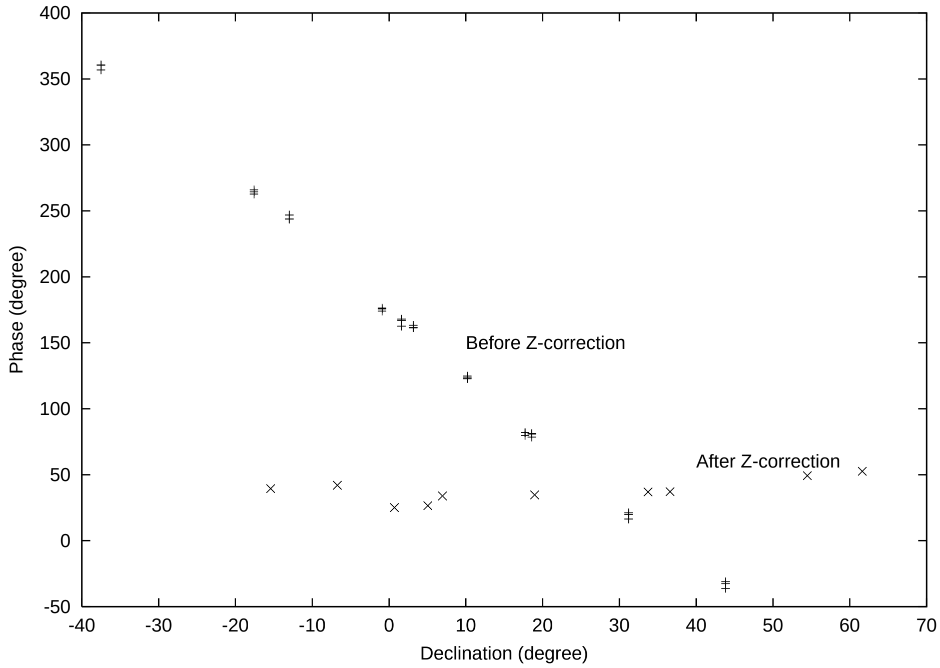

Figure 2.10: A typical antenna based phase variation due to an error in the Z co-ordinate of the antenna, before and after the application of co-ordinate correction. The '+' symbol marks the measurement of an antenna based phase before the correction and the '×' symbol represents the measurement taken after the correction.

where ν_i is the centre frequency of the i^{th} frequency channel and equal to $i\nu$ where $\Delta\nu$ is the channel width. ν^o_{RF}, ν^o_{IF} and ν^o_{BB} are the centre frequencies of the RF, IF and the base-band respectively. Noting that $\nu^o_{BB} = 0$ the above equation can be written as

$$\tau_{corr} = (\tau_{Int} + \tau_{FSTC}) = (\tau_g + \tau_{Fix}) + \frac{\tau_g \nu^o_{RF} + \tau_{Fix}\nu^o_{IF}}{\nu_i} \tag{2.28}$$

τ_{Int} corresponds to the time delay applied at the *Delay/DPC* stage while τ_{FSTC} corresponds to the residual delay applied in the *FSTC* operation (see Section 2.5.2).

In terms of the various frequency conversions in the signal flow, the RF band, for the purposes of delay compensation, can be written in terms of the first and the second local oscillator frequencies (which convert the RF signal to IF signal and the IF signal to baseband signal respectively) as $\nu^o_{RF} = \nu_{LO1} + \nu_{LO2}$ where, ν_{LO1} and ν_{LO2} are the the first and the second local oscillator frequencies respectively.

The residual phase across the band after delay compensation can therefore be written as

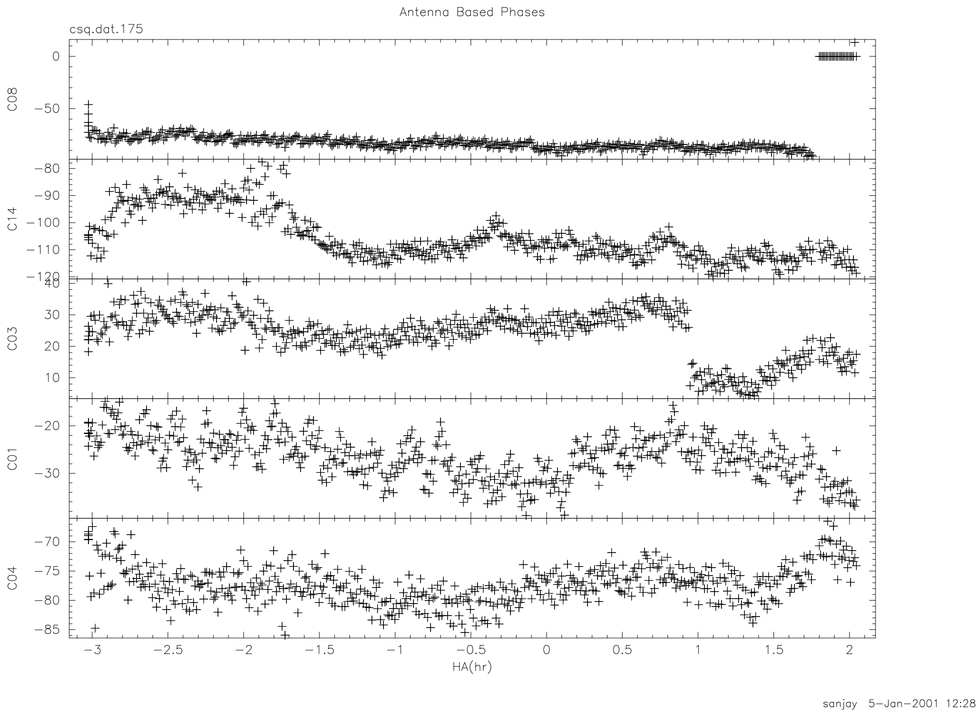

Figure 2.11: A typical antenna based phase variation at 327 MHz for a representative set of *Central Square* antennas. The y-axis represents the phase in degrees. The variation in phase over time scales of hours is probably due to ionospheric changes. The phase jump seen in C03 at around HA= 1^h is either due to a phase jump in the local oscillator or due to errors in the FSTC.

$$\frac{\phi}{2\pi} = (\tau_g + \tau_{Fix} - \tau_{Int} - \tau_{FSTC})\nu_i + \tau_g(\nu_{LO1} + \nu_{LO2}) + \tau_{Fix}\nu_{LO2} \tag{2.29}$$

Assuming that $\tau_{Int} + \tau_{FSTC}$ accurately compensates for τ_g, τ_{Fix} can be written as

$$\frac{1}{2\pi}\frac{\partial\phi}{\partial\nu} = \tau_{Fix} \tag{2.30}$$

The largest contribution to the fixed delay is due to the propagation delay in the optical fibers from the antenna base to the Central Electronics Building (CEB). These delays were measured by computing the antenna based complex gains for each of the 128 channels using the off-line program `rantsol`, for a strong point source observed at 327 MHz using the full band 16 MHz. This essentially provided the antenna based amplitude and phase across the band. The slope of the phase across the band was measured and τ_{Fix} derived using the Equation 2.30 (the slope of phase as a function of frequency). The fixed

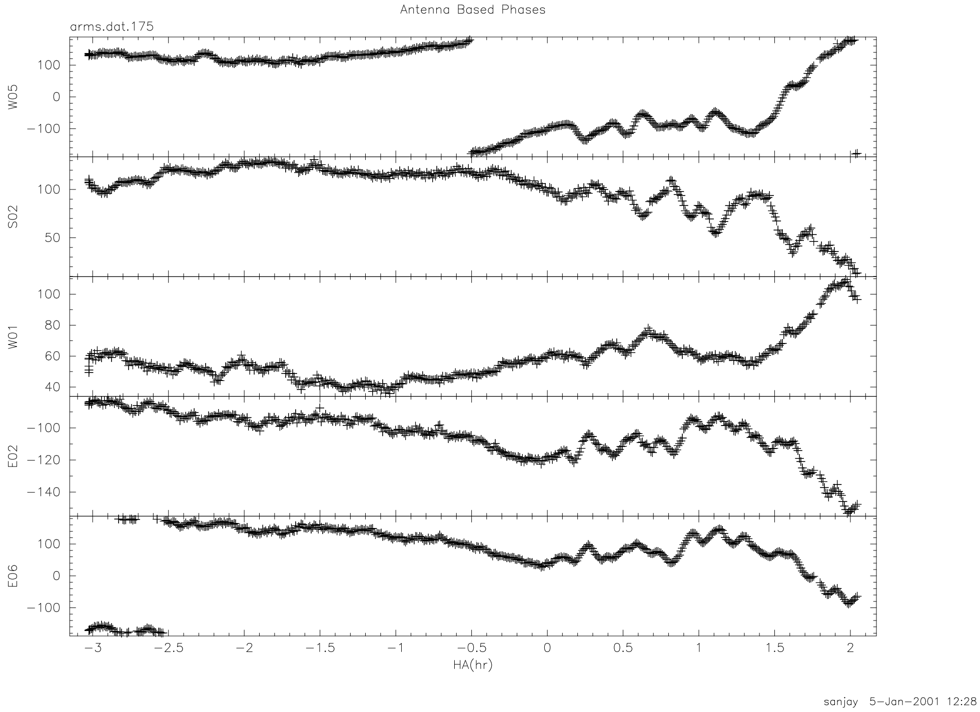

Figure 2.12: A typical antenna based phase variation at 327 MHz for a representative set of arm antennas. The y-axis represents the phase in degrees. The long term systematic variation corresponds to a position error of few centimeters but the corrections do not repeat for different days.

instrumental delays thus measured are also listed in Table 2.3. The phase across the band before and after the fixed delay correction is shown in Figs. 2.13 and 2.14 respectively for a representative set of antennas.

For interferometric observations, frequency averaging (to produce continuum or multi-channel continuum visibilities) is done after correlation and only the *relative fixed delays* are important. Since the same set of reasonably identical filters are selected at all antennas, the relative change in the fixed delays due to change of filters is not large. Also, since the ground temperature variation is similar from antenna to antenna and slowly varying over the scale of the array, its contribution to change in delays is not large. Although the delay component due to the filter selection and that due to diurnal variations must ultimately be tabulated and used for the delay compensation software, it is not a limiting factor and can be easily calibrated. The phase calibrators used for the continuum mapping observations used in this dissertation were strong (> 5 Jy) and were observed every half-an-hour. The antenna band shapes were computed from the data on these calibrator scans and the interpolated gains for each channel applied to the visibilities of the

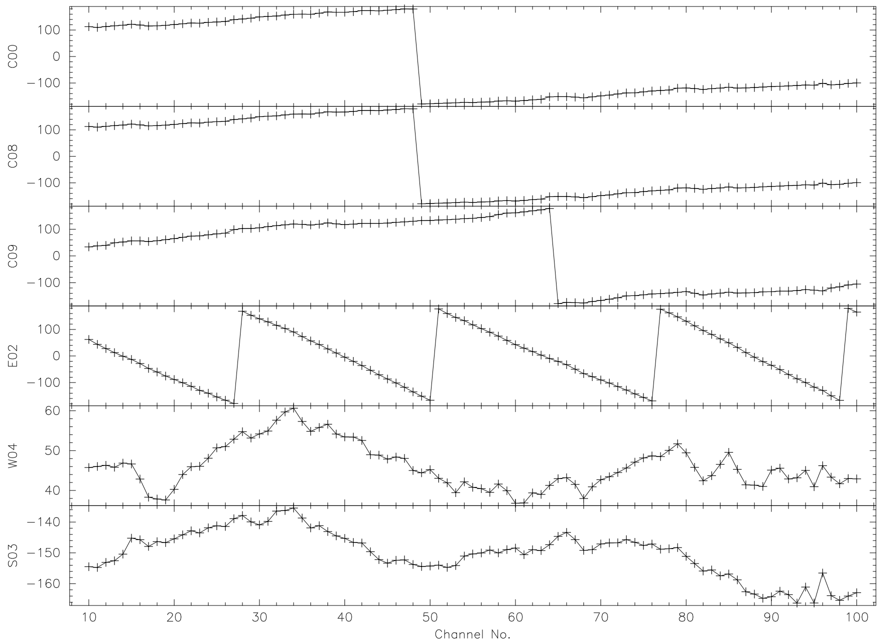

Figure 2.13: Antenna based phases across the band are plotted as a function of channel number before the fixed delay correction. The y-axis for each panel corresponds to the phase in degrees and the channel width corresponds to ~ 128 kHz.

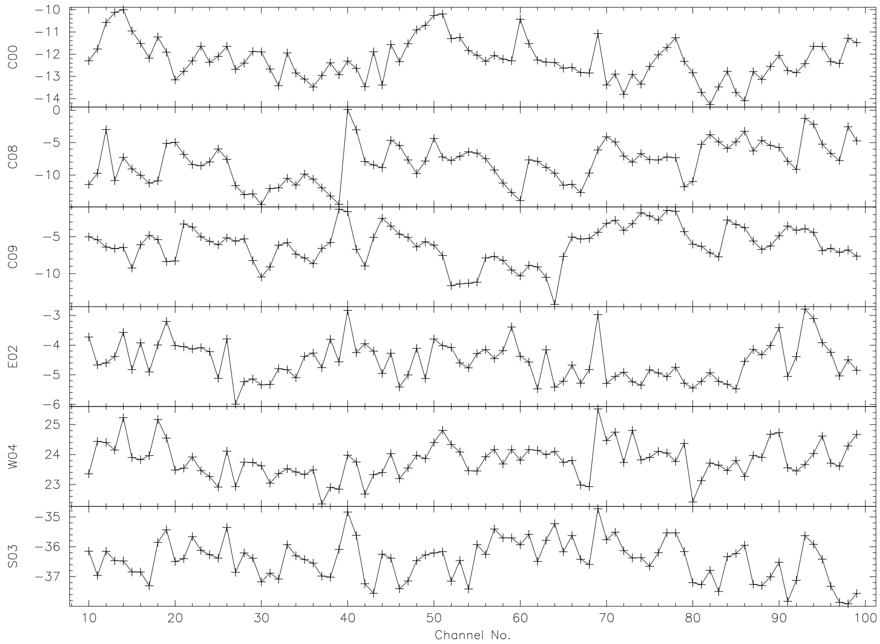

Figure 2.14: Antenna based phases across the band are plotted as a function of channel number after the fixed delay correction. The y-axis for each panel corresponds to the phase in degrees and the channel width corresponds to ~ 128 kHz.

target source. This provided the calibration for changes in the delay due to filters (small and fixed as function of time) and diurnal variations (small and slowly varying in time).

Chapter 3

Data analysis software

This chapter describes briefly the off-line data analysis software, developed to satisfy the data analysis needs for debugging the GMRT as well as for developing new algorithms for calibration and imaging at low frequencies. A modular, hierarchical software environment was therefore developed over the course of this dissertation. This software system is organized in the form of general purpose libraries at the lowest layer and a suit of general purpose application programs at the top-most layer. This design required much extra work, but it was perceived to be well worth the effort with the hope that ultimately, at the highest software layer, a large number of programmers would be professional astronomers writing complicated (but interesting) numerical analysis code.

The entire software now constitutes in excess of 50,000 lines of `C++` code and in excess of 10,000 lines of `C` and `FORTRAN` code. Some others in the GMRT group have used these general purpose tools to write more software. In a software development cycle, the number of bug reports per unit of time (week or month) is generally considered to be an indicator of the stability of the software. Assuming this to be a good measure, the libraries are now well debugged and stable (however, a low rate of bug reports could also be due to lack of sufficient number of careful users).

3.1 Introduction

The correlator output is used for on-line monitoring of the health of the array (cross and self correlated band-shapes, closure phases, amplitude and phase of various baselines, antenna based amplitude and phase, system temperature (T^s), antenna temperature (T^a) variations as a function of time, etc.) as well as for on-line phasing of the array for the phased array mode. Recorded data is extensively used for the measurements of various telescope parameters (baseline calibration, *fixed delay* calibration, antenna pointing calibration, beam shape measurements at various frequency bands, measurement of T^s, T^a, antenna sensitivity (η) and their variation as a function of time/elevation, etc.). All this requires extensive data analysis and data display capabilities to be easily available for on-line and off-line usage. The GMRT correlator produces 435 cross correlations plus 30 self correlations corresponding to 465 complex numbers per integration time per IF per frequency channel. If all the 128 frequency channels are recorded, this corresponds to 465 baselines $\times$ 128 channels $\times$ 2 IFs $\times$ 2 floating point numbers of size 4 bytes each$=952320$ bytes of data per integration cycle. With a typical observing time of 8 hours with an integration time of ~ 20 seconds, this corresponds to a database of size ~ 1.5 GBytes. Hence the software should also efficiently handle such large multi-dimensional database and allow easy browsing through the database.

The visibility data is an explicit function of the baseline length (projected separation between the antennas). Implicitly however, it is a function of many other parameters like local sidereal time (LST), observing frequency, the antenna co-ordinates, the co-ordinates of the *phase center*, *compensating delay* applied to the various antennas, etc. Most of the processing (on-line as well as off-line) requires efficient access to the visibility data potentially as a function of many of these parameters. During the debugging stage of the telescope, it is also important to have a short turn-around time between observations and results. This in turn demands a fairly sophisticated data analysis package to analyze the data recorded in the native recording format as well as evolve continually with the potentially rapidly changing environment (including the format itself!). Preferably, such a data analysis package should also be usable on-line. The application programs must also provide a user interface for the software to be usable by a larger community.

Section 3.2 describes the design of the software system which was designed to meet most of the above mentioned requirements. Section 3.3[1] briefly describes the design of the low level libraries used for accessing the visibility database. Section 3.4 describes the design of the user interface, while Section 3.5 describes some of the application programs used in the observations and data analysis for this dissertation.

[1]A description of the latest application programs and libraries is available via http://langur.ncra.tifr.res.in/~sanjay/Offline

3.2 The software design

The GMRT off-line data analysis package was designed to (1) provide efficient means for browsing the multi-dimensional dataset represented by $V(b_{ij}(t), \nu, \tau, \partial\tau/\partial t, ...)$ (2) be robust to changes in the database format (3) provide a higher level astronomically useful view of the data, (4) provide a programming environment which can be used by knowledgeable astronomers to write novel instrumental debugging, data calibration and analysis tools, (5) provide easy means of data selection and (6) provide a simple user interface to the data analysis program.

The design for the entire software was therefore dominated by the following basic design goals:

- the application programming interface (API) be such that the application developer need not manage software/book keeping details not relevant for the goal in mind.

  In terms of the design of the libraries, this translates to a modular software with the API of each module carefully designed to mesh well with the other modules

- to keep the user interface simple and easy (but robust) while still providing mechanisms for more general, possibly more complicated usage by more enterprising users.

  In terms of software development, this translates into implementing generalized software solutions with a programmable interface.

- it should be easy to supply the results from one application program to another.

  With this, it is often possible to effectively perform a complicated data processing/filtering operation using a number of stand-alone programs without writing a monolith program (which is difficult both to write as well as maintain).

- it should be easy to display and view the data and the results of data processing.

  Since it is virtually impossible to write a data display software which satisfies all present and future needs, it is best to design the data analysis software such that external stand-alone display software can be used. This way, the task of development of display software (requiring very different software skills and professional motivation) is separated.

  This also allows the freedom to use a display software that one is most familiar with and satisfies the needs. A large number of stand-alone plotting/data display software packages are now freely available. With such a design, one is not restricted to use locally designed specific display software allowing enormous scope for creativity and an unrestricted, independent development path.

The Object Oriented design methodology was used to design a hierarchical software where each layer hides the details of the layers below it via the interface presented by each layer. Data access, manipulation, extraction and selection mechanisms have, wherever possible, been implemented in a general form in the libraries (see Section 3.3) while keeping their usage as simple as possible at higher levels via their API.

The package is organized in the form of three layers of libraries over which a suite of application/data analysis programs are built. The lowest layer has been written in the `C` programming language while the rest of the software have been written in `C++`. With a lightweight wrapper (also written but almost never used), this lowest layer provides a `FORTRAN` interface for basic access to the LTA database. The user interface was designed as an embedded shell and is implemented as a set of four separate libraries including an arbitrary mathematical expression parser. An application using this interface provides an interactive shell which is largely independent of any external files.

Most application programs have been written as filters (which operate on an LTA database and produce an LTA database) . The user interface provides easy mechanisms for piping such filters to effectively perform complicated tasks.

3.2.1 On-line usage of the software

The correlator output is first written in a shared memory resource provided by POSIX compliant operating systems. The program `record`, which is part of the Data Acquisition Software, converts the data in the shared memory format to the *LTA-format*. This program was modified to write the output LTA formatted visibility data to the standard output instead of writing to a disk file. As mentioned above, most off-line programs have been written to accept the input data from a pipe. This feature of the off-line software system can then be used, in combination with the modified `record`, for on-line data analysis by piping the data to the programs from the shared memory. Thus, *all* programs used for off-line data browsing, data validation, automatic detection of bad data, etc. (see Sections 3.5.1, 3.5.2, 3.5.3, 3.5.4) can also be used as on-line programs. The locally developed data display/plotting software also accepts plotting instructions and arbitrary data via `UNIX` sockets. The output of the off-line programs, along with embedded plotting instructions, can be easily supplied to the display software over `UNIX` sockets. Thus, with a combination of the data piping facility, modified `record` and the display software, the off-line software can be effectively used for on-line data display.

3.3 Data manipulation libraries

The GMRT visibility database is recorded in the *LTA format*. The database is always multi-channel and is composed of zero or more *scans*. Each scan represents the data for one pointing direction and is composed of zero or more data records. The database begins with an ASCII header referred to as the *global header* which carries information about the observations common to all the scans. Each scan begins with an ASCII header of its own, referred to as the *scan header*. The *scan header* constitutes information relevant for the scan alone (e.g. source RA, DEC, object name, information about the frequency contents of the data, time reference information, etc.).

The LTA data manipulation libraries are organized in three layers. The lowest layers is written in `C` and is responsible for parsing and reading/writing the LTA database headers. It is also responsible for maintaining the consistency of the output LTA database. The interface for reading from and writing to the *global* and *scan* headers in the memory is provided by this layer. Higher level `C` and `FORTRAN` bindings are provided via light weight wrappers, which hide the details of managing the linked lists etc. However, using these interfaces, only one LTA database can be opened in a single application. Using the `C++` interface, a single application program can handle any number of databases. This interface also provides many more astronomically useful features while manipulating the visibility database, and is the recommended interface to use. These libraries maintain two copies of the *global header* in the memory as a doubly linked list for the entire lifetime of the application (unless explicitly destroyed). Hence all changes, if any, in the output are represented in the output-header in the memory, which becomes the header of the output LTA database. One of them represents the input database while the other applies to the output database. However, only the latest *scan header* is maintained in the memory.

At even higher level, the `C++` classes (also referred to as `C++` *objects*) called `LTAFMT`, `LTAVIEW` and `LTARec` encapsulate the LTA format. Any number of these objects can be instantiated in a single `C++` application allowing the handling of multiple LTA databases. These objects, briefly described below, were used in application programs for data calibration and testing some automatic data filtering algorithms. There are other `C++` objects which were used for maintaining and manipulating antenna gains and other tables (in the memory and on disk), which are not described here. Those are described in a set of NCRA Technical reports.

3.3.1 The `LTAFMT` Object

The `LTAFMT` object is the base class for handling LTA database. This object encapsulates the functionality which is expected to be a common factor between all classes which manipulate LTA databases and perform higher level operations (e.g. see the `LTAVIEW` object below). It provides the I/O interface to the LTA headers, and presents the visibility data as a two dimensional array of complex numbers. The data-records, along with the visibility data, also carry other auxiliary data (e.g., parameters for *fringe stopping*, *fringe rotation*, *FSTC*, etc.). The interface to this auxiliary data is also provided by this object.

All higher level objects derived from this class (also referred to as *derived* classes) would have all the functionality of `LTAFMT` object plus the additional functionality of the inherited class. Almost all the methods of the `LTAFMT` (functionally, the services offered by this object), have been declared as `virtual` which allows the *derived* objects to modify the behavior of these methods. A redefinition of these methods in a derived object would override their functionality. This leaves the scope for development of higher level objects with minimal effort.

3.3.2 The `LTAVIEW` object

This is an object derived from `LTAFMT` and is designed to provide a *view* of the data with selection on the source name and integration in time and/or frequency applied to the data.

With a source selection, this object behaves exactly as `LTAFMT` except that it will give a view of the database with scans only of the selected source. The source selection can be specified via a `POSIX egrep` compliant regular expression (with the exception that '+' regular expression operator has been disabled since its interpretation as a regular expression operator causes conflict with the astronomical source naming convention where '+' appears as a valid character in the name). Data selection based on scan number is also possible.

Vector, scalar and robust averaging algorithms are built into this object and can be used to average the data in time or frequency. The averaging interval is supplied as the number of seconds of effective integration required. `LTAVIEW` will then average the data for the closest possible interval of time. This averaging of the data is, however, restricted to the scan and does not cross the scan boundary. Most of the application programs use this object for data manipulation.

3.3.3 The `LTARec` object

Data recorded in the LTA database is composed of the data timestamp and the auxiliary data, followed by the real and imaginary parts of the visibility and self correlation data for each baseline for all recorded frequency channels. The `LTAVIEW` and `LTAFMT` objects provide access to the *raw* contiguous buffer of floating point numbers in the memory representing the complex visibility data record.

The `LTARec` object provides an astronomically useful view of this *raw* buffer. It is initialized using an LTA database object (`LTAFMT` or `LTAVIEW`). It can then be used to access the data timestamp, auxiliary data indexed by the antenna number, and the visibility data as a two dimensional array of complex numbers. The array indexing operator (the '`operator[]`' in `C++` syntax) is overloaded in this object to allow indexing inside the array of visibility with the baseline and channel number as the index. It also provides services for mapping between the baseline number and the two antenna numbers which constitute the baseline.

3.4 The user interface for off-line programs

The user interface libraries provide an embedded interactive shell in the application programs – the user interface is part of the compiled binary code of the application programs. In an interactive session, the user is presented with a list of keywords corresponding to the parameters which control the behavior of the application. The user can set/reset, save, load and transfer values from one keyword to another, etc. in the interactive shell. Each keyword can potentially take multiple values which can be supplied as a set of comma-separate values. Numerical values can be expressed as arbitrary mathematical expressions which are parsed at run-time.

The keywords presented to the user are detected automatically at runtime. Since the code for the user interface is part of the binary executable file, this ensures that the interface presented to the user is *always* consistent with the functionality of the program. This eliminates the possibility of the application program and the user interface going out of synchronization, which is, in the long term, a very desirable property. The user interface can (and frequently does!) go out of synchronization with the functionality of the programs, when the user interface depends on external files to determine the keywords; these must be independently maintained and evolved as the application code evolves.

The input data file name is usually specified via the `'in'` keyword while the output file name by the `'out'` keyword. By default, the input is read from the standard input and output written to the standard output. If the input file name begins with the '<' character, the rest of the file name is treated as a command of the underlying operating system. The output of this command becomes the input of the application. Similarly if the output file name begins with the '|' character, the rest of the file name is treated as a command which reads the output of the parent application. These features are used to supply the output of one program to another.

The applications can also be started in the non-interactive mode by supplying "`help` = *noprompt*" as one of the command-line options. Other keywords of the application can also be set via "`key=<val0>,<val1>,<val2>,...`" styled command-line options. This is often useful in setting up a `UNIX` pipe consisting of a number of programs or when using these off-line programs as part of a shell script. On-line help is also available via the "`explain`" command in the interactive sessions and via the "`help=explain`" as one of the the command-line options in non-interactive sessions.

The user interface can be customized to a large extent and can also be used to effectively generate specialized versions of existing applications (see Appendix A). These can be generated by writing the `.def` and `.config` files for the applications (see the explanation for the environment variables `GCONF` and `GDEFAULTS` in Section A.2).

3.5 Data analysis and display programs

This section describes a few of the application program which were extensively used while observing with the GMRT as well as for instrumental calibration and the measurement of various telescope parameters.

3.5.1 The program `xtract` and its variants

The visibility function, denoted by V, depends on a number of parameters such as the local sidereal time (LST), observing frequency, the antenna co-ordinates, the co-ordinates of the *phase center*, the *compensating delays* applied to the various antenna, antenna fixed delays, antenna positions, etc. (i.e. $V(b_{ij}(t), \nu, \tau, \partial\tau/\partial t, ...)$). During debugging, it was frequently required to view this data in various representations (e.g., Cartesian versus polar representation of complex numbers). Also, V depends on a multitude of parameters, and different debugging purposes require viewing V with respect to different quantities. It was therefore not useful to implement a program to extract the data as a function of a fixed set of parameters. Since, as a design philosophy, stand-alone data display software was used, the need for the extracted data to be in a variety of formats (binary as well as in plain ASCII) directly readable by the display/plotting programs was also frequently felt. It was therefore necessary to develop a compact macro language parser to extract and display the data in a flexible and programmable manner.

`xtract` (Bhatnagar 1997b) was designed to extract the visibility data and its parameters in a programmable fashion via a compact macro language. It was also designed to be as general as possible and easily interface with the many stand-alone data display programs in use. *In fact, it was designed with the wider goal of making it easier for a large spectrum of astronomers/engineers using the GMRT to be able to access the visibility data and do further processing if required.* This program was extensively used for this dissertation and is now being regularly used for a variety of applications ranging from on-line and off-line data browsing and display, beam shape, pointing offset, antenna sensitivity measurements, band shape monitoring, etc.

The `xtract` macro language (described in Appendix B) provides a mechanism to define the contents and the output data format. The macros are constructed using the three operators of the language, namely `ant`, `base` and `chan` and the various *elements* (Table B.1). The three operators loop over all the selected antennas, baselines and frequency channels respectively. The language syntax allows arbitrary grouping of the operators with a semi-colon separated list of *elements* as the body of these operators. This effectively provides a compact way of defining macros to extract visibilities and/or other parameters as a function of antenna, baseline and/or frequency channel number. These macros are, in fact, nested loops over the lists of antennas, baselines and/or frequency channels. The entire macro is implicitly the body of the loop over time and is executed for every input data record. The list of available *elements* are listed in Table B.1.

For example, the `xtract` macro to produce a table with the first column containing the time stamp (Indian Standard Time (IST)) followed by two columns for the amplitude and phase of the visibility from each selected baseline, will be "`ist;base{chan{a;p}};\\n`". The list of baselines and channels for which data is to be extracted can be specified via the user interface keywords `baselines` and `channels`. Similarly the u, v, w co-ordinates of antennas can be extracted in a table as a function of HA by the macro "`ha;ant{ua;va;wa};\\n`".

The list of antennas can be specified via the `antennas` keyword.

The `xtract` macro language complier is also available as a stand-alone library. The API of this library can be used by other application programs to parse, execute and get the result of the macros. An attempt was also made to write one such application for the graphical display of the LTA database (line and gray scale plots). This application unfortunately did not stabilize and is not in use.

Antennas are identified by the correlator sampler to which they are connected. In the final double sideband GMRT correlator, there will be 4 samplers per antenna, i.e. 2 samplers for the two polarization channels per sideband. The four signals from each antenna (2 polarizations from each sideband) can therefore be treated as four *logical antennas*. All samplers in the correlator are also uniquely numbered. The *logical antennas* can therefore be specified by the sampler number to which they are connected, or by an antenna name consisting of three hyphen separated fields – the antenna, the side-band and the polarization names. A name for a *logical antenna* is said to be "fully qualified" when all the three fields in the name are specified. All these fields can be regular expressions. Similarly, baselines can be specified by a baseline number or by a baseline name composed of colon (':') separated *logical antenna* names. Here again, the *entire* antenna names (before and after the ':') can be regular expressions. The use of regular expressions for the components of *logical antenna* names as well as for specifying the two antennas of a baseline provides a very general, compact and powerful selection mechanism. The antenna and baseline naming conventions are described in detail in Appendix C. This convention is uniformly followed in all off-line programs where data selection based on antenna and/or baselines is required.

`xtract` normally writes the output in ASCII format with a header specifying the names of different columns and other information about the extracted data. Formats required by a number of freely available line and gray scale plotting programs can be generated by writing the required `xtract` macro. The extracted data can be directly read by these programs for display. The data can also be extracted with the header in ASCII followed by the data in binary format by specifying the output file name beginning with the character '`*`' (it is conceivable to write a `xtract` macro to produce a FITS file to be displayed using any of the FITS image display programs, e.g. for the dynamic spectra from selected baselines).

The user interface provides mechanisms to externally set keywords to some fixed default value(s) and to suppress these keywords from the user interface. This is used to effectively generate specialized variants of `xtract`. One such variant named `oddix` was extensively used for on-line display of the amplitudes and phases from various baselines. The data was read from the shared memory using a modified version of the `record` program, and an `xtract` macro defined to produce the output as a binary table with each row corresponding to a single integration time. The output was then piped to a program which further supplied the data to a display program over the network via a `UNIX` socket. The display program, also written as part of the off-line package, displays an arbitrary number of stacked scrolling line plots. The display surface itself is scroll-able, allowing the viewing of a very large number of line plots at a time.

3.5.2 The `rantsol` and `badbase` programs

The observed normalized visibility can be written as

$$\rho_{ij}^{Obs} = g_i g_j^{\star} \rho_{ij}^{\circ} + \epsilon_{ij} \tag{3.1}$$

where g_i is the antenna based complex gain, ρ_{ij}° is the ideal point source visibility and ϵ_{ij} is the baseline based noise. For an unresolved source of unit flux density, $\rho_{ij}^{\circ} = 1$. For an N antenna array, the g_is represent $2N - 1$ unknowns - the amplitudes and phases of all the g_is (the phase of one of the antennas can be treated as the reference and hence set to zero). ρ_{ij}^{Obs} represents $N(N-1)/2$ observed complex quantities. For $N > 4$ this is an over-determined problem and hence solvable. The program `rantsol` implements an algorithm to solve for the antenna-based complex gains for an unresolved source. The algorithm itself is described in Appendix D.

The visibility data includes data from non-working or malfunctioning antennas as well as data affected by closure errors due to any malfunctioning of the correlator. Since the antenna based complex gains are obtained using a global fit involving all the data, the presence of bad data can result into problems ranging from noisy solutions even for the good antennas to no convergence at all. This can happen even in the presence of a few bad antennas and/or presence of as few as $10 - 20\%$ bad baselines. It is therefore important to remove bad data before attempting to solve for the antenna gains.

This identification and flagging of bad data is done automatically in two passes for every solution interval. Antenna based complex gains are first solved for using *all* the data. Solutions from the first pass are then examined and antennas with amplitude gain less than the user defined threshold are flagged for the second pass. Antennas which are found to be bad in this manner are assigned a complex gain of 1. The solution for an antenna can also be interpreted as a weighted average of the complex visibilities from all baselines with the given antenna (see Section D.1). This averaging in each successive iteration can be done robustly by on-the-fly flagging of data points, which deviate by more than a threshold defined in units of the variance of the series of complex numbers being averaged. Data from a baseline with large closure errors will have large deviations from the mean defined by the data from 'good' baselines. Such data will be identified and flagged in robust averaging. Both these techniques are used in the algorithm implemented in the program `rantsol` to make it robust, even in the presence of time variant closure errors (the latter have been noticed on several occasions).

In practice, `rantsol` has been found to be very robust in the presence of non-working or malfunctioning antennas and malfunctioning `MAC`s in the correlator (which produce large closure errors). It can be used almost as a black box for most of the calibrator databases without the need to identify and flag bad data. `rantsol` was regularly used to compute the antenna based complex gains and another program, `badbase` was used to identify bad data from calibrators scans. `badbase` examines the amplitude and phase of the calibrated visibilities (defined as $\rho_{ij}/g_i g_j^\star$) and reports the fraction of time a given baseline was found to be bad (badness defined as $|\rho_{ij}|$ and $arg(\rho_{ij})$ greater than a user defined threshold). Antennas and baselines which are continuously bad for large fractions of the total observing time were easily identified and flagged before mapping. *This was found to be extremely important as the calibration tasks of the* `AIPS` *package (used for calibration and mapping) are very sensitive to bad data and sometimes resulted in no convergence at all due to the presence of about 10% bad baselines!*

The GMRT typically produces a few hundred baselines per snapshot. Monitoring the data quality for phase, amplitude and closure errors corresponds to monitoring data streams from each of these baselines. This is obviously not practical. However there are only N antenna based complex gains corresponding to N antennas. Solution for antenna-based complex gains using `rantsol` effectively enforces closure constraints. On-line monitoring of these antenna based complex gains, derived using `rantsol` therefore gives a good summary of the data quality. `rantsol` output was also therefore routinely used to on-line inspect the quality of data. The gains were supplied to the online display software mentioned above which displayed the solutions as a set of scrolling line plots (the antenna based amplitudes and phases for the calibrator scans). This was of immense use in identifying time variable problems while observing and ensured that the recorded data was of reasonably good quality.

`rantsol` is now regularly used as a black box for a variety of purposes ranging from baseline and fixed delay calibration (Figs. 2.11 and 2.12 are examples of typical `rantsol` output), pointing offset, beam shape, sensitivity, system temperature measurements to the GMRT phase array operations for pulsar observations (Sirothia 2000).

The output of `rantsol` can be formatted to be directly read by the `QDP`[2] plotting package using the `awk` scripts `getamp`, `getphs` and `getres`. These scripts extract the amplitude and phase of the calibrated visibilities ($\rho_{ij}/g_i g_j^{\star}$) respectively.

3.5.3 The `closure` program

The antenna based complex gain g_i can be written as $g_i = a_i e^{-\iota\phi_i}$ where a_i and ϕ_i are the antenna based amplitude and phase. For the ideal case with no baseline based errors ($\epsilon_{ij} = 0$ for all i and j), the phase of the triple product for an unresolved source, $\rho_{ijk} = arg(\rho_{ij} \cdot \rho_{jk} \cdot \rho_{ki}) = 0$ and the amplitude of $\rho_{ijkl} = |\rho_{ij} \cdot \rho_{kl}/\rho_{kj} \cdot \rho_{il}| = 1$. The phase of ρ_{ijk} is referred to as the *closure phase* and the amplitude of ρ_{ijkl} is referred to as the *closure amplitude*. These closure quantities are a good measure of the baseline based errors in the system. Ideally, the signals from various antennas, flowing through independent paths, are mixed *only* in the *MAC* stage of the correlator. Although there are several sources which can produce small closure errors, catastrophic closure errors, which severely limit the final dynamic range in the maps, can be traced to malfunctioning *MAC*s in the correlator. The closure phases are therefore a very important quantity to monitor during the observations. It is also important to examine these closure quantities while processing so as to identify bad data; this is done using the `closure` program.

The output of this program, which computes all the closure quantities from the data, was also used for on-line display of the closure phases. This output was simultaneously also supplied to another program which raised an alarm in case the closure phases for the calibrator scans deviated from the expected value by more than some threshold amount. This helped in identifying problems with data before spending long hours of observing and recording of otherwise unusable data.

[2]Written by Allyn Tennant, originally at Cambridge, but developed at NASA Marshall Space Flight Center

3.5.4 Conversion to `FITS` format

The final inversion and mapping of the visibility data was done using the `AIPS`[3] package. The visibility data was imported into `AIPS` by first converting the data from the *LTA format* to `FITS` format using the off-line program `gl2fit`[4] (however, see Section 4.4.1 for some details about use of other data filters before `gl2fit`). The `FITS` file was then imported to `AIPS` using the `AIPS` task `FITLD`.

3.5.5 Miscellaneous programs

In addition to the programs mentioned above, various other programs, which were routinely used during the course of this work, were also developed. Although these programs are not used for numerical computation, they are nevertheless useful and often indispensable.

- The program `ltainfo` lists the astronomically useful summary of each scan in the LTA database (total number of scans in the database, string identifier for the astronomical object, RA and Dec of the pointing center (in date epoch), the hour angle corresponding to the first data record, centre frequency of the RF band and the width of each frequency channel).

- The program `ltacat` concatenates multiple LTA databases into a single database. Since the LTA-*global header* applies to the entire database, all constituent databases are checked for consistency with the first LTA database. Those LTA databases which do not conform to the *global header* of the first database are rejected.

  Quite often, due to various interruptions during long observations, the LTA database was split into several files. These individual files were concatenated into one using `ltacat` (this was necessary for data browsing and detection of bad data as discussed in Chapter 4).

- The program `ltacleanup` checks a LTA database for conformity with the LTA format and attempts to fix some of the inconsistencies. It can also be used as a filter to select scans and/or perform integration in time and/or frequency.

  Due to problems related to synchronization between the online array control and correlator control softwares, bad scans may be recorded in the LTA database (e.g.

[3]Developed by the National Radio Astronomy Observatory (NRAO), USA., primarily for calibration and analysis of the data from the Very Large Array (VLA) but now used for other telescopes as well.

[4]Developed by V.K.Kulkarni of NCRA(TIFR), Pune

scans with zero data records, scans with wrong values for the frequency/bandwidth settings, scans with wrong pointing centre, scans with un-usable data due to a variety of reasons, etc.). Such scans need to be removed to produce a database with only usable scans. `ltacleanup` was used to remove such scans as well as to correct some inconsistencies with respect to the LTA format.

- The program `fixit` was used to edit the values of keywords in the *global header* and/or the *scan headers*.

- The program `tmac` checks for time stamp related errors in the LTA database. Due to synchronization problems between the various network programs comprising the Data Acquisition System (DAS), situation sometimes arise where the time stamp of successive data records does not monotonically increase. `tmac` rejects all data records till it finds a valid time stamp. It was often used as a filter before `gl2fit` to eliminate any offending data records.

- The program `offstop` was written for off-line fringe stopping when on-line fringe stopping in the correlator was not implemented. It later evolved into a program to apply residual compensating delay due to frequency offsets or antenna position offsets. The frequency and/or antenna position offsets for which fringe-stopping should be carried out are the input parameters. This program was extensively used to test the derived antenna co-ordinate corrections and fixed delay corrections during baseline and delay calibration efforts.

- The program `calibbp` does primary phase and bandpass calibration. This was written to allow freedom to test various calibration schemes for the GMRT data. The antenna based complex gains are determined using the phase calibrator scans and antenna based band-passes are determined using the bandpass calibrator. Average gains can be found by integrating the calibrator visibility data. As an alternative, antenna based gains can be averaged to determine the average gains. The latter has the advantage that the automatic bad data detection algorithm is effective while determining the antenna gains.

- The program `lin` subtracts linear slopes across the band for each baseline. This was required for tracing the source of spectral features across the band at P-band (and possibly at other bands as well). The data was time and bandpass calibrated using `calibbp` and linear slopes removed from each baseline. This is the equivalent of the `UVLIN` (Cornwell et al. 1992) operation done for spectral line data analysis. The spectral features seen across the band after passing it though the program `lin`, probably limits the detection of weak spectral lines, at least at P-band, and this is still an unsolved problem.

Chapter 4

The GMRT Data

Recent Galactic plane observations at 843 MHz, using the Molonglo Synthesis Telescope (MOST) (Gray 1994a) and at 2.4 GHz, using the Parkes 64-m single dish (Duncan et al. 1997b), have revealed a number of new candidate SNRs. However many of these objects were in complicated regions of the Galaxy and these observations also suffered from contamination due to thermal emission at these high frequencies. Although the MOST observations were at a relatively low frequency, the side-lobes due to nearby strong sources severely limited the fidelity of images. With only single frequency data available for most of these fields (these observations did not have any overlapping fields), the identification of the candidate SNRs in these fields remained inconclusive.

A sample of candidate SNRs, accessible to the GMRT, were selected from these observations. Continuum observations of this sample were done with the GMRT at 325 MHz during the period of 1998 to 2000. The telescope hardware, on-line and off-line software were all in a state of being debugged during this period and observations were invariably intermingled with debugging activity and related observations. Consequently, the data acquired was often unusable, sometimes requiring several observing sessions involving the same field to get good data. This chapter describes the procedure used for on-line data monitoring and identification of a potential source of data corruption, off-line data flagging and finally imaging using the `AIPS` package.

Section 4.1 gives the general description of the observations done at 325 MHz. Imaging at these low frequencies requires the use of algorithms and techniques not usually used for mapping at higher frequencies. These low frequency specific problems for inversion of visibilities and image deconvolution, and the techniques used to overcome these problems are discussed in Section 4.2. Section 4.2.2 discusses the problem of bandwidth smearing of sources away from the phase centre, which necessitates the multi-channel mode of observations. The procedures used for on-line system and data monitoring are described in Section 4.3. The detailed procedure used for off-line data editing and calibration is described in Sections 4.4. Section 4.5 describes the procedure used to finally map the data and while Section 4.6 presents the full primary beam images after correcting for the primary beam attenuation.

4.1 GMRT Observations

325 MHz observations for continuum imaging of a sample of nine candidate SNRs were done during the period of 1998-2000. The parameters of these observations are summarized in Table 4.1. Most of the objects of interest in these fields were extended, with emission at angular scales $\sim 2-20$ arcmin requiring reliable observations at the smallest available baselines. Observations at 325 MHz are often affected by intermittent radio frequency interference (RFI) and, since RFI from nearby sources of emission remains partially correlated for the smallest baselines, data from the smallest baselines are also most severely affected by RFI. Fortunately, RFI is often narrow band and can be identified if the observing band is split into a number of narrow band frequency channels. The observations were therefore done with the full 16 MHz band split into 128 frequency channels of each having a width of ~ 125 kHz.

The current single side-band GMRT correlator measures only the co-polar visibilities, i.e. only signals of the same polarization are correlated using the *Indian mode* of the VLBA Multiplier and Accumulator chips (MACs). All the 128 frequency channels of the co-polar visibilities corresponding to the right and left circular polarized signals were recorded for all available baselines. The data was kept in the multi-channel format throughout the imaging process to minimize the band-width smearing of sources away from the phase centre (see Section 4.2.2). After editing the RFI-affected or otherwise bad data, a typical bandwidth of about $5-6$ MHz was finally used for imaging giving a typical RMS noise of ~ 10 mJy/beam.

The background sky temperature can vary by a factor of $2-3$ within the Galactic plane, resulting in a change in the total power output by similar factors. The correlator samplers are, however, optimized to work with an input signal of 0 dBm. To keep the sampler inputs at this level, *automatic level controllers* (ALCs) are introduced at the output of the baseband (BB) which effectively changes the gain to keep the output at 0 dBm. To keep

Table 4.1: Parameters of observations with GMRT

Frequency of Observations (MHz)	325
RF Bandwidth (MHz)	16
Bandwidth used (MHz)	$5-6$
Integration time (sec)	16.9
Average time spent on the source (hr)	5
No. of Antennas used	$20-27$
Max. baseline (kλ)	$15-25$
Min. baseline (λ)	$60-100$
Max. spatial scale(arcmin)	~ 30
Average Antenna Sensitivity (K/Jy)	0.32
Primary beam (degree)	1.4
Synthesized resolution (arcsec)	$10-20$
RMS noise (mJy/beam)	~ 10

the ALC operating point within its linear operating range, an attenuation of 16 db was typically used for the IF and BB signals.

As mentioned earlier, the GMRT was in a state of being debugged during the period of the observations. Consequently, the number of antennas and the longest baseline available changed from observation to observation. As a result, the resolution changes from observation to observation. However, most of the *Central Square* antennas, plus some of the arm antennas were available for all observations giving angular resolution in the range $\approx 60-10$ arcsec. Some of the fields, which needed higher resolution were observed when the long baselines antennas were available. Since most of the target objects were extended, it was essential that the short antenna spacings were well sampled. Hence the three antennas, C05, C06 and C09 which provide the shortest spacings, were used for all observations giving a shortest baseline of $\sim 100\lambda$ (after flagging bad data) for which reliable data was measured. This corresponds to a largest angular scale of ~ 30 arcmin. Most of the sources of interest were well within this limit in angular size and we believe that most of the emission up to angular scales of ~ 30 arcmin is well represented in the GMRT 325-MHz images.

4.2 Low frequency specific problems

The visibility measured by a properly calibrated interferometer is given by

$$V(u,v,w) = \iint I(l,m)P(l,m)e^{-2\pi\iota(ul+vm+w(\sqrt{1-l^2-m^2}-1))}\frac{dldm}{\sqrt{1-l^2-m^2}} \tag{4.1}$$

where (u,v,w) are the antenna co-ordinates in the uvw co-ordinate system, l,m, and n are the direction cosines in this system, $I(l,m)$ is the source brightness distribution (the image) and $P(l,m)$ is the far field antenna reception pattern (the primary beam). For further analysis we will assume $P = 1$, and drop it from all equations (for typing convenience!), remembering all along that the effect of $P(l,m)$ is to limit the part of sky from which the antenna can receive radiation to $\sim \lambda/D$ radians, where D is the diameter of the antennas.

For a small field of view ($l^2+m^2 << 1$), the above equation can be approximated well by a 2D Fourier transform relation. The other case in which this is an exact 2D relation is when the antennas are perfect aligned along the East-West direction. Here, we discuss the problem of mapping with non-East-West arrays. The derivation presented here of results for devising algorithms used for imaging large fields of view presented here follow the treatment of Cornwell & Perley (1992) and Cornwell & Perley (1999).

4.2.1 Mapping with non co-planar arrays

Equation 4.1 also reduces to a 2D relation for a non-East-West array, if the integration time is sufficiently small (snapshot observations). However modern arrays are designed to maximize the *uv-coverage* with the antennas arranged in a 'Y' shaped configuration (non East-West arrays) (Mathur 1969). Fields, such as the ones observed for this dissertation, with emission at all angular scales, require maximal uv-coverage. Telescopes such as the GMRT use the rotation of earth to improve the uv-coverage and observations of complex fields typically last for several hours. Hence, Equation 4.1 needs to be used to map the full primary beam of the antennas, particularly at low frequencies.

Let $n = \sqrt{1-l^2-m^2}$ be treated as an independent variable. A 3D Fourier transform of $V(u,v,w)$ can be written using (u,v,w) and (l,m,n) as a set of conjugate variables as

$$F(l,m,n) = \iiint V(u,v,w)e^{2\pi\iota(ul+vm+wn)}dudvdw \tag{4.2}$$

Substituting for $V(u,v,w)$ from Equation 4.1 we get

$$F(l,m,n) = \iint \Bigg\{ \frac{I(l',m')}{\sqrt{1-l'^2-m'^2}} \iiint e^{-2\pi\iota(u(l'-l)+v(m'-m)+w(\sqrt{1-l'^2-m'^2}-n-1))} dudvdw \Bigg\} dl'dm' \tag{4.3}$$

The -1 in the coefficient of w in Equation 4.1 comes from fringe rotation. In the above equation, it corresponds to a shift by one unit along the $n-$axis. Since this is only a change of the origin of the co-ordinates system, it can be absorbed in the n without loss of generality. Using the general result

$$\begin{aligned} \delta(l'-l) &= \int e^{-2\pi\iota u(l'-l)} du \\ &= \begin{cases} 1 & : \quad l = l' \\ 0 & : \quad otherwise \end{cases} \end{aligned} \tag{4.4}$$

we get

$$\begin{aligned} F(l,m,n) &= \iint \frac{I(l',m')}{\sqrt{1-l'^2-m'^2}} \delta(l'-l)\delta(m'-m)\delta(\sqrt{1-l'^2-m'^2}-n)dl'dm' \\ &= \frac{I(l,m)\delta(\sqrt{1-l^2-m^2}-n)}{\sqrt{1-l^2-m^2}} \end{aligned} \tag{4.5}$$

This equation then provides the connection between the 2D sky brightness distribution given by $I(l,m)$ and the result of a 3D Fourier inversion of $V(u,v,w)$ given by $F(l,m,n)$ referred to as the *Image volume*. Here after, I use $I(l,m,n)$ to refer to this *Image volume*.

The effect of including the fringe rotation term $(-2\pi w)$ would be a shift of the *Image volume* by one unit in the conjugate axis ($n-$axis) (shift theorem of Fourier transforms; Bracewell 1986 [and later eds]). Hence, the effect of fringe stopping is to make the $lm-$plane coincide with the tangent plane at the phase center on the Celestial sphere (the point where the tangent plane touches the Celestial sphere) with the rest of the sphere completely contained inside the *Image volume* (Fig. 4.1).

Noting that the third variable n of the *Image volume* is not an independent variable and is constrained to be $n = \sqrt{1-l^2-m^2}$, Equation 4.5 gives the physical interpretation of $I(l,m,n)$. Imagine the Celestial sphere defined by $l^2+m^2+n^2 = 1$ enclosed by the *Image volume* $I(l,m,n)$, with the top most plane being tangent to the Celestial sphere as

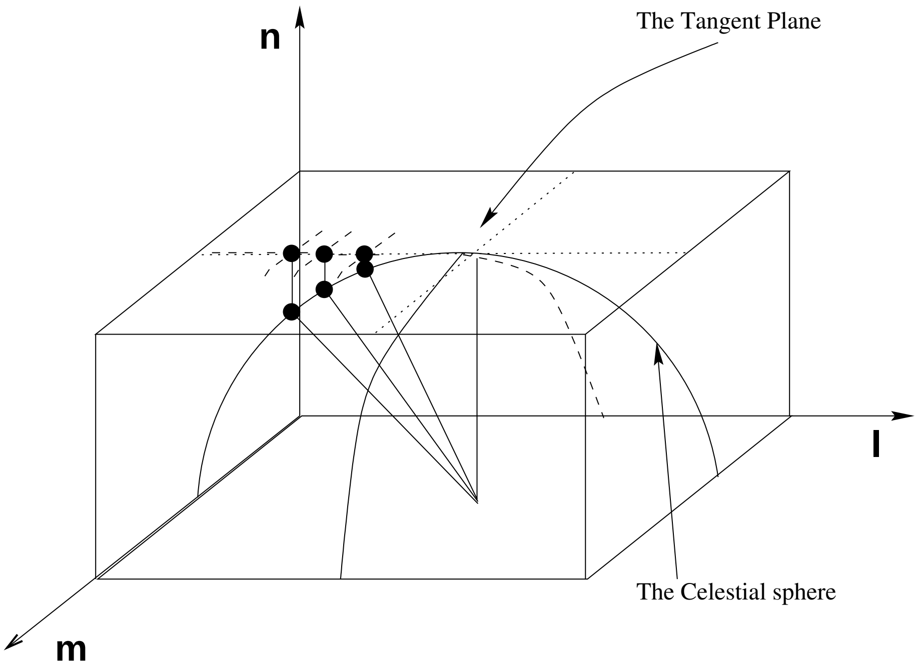

Figure 4.1: Graphical representation of the geometry of the *Image volume* and the Celestial sphere. The point at which the Celestial sphere touches the first plane of the *Image volume* is the point around which the 2D image inversion approximation is valid. For wider fields, emission at points along the intersection of Celestial sphere and the various planes (labeled here as the Celestial Sphere) needs to be projected to the tangent plane to recover the undistorted 2D image. This is shown for 3 points on the Celestial sphere, projected on the tangent plane.

shown in Fig. 4.1. Equation 4.5 then tells that only those parts of the *Image volume* correspond to the physical emission which lie on the surface of the Celestial sphere. However, the *Image volume* will be convolved by the telescope transfer function. The telescope transfer function is the Fourier transform of the sampling function S in the uvw frame (see Chapter 2, page 48). The telescope transfer function, referred to as the *dirty beam* and defined as $B(l,m,n) = \mathcal{FT}[S(u,v,w)]$, also defines a volume in the image domain. The *dirty image volume* defined by the relation $I^d(l,m,n) = I(l,m,n) \star B(l,m,n)$ is a convolution of $I(l,m,n)$ with $B(l,m,n)$. Since the *dirty beam* is not constrained to be finite only on the Celestial sphere, I^d will be finite away from the surface of the Celestial sphere corresponding to non-physical emission due to the side lobes of $B(l,m,n)$. A 3D deconvolution using the *dirty image* and the *dirty beam volumes* will produce a *Clean image volume*. An extra operation of projecting all points in the *CLEAN image-volume* along

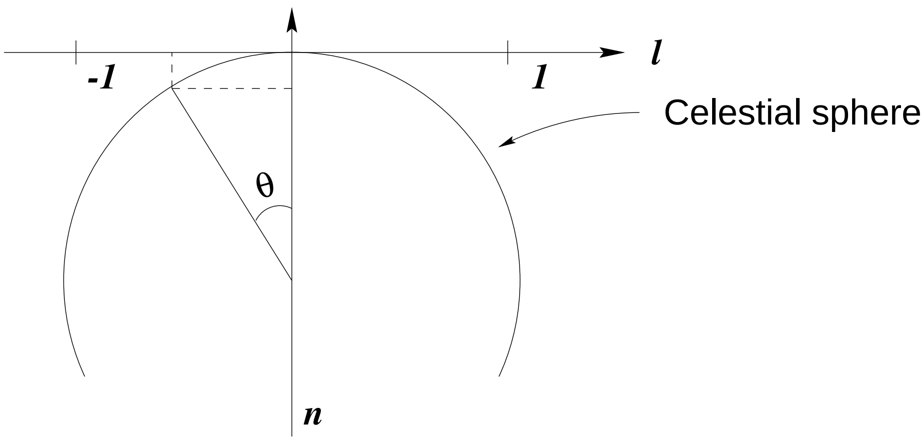

Figure 4.2: Graphical illustration to compute the distance between the tangent plane and a point in the sky at an angle of θ.

the Celestial sphere onto the 2D tangent plane to recover the 2D sky brightness distribution is therefore required. Graphical representation of the geometry for this is shown in Fig. 4.1.

3D imaging

The most straight forward method suggested by Equation 4.5 for recovering the sky brightness distribution, is to perform a 3D Fourier transform of $V(u, v, w)$. This requires that the w axis be also sampled at the Nyquist rate (Bracewell 1986 [and later eds]; Brigham 1988 [and later eds])). For most observations, it turns out that this is rarely satisfied and doing a FFT along the third axis would result into severe aliasing. Therefore, in practice, the Fourier transform on the third axis is usually performed using the direct Fourier transform (DFT) on the un-gridded data.

To perform the 3D FT (FFT along the $u-$ and $v-$ axis and DFT along the $w-$axis) one still needs to know the number of planes needed along the $n-$axis. This can be found using the geometry shown in Fig. 4.2. The size of the synthesized beam along the $n-$axis is comparable to that along the other two directions and is given by $\approx \lambda/B_{max}$ where, B_{max} is the longest projected baseline length. The separation between the planes along n should be $\leq \lambda/2B_{max}$. The distance between the tangent plane and a point separated by θ from the phase center, for small values of θ, is given by $1 - \cos(\theta) \approx \theta^2/2$. For a field of view of angular size θ, critical sampling would be ensured if the number of planes along the $n-$axis, N_n, is

$$\begin{aligned} N_n =& B_{max}\theta^2/\lambda \\ =& \lambda B_{max}/D^2 \text{ (for } \theta = \text{Full Primary beam)} \end{aligned} \tag{4.6}$$

where D is the diameter of the antenna ($B_{max} \approx 25$ km for the GMRT at 325 MHz). Therefore, for mapping a 1° field of view without distortions, one would require 8 planes along the n-axis. However, for mapping with *Central Square* alone ($B_{max} \approx 1$ km), one plane is sufficient. At these frequencies, it becomes important to map most of the primary beam since the number and often the intensity of the sources in the field increase and the side-lobes due to these sources limit the dynamic range in the maps. Hence, even if the source of interest is small, it requires a full 3D inversion (and deconvolution).

Another reason why more than one plane would be required for very high dynamic range imaging is as follows. Strictly speaking, the only point which lies in the tangent plane is the point at which the tangent plane touches the Celestial sphere. All other points in the image, even close to the phase center, lie slightly below the tangent plane. Deconvolution of the tangent plane then results into distortions for the same reason as the distortions due to the deconvolution of a point source which lies between two pixels in the 2D case (Briggs 1995). As in the 2D case, this problem can be minimized by over sampling the image which, in this case, implies having more than one plane along the n-axis, even if Equation 4.6 implies that one plane is sufficient.

Polyhedron imaging

As mentioned above, emission from the phase center and from points close to it, lie approximately in the tangent plane. Polyhedron imaging relies on exploiting this by approximating the Celestial sphere by a number of tangent planes, referred to as facets, as shown in Fig. 4.3. The visibilities are recomputed to shift the phase center to the tangent points of each facet and a small region around each of the tangent points is then mapped using the 2D approximation.

The number of planes required to map an object of size θ can be found simply by requiring that the maximum separation between the tangent plane and the Celestial sphere be less than λ/B_{max}, the size of the synthesized beam. As shown earlier, this separation for a point θ degrees away from the tangent point is $\approx \theta^2/2$. Hence, for critical sampling,

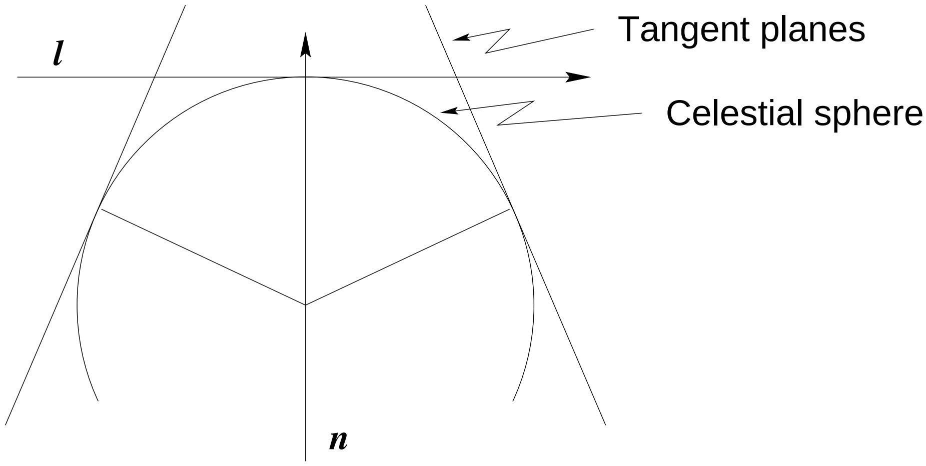

Figure 4.3: Approximation of the Celestial sphere by multiple tangent planes (polyhedron imaging).

the number of planes required is equal to the solid angle subtended by the sky being mapped (θ_f^2) divided by $\theta^2/2 (= \lambda/2B_{max})$

$$\begin{aligned} N_{poly} &= 2\theta_f^2 B_{max}/\lambda \\ &= 2B_{max}\lambda/D^2 \;\; (\text{for } \theta_\mathrm{f} \; = \; \text{Full primary beam}) \end{aligned} \tag{4.7}$$

Notice that the number of planes required is twice as many as required for 3D inversion. However, since a small portion around the tangent point of each plane is used, the size of each of these planes can be small, off-setting the increase in computations due to the increase in the number of planes required. Another approach which is often taken for very high dynamic range imaging, is to do a full 3D imaging on each of the planes. This would effectively increase the size of the field that can be imaged on each tangent plane, thereby reducing the number of planes required.

The polyhedron imaging scheme is implemented in the current version of the `AIPS` data reduction package and the 3D inversion (and deconvolution) is implemented in the (no longer supported) `SDE` package developed by T.J. Cornwell et al. Both these schemes, in their full glory, are available in the (recently released) `AIPS++` package.

The GMRT 325-MHz data was imaged using the `IMAGR` task in `AIPS`. This program implements the polyhedron algorithm and requires the user to supply the number of facets to be used and a list of the locations of the centre of each facet with respect to the image centre and the size of each facet. This list of facets and their parameters were computed using the task SETFC in AIPS, typically resulting in a grid of 5×5 facets, each of size 256×256 pixels.

4.2.2 Bandwidth Smearing

The effect of a finite bandwidth of observation as seen by the multiplier in the correlator, is to reduce the amplitude of the visibility by a factor given by $\frac{sin(\pi l \Delta\nu/\nu_o \theta)}{(\pi l \Delta\nu/\nu_o \theta)}$ where θ is the angular size of the synthesized beam, ν_o is the center of the observing band, l is location of the point source relative to the field center and $\Delta\nu$ is the bandwidth of the signal being correlated.

The distortion in the map due to the finite bandwidth of observation can be understood as follows. For continuum observations, the visibility data integrated over the bandwidth $\Delta\nu$ is treated as if the the observations were made at a single frequency ν_o – the central frequency of the band. As a result the u and v co-ordinates and the value of visibilities are correct *only* for ν_o. The true co-ordinates at other frequencies in the band are related to the recorded co-ordinates as

$$(u, v) = \left(\nu_o \frac{u_\nu}{\nu}, \nu_o \frac{v_\nu}{\nu}\right) \tag{4.8}$$

Since the total weights W, used while mapping, does not depend on the frequency, the relation between the brightness distribution and visibility at a frequency ν becomes

$$V(u, v) = V\left(u_\nu \frac{\nu_o}{\nu}, v_\nu \frac{\nu_o}{\nu}\right) \mathcal{FT} \left(\frac{\nu}{\nu_o}\right)^2 I\left(l\frac{\nu}{\nu_0}, m\frac{\nu}{\nu_0}\right) \tag{4.9}$$

Hence the contribution of $V(u, v)$ to the brightness distribution get scaled by $(\nu/\nu_o)^2$ and the co-ordinates get scaled by (ν/ν_o). The effect of the scaling of the co-ordinates, assuming a delta function for the *Dirty Beam,* is to smear a point source at position (l, m) into a line of length $(\Delta\nu/\nu_o)\sqrt{l^2 + m^2}$ in the radial direction. This will get convolved with the *Dirty Beam* and the total effect can be found by integrating the brightness distribution over the bandwidth as given in Equation 4.9

$$I^d(l, m) = \left[\frac{\int_0^\infty |H_{RF}(\nu)|^2 \left(\frac{\nu}{\nu_o}\right)^2 I\left(\frac{l\nu}{\nu_0}, \frac{m\nu}{\nu_0}\right) d\nu}{\int_0^\infty |H_{RF}(\nu)|^2 d\nu}\right] * DB_o(l, m) \tag{4.10}$$

where $H_{RF}(\nu)$ is the band-shape function of the RF band and DB_o is the *Dirty Beam* at frequency ν_o. If the synthesized beam is represented by a Gaussian of standard deviation $\sigma_b = \theta_b/\sqrt{8\ln 2}$ and the bandpass by a rectangular function of width $\Delta\nu$, the fractional reduction in the strength of a source located at a radial distance of $r = \sqrt{l^2 + m^2}$ is given by

$$R_b = 1.064 \frac{\theta_b \nu_o}{r\Delta\nu} \mathrm{erf}\left(0.833 \frac{r\Delta\nu}{\theta_b \nu_o}\right) \tag{4.11}$$

Equation 4.10 is equivalent to averaging a large number of maps made from quasi-monochromatic visibilities at ν. Since each such map scales by a different factor, a source away from the center would move along the radial line from one map to another, producing the radial smearing mentioned above, convolved with the *Dirty Beam*.

The effect of bandwidth smearing can be reduced if the band is split into frequency channels with smaller channel widths. This effectively reduces the bandwidth $\Delta\nu$ as seen by the mapping procedure and while gridding the visibilities, u and v can be computed separately for each channel and assigned to the appropriate uv-cell. The FX correlator used in GMRT provides up to 128 frequency channels over the entire bandwidth of observation and the visibilities can be retained as multi-channel in the mapping process to reduce bandwidth smearing. Although purely from the point of view of bandwidth smearing, averaging ~ 10 channels at 325 MHz would be acceptable, keeping the visibility database with all the 128 channels is usually recommended to allow identification and flagging of narrow bands RFI.

4.3 Observational procedure

For $T^a \ll T^{sys}$, the amplitude of the visibility function V is proportional to the flux density of the source and the normalized visibility amplitude is converted to flux density units using the measurement of V for a source of known but non variable flux density (referred to as the flux density calibrator). Also, the complex antenna based gain can potentially vary as a function of time. These slow time variations can be corrected using periodic observation of a source of known structure, usually an unresolved source, referred to as the phase calibrator. The flux density of the phase calibrators, the flux density of which is potentially variable over time scales of days, is also calibrated using the flux density calibrator. Each observation therefore requires at least one observation of a flux density calibrator and periodic observation of phase calibrators to properly calibrate the data.

The VLA flux density calibrators, `3C48` and `3C286` was used for all observations. One of three calibrators close to the Galactic plane namely, `1830-36`, `1709-299` and `1822-096`, were used as the phase calibrator. A flux calibrator was observed for ~ 10 min at the beginning and at the end of each observing session and the phase calibrator was observed for ~ 10 min at an intervals of ~ 30 min.

The planned periodic injection of noise from a calibrated noise source to measure the system temperature has not yet been implemented for the GMRT. As a result, the system temperatures for the flux density calibrator fields (T^{sys}_{Cal}) and the field being mapped (T^{sys}_{s}) must be measured and a correction equal to $T^{sys}_{s}/T^{sys}_{Cal}$ be applied as part of the flux density calibration. T^{sys}_{Cal} was measured to be ~ 110 K while T^{sys}_{s} was estimated from the all-sky maps at 408 MHz (Haslam et al. 1981, 1982, 1995). For a few fields, T^{sys}_{s} was also measured at few points around the source of interest and the measured system temperature was consistent with that estimated from the 408 MHz data to within $\sim 10\%$. None of the phase calibrators used for these observations are known to be variable over few hours. These calibrators were therefore also used as secondary amplitude calibrators to effectively correct for any slow variation in the receiver temperature.

The observing schedule if the GMRT on-line array control system can be supplied via a computer readable file. This file, apart from a few other system-related commands, contain instructions about the source to be tracked and the integration time on each source. However since the feedback of the antenna pointing status is not used, this file needs to be tweaked by inserting delays between various commands. For example, the amount of time taken for antennas to move from one tracking direction to another varies from antenna to antenna, and appropriate time delays must be inserted between the various commands in this file to make sure that the data recording begins only after *all* antennas have reached a given tracking position. The commands for alternately tracking the phase calibrator and the target source were put in an infinite loop, which allowed the above mentioned periodic observations of the phase calibrator. However, since only an infinite loop is possible, the observations had to be manually terminated at the end of observing session. Information about the status of the antennas as well as a mechanism to derive time-of-the-day information in the command syntax used in this file is highly desirable and will allow a better and more automated observing session.

4.3.1 On-line monitoring

The data could be corrupted due to a number of reasons including (1) RFI, (2) catastrophic hardware failures (irrecoverable in a short time), (3) intermittent hardware failures from which a quick recovery is possible (e.g. breakdown of communication between correlator control hardware and software), (4) antenna-based breakdown (for e.g., failure of the servo system resulting in stoppage of source tracking), (5) failure of the communication link between the antenna based computer (ABC) and the on-line control computer at the CEB, (6) power supply failure to some of the antennas, (7) loss of phase-lock for the four local oscillators (LOs) or a phase jump in the LOs, (8) onset of ionospheric scintillations, (9) problems in the online array control, (10) problems in the correlator control software/hardware, etc. Data affected by any or many of these sources manifests itself in various forms in the recorded data. Such data needs to be flagged from the database before it is used for mapping. The flagging information for the database was generated by on-line monitoring of the critical array control parameters as well by off-line examination of the data itself. The procedure used for this is described below.

System monitoring

It was noticed that problems related to items (3), (4), (5) and (10) listed above, occurred frequently enough to require careful monitoring of various related telescope parameters as well as on-line monitoring of the visibility data. The GMRT on-line array control system maintains a large amount of information about the status of the various subsystems. This information is updated once every few seconds and is available in the shared memory resource of the control computer. Any arbitrary information from this resource can be extracted using the `table`[1] program. This program was used to extract the following information as a function of time:

- the packet sequence number
- the azimuth and elevation angles of the antennas
- the error between the target and current antenna azimuth and elevation angles
- the antenna servo system related flags

The `table` program produces the output in the form of a table which was supplied to a shell script which generated an alarm if any of the following conditions occurred:

[1] Developed by R.K.Singh of NCRA(TIFR), Pune

- the error on azimuth or elevation angles of any of the antennas exceeded a threshold value. This usually was an indication of the antenna not receiving the the periodic tracking instructions from the GMRT on-line array control system computer

- the packet sequence number did not change for a threshold length of time. This usually indicated loss of communication between the antennas and the GMRT on-line array control system computer

- the flag for servo brakes was raised for any of the antennas. This usually indicated either a malfunctioning antenna servo system and/or the detection of extra antenna load (due to wind loading or due to some spurious signal indicating extra load)

In case of any of the above problems, manual intervention was required. However, this rather primitive "automation" did help enormously in long observing sessions. This procedure, while already quite useful, should ultimately be made part of the link between the GMRT on-line array control system and the correlator control software to (1) record on-line flagging information, and (2) control the recording of the data.

Data monitoring

On-line monitoring of the visibility data was done in two ways. First, the `matmon`[2] program was used to monitor the normalized correlation coefficient for the phase calibrators. This program displays single integration cycle snapshots of the amplitude (or the phase) of the visibility data for all baselines in the form of a matrix. This display was used to determine the general health of the system before starting the observations and was useful in quickly locating catastrophic problems. Once the observations were started, the data from the correlator was monitored using the programs `xtract`, `rantsol` and `closure` (see Chapter 3). The amplitude and phase from all baselines were continuously displayed as a set of stacked scrolling line plots using the program `oddix` (which uses `xtract` and the plotting package of the GMRT off-line software). This display provided a $1-2$ hour long snapshot of the data covering two or more observations of the phase calibrator. Since most problems in the system can be detected using the data from the phase calibrators, the onset of a problem in the data between two calibrator scans was easily detected using these plots.

[2] Developed by A.P.Rao of NCRA(TIFR), Pune

The output of `rantsol` (namely, the antenna based complex gains) for the calibrator scans was also similarly plotted. These plots provided information about the health of the system containing all the data on the calibrator scans. Problems ranging from a significant loss in antenna sensitivity (e.g. due to change in the antenna pointing offset across $HA = 0$h seen for some of the antennas) to the onset of closure errors due to a malfunctioning correlator or the onset of ionospheric scintillations were quickly detected from these plots.

The output of `closure` (the closure phase for all possible triangles) was supplied to another program which raised an alarm if the closure phases exceeded a threshold value for a threshold length of time. This procedure quickly identified time varying correlator related problems quite effectively.

The output of the `table` and `closure` programs as a function of time were also saved in a file. This data was later examined and used to generate a flagging table readable by `AIPS`. These procedures, effectively generated first order on-line data flagging information, which is the crucial first step in improving the final data quality. Lack of time did not permit implementing these procedures as part of the on-line array control and correlator control software, but must be done in the near future to improve the reliability and quality of the final data.

4.4 Data Analysis

Two types of data analysis were required for mapping: (1) off-line data analysis (before and after importing the data into `AIPS`) for further, more careful identification of bad data, and (2) data analysis involving 3D inversion, deconvolution and phase calibration for the purpose of imaging. This section describes the procedure used for the data analysis required for data editing and calibration. Section 4.5 describes the procedure used for mapping.

4.4.1 Data Editing

In addition to the data flagging information derived from on-line system and data monitoring, the data was also examined off-line using the programs `xtract`, `rantsol` and `badbase` (see Chapter 3). In long observing sessions, there were invariably antennas which did not produce usable signals for some fraction of time. Often, this was either due to th malfunctioning of a subsystem or the antenna being taken for some kind of maintenance work over time scale much longer than the threshold time intervals set in the on-line monitoring programs (see Section 4.3.1). Such situations were easily identified from the plots of amplitude from all baselines (or for all baselines with a single antenna) as a function of time for the calibrator scans. The `calibbp` program was also used for bandpass calibration of the data, using the phase calibrator scans. The antenna-based average bandpass solutions and the baseline based band-passes were examined to identify frequency channels affected by intermittent narrow band RFI or by any other source of data corruption.

The program `badbase` uses the output of `rantsol` to generate a summary of the antenna based solutions (see section 3.5.2, Chapter 3). This was found to be very useful in identifying intermittent baseline based problems in the data. The `AIPS` tasks used for calibration are rather sensitive to the presence of bad baselines in the data. Flagging data corrupted by baseline based errors was therefore essential. The algorithm for the computation of antenna based complex gains implemented in `rantsol` is robust in the presence of such data and was hence crucial for the identification and flagging of such data.

The above mentioned procedure was followed for data from both the polarization channels separately. All the flagging information generated from on-line monitoring and off-line data analysis, was converted to flagging tables to be used later for flagging data in `AIPS`.

Data recorded in the native LTA format was imported to `AIPS` via the FITS format. The program `gl2fit` was used to convert the LTA database into FITS format. It was noticed that data for some of the baselines was in the illegal number representation identified as `NaN` (not-a-number) or `Inf` (infinite) numbers. Most of the data analysis programs (including the robust algorithm of `rantsol`) behave erratically in the presence of such numbers. However, computer representation of such numbers is well documented in the IEEE number representation format and can be easily and reliably identified in the software. This form of bad data was therefore removed using an on-the-fly filter used in all off-line data analysis programs, including `gl2fit`. Another form of bad data manifests itself in the form of the normalized visibility amplitude being greater than unity. This is again easily identified in the software, and the `gl2fit` program flags such data while converting it to the FITS format.

Due to synchronization problems between the various network programs of the GMRT data acquisition software and the online array control software, the time stamp of the data records is sometimes corrupted and the value of time stamp of the successive data records does not increase monotonically. Data with such time stamp corruption is unusable in AIPS. Also, a few data records at the beginning of each scan were found to be regularly bad. All such data records were filtered out using the program `tmac`. `tmac` was used as a data filter in a data pipe-line, before the program `gl2fit`. If the observation was split into a number of LTA files, the program `ltacat` was also used before `tmac` in the data pipe-line to concatenate the various LTA files into one file. LTA files for some observations also required changing the values of some of the keywords in the Global an Scan headers of the LTA data base. This was done using the program `fixit`.

A typical data pipe-line set up to convert the and LTA file to FITS format was therefore, `[ltacat]`⇒ `[fixit]`⇒ `tmac`⇒ `gl2fit`, where '⇒' indicates the flow of data and the parenthesis are used to indicate that the program were used only if necessary. Use of UNIX pipes eliminated the necessity of saving the intermediate LTA files, which would otherwise have required several giga bytes of disk space.

Further data editing was done after importing the data into AIPS. The bad data/ antennas/ baselines identified earlier were translated to AIPS readable flagging files and applied inside AIPS. Various steps used for further data editing and calibration inside AIPS are described below.

4.4.2 Data Editing and Calibration in AIPS

The first step in the sequence of data analysis is the amplitude and phase calibration of the visibilities. This section describes, in a stepwise fashion, the sequence of various AIPS tasks that were used for data calibration. A typical AIPS task depends on a large number of parameters, which control the behavior of the tasks. The settings of the relevant parameters of these tasks are also discussed below.

1. The FITS file generated using the procedure described above, was imported into AIPS using the task FITLD. This results into a multi-source visibility database written in AIPS, by default in the compressed format.

2. Normally, multi-source file contains a number of tables, including the CL table, version 1 (CL1)

   At present, the CL1 table is not generated when the GMRT data is converted into FITS format. This table is also used by AIPS calibration programs as a template to determine the time resolution for the subsequent CL and antenna gain tables (the

SN tables). Hence, the task INDXR was always run to generate the table CL1. This also generates the NX table, which is used by AIPS to navigate in the database. This, by default, produces a CL table with a time resolution of 5 min. Since the phase calibrators used for all the observations were strong enough to provide sufficient signal to noise ratio, the antenna based gain solutions could be computed for every integration cycle of ~ 17 sec. The CL and SN tables were later used to not only calibrate the data but also identify bad data. The minimum time resolution for gain solutions was therefore set to ~ 20 sec by setting APARM=0.33,0 before running INDXR.

3. The flux density for the flux calibrators must be accurately set before proceeding for calibration. The flux density scale of the standard VLA flux calibrators 3C48 and 3C286 is encoded in the task SETJY. This task was run on the multi-source visibility database to set the flux densities for these flux density calibrators using the following settings: OPCODE='calc'; SOURCE='3C286','3C48',''.

4. The task UVFLG reads the data flagging information from a disk file supplied via the INFILE keyword. This task was used to apply all the flagging information generated from the on-line monitoring and off-line data analysis described earlier.

5. The visibility amplitude of an unresolved source remains constant as a function of baseline length. Plot of visibility amplitudes as a function of $\sqrt{u^2+v^2}$ for the flux density calibrator scans was examined using the task UVPLT. The SOURCE keyword was appropriately set for the purpose. Obviously discrepant data were identified, after allowing for some spread due to differences in antenna sensitivities. Such data, which either had very low or very high amplitude can have severe repercussions for calibration.

   UVFLG was used to flag these discrepant points with INFILE=''. The keywords ANTENNA, BASELINE, and TIMERANGE were used to specify the offending antennas/baselines and any time range for which the data was required to be flagged.

   The primary task for calibration in AIPS is CALIB. This task is, however, rather sensitive to the presence of bad/dead antennas. (e.g., in one case (G356.3-1.5) the presence of about 10 bad baselines out of a total of about ∼360 good baselines (for antennas C06 and C05) gave severely under estimated antenna gains). The initial effort outside AIPS to identify and flag bad data/baselines paid good dividends at this stage of processing.

6. In some cases, the graphical flagging task TVFLG was also used to interactively flag bad data.

7. CALIB was then used to compute the antenna based complex gains for the flux density calibrator scans with SNVER=0, GAINUSE=0, SOLINT=0.33. This generates the first antenna gains table (SN1) containing complex gain solutions with a time resolution of ~ 20 sec.

8. To further identify bad data, the data was examined using UVPLT and VPLOT with DOCALIB=1 and SNVER=1. With these settings, the SN1 table is applied to the data on-the-fly. This essentially takes care of any short term variations in the antenna gains as well as variations in the sensitivity of the antennas.

   This procedure helps in identifying mildly discrepant data, which cannot be corrected by any antenna based correction. As before, UVFLG was used to flag such data. SN1 was then deleted using the task EXTDEST with INEXT='SN' and INVERS=0. This deletes the latest SN table generated in any previous run of CALIB. Steps 5 to 8 were repeated till a satisfactory SN1 table was generated for the flux density calibrator.

9. The task CLCAL was then used with INTERPOL = 'MWF'; INTPARM = 0.5,0.5; CALSOURCE = '3C286','3C48',''; SOURCE = '' to generate the second version of CL table (CL2) containing the median window filtered solutions derived from SN1. The resulting table CL2 contains flux calibration for *all* sources in the database and constitutes the basic flux calibration table.

10. Steps 5 to 9 were repeated for each phase calibrator to identify and flag bad data. This resulted into the third CL table (CL3) containing the median window filter solutions for the antenna gains, derived from the phase calibrator scans; this was used later to correct for slow variations in the antenna based complex gains.

    A fourth CL table (CL4) was also generated containing the the gain solutions for the phase calibrator with a time resolution of ~ 20 sec (INERPOL='2PT'). This was later used for band pass calibration.

11. GETJY was then used with CALSOURCE='3C286','3C48' and SOURCE='' to derive the flux density of the phase calibrator. If all was well in the above procedure, the derived flux density should be close to the value listed in the VLA calibrator manual and the error bars of less than 10% (after multiplication by the ratio of the sys-

tem temperatures for the flux and phase calibrator fields, since the GMRT visibility database as yet does not contain the T^{sys} table). This corrects for the difference in the system temperatures between the flux and phase calibrators.

12. In all the above, a single, clean frequency channel, free from RFI, was used. All the calibrators used were strong enough to warrant the use of a single frequency channel. However, to use other channels for the purpose of imaging, a bandpass calibration also needs to be applied to calibrate any channel dependent gain variations.

    In the calibration procedure adopted here, it is assumed that the time calibration (determined in the above procedure) and bandpass calibration can be separated and determined independently. The time calibration table (`CL4`) was therefore applied to all the channels before deriving the band pass calibration table, the `BP` table. `AIPS` offers interpolation of the `BP` table in time to apply band pass calibration to data of the target source. Hence, the time calibrated data within the calibrator scans needs to be averaged, to generate a scan averaged band pass solution. The resulting band pass solutions (one per calibrator scan) can then be interpolated in time to take care of any slow variations in the band shape.

    However, data affected by intermittent RFI needs to be flagged before the data is averaged in time. RFI on calibrator scans was identified using the task `FLGIT` on these calibrator scans. This task examines the data after subtracting a linear fit to the band shapes from individual baselines. A user specified set of channels is used to determine the linear fit. All data with residuals outside the user specified limits are then flagged. All channels were flagged for a given integration time containing bad data. This was achieved with the following settings for `FLGIT`: `BCHAN=C0; ECHAN=C1; DOCALIB=1; GAINUSE=4` where, `C0` and `C1` are the first and the last frequency channels to be used. Several sets of (`C0, C1`) for range of clean frequency channels can be specified, which alone will be used for the linear fits, via the `NBOXES` and `BOX` keywords. The flagging criterion can be specified via the `APARM` keyword.

    `FLGIT` was also used later on the calibrated data on the target sources. However, since the signal to noise ratio on individual baselines for extended sources can vary a lot, such automated procedures are of limited use. Identification of bad data on the target source was therefore usually done manually using tasks like `UVPLT`, `UVFLG`, `TVFLG` and `SPFLG`.

13. The graphical data editing task SPFLG was sometimes used at this stage to identify and flag bad data. This task displays the data in the time-frequency plane from one baseline at a time and provides the same interface as that of TVFLG to graphically flag data.

14. Next, the BP table was derived by time averaging the data within the phase calibrator scans (after application of the time calibration). This was done using the task BPASS with DOCALIB=1; GAINUSE=4; BPASSPRM(5)=1; BCHAN=C0; ECHAN=C1 where C0 and C1 refer to the first and the last frequency channel to be used.

15. The BP table and band pass corrected band shapes were examined using the task POSSM. Large oscillations across the band were sometimes found in a few antennas. These antennas were usually flagged from the entire data base.

16. Finally, the task SPLIT was used to apply the time and band pass calibration (the CL and BP tables respectively) to the data on the phase calibrators as well as the data on the target source and single source multi channel calibrated databases generated. This was done using the following settings: DOCALIB=1; GAINUSE=3; DOBAND=3; BPVER=1.

Flux density calibration

Flux density calibration was done using observations of one of the two VLA flux density calibrators, 3C286 or 3C48. Time variability of these sources has been found to be small from the VLA monitoring of the flux densities of these sources. The absolute flux densities of these sources was derived by careful observations by Perley & Crane (1986) using the VLA in D-array configuration and they found that the Baars scale (Baars et al. 1977) was slightly in error. They adjusted the flux density of 3C295 to that of Baars value and derived corrections for the flux densities of 3C286 and 3C48. These corrected flux densities are encoded in the AIPS task SETJY which was used to set the flux densities for these sources used for flux density calibration. The adopted flux densities of 3C286 and 3C48 were 28 and 42.7 Jy respectively (at 325 MHz). Observations of 3C48 with the VLA has shown that the flux density derived using SETJY gives the 325-MHz flux density with an accuracy of $\sim 2\%$.

The flux density calibrators were typically observed at the beginning and at the end of each observation. The phase calibrators used for these observations are also listed as good secondary VLA calibrators. The flux density calibrator scans were used to derive the flux densities of these secondary calibrators as a consistency check. The phase calibrators were also used as secondary calibrators to correct for any slow variations in the antenna gains. All fields observed for this dissertation also had many other sources in the field. For some of these sources, the 325-MHz flux densities were available from other independent observations as well (VLA calibrators, targeted VLA observations or the Texas survey (Douglas et al. 1996) which gives the spectral index and point source flux densities at 365 MHz). These flux densities were also used for a consistency check on the flux calibration and to eliminate the possibility of any systematic flux calibration error.

The background temperature in the Galactic plane can change quite substantially for separate pointings. For accurate flux density calibration, one must measure the system temperature for the flux density calibrator field as well as for the target field. To also account for small time dependent variations in the system temperature, it should be monitored regularly during the length of the observations. The planned periodic injection of calibrated noise at the front-end of each antenna to measure the system temperature has not yet been implemented at the GMRT. In its absence, the system temperature was measured at a few positions around the target source in the Galactic plane and the measured system temperature used to correct for the differences in the background temperature between the field of interest and the flux density calibrator. The background temperature from the 408-MHz all sky survey (Haslam et al. 1995) was also estimated as a consistency check. With this scheme, we estimate that the 325-MHz flux densities from GMRT are accurate to $\sim 15\%$.

Phase calibration

Slow variations of the antenna based complex gains occur on time scales of a few tens of minutes. The relative phase variations between the antennas due to this needs to be corrected so as to phase the array over several hours. These slow variations are measured using periodic observations of a phase calibrator. Since the system temperature at 325 MHz in the Galactic plane is a factor of 3-5 higher than away from the plane, the phase calibrators must also be strong (typically > 10 Jy) to provide enough signal to noise ratio for the computation of antenna based complex gains. Temporal as well spatial variations in the ionospheric total electron content at 325 MHz is expected to be the major source of phase corruption. This can produce phase variations over the scale of the array (and sometimes even across the primary beam of each antenna). It is therefore not advisable to use a phase calibrator too far from the target field since the antenna based complex gains obtained from the phase calibrator may not reflect the phase variations in the direction of the target field.

Using the antenna based phase variation derived from continuous observations of the phase calibrators for several hours (Figs. 2.11 and 2.12), it was estimated that phase variations over a time scale of about half an hour could be approximated well by linear interpolation. This is thus the time scale at which one needs to observe the phase calibrator (~ 30 minutes). The three VLA 327 MHz calibrators `1709-299`, `1830-36`, and `1822-096` with 327-MHz flux densities of 6, 28, and 13 Jy respectively, were used as phase calibrators. The angular separation in the sky between the phase calibrators and the target field was typically $10 - 15°$. The maximum error in phase due to errors in the antenna coordinates, when the phases from the phase calibrator are transferred to the target source was estimated to be a few degrees (see Section 2.6.1). Tests done by phasing the data from one calibrator using periodic observations of another calibrator show that the array is phased over time scales of $\sim$half an hour using this procedure.

Bandpass calibration

The antenna based complex gains vary across the passband, primarily due to the antenna based band shape and residual fixed delay errors. These variations in the complex gains must be corrected before the visibilities from individual frequency channels are averaged.

As mentioned above, the phase calibrators were strong enough to provide enough signal to noise ratio for the computation of channel dependent antenna based complex gains. The antenna band shape corrections were therefore derived using the phase calibrators. An average gain was computed for each of the phase calibrator scans per channel and the linearly interpolated values applied to the target source data to correct for the channel dependent complex gains.

4.5 Inversion and deconvolution of GMRT data

The 325-MHz primary beam of GMRT antennas has a full width at half maximum (FWHM) of $\sim 1°.4$. The central square provides a maximum baseline of ≈ 1 km equivalent to an angular resolution of ~ 3 arcmin. At this resolution, the full GMRT primary beam can be mapped without severe degradation due to non-coplanar effects. As a first step, with the dual purpose of gauging the data quality and locating strong confusing sources, single facet images were made at a resolution of ≈ 1 arcmin using the task IMAGR.

Having identified the sources in the field of view from this lower resolution image, higher resolution imaging was attempted. Typically, a maximum baseline of 20kλ was used corresponding to an angular resolution of ~ 15 arcsec. Most of the fields had strong extended sources all over the field of view forcing the mapping of the full primary beam. At these resolutions, the number of planes required along the n-axis is 8. Hence, a 3D inversion was required. The IMAGR task of AIPS performs a 3D inversion using the polyhedron imaging algorithm. In this, the entire field of view is divided into a two dimensional grid of facets. A small part of the sky (corresponding to the size of the facet) centred around each facet is then imaged by first shifting the phase centre of the visibility to the centre of the facet and then performing the normal 2D inversion and CLEANing. Since, the 2D approximation is assumed to be valid within the facet, it is important to make sure that the facet is not so big as to re-introduce distortions at the edges of the facets.

The number of facets required for 3D inversion using IMAGR and the appropriate RA and DEC shifts for the centre of each facet, were computed using the relatively new task in AIPS called FCSET. Essentially, given the size of each facet, the size of the field of view and the RA and DEC of the phase center, this task writes out a IMAGR readable list of field specifications (the field number, its RA and DEC shifts and its size in number of pixels along the RA and DEC axis). Typically, this resulted in a 5×5 grid of facets, each of size 256×256.

After the inversion of each of the facets, the IMAGR task uses the usual 2D Clark CLEAN (Clark 1980) on each facet. The class of CLEAN and MEM based deconvolution algorithm treats each pixel in the image as a degree of freedom. Even when mapping in the Galactic plane (or close to it), it is clear from the images that most of the pixels do not have any physical emission associated with them. Reconstruction of the physical emission in the field of view should therefore be somehow constrained to use only those pixels where there is significant physical emission from the sky. Not doing so is equivalent to giving more freedom to a non-linear fitting process (the deconvolution process), than is justified by the data. CLEAN based algorithm (and its variants) are themselves unconstrained. This constraint must therefore be provided externally by setting boxes around the dominant sources in the field of view at each cycle of CLEAN. It has been shown by Briggs (1995) that the best results are obtained by putting as tight a box as justified by the data (essentially by inspection). During the deconvolution process, the IMAGR task provides a facility to dynamically define boxes for each field for every cycle of CLEAN.

However, since the emission was usually of complex morphology making it difficult to define tight boxes, simple square boxes enclosing the source of emission were used. This was manually done for each facet.

The resulting set of facet images were put together to reconstruct the sky using the task `FLATN`. The `FLATN`ed image was then primary beam corrected using the task `PBCOR`. The GMRT visibilities correspond to the date-epoch at the time of observations. The final image was therefore rotated to the J2000 epoch using the task `REGRD`.

4.6 The Images

This section presents the final images produced via the procedure described above. All images were corrected for primary beam attenuation using a polynomial approximation of the GMRT primary beam. As mentioned earlier, the resolution in these images changes from image to image due to a combination of declination dependent uv-coverage, changes in the number of available antennas and the flagging of bad data. Images of fields with large angular size sources are presented at a few arcmin resolution. Higher resolution images of some of the fields were also made where necessary (due to the presence of small angular size sources of interest in the field, e.g. the field containing G003.6-0.1).

Fig. 4.4 shows the GMRT image of the field containing the SNR G001.4-0.0 at the centre of the image. Other well known sources (SNRs and H II) regions in the Galactic Centre region are clearly visible in this image. The RMS noise is relatively high, possible due to the Galactic Center which lies at the south-western edge of the primary beam. Few of the GMRT antennas had servo related errors due to which there were small oscillations in the antenna pointing while tracking. This, in the presence of strong sources at the edge of the fields, results in short time scale differential gain variations which are not easy to correct later and also results in a higher RMS noise.

Fig. 4.5 shows the full primary beam corrected images of the field containing the SNRs G004.7-0.2, G003.8+0.3 and the unclassified source G003.6-0.1. The low resolution image in the left panel was made using a single facet, while the higher resolution image was made using a grid of 4×4 facets. The lower surface brightness SNR G003.8+0.3 is better discerned in the low resolution image.

The dominant extended source in Fig. 4.6 is a known Ultra Compact H II region (Becker et al. 1994). A small angular size SNR G004.2-0.0 was reported by Gray (1994a) in this field at the centre of this image. However there is no indication of this source at the level of

10 mJy/beam in this image. It is, however detected as a compact flat spectrum source in the low resolution image. This sources is unlikely to be an SNR.

Fig. 4.7 shows the GMRT 325-MHz image of the shell type SNR G004.8+6.2. The strong, marginally resolved source due west of this SNR is the well known Kepler's SNR (Fig. 5.14). G004.8+6.2 is again clearly detected in the NVSS image of this region (Fig. 5.7). This SNR is also detected in the image made from a 327-MHz VLA observation of a region close to this source (Fig. 5.8).

Fig. 4.8 shows the field containing the barrel shaped SNR G356.2-1.5. The 843-MHz image of this SNR by Gray (1994a) was severely affected by artifacts due to the grating response of nearby sources. This SNR is however clearly detected in the GMRT 325-MHz image. A marginally extended source of emission is also visible in this image in the north-eastern direction.

Fig. 4.9 shows the GMRT image of the shell type SNR G356.2+4.5. This SNR is also clearly visible in the NVSS image of this region (Fig. 5.10). The quality of NVSS images close the Galactic plane is usually poor. However, a few degrees away from the plane, low surface brightness SNRs are often easily visible in NVSS fields (Trushkin 1999; Bhatnagar 2000; Green 2001). A careful examination of the NVSS fields, few degrees away from the plane is therefore likely to result in the identification of more, hitherto unknown SNRs. Deep imaging of such objects can then be followed up with the GMRT/VLA. Detailed multi frequency imaging of a number of high Galactic latitude SNRs can be used to possibly deduce the distribution of ionized gas and examine the statistical significance of the Σ-D-z relation (Caswell & Lerche 1979).

Fig. 4.10 shows the GMRT image of the incomplete shell of the SNR G358.0+3.8. This is a low surface brightness SNR, but also detected in the NVSS image (Fig. 5.11).

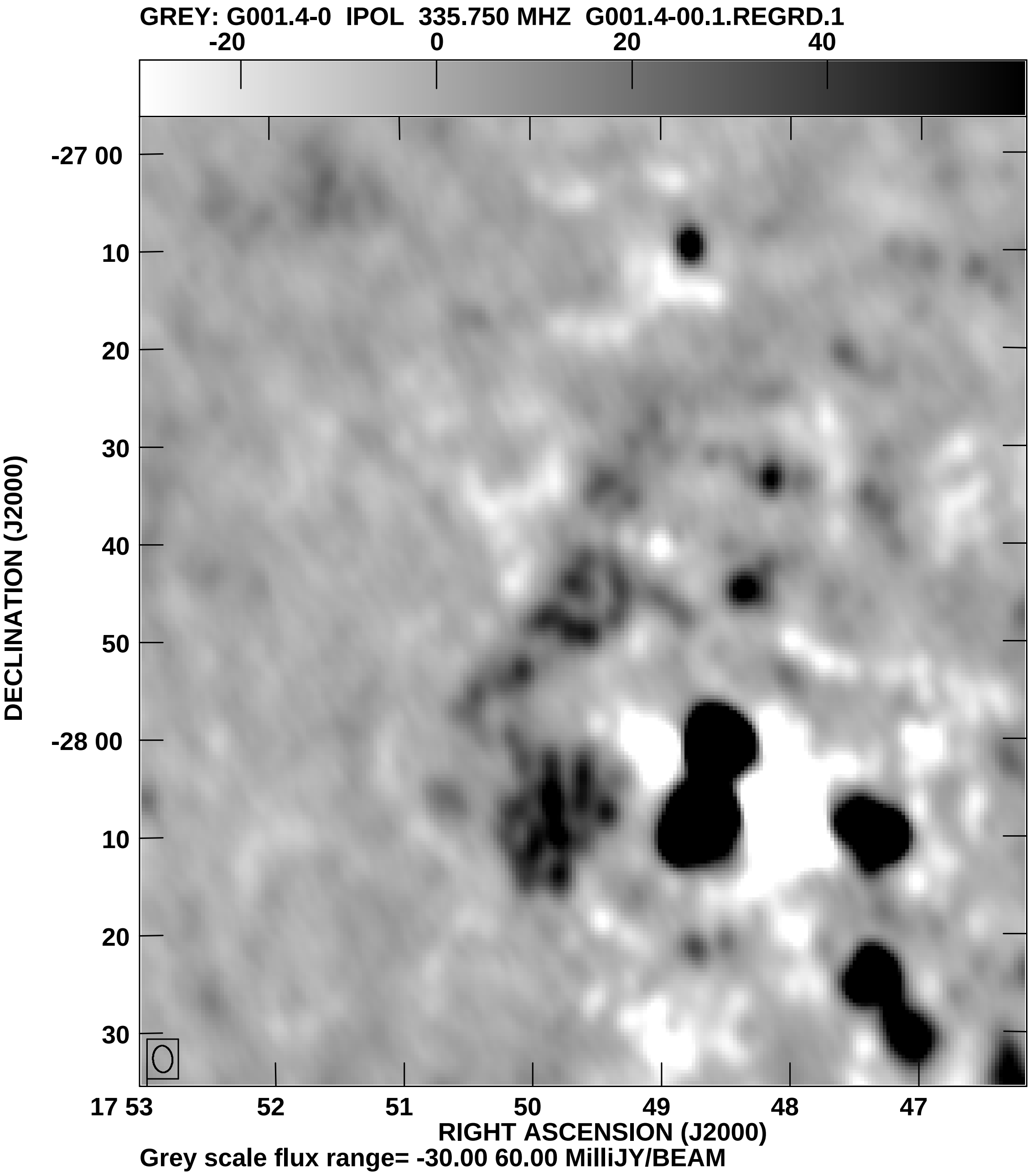

Figure 4.4: Full primary beam image of the field containing the sources G001.4−0.0 at the centre of the image. The resolution in the image is $\approx 3 \times 2\,\mathrm{arcmin}^2$. The RMS noise in the images is ~ 30 mJy/beam. The Galactic Centre sources (LaRosa et al. 2000) Sgr D HII region and Sgr D SNR pair, the SNR G000.9+0.1, Sgr B1 and Sgr B2 are the dominant sources in the south-east direction.

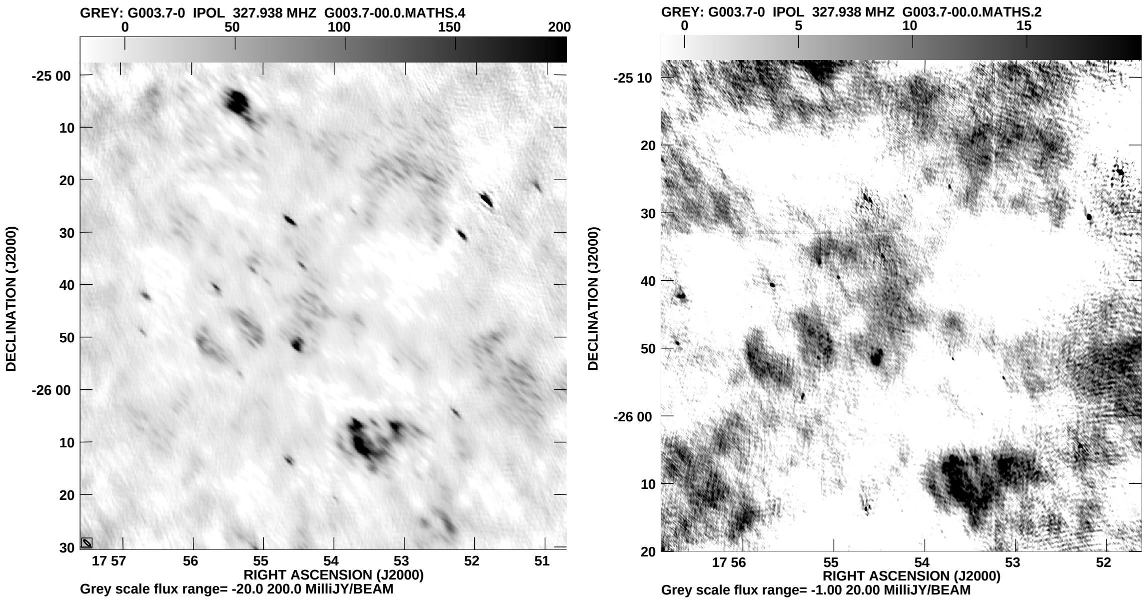

Figure 4.5: Full primary beam image of the field containing the sources G003.6−0.1, G003.7-0.2, and G003.8+0.3. The resolution in the image in the left panel is this image $\approx 98 \times 29\ \mathrm{arcsec}^2$ while that in the image in the right panel is $\approx 20 \times 11\ \mathrm{arcsec}^2$. The RMS noise in the images is ~ 5 mJy/beam. The extended emission is more clearly visible in the low resolution image, which was generated using a single facet. The higher resolution image was made with multiple facets.

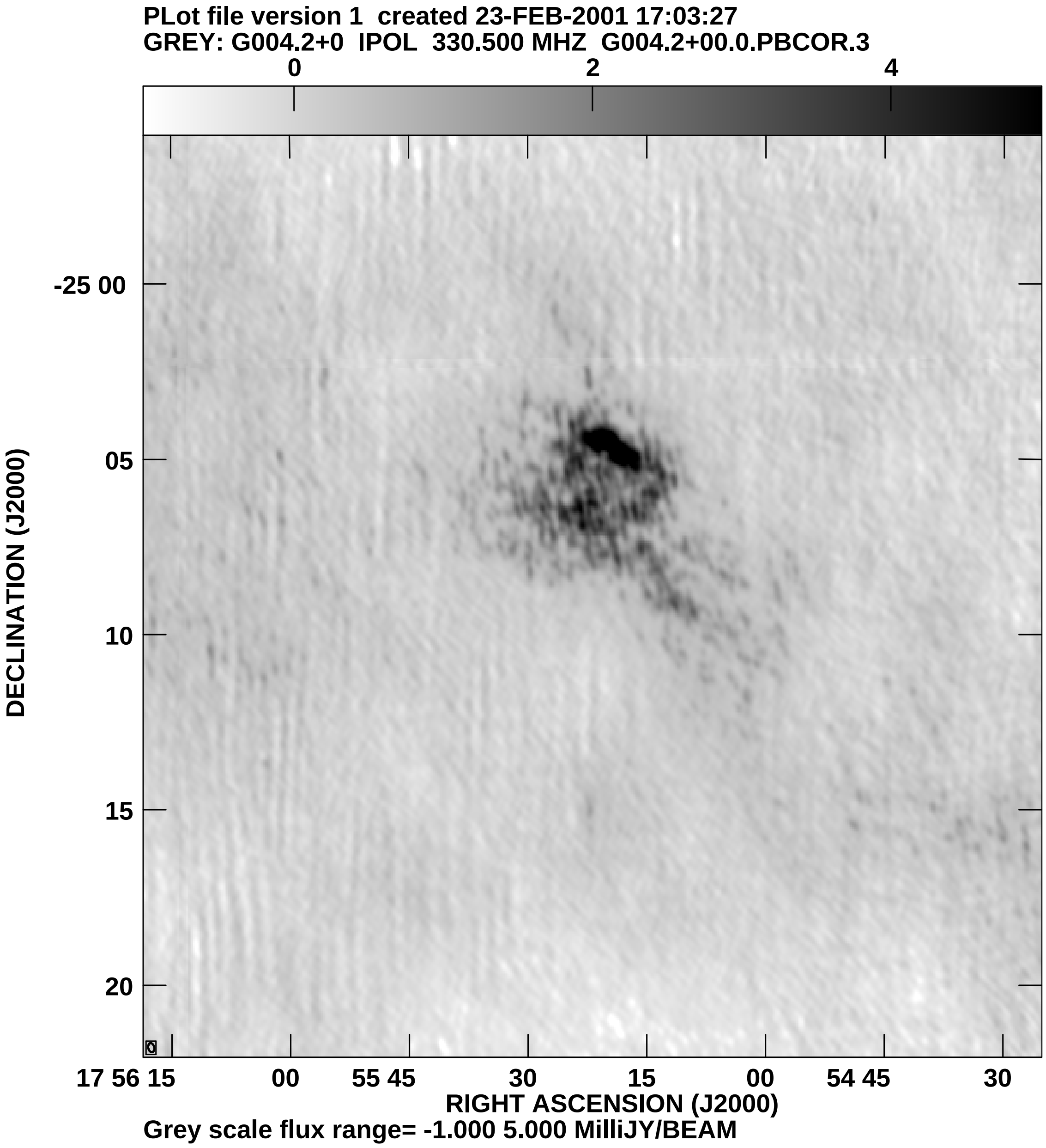

Figure 4.6: High resolution, multi facet image of the field containing G004.2−0.0. The resolution in the images is $\approx 15 \times 10 \ \mathrm{arcsec}^2$ and the RMS noise ≈ 5 mJy/beam. The dominant extended source in the field is an Ultra Compact H II region. There is a hint of a emission at the location of G004.2−0.0, but much below the expected level, probably indicative of thermal source (see Figure 5.5 for a low resolution image where G004.2−0.0 is detected as compact source).

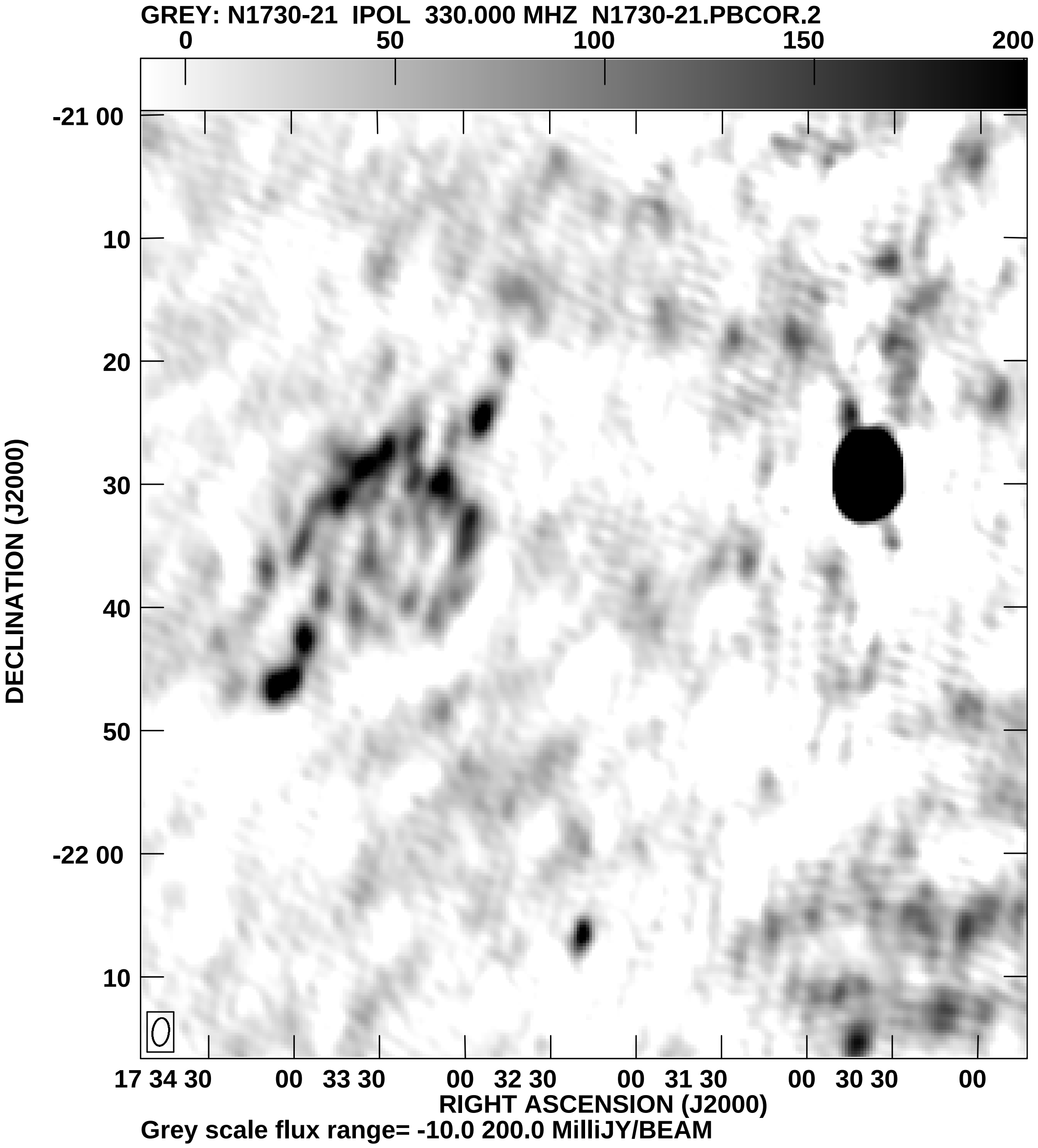

Figure 4.7: Full primary beam corrected image of the field containing G004.8+6.2. The weaker source, due east of the centre of the image is the SNR G004.8+6.2. The strong source due west of the image centre is the 38 Jy Kepler's SNR. The resolution in the image $\approx 2.3 \times 1.4\ \mathrm{arcmin}^2$ and the RMS noise is ≈ 23 mJy/beam. Apart from other unknown sources of noise, the higher RMS noise in this image is also due to the wobble in the antenna pointing for some of the antennas used for this observation.

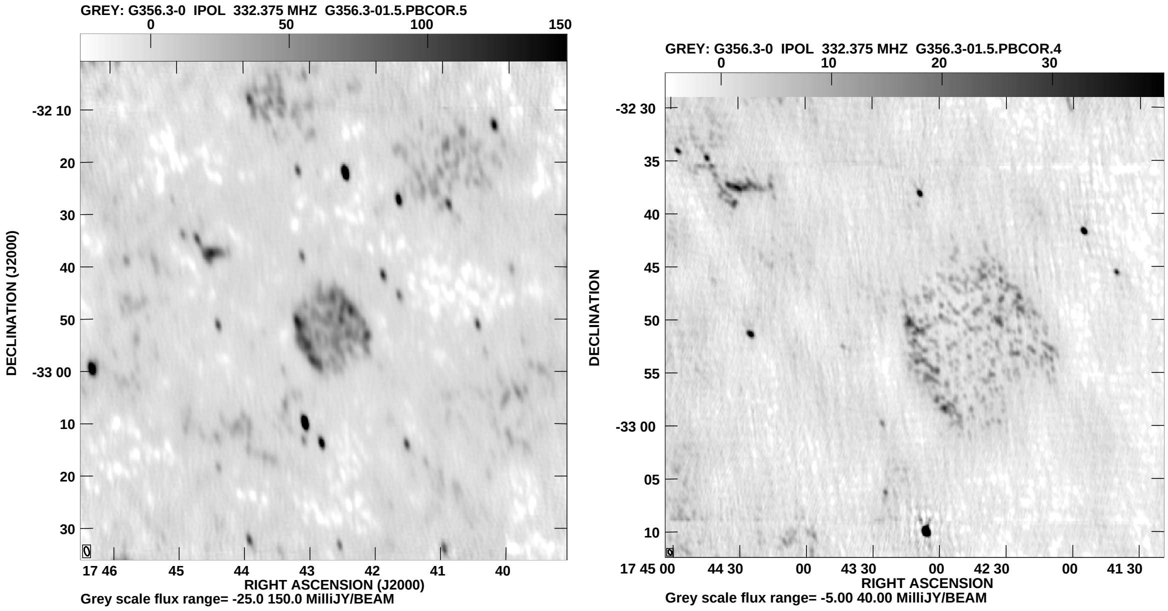

Figure 4.8: Multi facet image of the field containing G356.2-1.5. The resolution in the image on the left is $\approx 1.7 \times 0.8$ arcmin^2 and the RMS noise is ≈ 5 mJy/beam. Notice the extended emission north-east of the barrel shaped SNR in the centre of the field. The panel on the right shows a high resolution image of this extended source.

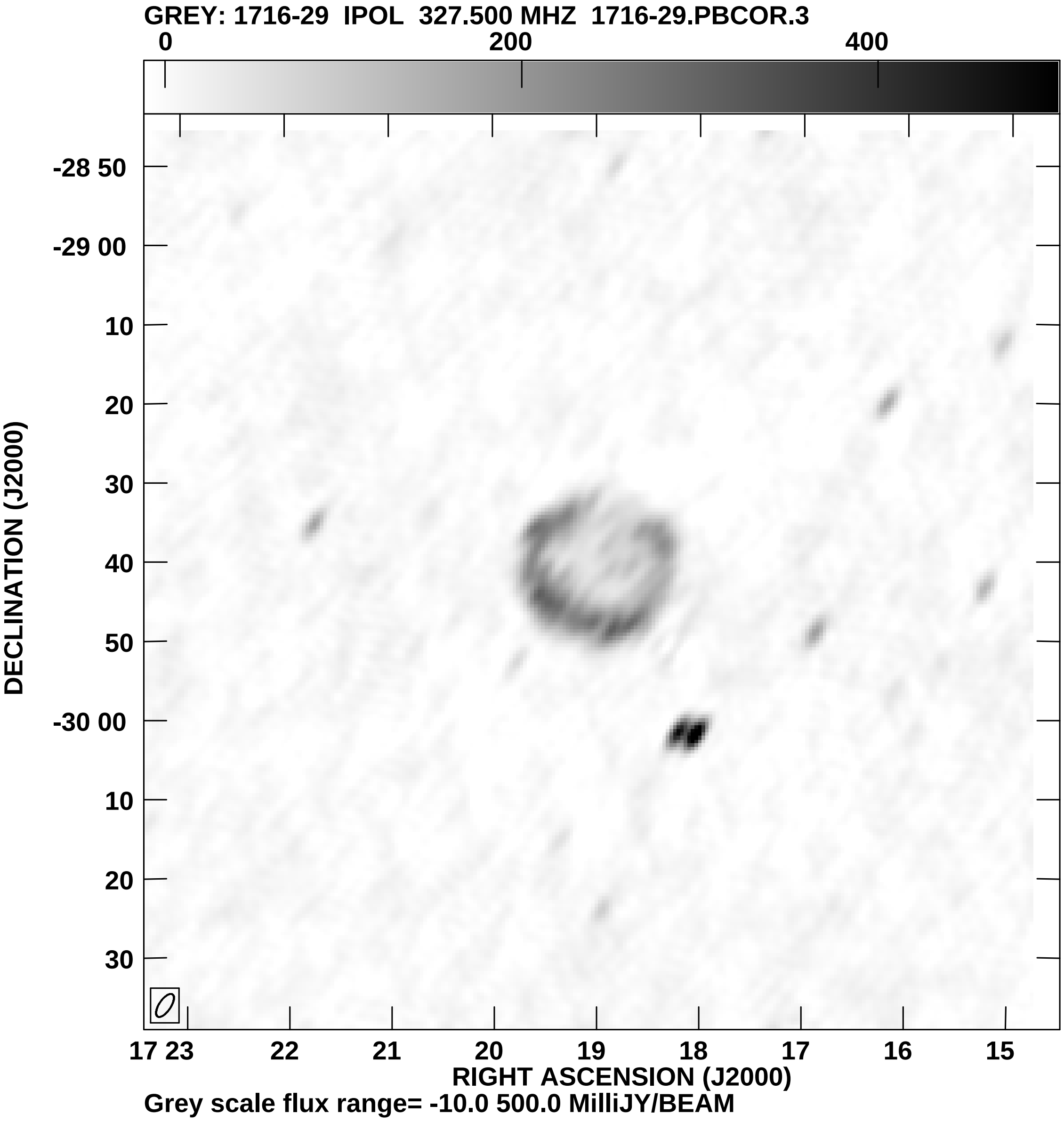

Figure 4.9: Full primary beam corrected image of the field containing G356.2+4.5. The resolution in the image is $\approx 3 \times 1.5\ \mathrm{arcmin}^2$ and the RMS noise is ≈ 10 mJy/beam.

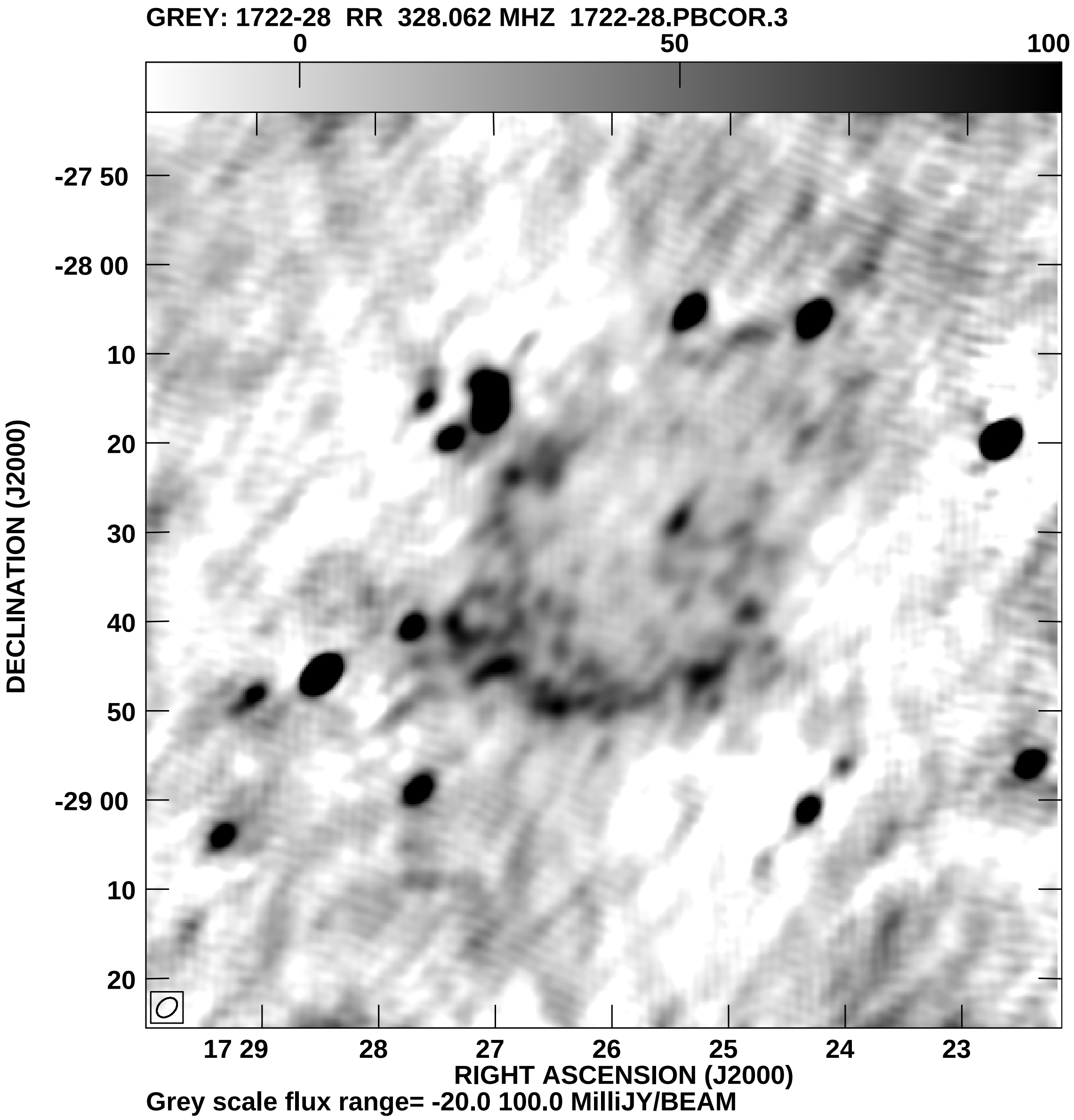

Figure 4.10: Full primary beam corrected image of the field containing G358.0+3.8. The resolution in the image is $\approx 2.6 \times 1.5\ \mathrm{arcmin}^2$ and the RMS noise is ≈ 15 mJy/beam.

Chapter 5

Observations of Supernova Remnants

This chapter discusses the GMRT 325-MHz observations of candidate and known SNRs. The motivation behind this exercise was two-fold. Firstly, to use the higher sensitivity and resolution provided by GMRT at low frequencies which would unambiguously identify the SNRs. Secondly, GMRT has only recently come to a stage where enough antennas are available in the interferometric mode to attempt imaging of weak extended sources, which truly tests the imaging performance of the instrument. In these early stages of the telescope where a large fraction of time and effort goes into debugging the instrument, it was important to have a scientific goal in mind to provide the focus, direction and motivation to debug the telescope and bring it to a level where it can be used for scientific purposes. These observations provided the required focus where the scientific returns for the debugging effort put-in were perceived to be substantial.

5.1 Introduction

Radio emission from Supernova remnants (SNRs) is due to the synchrotron radiation mechanism which has a non-thermal power law dependence on frequency with a negative spectral index α ($S \propto \nu^{\alpha}$). This makes the emission progressively stronger at lower frequencies (see Section 1.1). On the other hand, thermal emission from typical HII regions, the other class of objects with extended radio emission in the Galaxy, has a flat spectrum above ≈ 1 GHz. Below this frequency, the optical depth is much greater than 1 and the spectrum turns over with a spectral index of 2. The low frequency continuum spectra of Galactic objects are therefore frequently used to distinguish between thermal and non-thermal sources of emission (Kassim et al. 1989a; Kassim & Weiler 1990; Subrahmanyan & Goss 1995). The other key observational evidence used to identify SNRs is their morphology. Detection of an extended non-thermal source with no thermal emission has been the criterion used to identify Galactic sources as SNRs.

Kassim (Kassim 1989), in a study of non-thermal emission from known Supernova remnants in the Galaxy, demonstrated that the radio emission from most SNRs gets absorbed at frequencies below about 100 MHz. He observed a number of SNRs, widely distributed in the inner Galaxy and showed that about two thirds of all SNRs show this spectral turn-over due to free-free absorption by the intervening ISM; this indicates the presence of an extended low density warm ionized medium (ELDWIM) in the Galaxy. Since then, many more SNRs has been imaged at frequencies between 1 GHz and 327 MHz (and in some cases even below 327 MHz). A collection of the radio spectra of SNRs have been compiled by Trushkin (1998)[1]. His catalogue of SNR spectra also gives the spectral indices above and below the turn-over frequency and the frequency at which the spectrum turns over. Spectra of about 35% of the SNRs from this catalogue show a low frequency turn-over. The measurement of this turn-over frequency for SNRs distributed throughout the Galaxy can be used to indirectly measure the distribution of this phase of the ISM, which is otherwise inaccessible to direct observations.

Imaging of HII regions at frequencies below ~ 1 GHz, together with the electron temperature derived from RRL observations have been used to deduce improved estimates of the physical properties of HII regions (Shaver 1969; Subrahmanyan 1992b,a; Kassim et al. 1989b). Low frequency continuum mapping in the Galactic plane is therefore important from the point of view of identification of SNRs, separating thermal emission from non-thermal emission and for studying the intervening ISM.

Radio emission from SNRs is typically extended, often with a low surface brightness. Telescopes which are sensitive to extended emission as well as to total flux, are required to image such objects. Single dish observations are sensitive to emission at all scales in the field. While interferometric telescopes typically provide much higher resolution, they are insensitive to scales larger than those corresponding to the smallest projected baseline. Single dish telescopes, at high frequencies, provide the sensitivity and moderate resolution required for such work. Till recently many observations were therefore done using single dish instruments. However, single dish observations pose a separate problem.

[1]Available from http://www.ratan.sao.ru/~cats on the web

While single-dish observations do not discriminate against extended emission, they are more prone to large scale confusing emission, which is abundantly present in the Galactic plane. Low frequency single dish observations do not provide the required resolution to resolve the extended nature of the SNR emission. For these reasons, most Galactic SNRs have been observed using single dishes at high frequencies (> 1 GHz) which provide reasonable resolution (better than $1'$). Higher resolution interferometric observations of some Galactic SNRs have also been done. However, such observations are often restricted to observing relatively small sized SNRs. Imaging at low frequencies using interferometers is also relatively difficult due to problems arising from higher level of RFI, higher phase noise at low frequencies (due to various reasons ranging from cross talk to ionospheric phase corruption), non-co-planarity of array requiring much more complex software and higher computing power. Hence, even interferometric observations have been typically done at frequencies > 1 GHz.

However, observations at high frequencies have another source of emission, namely the thermal emission from HII regions which, in some cases, is fairly strong. The non-thermal emission from SNRs becomes progressively diminished at higher frequencies, while the thermal emission remain fairly constant as a function of frequency at frequencies higher than about 1 GHz. High frequency observations therefore miss extended low surface brightness emission from SNRs. Such observations alone can also wrongly classify sources which have thermal and non-thermal components in the radiation (for example, due to line-of-sight super-position of thermal and non-thermal emission). Thus, while high frequency telescopes provide the required resolution and sensitivity, they alone are not adequate for the identification of Galactic objects as SNRs.

Recently, synthesis telescopes like the GMRT (Bhatnagar 2000) and MOST (Gray 1994a) have been used to image parts of the Galactic plane. The MOST survey, at a resolution of $\approx\ 90 \times 43.5\ \mathrm{arcsec}^2$ and is sensitive to angular scales up to $30'$, identified seventeen candidate SNRs. Most of these object are large ($> 5 - 10'$). Many of the fields however suffer from the grating response due to nearby strong sources and from confusing thermal emission from nearby strong HII regions.

Duncan et al. (1997b) used the Parkes 64-m single dish telescope to image a set of large, high latitude SNRs at 2.4 GHz. These observations identified about a dozen new large SNRs ($> 15'$) south of $-25°$ declination. Again, besides the lower angular resolution of the single dish, these observations suffered from the problem of separating extended diffused non-thermal emission from thermal emission in and around the Galactic plane

Table 5.1: Observed and derived physical parameters of the candidate SNRs in the fields. Type code 'S' implies shell-type, 'B' implies barrel-type while 'N' means that the object is most likely not an SNR.

Name	RA_{J2000} ($h\ m\ s$)	Dec_{J2000} ($^\circ\ '\ ''$)	S_{327MHz} (Jy)	Size (arcmin)	Type	α ($S \propto \nu^{\alpha}$)
G001.4−0.1	17 49 39	-27 45	4.2 ± 0.5	8.0	S	-0.8 ± 0.3?
G003.7−0.2	17 55 29	-25 50	4.5 ± 0.3	-	B	-0.7 ± 0.1
G003.8+0.3	17 53 02	-25 24	8.7 ± 0.3	18	S	-0.9?
G004.2−0.0	17 55 22	-25 15	0.1 ± 0.2	-	N	-
G004.8+6.2	17 33 24	-24 34	5.5 ± 1.2	17	S	-0.6 ± 0.1
G356.2+4.5	17 18 58	-29 40	8.1 ± 1.7	25	S	-0.7 ± 0.2
G356.3−1.5	17 42 40	-32 52	5.7 ± 0.2	15	S/B	$> -0.7 \pm 0.1$
G358.0+3.8	17 26 03	-28 36	2.5 ± 1.3	37×39	S	-

using these high frequency.

The GMRT at 327 MHz provides a resolution of up to $\sim\ 20$ arcsec and is sensitive to spatial scales up to 30 arcmin. The relatively smaller field-of-view (half-power beam width of $\approx 1^\circ.4$) of the GMRT also provides an advantage in terms of attenuating confusing emission from near by strong sources. At this frequency, the thermal emission from typical HII regions is severely diminished, while the emission from SNRs remain relatively strong. The higher resolution and sensitivity at these low frequencies, make the GMRT an ideal instrument for studies of Galactic SNRs. Compared to the resolutions of about $1'$ and $1.5'$ and RMS noise of $\approx\ 20$ mJy/beam and 35 mJy/beam in the survey by Duncan et al. (1997b) and Gray (1994a) respectively, the GMRT at 327 MHz provides a factor of 2 lower RMS noise and, depending upon the largest baselines used, up to 2–5 times better resolution.

5.2 Candidate SNRs

This section presents the results from the 327-MHz GMRT observations of fields containing candidates SNRs. The list of fields observed and the parameters of SNRs found in these fields are list in Table 5.2.

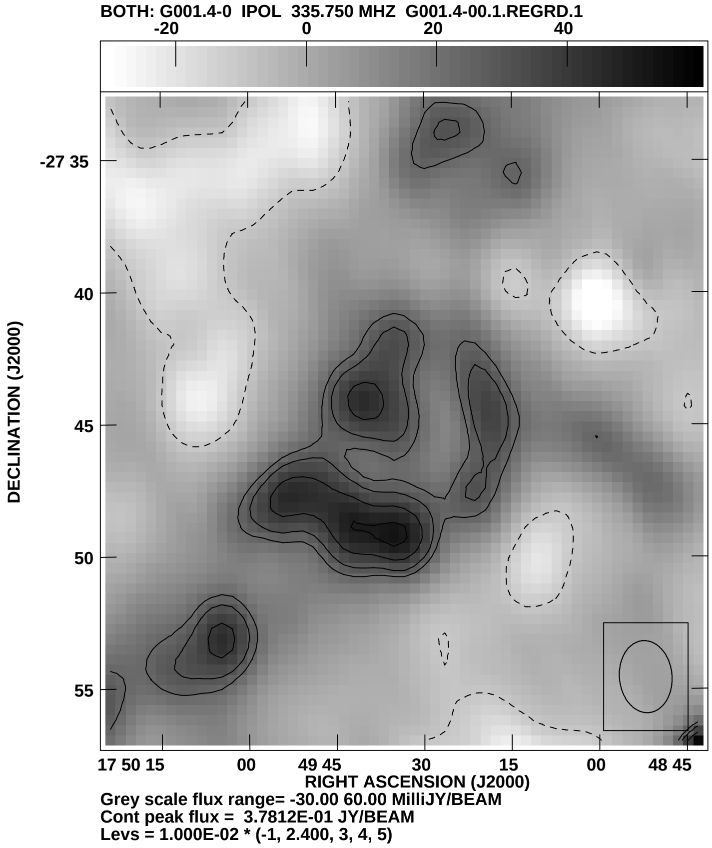

Figure 5.1: 327-MHz image of G001.4−0.0 using GMRT. A partial shell with compact source located almost at the centre is clearly detected.

5.2.1 G001.4−0.1

The GMRT 327-MHz image of G001.4−0.0 is shown in Fig. 5.1. A partial arc of ~ 8 arcmin diameter is clearly visible in this image. A compact source, almost at the geometric centre of the arc is also clearly visible. The morphology is very similar to that of the nearby composite SNR G000.9+0.1 which has a flat spectrum, X-ray emitting compact central source (Mereghetti et al. 1998). This SNR lies just north-east of the Sgr D HII region and at the very edge of the VLA 327-MHz wide-field image of the Galactic centre region (LaRosa et al. 2000). A weak fuzz of emission is seen in this wide-field image corresponding to this SNR. However, the image quality for this region is too poor (due to primary beam attenuation) to be able measure the flux density or decipher the morphology.

The 327-MHz flux density measured from our observation was found to be 4.2 ± 0.5 Jy. The 843-MHz image (Gray 1994a) suffers from artifacts due to the grating response of

Sgr A and the flux density of $\sim$ 2 Jy is hence only a "tentative" figure. From their 1616 MHz VLA observations of this region, Liszt (1992) reported "an arc of incomplete shell" of diameter $\sim$ 7 arcmin at this location. The incomplete arc seen in the GMRT image agrees well with the incomplete arc seen in the 1616-MHz image. The MOST image of this object shows a relatively featureless source of emission and the "complete shell" reported by Gray (1994a) is difficult to decipher.

This source was also the target of observations for the detection of OH (1720 MHz) maser emission by Yusef-Zadeh et al. (1999). In the VLA A-array observation, they detect a maser spot, coincident with the western edge of the arc. Their VLA D-array observations detect an extended arc of emission, almost coincident with the arc seen in the radio continuum images.

The spectral index between 327 and 843 MHz is -0.8 ± 0.3 for the shell. However, given that the 843-MHz flux density is quite uncertain, this value of the spectral index remains tentative and is used only to show the non-thermal nature of emission. Based on the morphology, non-thermal nature of emission and association of OH (1720 MHz) emission, we propose that this is a shell-type SNR in the Galactic plane.

5.2.2 G003.8+0.3

Gray (1994a) describes G003.8+0.3 as a "fairly weak, incomplete ring structure most perfectly centered on a slightly extended source". The morphology of this object in the GMRT 327-MHz image, shown in Fig. 5.2, matches well with the 843-MHz MOST image. This SNR is also in the field of view for the pointings for G003.7−0.2 and G004.2−0.0. The partial shell is clearly visible in both the images. The IRAS 60μm image, shown in Fig. 5.3, does not show any significant emission at this position. However, this SNR lies within a ring of IR emission seen clearly in this image. The northern rim of the radio ring is significantly brighter and more extended, almost filling the IR ring, making it difficult to define the center of the radio ring structure. The "central source" in the radio image is fairly close to the center defined by the inner edge of the ring structure, but not close to the center defined by the outer edges. The bridge of emission connecting the central source and the ring is not so clearly seen at 327 MHz.

The integrated flux density of this region at 327 MHz is 8.7 ± 0.3 Jy. The diameter of the ring structure (including the northern extension) is $\approx 18'$ while its center is at $\mathrm{RA}_{J2000} = 17^h53^m02^s$, $\mathrm{Dec}_{J2000} = -25°24'$. The position of the emission peak for the 'central source' is $\mathrm{RA}_{J2000} = 17^h52^m54^s$, $\mathrm{Dec}_{J2000} = -25°28'$. The flux density of the VLA

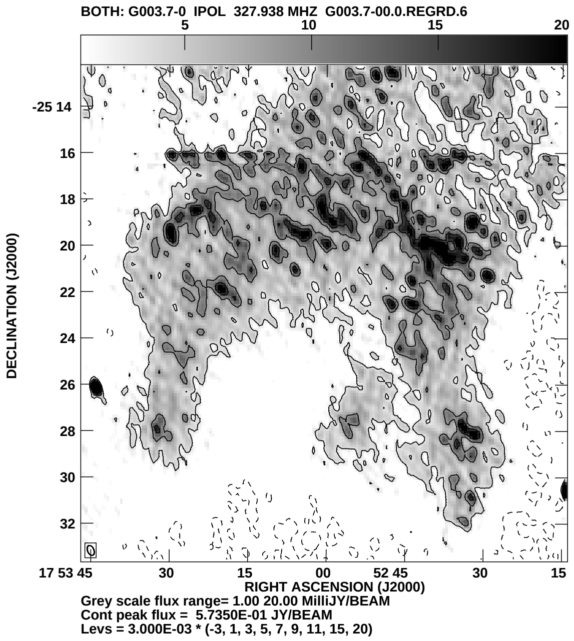

Figure 5.2: GMRT image at 325 MHz of G003.8+0.3. The shell morphology of G003.8+0.3 is clearly visible.

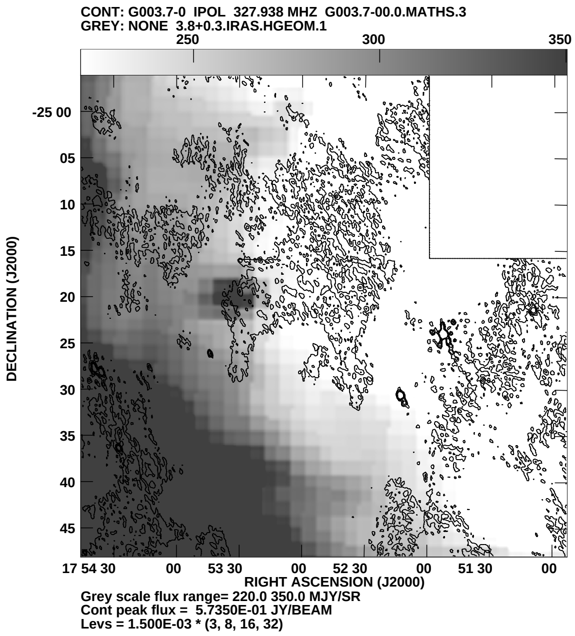

Figure 5.3: 327-MHz contours overlayed on the 60μm IRAS gray scale image of G003.8+0.3. A shell of IR emission is visible and the radio emission from the SNR is completely within the IR shell and almost fills the IR shell in the north. There is, however, no significant IR emission at the location of the SNR itself. The small extension in the eastern edge of the radio shell is coincident with the strong IR compact source.

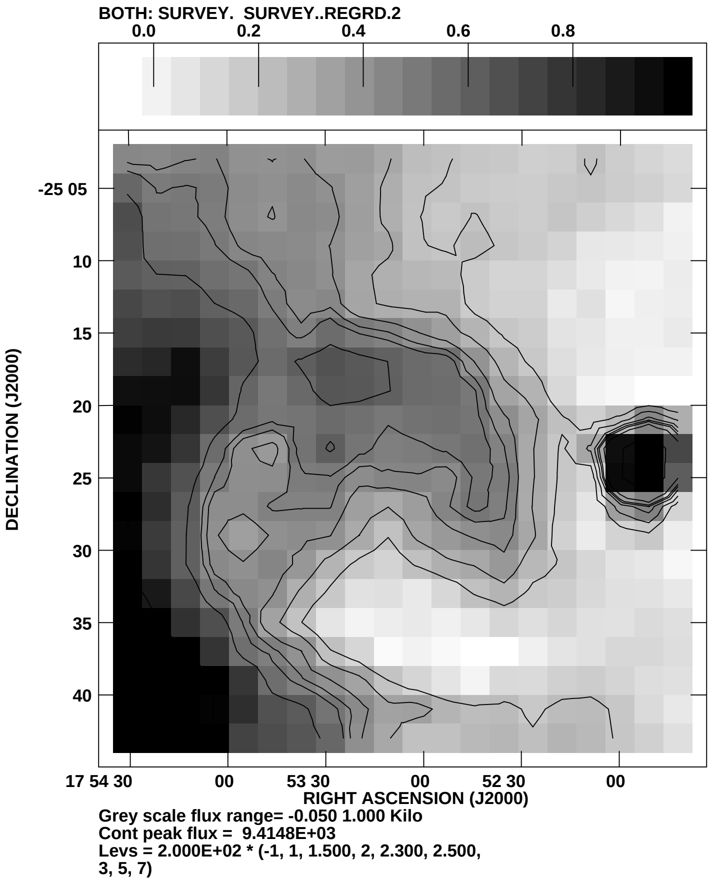

Figure 5.4: Image of G003.8+0.3 at 11 cm from the 100-m Effelsberg single dish survey. An arc of emission similar to that seen at lower frequencies is clearly visible.

21-cm calibrator $J1751-253$, which is just west of this region is measured to be 1.3 ± 0.2 Jy. Flux density of this source from Texas survey (Douglas et al. 1996) is $1.41\pm.09$ Jy.

The flux density reported by Gray (1994a) at 843 MHz is ≈ 3.5 Jy giving a spectral index of -0.9. Based on the morphological evidence and evidence for non-thermal nature of emission, we propose that this source is a weak, Galactic SNR.

The 'central source' is detected as a point source at 1400 MHz in the NRAO-VLA All Sky Survey (NVSS) with a flux density of 15.1 mJy. Although it is a weak source in the 327-MHz image with flux density barely at the 2σ level, it is nonetheless stronger than 15 mJy, proving that it is a non-thermal source. With a large error in the measurement of the 327-MHz flux density, it is difficult to determine an accurate spectral index.

Image of this SNR from the radio continuum survey of the Galactic plane at 11 cm using the 100-m Effelsberg telescope (Reich et al. 1990) is shown in Fig. 5.4. Here too, a partial shell of emission is visible, which matches well with the morphology of this SNR seen at 843 and 327 MHz. Significant amount of linear polarization is also detected in the 11 cm polarized images.

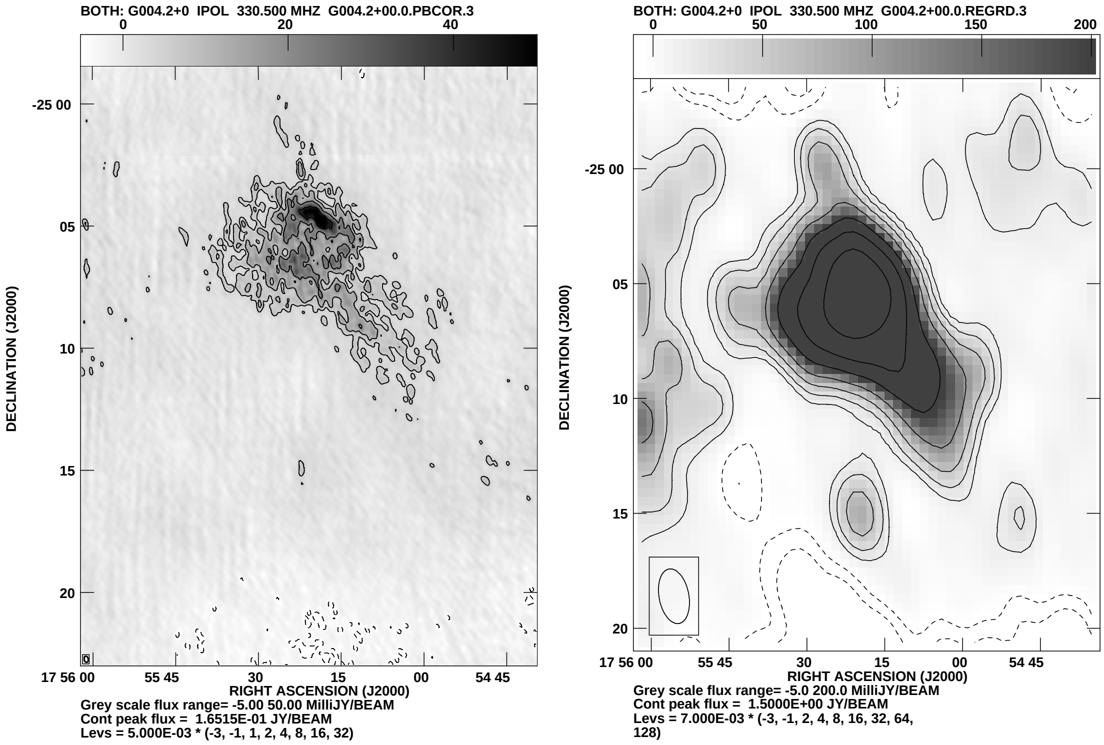

Figure 5.5: GMRT 327-MHz image of the region containing G004.2+0.0. The strong extended source in this field is a classified Ultra Compact H II region G004.417+0.126. The left panel shows the high resolution image ($\sim 15 \times 11$ arcsec^2) of this region where the core-halo morphology of G004.417+0.126 is clearly visible. It's south-western tail is visible in Grey's 843-MHz image of this region. The RMS noise in the map is about 5 mJy/beam. The right panel shows the low resolution image where an unresolved source is detected at the location of the candidate SNR just south of G004.417+0.126. The RMS noise in this image is ~ 8 mJy/beam.

5.2.3 G004.2−0.0

This source is the smallest diameter candidate SNR (size ~ 3.5 arcmin) reported by Gray (1994a). He reported the location of this object as $\mathrm{RA}_{J2000} = 17^h 55^m 17^s, \mathrm{Dec}_{J2000} = -25^\circ 14' 51''$. The total 843-MHz flux density was reported to be 200 mJy. However this ob-

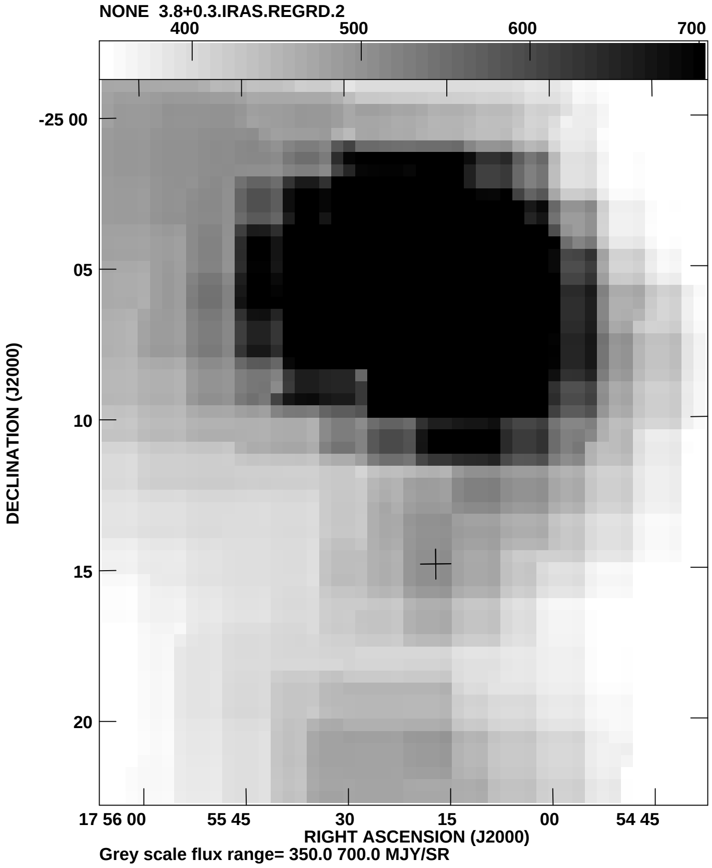

Figure 5.6: The IRAS 60μm image of the region containing G004.2+0.0. The strong source seen just north of G004.2+0.0 in the GMRT 327-MHz image is the strongest source in the IRAS image. A faint source, indicated by a cross at the position of G004.2+0.0 is also detected in this IRAS image.

ject sits in a negative bowl and the measured value after tentative correction for this bowl is in the range of $100 - 300$ mJy (Gaensler, private communication). A high resolution image of this field was made to look for the shell-type structure at 327 MHz. There is a hint of a compact source in this image at $\mathrm{RA}_{J2000} = 17^h 55^m 22^s, \mathrm{Dec}_{J2000} = -25^\circ 15' 01''$, but barely at the 2σ level. No shell-type structure was detected at the level of ~ 5 mJy/beam with a resolution of ~ 15 arcsec. The low resolution image, shown in Fig. 5.5 has a ~ 100 mJy object at the location of this source. There is probably a compact source in the NVSS image at this location, but again at the $1 - 1.5\sigma$ level. The $60\mu m$ IRAS image of this region (Fig. 5.6) also shows significant extended emission at the location of this source (indicated by a cross in the figure), which appears to be associated with the HII region in the north, indicating that this may be a thermal source. This source, based on the available radio flux densities is therefore consistent with it being a flat spectrum thermal source and may not be an SNR.

The dominant extended source in the image shown in Fig. 5.5 is a known HII region, G004.4+0.1 located at $\mathrm{RA}_{J2000} = 17^h55^m26^s, \mathrm{Dec}_{J2000} = -25°05'08''$ (Kuchar & Clark 1997). A compact core surrounded by a halo of lower surface brightness is clearly visible in this image and this core-halo morphology is suggestive of this being a compact HII region (Wood & Churchwell 1989b). In combination with high resolution images at other frequencies, these data can provide information about the physical conditions in this HII region.

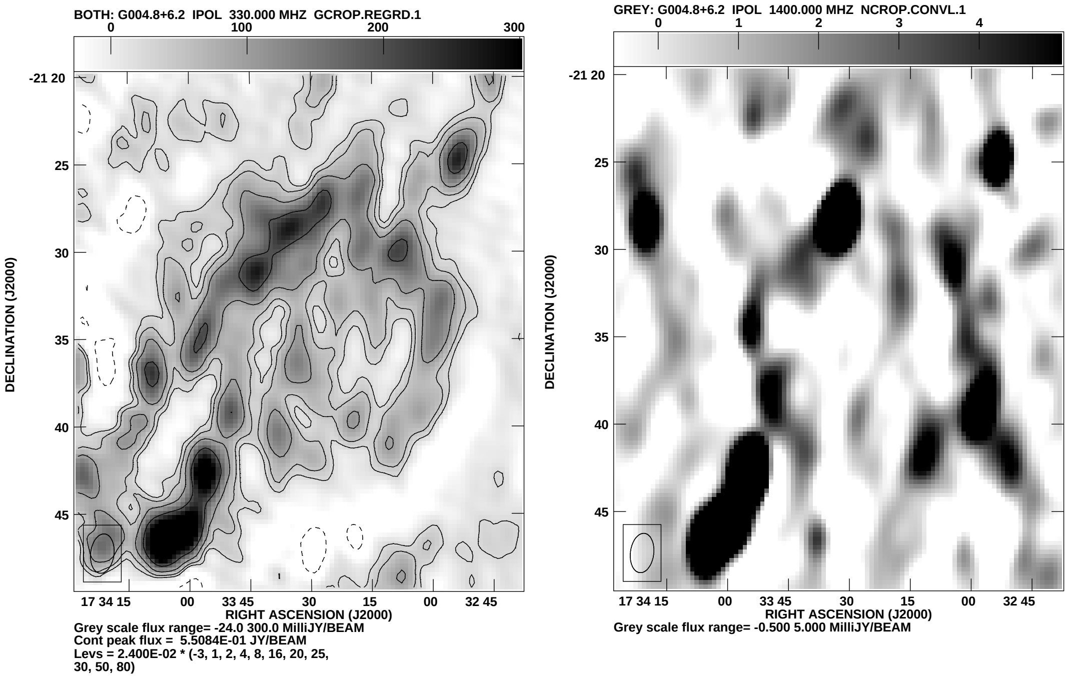

Figure 5.7: GMRT image of G004.8+6.2 at 327 MHz and NVSS image at 1400 MHz. The resolution in the GMRT image is $2.2' \times 1.3'$ along PA $-07°$ and the RMS noise is 23 mJy/beam. The NVSS image has been smoothed to the resolution of the GMRT image and has a RMS noise of 0.5 mJy/beam.

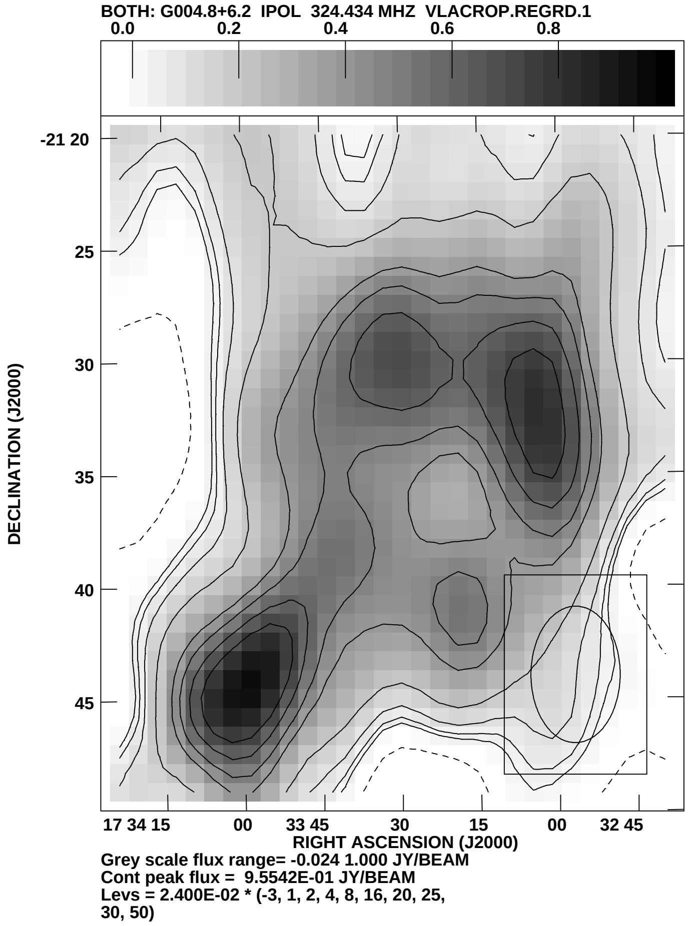

Figure 5.8: VLA image of G004.8+6.2 at 325 MHz. The resolution in this image is $6' \times 4'$ along PA $-0.8°$ and the RMS noise is 24 mJy/beam.

5.2.4 G004.8+6.2

Fig. 5.7 shows the GMRT 327-MHz and NVSS 1400-MHz images of G004.8+6.2 (formerly designated as G004.5+6.2). This object of size $17' \times 18'$ is located $40'$ east of Kepler's SNR (Fig. 5.14). The total flux density at 327 MHz is 5.5 ± 1.2 Jy and the co-ordinates of the center of the ring are $\mathrm{RA}_{J2000} = 17^{\mathrm{h}}33^{\mathrm{m}}24^{\mathrm{s}}$, $\mathrm{Dec}_{J2000} = -21°34'$. The apparent flux density of Kepler's SNR in the GMRT image before primary beam correction was approximately 20 percent lower than the value of 38 Jy after primary beam correction. The integrated flux density of G004.8+6.2 at 2.4 GHz was reported to be 1.3 ± 0.2 Jy and the value at 4.85 GHz from PMN image of this region was found to be 1.12 ± 0.07 Jy, which gives a spectral index of -0.57 ± 0.13. The NVSS image shows a well resolved ring coincident with the emission at 327 MHz. Since NVSS misses most of the extended emission, we did not attempt to use the NVSS flux density to determine the spectral index of the source. We attribute the lower signal-to-noise ratio in this map to the presence of side lobes of the synthesized beam from Kepler's SNR contaminating the entire map. It could also be partly due to the non-isoplanacity of the ionosphere at these scales as well as pointing errors in the antennas.

This SNR was also in the field of view of a VLA D-array multiple snap-shot observation at 325 MHz in March 1999. This observation was part of another project not included in this dissertation to make continuum images of Galactic SNRs at 325 and 74 MHz to get reliable low frequency spectra and, wherever possible, spectral index maps. The image from these observations is shown in Fig. 5.8. The resolution is $6' \times 4'$, but the image is in good agreement with the higher resolution GMRT image. The integrated flux density from the VLA 327-MHz image is 4.9 ± 1.3 Jy, which is consistent with the flux density from the GMRT image within the errors bars.

5.2.5 G356.3-1.5

This SNR is classified as a 'classic barrel' SNR by Gray (1994a) from the 843-MHz image. The GMRT 327-MHz image (Fig. 5.9) shows the basic structure seen in the 843-MHz image where the two edges are relatively brightened compared to the center of the remnant. However, at 327 MHz, the center is also filled with significant emission, not seen in the 843-MHz image. Although it does show the brightened rims (probably of the shell), which were seen as the dominant sources of emission in the 843-MHz image, there is no well defined minimum of emission in a direction perpendicular to these rims. Gaensler (1998) laid down the following criterion to classify a SNR as 'barrel' shaped:

1. It must be of the shell- or composite-class

2. The highest resolution image available must have a minimum of 10 beams across its diameter

3. It must have clear minima in emission separated by position angles of $180^\circ \pm 30^\circ$ relative to the assumed center of the SNR (this defines the axis of symmetry for the 'barrel').

4. It must have well-defined maxima and at approximately perpendicular position angles to the minima

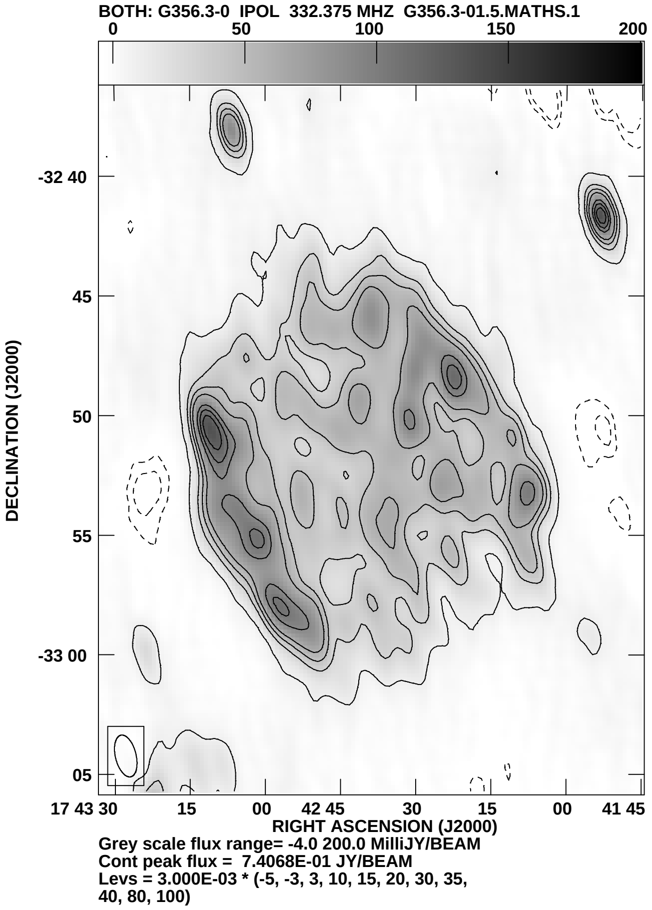

Figure 5.9: 327-MHz image of G356.3-1.5 using the GMRT. The box shaped morphology of the object is apparent. The emission filling the center of the object is not detected in the 843-MHz MOST image of Gray. The RMS noise in the image is 7 mJy/beam and the total flux density of the source is 5.7 ± 0.2 Jy

5. A clear bilateral axis should be identifiable, passing through the two minima and through the center of the SNR.

The clear minima along the circumference of an otherwise shell-type SNR makes its classification as a 'barrel' shaped secure. The 843-MHz image, where questionable data processing was done (namely, the subtraction of a smooth component to remove the effect of the grating response from a nearby strong source), shows a well defined minimum of emission between the two rims of emission which is filled by emission in the 327-MHz image. Although morphologically this central emission appears to be emission from the edges of the 'barrel' seen in projection, it is important to measure the spectral index of this emission to evaluate the possibility of this being a filled-center SNR. With a size of $\approx 15'$, this can be reliably mapped at 610 and 233 MHz with the GMRT.

The integrated flux density measured at 332 MHz from the GMRT image is 5.7 ± 0.2 Jy. The RMS noise in the image in the vicinity of this object is about 4 mJy/beam. The integrated flux density in the modified image at 843 MHz is reported to be 2.8 Jy. This implies a spectral index of -0.7 ± 0.1 between 843 and 332 MHz. However the 843-MHz image is marred by a grating response due to G357.7-0.1 and a smooth model of this artifact has been removed, though not entirely successfully (as reported by Gray (1994a)). The 843-MHz flux density is therefore likely to be under estimated and the resulting spectral index an upper limit.

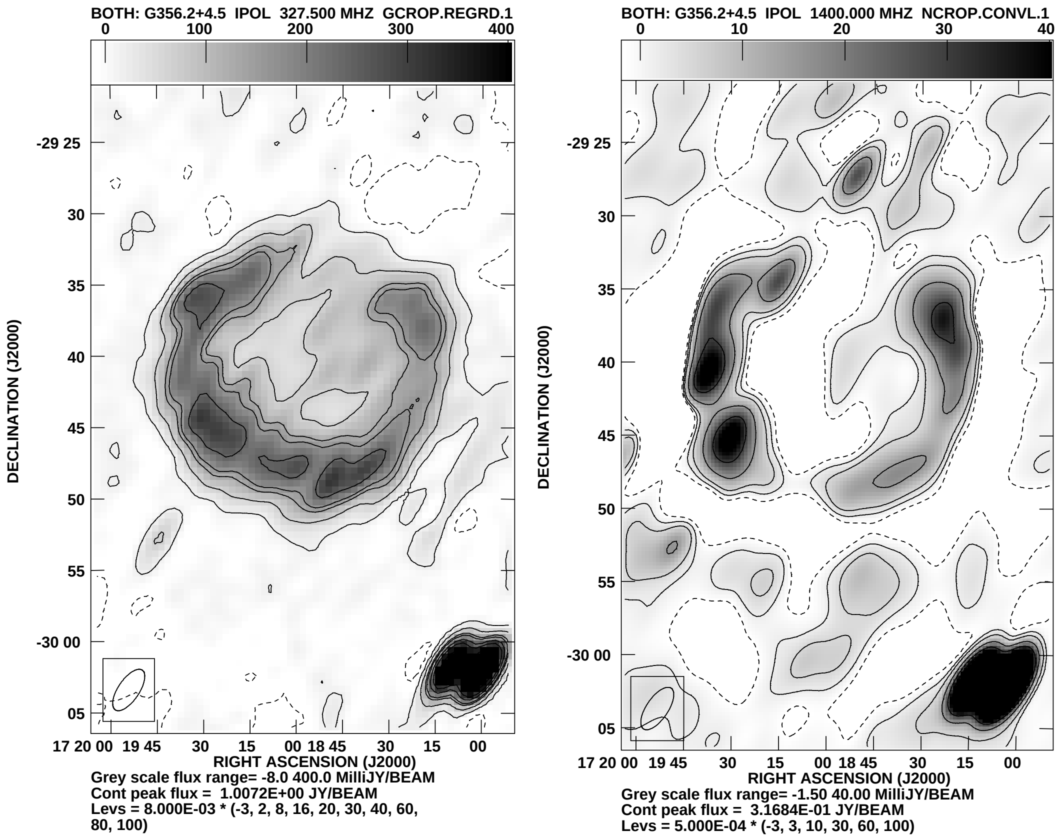

Figure 5.10: The GMRT image of G356.2+4.5 at 327 MHz is shown in the right panel and NVSS image at 1400 MHz in the left panel. The resolution in the GMRT image is $3' \times 1.5'$ along PA $-34°$ and the RMS noise in the map is 10 mJy/beam. The NVSS image has been smoothed to the resolution of the GMRT image and has a RMS noise of 0.5 mJy/beam.

5.2.6 G356.2$+$4.5

Fig. 5.10 shows the GMRT 327-MHz and NVSS 1400-MHz images of G356.2+4.5 where a well defined circular shell of emission of size $25'$ is evident. The co-ordinates of the center of the shell are $\mathrm{RA}_{J2000} = 17^{\mathrm{h}}18^{\mathrm{m}}58^{\mathrm{s}}$, $\mathrm{Dec}_{J2000} = -29°40'$. The RMS noise in the GMRT map is 10 mJy/beam. Low-level emission is seen projected against the central region. The NVSS image is shown in the right panel of Fig. 5.10. The SNR appears to be of shell-type morphology in both maps. The larger scale emission could be missing in the NVSS map due to poorer short spacing uv-coverage, plus the poorer overall uv-coverage of snap-shot observations.

There is significant variation in the brightness along the shell seen in both the 327- and 1400-MHz maps. Although there is a broad correlation between these variations at both frequencies, there are significant differences too. The gap in the emission seen to the south-east of the ring in the NVSS image is also seen in the PMN survey image (Duncan et al. 1997b). However it is filled with prominent emission in the 327-MHz GMRT image. These variations in the morphology could imply variations in the spectral index around the ring. The integrated flux density for this SNR at 327 MHz is 8.1 ± 1.7 Jy. The integrated flux density at 2.4 GHz was reported to be 3.0 ± 0.3 Jy and the value at 4.85 GHz from the PMN image was found to be 1.48 ± 0.13 Jy. This gives a spectral index of -0.66 ± 0.17 ($S \propto \nu^{\alpha}$). We did not use the total flux density from NVSS to determine the spectral index because of the missing emission in this image.

The presence of pulsar PSR B1717-29 in the field was noted by Duncan et al. (1997b). The Taylor et al. (1993) pulsar catalogue provides a characteristic age for this pulsar of 7.12×10^{6} yr and a dispersion measure of 42.6 ± 0.4 pc cm^{-3}. Using the Taylor & Cordes (1993) model for the electron density distribution in the Galaxy, the derived distance to the pulsar is 1.4 kpc, placing it just in front of the Sagittarius arm.

5.2.7 G358.0$+$3.8

Fig. 5.11 shows a $37' \times 39'$ region of emission, roughly circular in morphology with marginally brightened ring, whose emission closer to the plane, namely the south-eastern part is significantly brighter than on the opposite side. The morphology appears to be that of a shell-type SNR. Again there is broad correlation between the emission at 1400 and 327 MHz along the ring, though with significant detailed differences. Although the signal-to-noise ratio in both maps is low, there is good morphological correlation between the 327-MHz image and 4.85-GHz image from the PMN survey presented by Duncan et al.

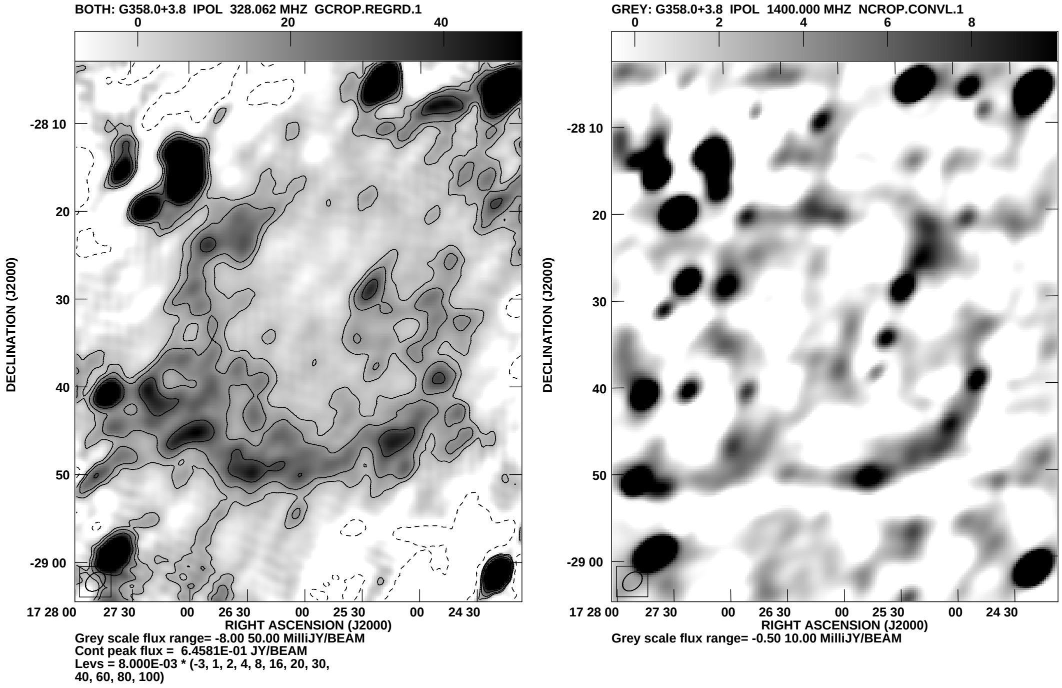

Figure 5.11: GMRT image of G358.0+3.8 at 327 MHz and NVSS image at 1400 MHz. The resolution in the GMRT image is $2.6' \times 1.8'$ along PA -48° and the RMS noise is 15 mJy/beam. The NVSS image has been smoothed to the resolution of the GMRT image and has a RMS noise of 0.5 mJy/beam.

at a comparable resolution. Brightening of the eastern arc is seen in both the images, while the rest of the ring is fainter. The integrated flux density at 2.4 GHz for this SNR was reported to be 2.4 ± 0.4 Jy, with a peak flux density of 400 mJy/beam. The value at 327 MHz is 2.5 ± 1.3 Jy and 0.79 ± 0.15 Jy at 4.85 GHz from the PMN image. Given the large angular size of this SNR, it is possible that some flux density may be missing in the GMRT image at 327 MHz. Duncan et al. (1997b) also noted that the 2.4-GHz emission might include a thermal component and therefore the flux densities at 2.4 and 4.85 GHz might be over estimated. Because of all these uncertainties, we did not compute the spectral index for this SNR. The co-ordinates of the center of the shell are ($\mathrm{RA}_{J2000} = 17^{\mathrm{h}}26^{\mathrm{m}}03^{\mathrm{s}}$, $\mathrm{Dec}_{J2000} = -28^\circ 36'$).

Note that the south-east protrusion seen in the GMRT image coincides with faint emission in the form of a smaller arc at the same location in the NVSS map, suggesting either the presence of another faint SNR in the field or a bi-annular morphology. Higher resolution, more sensitive mapping of this region is required to evaluate this possibility.

5.3 Continuum flux densities of known SNRs

With a $1^\circ.4$ field of view of GMRT at 327 MHz, there were other known SNRs in some of the fields. Many of them have been mapped at 327 MHz using the VLA, but there were some for which these GMRT images constitute the first 327 MHz images at a resolution of ~ 1 arcmin or less, with an, RMS noise of 3-15 mJy/beam. This section presents the results and discussion for these known SNRs.

5.3.1 G003.7$-$0.2

This is a classic barrel shaped SNR, first reported by Gray (1994a) where it was classified as a SNR based on the morphology alone. Gaensler (1999) mapped this at 1.4 GHz using the VLA in `CnD` and `BnC` array configurations and established the non-thermal nature of emission. This higher quality image at 1.4 GHz, and the 843 MHz image by Gray are in good agreement with the GMRT image at 327 MHz. The resolution in the GMRT image, shown in Fig. 5.12, is $20 \times 10\ \mathrm{arcsec}^2$, almost the same as that in the 1.4 GHz (Gaensler 1999). In all these images, this SNR satisfies the criterion used by Gaensler (1998) to classify it as a barrel shaped SNR. It has a clear ridge where there is practically no emission, even at the lowest frequency, which defines the axis of symmetry. It also has a clear point of maximum emission, almost perpendicular to the axis of symmetry.

The flux density in the GMRT 327-MHz image was found to be 4.5 ± 0.3 Jy. The flux density at 1.4 GHz is 1.7 ± 0.1 Jy and that at 843 MHz is 2.4 Jy, giving a spectral index of -0.66 ± 0.04. The spectral index listed in Greens catalogue (Green 2000)[2] is -0.65.

5.3.2 G355.9$-$2.5

This SNR, first identified by Clark et al. (1973) using 408 MHz and 5 GHz observations, is listed as a "distorted shell, brightest towards the south-east" in Green's catalogue (Green 2000) with a spectral index of -0.5 and a size of 13 arcmin. The flux density at 408 MHz (resolution of 3 arcmin) is reported to be 12.3 Jy while at 5 GHz (resolution of 4 arcmin) the value is 3.4 Jy. The highest resolution image made by Dubner et al. (1993) using VLA at 1.4 GHz confirms this general morphology. Polarization observations by these authors

[2]Available from http://www.mrao.cam.ac.uk.surveys/snrs on the web

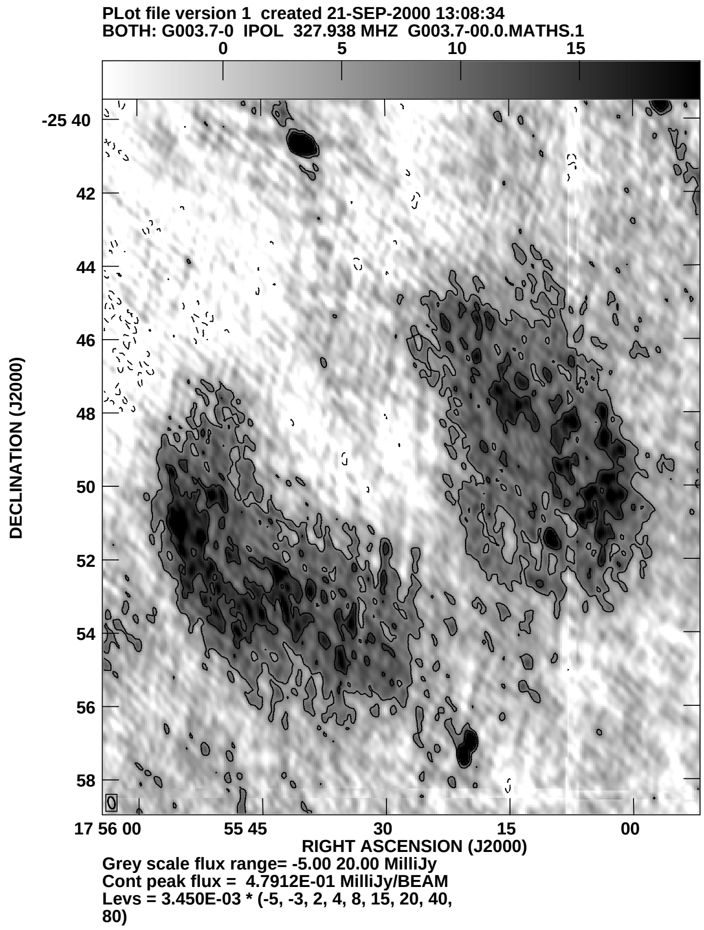

Figure 5.12: GMRT 327-MHz image of G003.7−0.2. The resolution in the image is $\sim 20 \times 10\,\mathrm{arcsec}^2$ and the RMS noise ~ 5 mJy/beam. The extended emission "breaks up" possibly due to a combination of uncorrected phase errors and the well known problem of deconvolution of extended sources using the CLEAN algorithm.

at 1465 MHz indicate significant linearly polarized intensity with a mean fractional polarization of 6% with the brightest region also most strongly polarized. Weaker emission, towards the east appears to complete the shell.

Gray (1994b) published a MEM deconvolved image at 843 MHz and measured a flux density of 6.5 Jy, a good 24% lower than expected from a source of spectral index of -0.5. The flux density of 5.0 Jy at 1465 MHz is also 21% lower than expected. The authors attribute this discrepancy to the missing extended flux in interferometric images.

The GMRT image at 332 MHz is shown in Fig. 5.3.2. In this pointing, this source lies at half power point of the primary beam. The smallest uv-spacing from which the visi-

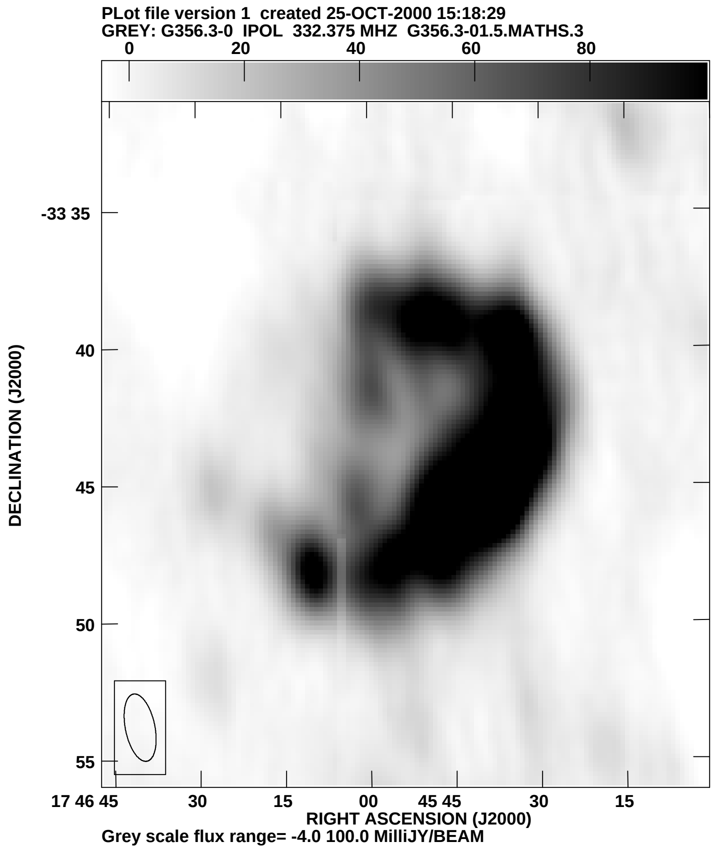

Figure 5.13: 327-MHz image of G355.9-2.5 using GMRT. The RMS noise in the image is about 10 mJy/beam and the resolution is $1.6' \times 0.8'$. This SNR lies on the very edge of the GMRT primary beam. The incomplete nature of the shell is apparent. However, there is an indication of weak emission in the east where the shell is incomplete. The vertical ridge passing through the middle is an artifact of combining different facets along the celestial sphere in a polyhedron imaging algorithm.

bility was reliably measured was about 90λ, corresponding to a largest angular scale of ~ 30 arcmin. The total angular size of this source is about 13 arcmin. Hence this source is not affected by the missing flux problem of interferometric images. A flux density of 14.2 ± 0.3 Jy was measured from the primary beam corrected image for this pointing, in close agreement with the expected flux density of 13.9 Jy at this frequency, corresponding to a spectral index of -0.5. The weak emission seen in the 1.4 GHz image is more clearly seen at 327 MHz and indeed there is a more complete shell than was seen at higher fre-

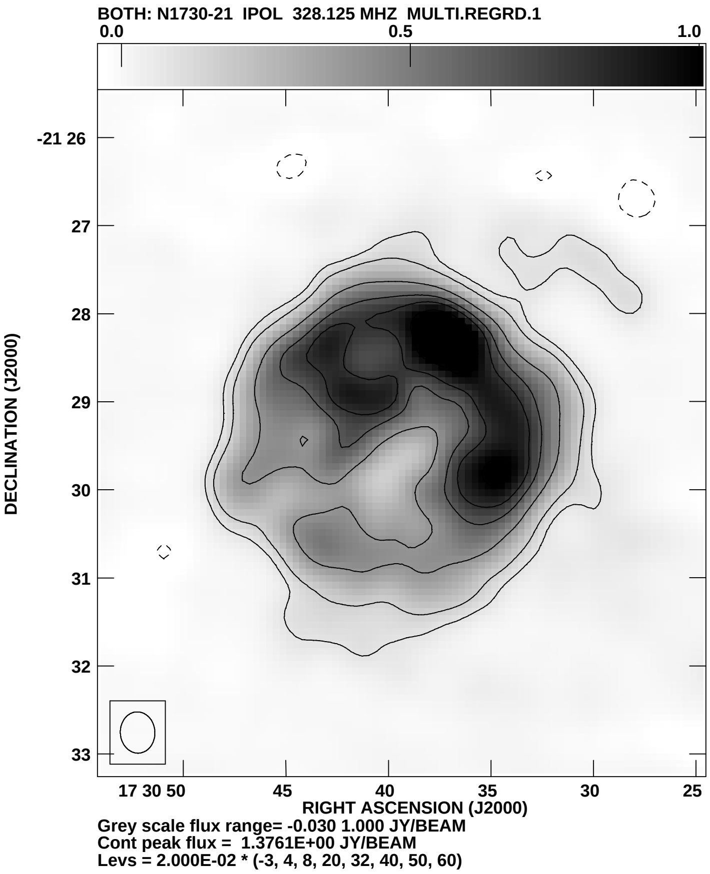

Figure 5.14: 327-MHz image of the Kepler's SNR (G004.5+6.8). The RMS noise in the image is about 25 mJy/beam and the resolution is 28×24 arcsec^2. The edge brightened morphology with the brighter norther rim (*away* from the Galactic plane) is clearly visible. The ridge running right across the SNR with small protrusions on either size is also clearly visible.

quencies.

The linear features noted by Gray in the 843-MHz image are also visible in this image. Although it is commented that these features are not seen in the 1465-MHz image (Dubner et al. 1993), they are clearly seen in the polarized intensity and although weak, can also be identified in the total intensity at this frequency. The spectral index of these features is probably then not very different from the rest of the source; there may be the usual filaments seen in many other SNRs.

5.3.3 Kepler's SNR (G004.5+6.8)

The field of G004.8+6.2 contains the well known shell-type Kepler's SNR of angular size 3 arcmin. A higher resolution image of this field was made, for the purpose of imaging this SNR at 327 MHz at the highest possible resolution. This higher resolution, primary beam corrected image is shown in Fig. 5.14. This is the only map known to me at 327 MHz at a resolution comparable to that at higher frequencies. The edge brightened shell towards the north is clearly visible. The morphology in this 327-MHz image is similar to that seen in the 1.4 and 5 GHz VLA images (Matsui et al. 1984). The distance to this SNR is estimated to be between 4.8 and 6.4 kpc from HI absorption and emission profiles (Reynoso & Goss 1999). The ridge running right across the SNR with small protrusions on both sides is also visible in the image. The integrated flux after primary beam correction is $\sim 38.4 \pm 0.5$ Jy. This SNR is also an X-ray source and Matsui et al. (1984), in a study of correlation between X-ray morphology and de-polarization between 1.4 and 5 GHz, have shown that there is a mixture of thermal and non-thermal gas associated with this SNR. High resolution imaging of other X-ray loud SNRs in radio and X-ray bands will be useful in determining if this is more generally true for other objects of this class.

5.4 Discussion

Observations of new candidate SNRs at 327 MHz, presented here, confirm these objects as SNRs on the basis of their morphology seen clearly at resolutions of $1'$ or less, as well as based on the non-thermal nature of emission and absence of thermal emission in the 60μm IRAS images. Only one of the objects (G004.2−0.0) is not detected at 327 MHz at the resolution required to decipher its morphology. There is also significant emission in the IRAS image at its location, implying the presence of thermal emission. At lower resolution, a 100-mJy, unresolved sources is detected, at the location of this object. The estimated flux density at 843 MHz is between 100 and 200 mJy. The existing radio flux densities and emission at IR band are therefore consistent with this source being a flat spectrum thermal source.

The morphology of some SNRs has long been suspected to be shaped by their interaction with nearby molecular clouds. Recently it has been argued that the OH (1720 MHz) emission is a good tracer of this interaction (Frail et al. 1994). The OH (1720 MHz) maser emission is distinguished from the OH maser emission at 1665, 1667 and 1612 MHz by the former being positionally and kinematically associated with SNRs while the latter are associated with HII regions. Both theoretical and observational evidence (Reach & Rho 1998, 1999; Frail & Mitchell 1998) suggest that the OH (1720 MHz) masers are associated with C-type shocks and are collisionally pumped in molecular clouds at temperatures and densities of $50 - 125$ K and $10^5 - 10^6$ cm^{-3} respectively (Lockett et al. 1999, and references therein). OH masers at 1665, 1667 and 1612 MHz cannot be produced under these physical conditions and the absence of these lines in observations which detect the OH (1720 MHz) line favors this interpretation. Measurements of the post shock density and temperature for IC443 (van Dishoeck et al. 1993), W28, W44 and 3C291 (Frail & Mitchell 1998) are in excellent agreement with these theoretical predictions. A solution to the problem of producing OH, which is not directly formed by shocks, is proposed by Wardle et al. (1999). They suggest that the molecular cloud is irradiated by X-rays produced by hot gas in the interior of the SNR. This leads to photo-dissociation of the H_2O molecules, which are produced by the shock wave in copious amounts, behind the C-type shock resulting into the required enhancement of OH just behind the C-type shock. The observed association of OH (1720 MHz) with X-ray-composite SNRs (i.e, SNRs with a shell-type radio morphology and a filled centre morphology in X-ray) and strong correlation between the morphology of the molecular gas and synchrotron emitting relativistic gas (Frail & Mitchell 1998) offers observational evidence for the hypothesis that the OH (1720 MHz) maser originates in post-shock gas, heated by the SNR shock passing through dense molecular cloud.

If the extended OH (1720 MHz) emission seen towards G001.4$-$0.1 (Yusef-Zadeh et al. 1999) is due to the SNR driving a C-type shock in a molecular cloud, one would expect the OH (1720 MHz) emission to be morphologically and kinematically associated with the general morphology of the radio continuum emission. The detection of a clear arc in the radio continuum image and the remarkable correlation with the OH (1720 MHz) emission towards this source is suggestive of such a model. If this association is true, the arc of emission is the boundary of the C-type shock driven in the molecular cloud by the SNR. The absence of any such cloud on the north eastern side of this SNR can explain the incomplete arc seen in the radio continuum as well as the OH (1720 MHz) emission. Also, the similarity of the radio morphology of this SNR, with G000.9$-$0.1, which is known to be a X-ray-composite SNR, further suggests that this SNR may also be of the X-ray-composite class. Interestingly, an X-ray source designated as `1RXS J175017.6-274646`, is detected in the ROSAT All-Sky Survey Faint Sources catalogue about 10 arcmin away. An alternative explanation for the correlation between the OH (1720 MHz) and radio continuum emission is that the maser emission is excited in the intervening material by the background emission of the SNR, having a similar origin as in the widespread OH (1720 MHz) emission in the Galactic plane (Haynes & Caswell 1977; Turner 1982). However, as pointed out by Yusef-Zadeh et al. (1999), the absence of any reported OH (1720 MHz) absorption line, the correlation of OH (1720 MHz) and radio continuum emission and the coincidence of the compact and extended OH (1720 MHz) emission argues against this alternative. Determination of the radio spectra of the shell and the central source and X-ray observations of this SNR would be future useful observations to determine the nature of this SNR.

G003.6−0.1, located about 8 arcmin west of G003.7−0.2 appears in the field of view of the GMRT 327-MHz observation as well as at 1.4 GHz VLA observations by Gaensler (1999). This source is detected in the 60μm IRAS image as well as at 2.7, 4.9 and 14.8 GHz and is discussed in greater detail in Chapter 6.

Barring G356.3-1.5, which appears to be barrel shaped, all others are shell-type SNRs. All these shells (and the rims for G356.3-1.5) are well resolved and show significant variations in the brightness along the shell. Caswell & Lerche (1979) proposed a correction to the $\Sigma - D$ relation (Clark & Caswell 1976; Case & Bhattacharya 1998, and references therein), by correcting for the variation in the ISM density away from the Galactic plane. They used the variation of the brightness across SNRs with respect to the Galactic plane to estimate the scale height of the ISM and derived the $\Sigma - D - z$ relation. In their sample, $\sim 25\%$ of SNRs show enhanced emission towards the Galactic plane which they attribute to the variation of the ISM density as a function of the distance from the Galactic plane. However, 5 of the 13 SNRs which did show asymmetry, were brighter *away* from the plane leaving the statistical significance of this result in serious doubt (Green 1984). Except for G355.9−2.5, G356.2+4.5 and G358.0+3.8, all the objects presented here, also show an enhancement in the brightness away from the Galactic plane ($\approx 30\%$) hinting that brightness variations across SNRs might be dominated more by local effects (interaction with the ISM, variations in the local ISM density, interaction with nearby molecular clouds, etc.) rather than a more global effect. It is also curious that in the current data set, all sources in the fourth quadrant of the Galaxy show an enhancement in the emission towards the plane. This new data plus higher resolution data for known SNRs which has now become available can be used to re-evaluate the $\Sigma - D - z$ relation. The current sample of SNRs for which higher resolution images better resolve the structure better is significantly larger than that available to Caswell & Lerche (1979).

With the exception of Cas-A and a handful of other remnants, few SNRs have reliably determined spatially resolved spectral index maps. A reliable continuum spectral index is an indirect measure of the relativistic electron energy spectrum. Simple Fermi shock acceleration theory predicts a spectral index of -0.5, consistent with many shell-type SNRs. However, this inconsistent with substantially higher values of the spectral index, reliably measured for only a few SNRs. Reynolds & Ellison (1992) successfully reproduced the observed radio spectra for Tycho's and Kepler's SNRs by invoking self-consistent, nonlinear shock model of first-order Fermi acceleration. Such models predict a slightly concave spectrum and can also estimate the mean magnetic field, if the precise shape of the lower frequency spectrum is known.

The GMRT covers the low frequency range between 100 MHz and 1 GHz in 4 bands at 150, 233, 327 and 610 MHz and can also be used to observe at 1060 MHz. With a resolution of ~ 20 arcsec at the lowest frequency to ~ 2 arcsec at the highest frequency, the GMRT can be used most effectively to determine the low frequency integrated spectra for most of the SNRs in the Galaxy and potentially remove the '?' (indicating that the quoted number is not reliable) from the quoted spectral indices in the SNR catalogue (Green 2000).

The GMRT frequency coverage is also well suited to the separation of sources of thermal and non-thermal emission. Emission from a typical Galactic thermal sources have a flat spectra above ~ 1 GHz. Below 1 GHz, the emission progressively decreases, with a typical spectral index of 2.0. The spectrum of a typical Galactic SNR has a negative spectral index (typically -0.5) above about 100 MHz and turns over below this frequency due to free-free absorption (see Fig. 5.15). The frequency range from 100 MHz to about 1 GHz is therefore very well suited to distinguish between thermal and non-thermal emission in the Galaxy. At the range of frequencies available at the GMRT, the distinction between the typical thermal and non-thermal spectra is most pronounced. With the high angular resolution provided by the GMRT, multi-frequency GMRT observations in the Galactic plane will easily distinguish between thermal and non-thermal sources as well as separate superimposed thermal and non-thermal components and help in identifying compact SNRs which may have been classified as thermal sources due to lack of resolution.

Measurement of a low frequency turnover below 100 MHz in the integrated spectrum of a sample of SNRs, due to free-free absorption, is a powerful probe of the distribution of low density ionized gas in the ISM, providing continuum optical depths towards various lines of sight in the Galaxy. It has been suggested that this same low density gas gives rise

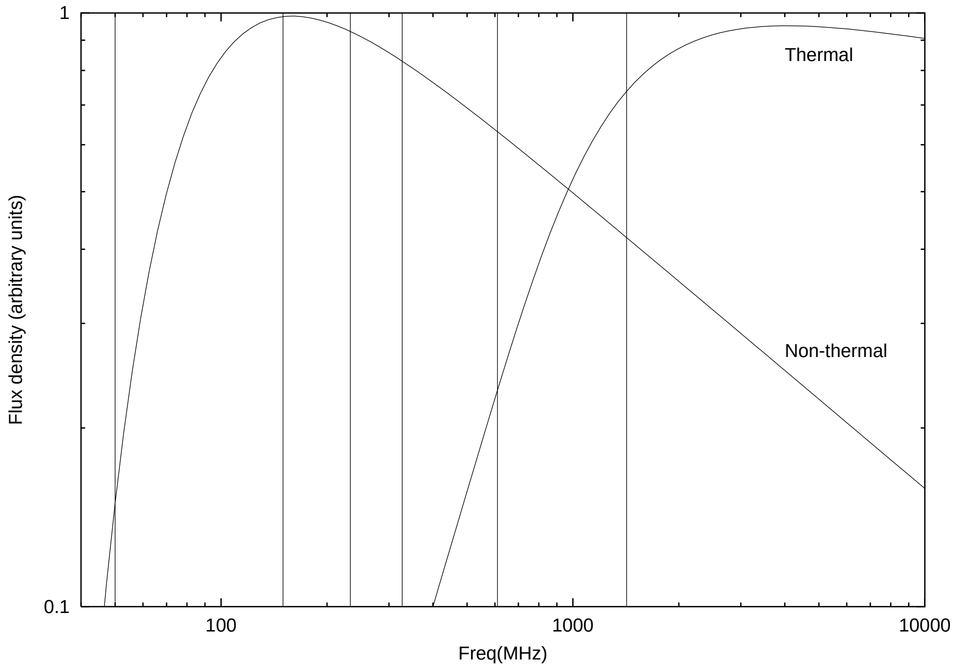

Figure 5.15: Comparison of typical spectra of Galactic SNRs and HII regions (thermal and non-thermal respectively). The first vertical line corresponds to 74 MHz (now available for observing with the VLA). Other vertical lines mark the GMRT frequency bands. GMRT covers the region of the spectra best suited for separating thermal and non-thermal sources in the Galaxy.

to low frequency RRLs which have been detected in almost every direction in the inner Galaxy (Kassim 1989). The detection of low frequency RRLs (Roshi & Anantharamaiah 2000) suggests (Anantharamaiah 1985b, 1986) that this same gas may be the low density extended HII envelope (EHEs) surrounding higher density HII regions. However, past low frequency observations have had insufficient resolution to study individual cases in sufficient detail to confirm this physical picture. The detection of spatially resolved continuum absorption against SNRs using the VLA at 74 MHz and using the GMRT and/or the VLA at 327 MHz for RRL observations will make significant advances in this area and resolve a long standing and important question.

A large number of known SNRs will be well resolved by the GMRT at all GMRT frequency bands. The spectral index of the radio emission changes across the SNR, giving information about the radiation and electron acceleration mechanism as well as about the interaction with the ISM. Apart from morphology, the difference in the spectral index between the Plerionic emission (filling the central portion of the SNR) and the emission from the shell is crucial in identifying filled-center or composite SNRs. Both the low frequency integrated spectral index as well as high resolution images of these SNRs, will be very useful for statistical studies of Galactic SNRs, as well as for the studies of the interaction of individual SNRs with the local ISM. For many of these SNRs, such observations will also be the first observations below 1 GHz and often the first observations below 2.4 GHz. The GMRT primary beam at 1420 MHz has a FWHM of 25 arcmin. Hence, SNRs of size ≤ 15 arcmin can be easily observed for HI absorption to estimate the kinematic distance using the Galactic rotation model.

Strictly speaking, spectral index maps can be reliably made only when the spatial frequency coverage at different frequencies is identical (or close to it). However, one can determine the average spectral index at different positions across the SNR via the "T-T plots" successfully used by Anderson & Rudnick (1993) to generate spectral index maps for G039.2−0.3 and G041.1−0.3. Essentially, the local gradient of the emission at two frequencies is used to measure the local (average) spectral index eliminating the error due to differing constant offset between images due to differing spatial frequency coverages. Such spectral index maps, although at a lower resolution, provide information needed to relate the observed spectral properties to the local dynamical situations in individual SNRs. Recently, Katz-Stone & Rudnick (1995) and others have used the technique of spectral tomography to study the spectral variations within the Tycho's SNR (Katz-Stone et al. 2000b).

All these observations can be done with the GMRT in the current state. This dissertation has extensively used the 327-MHz band and a RMS noise of about ≤ 10 mJy/beam has been regularly achieved. RMS noise of few mJy/beam has also been achieved at 1420-MHz band and 610 MHz bands. The imaging performance at 233 and 150 MHz is yet to be established with some careful data analysis. Therefore, as a future extension of this work, the above mentioned observations should be done with the GMRT.

Chapter 6

Other objects in the fields

With the GMRT field of view of $\sim 1^\circ.4$ at 327 MHz, maps of all the fields presented in this dissertation reveal a number of other compact as well extended objects. These objects include known HII regions, SNRs, background extragalactic objects and others which are not yet classified in any of these categories.

A list of compact sources from each of the fields along with their measured positions and 327-MHz flux densities is presented in this chapter. Where possible, flux densities at other frequencies have been used to determine the nature of these sources. The nature of other, unclassified source of extended emission seen in a few fields is then discussed, and suggestions for follow-up observations are made especially for Ultra compact HII (UC H II) regions.

6.1 Introduction

The Galactic longitude of all the observations presented in this dissertation were within $\pm 5^\circ$. The Galactic latitude of three out of the six independent pointings was within $\pm 0^\circ.2$, while the rest were at $> \pm 1^\circ$. Most of the emission from the Galactic plane at radio comes from many sources - (1) normal HII regions (Wink et al. 1982; Lockman 1989), (2) bright Ultra compact H II (UC H II) regions with a lower surface brightness extended emission (Wood & Churchwell 1989b; Kurtz et al. 1994), (3) compact HII regions with no detectable extended emission (Wink et al. 1983; Kuchar & Clark 1997), (4) SNRs (Green 2000), (5) background sources seen through the Galactic disk, and (6) the large scale Galactic background emission (Haslam et al. 1982). The $\sim 1^\circ.4$ field of view of GMRT observations at 327 MHz therefore reveal a number of compact as well as a few extended sources of emission.

The physical mechanism for the radio emission from HII regions and SNRs is, however, quite different. Radio emission from HII regions is due to the interaction between electrons and ions. The resulting thermal spectrum is almost flat (with a spectral index of ~ 0.1) at frequencies typically greater than ~ 1 GHz and turns over below this frequency due to free-free absorption by the intervening material. High resolution imaging of many compact HII regions reveal a halo surrounding a compact core (Wood & Churchwell 1989b). Detailed models of HII regions which include such temperature gradients and departure from LTE have been developed (Wilson & Jaeger 1987). However, these models have been applied only to objects where resolved images at a number of frequencies are available. High resolution multi frequency observations of HII regions, particularly of a larger sample of compact HII regions, will test these models more rigorously and provide improved estimates of the physical parameters. Most HII regions are also sources of radio recombination line (RRL) emission which has been detected at high radio frequencies (Caswell & Haynes 1987; Lockman 1989). Detection of high frequency RRL emission is one of the signatures used to identify H II regions. Emission from SNRs on the other hand is synchrotron radiation from free electrons accelerated to relativistic energies in the supernova shock front or due to the transfer of rotation energy from the neutron star, to the surrounding medium. The magnetic field in which the electrons move is also amplified. The spectral index is typically negative with no associated thermal or RRL emission.

The measured flux densities of all sources detected at 327 MHz, along with the 1420-MHz flux densities from NVSS images, are listed here. Two objects, namely G004.4+0.1 and G003.7−0.1, both catalogued as HII regions, reveal the core-halo morphology in the GMRT image and these GMRT observations constitute the first resolved low frequency images of these, possibly compact or UC H II regions.

6.2 Point sources in the fields

Tables 6.1 to 6.5 presents a list of point source flux densities at 327 MHz from the GMRT observations and 1420-MHz flux densities from the NVSS images. Reliable flux densities for point sources in the field of G001.4+0.0 were not available at either of these frequencies because of higher noise and poor image quality due to proximity to the Galactic centre. Also, no compact sources was detected in the field of G004.2−0.0. Data from IRAS and other RRL surveys have been used by Becker et al. (1994) to classify the compact

Table 6.1: List of point sources and their 327- and 1400-MHz flux densities in the field of G003.7−0.1

Name	RA$_{J2000}$ ($h\ m\ s$)	Dec$_{J2000}$ ($^{\circ}\ '\ ''$)	S_{327} (mJy)	S_{1400} (mJy)
1756-2549	17 56 41.4	-25 49 10.9	99.5 ± 10	26.9 ± 1
1756-2542	17 56 38.1	-25 42 15.0	221.8 ± 10	70.7 ± 1
1755-2540	17 55 39.2	-25 40 44.0	207.9 ± 10	50.0 ± 1
1755-2535	17 55 22.3	-25 35 44.0	232.1 ± 10	6.0 ± 1
1755-2537	17 55 08.4	-25 37 24.0	108.1 ± 10	148.4 ± 1
1754-2539	17 54 56.3	-25 39 31.8	< 10	17.2 ± 1
1755-2543	17 55 10.2	-25 43 59.9	< 10	79.6 ± 1
1754-2534	17 54 39.4	-25 34 43.4	192.2 ± 10	31.2 ± 1
1754-2536	17 54 27.6	-25 36 23.2	177.7 ± 10	13.2 ± 1
1754-2540	17 54 10.7	-25 40 22.7	< 10	44.3 ± 1
1754-2544	17 54 10.4	-25 44 06.6	< 10	44.3 ± 1
1754-2556	17 54 46.4	-25 56 03.6	< 10	21.9 ± 1
1755-2557	17 55 19.9	-25 57 20.0	114.7 ± 20	16.1 ± 1
1755-2556	17 55 19.0	-25 56 56.0	78.1 ± 20	21.7 ± 1
1755-2551	17 55 09.6	-25 51 27.9	100.5 ± 30	11.4 ± 1
1755-2549	17 55 40.4	-25 49 52.0	< 10	11.6 ± 1
1754-2609	17 54 38.9	-26 13 47.5	183.3 ± 10	47.0 ± 1
1754-2609	17 54 36.4	-26 13 26.5	44.8 ± 10	47.0 ± 1

Table 6.2: List of point sources and their 327- and 1400-MHz flux densities in the field of G004.8+6.2

Name	RA$_{J2000}$ ($h\ m\ s$)	Dec$_{J2000}$ ($^{\circ}\ '\ ''$)	S_{327} (mJy)	S_{1400} (mJy)
1732-21	17 32 53.7	-21 24 43.3	416 ± 60	22.7 ± 0.7
1732-22	17 32 19.4	-22 06 43.8	530 ± 50	274.0 ± 0.7
1734-21	17 34 04.0	-21 46 25.8	1120 ± 65	100.2 ± 1
1733-21	17 33 56.2	-21 42 41.3	716 ± 70	66.5 ± 0.7

Table 6.3: List of point sources and their 327- and 1400-MHz flux densities in the field of G356.2+4.5

Name	RA_{J2000} ($h\ m\ s$)	Dec_{J2000} ($^\circ\ '\ ''$)	S_{327} (mJy)	S_{1400} (mJy)
1715-29	17 15 04.7	-29 12 21.1	194.0 ± 20	297.1 ± 2
1716-29	17 16 11.6	-29 20 01.6	274.8 ± 20	242.5 ± 2
1715-29	17 15 14.3	-29 43 17.1	213.8 ± 20	157.1 ± 2
1715-29	17 16 52.5	-29 48 59.4	373.9 ± 20	124.5 ± 2
1757-30	17 17 57.6	-30 00 43.17	1053.9 ± 20	315.6 ± 2
1757-30	17 18 12.6	-30 01 43.97	812.5 ± 20	183.1 ± 2
1719-29	17 19 46.4	-29 52 49.1	91.6 ± 20	17.7 ± 2
1721-29	17 21 43.5	-29 35 16.9	294.0 ± 20	127.9 ± 2

sources as HII regions, UC H II regions and Planetary Nebula. These surveys, however, are confined to $|b| < 0^\circ.4$ and only two fields used in this dissertation, namely G003.7−0.2 and G001.4−0.1, overlap with these surveys. For these fields, additional data at 5 GHz from the Galactic plane surveys by Helfand et al. (1992); Becker et al. (1994) was also used.

The barrel-type SNR G003.7−0.2 (field of Table 6.1) was mapped by Gaensler (1999) at L-band using the VLA (`CnB` and `DnC` configurations with the smallest spacing of $\sim 0.12k\lambda$). This image was available from Astronomy Digital Image Library (ADIL)[1]. After correcting for the primary beam attenuation, it was used to obtain the 1420-MHz flux densities of compact sources in this field. The flux densities of compact sources measured from this image are listed in Table 6.1.

Most of the compact sources detected at 327 MHz show a negative spectral index, indicative of non-thermal nature of emission from these sources. A few compact sources detected at 1420 MHz are not detected at 327 MHz to a limit of $10 - 30$ mJy (the RMS noise in the images). These could be Galactic thermal sources or extragalactic sources with absorption due to the intervening Galactic ISM. Most of these sources are also weak and even if they have a flat spectrum till 327 MHz, they are below the detection limit of the 327 MHz observations.

[1] `http://adil.ncsa.uiuc.edu/`

Table 6.4: List of point sources and their 327- and 1400-MHz flux densities in the field of G356.2−1.5

Name	RA_{J2000} ($h\ m\ s$)	Dec_{J2000} ($^\circ\ '\ ''$)	S_{327} (mJy)	S_{1400} (mJy)
1740-3228	17 40 53.6	-32 28 13.9	177.9 ± 15	26.4 ± 5
1740-3334	17 40 56.3	-33 34 44.8	131.6 ± 15	51.3 ± 2
1741-3141	17 41 54.1	-32 41 30.1	140.6 ± 15	35.6 ± 5
1741-3227	17 41 38.7	-32 27 29.9	263.9 ± 15	38.3 ± 5
1741-3245	17 41 38.6	-32 45 30.0	92.4 ± 15	29.6 ± 5
1741-3314	17 41 31.3	-33 14 00.0	119.1 ± 15	32.1 ± 5
1742-3313	17 42 49.0	-33 13 44.8	219.6 ± 20	57.1 ± 5
1742-3222	17 42 27.2	-32 22 14.9	631.6 ± 33	191.4 ± 5
1742-3333	17 42 32.4	-33 33 30.4	71.8 ± 15	19.8 ± 2
1743-3309	17 43 04.5	-33 09 59.0	606.5 ± 20	173.7 ± 5
1743-3313	17 43 05.8	-33 13 14.3	77.6 ± 20	33.1 ± 5
1744-3251	17 44 22.4	-32 51 19.3	106.8 ± 15	37.3 ± 2
1746-3259	17 46 18.8	-32 59 44.0	487.3 ± 15	120.5 ± 2
1740-3251	17 40 26.9	-32 51 02.7	103.4 ± 15	48.6 ± 2
1748-3241	17 48 31.1	-32 41 00.8	1211.0 ± 15	412.5 ± 2
1743-3238	17 43 06.6	-32 38 06.4	91.1 ± 15	10.2 ± 2
1742-3241	17 42 26.9	-32 41 00.7	293.6 ± 15	243.0 ± 2

Table 6.5: List of point sources and their 327- and 1400-MHz flux densities in the field of G358.3+3.8

Name	RA_{J2000} ($h\ m\ s$)	Dec_{J2000} ($^\circ\ '\ ''$)	S_{327} (mJy)	S_{1400} (mJy)
1728-28	17 28 28.9	-28 46 03.5	1605.4 ± 25	567.2 ± 3
1727-28	17 27 01.9	-28 15 55.5	87.4 ± 25	104.5 ± 3
1725-28	17 25 20.3	-28 05 19.8	386.4 ± 25	130.2 ± 3
1724-28	17 24 17.7	-28 06 05.6	812.1 ± 25	167.2 ± 3
1724-29	17 24 19.5	-29 01 05.8	244.9 ± 25	125.4 ± 3
1727-28	17 27 39.8	-28 59 06.2	299.5 ± 25	117.1 ± 3
1727-28	17 27 42.3	-28 40 42.1	154.8 ± 25	34.7 ± 3
1727-28	17 27 22.9	-28 19 42.9	153.9 ± 25	98.5 ± 3
1727-28	17 27 34.6	-28 15 18.4	114.2 ± 25	53.7 ± 3

6.3 Extended sources

6.3.1 G003.6-0.11

This source, seen just west of G003.7−0.2 in the 1428 MHz image by Gaensler (1999), is also detected as a resolved source at 327 MHz. The GMRT 327-MHz image and the VLA 1428-MHz images of this sources are shown in Fig. 6.1. The resolution in the 327- and 1428-MHz images is $\approx 20 \times 11$ arcsec^2 and 15×9 arcsec^2 respectively. This source was also observed by Yusef-Zadeh (private communications) using the VLA in the D-array configuration at 4.9 GHz. We therefore mapped this source at 4.9 GHz using the data acquired from the VLA achieves (Fig. 6.2). The size of this source is $\sim 1'$ with the centre located at $\mathrm{RA}_{J2000} = 17^h54^m32^s$, $\mathrm{Dec}_{J2000} = -25^\circ51'30''$. There is significant emission in the IRAS 60μm image peaking at $\mathrm{RA}_{J2000} = 17^h54^m32^s$, $\mathrm{Dec}_{J2000} = -25^\circ50'33''$ (Fig. 6.2).

Radio Recombination Lines (RRLs) have been detected towards $\mathrm{RA}_{J2000} = 17^h54^m30^s$, $\mathrm{Dec}_{J2000} = -25^\circ51'23''$ near 5 GHz (H109α and H110α lines) by Caswell & Haynes (1987) using the Parkes 64-m single dish with a HPBW of $\approx 4'$ and by Lockman (1989) at 3 cm with a HPBW of $\approx 3'$. The RRL parameters reported by Caswell & Haynes (1987) are: $T_l/T_c = 0.05/0.7$, $\theta = 2'$, $\Delta V = 28$ km sec^{-1}, $V = 3$ km sec^{-1}, $T_e = 5600$ K, $D = 1.5$ or 15.5 kpc (assuming the standard IAU parameters (Kerr & Lynden-Bell 1986) for solar orbital velocity $\theta_\circ = 220$ km sec^{-1} and distance to the Galactic Centre $R_G = 8.5$ kpc).

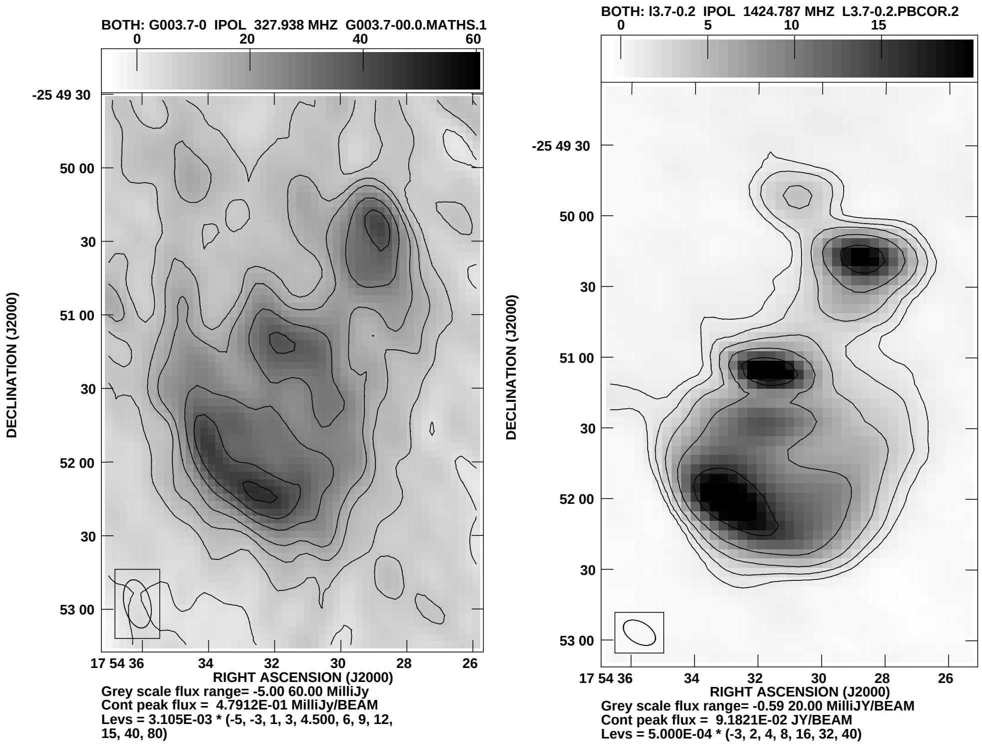

Figure 6.1: The left panel shows the GMRT 327-MHz image of G003.6−0.1. The resolution in this image is $\sim 15 \times 20\ \mathrm{arcsec}^2$ and the RMS noise of ~ 5 mJy. The VLA image at 1428 MHz (Gaensler 1999) is shown in the right panel. Resolution in this image is about $15 \times 9\ \mathrm{arcmin}^2$. The shell type structure of this object is clearly seen in this image. The general morphology is same as that seen in the 327-MHz GMRT image and the source in the north-west is also resolved as a separate compact source.

However, since the Galactic longitude is small, the measured radial velocity could entirely come from non-circular motion which makes the distance estimates unreliable and must be treated as a nominal distance. No optical counterpart is detected implying that a distance of 15.5 kpc is more likely. The surveys by Downes et al. (1980) and Wink et al. (1983) for H76α and H110α transitions respectively do not detect any RRL towards G003.7−0.1 due to the sensitivity limits of the surveys ($S_{4.9GHz} > 1$ Jy and $S_{14.7GHz} > 2$ Jy respectively). This source is listed as a HII region in the continuum survey done by Wink et al. (1982) at 14.8 and 4.9 GHz (HPBW=$2'.6$) and is also listed in the list of compact sources from the 11 cm Galactic plane survey by Fürst et al. (1990). The PMN source `PMN J1754-2551` at $\mathrm{RA}_{J2000} = 17^h 54^m 31^s$, $\mathrm{Dec}_{J2000} = -25^\circ 51' 02''$ covers all the components of

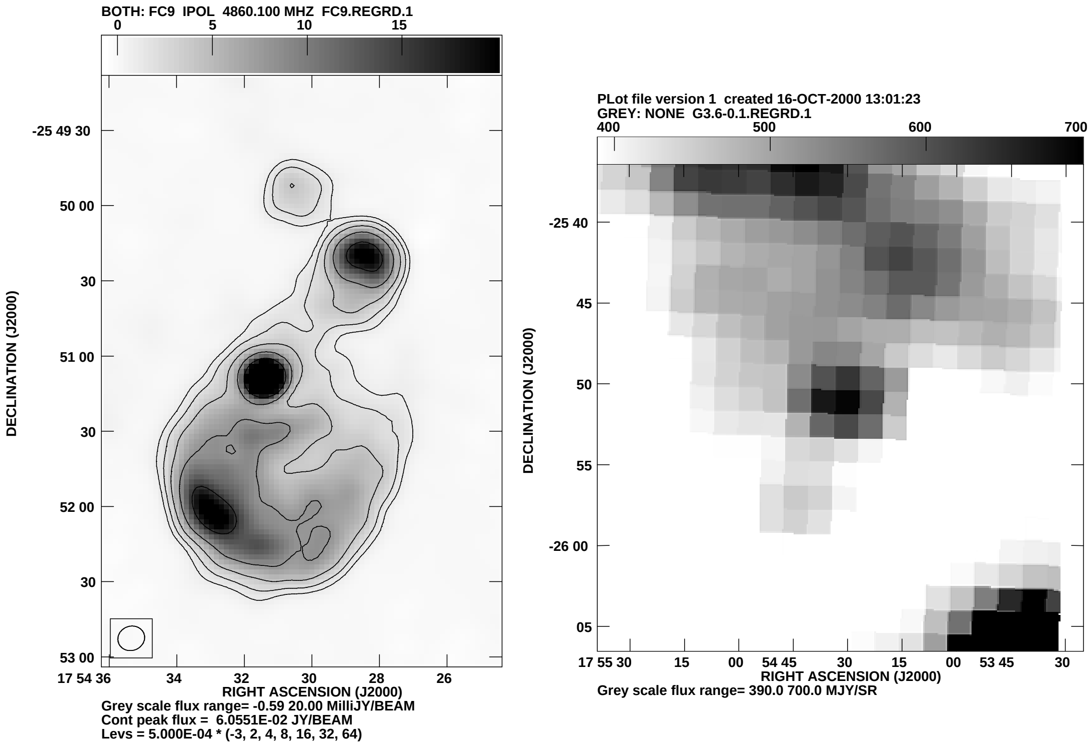

Figure 6.2: The VLA 4.8-GHz image of G003.6−0.1 using the data acquired by Yusef-Zadeh in Feb. 1987 is shown in the left panel. The resolution in this image is $\sim 11 \times 10\mathrm{arcmin}^2$, P.A.=$-70^\circ$. The general morphology of a compact core at the south-eastern edge of the lower surface brightness shell is clearly visible. The right panel shows the IRAS 60 μm image of this region. The peak in this image occurs at $\mathrm{RA}_{J2000} = 17^h54^m32^s$, $\mathrm{Dec}_{J2000} = -25^\circ50'33''$. With the coarse resolution of IRAS, this peak covers the entire radio source.

this source (Griffith et al. 1994).

A circular shell of emssion with a peak of emssion along the southern edge of the shell along with two compact sources in the north is visibile in the 327-, 1428- and 4850-MHz images. For further discussion of the nature of this source, we label the peak of emission in the south-eastern part of the shell as `A`, the shell itself as `B`, the compact source on the northern rim of the shell as `C` and the moderately resolved northern most source as `D`. There is an indication of a connecting bridge of emission between `C` and `D` in all the three images. The disctinct semi circular gap around `C`, followed by a concentric arc seen in both the 5 and 1.4 GHz images is suggestive of an interaction between `A` and `B/C`. HI

Table 6.6: Peak flux densities for the components A, C and D for G003.6−0.1 at 0.327, 1.4 and 4.8 GHz.

Component	S_{327MHz} (mJy)	$S_{1.4GHz}$ (mJy)	$S_{4.8GHz}$ (mJy)
A	48.2	32.5	33.5
C	38.6	24.8	46.1
D	42.5	22.4	26.2

absorption spectra was measured using the GMRT towards A, C and D (Fig. 6.3). The HI absorption spectra for A and C is very similar, implying that they are at a similar kinematic distance. The extra -27 km sec^{-1} feature in the spectra of D implies that this component is farther away compared to A and C. Kinematic distance of D corresponds to > 20 kpc and could also be extragalactic. The V_{LSR} of 3 km sec^{-1} for the RRL and the $+30$ km sec^{-1} feature seen in the spectra of all the three components implies that the line of sight absorber at a velocity of $+30$ km sec^{-1} is not associated with the RRL emitter. This absorber corresponds to a kinematic distance between 6 and 12 kpc. Assuming that the RRL is associated with extended nebula and the component A, a distance of 15.5 kpc is then consistent with the RRL and HI absorption velocities. The absence of the -27 km sec^{-1} feature in the spectra of A and C places these components in front of the component D and consequently the component D at > 20 kpc.

However, HI absorption at negative velocities are observed in the first quadrant of the inner Galaxy, possibly from clouds in the Galactic Centre region. If the observed RRL is not associated with the nebula or any of the components, and the -27 km sec^{-1} feature is due to line of sight clouds with anomalous chaotic motions (Shaver et al. 1982; Belfort & Crovisier 1984), the HI absorption profiles are consistent with components A and C at a distance between R_G and 6 kpc, while D at a distance $> R_G$. This ambiguity can be resolved with a high resolution RRL observation towards this direction to identify the RRL emitter.

The peak flux densities of the components A,C and D were measured from the 0.327, 1.4 and 4.8 GHz maps after convolving them to same resolution. The measured peak flux densities are listed in Table 6.3.1 and plotted in Fig. 6.4. Emission from the nebula itself is indicative of non-thermal emission. At 327 MHz, C does not appear to be distinct from the shell and the flux density at this frequency may be contaminated by that due to the

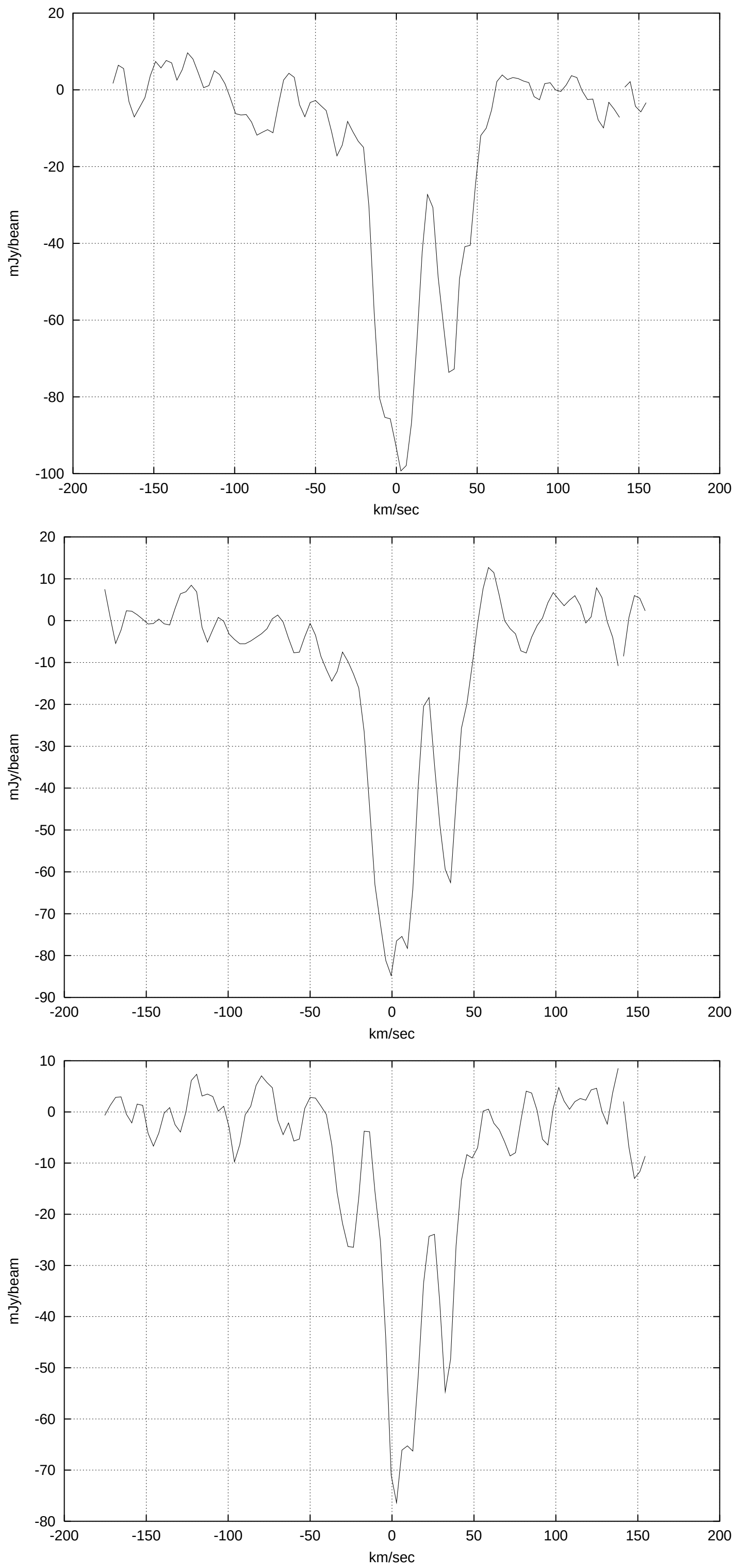

Figure 6.3: HI absorption profiles against the components `A`, `C` and `D` of G003.6−0.1 respectively, measured using the GMRT.

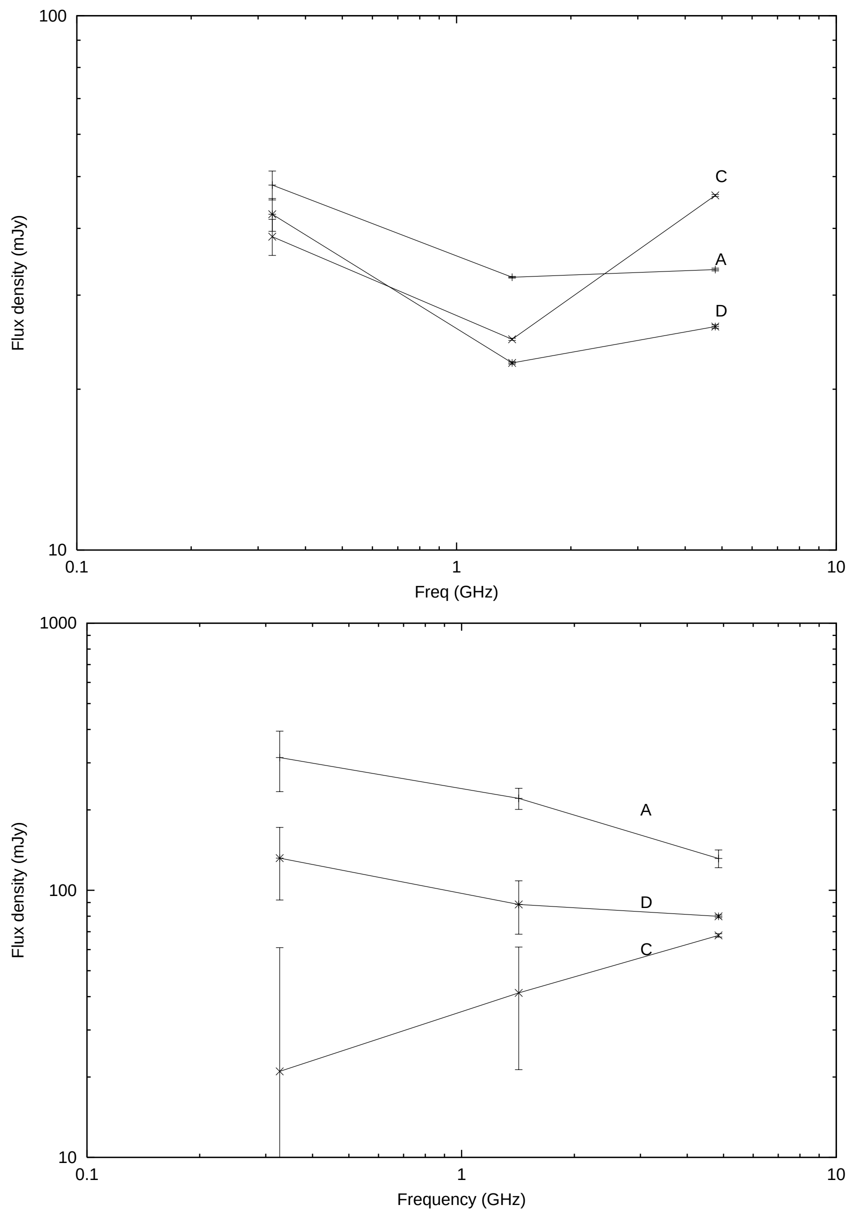

Figure 6.4: Continuum spectra of the components `A, C` and `D` of G003.6−0.1. Top panel shows the peak flux density spectra. The spectral index of component `C` between 1.4 and 4.8 GHz is ~ 0.5 while that of components `A` and `D` are 0.0 and 0.1 respectively. Bottom panel shows the integrated flux density spectra for the three components with the average 327-MHz flux density in the vicinity subtracted for the components `D` and `C` which are not distinctly detected as separate sources at 327 MHz.

shell itself. The 327-MHz flux density of `D` too may thus be contaminated. Subtracting the average flux density measured around these components may give an estimate of the 327-MHz flux density of these components. The bottom panel of Fig. 6.4 shows the integrated flux density spectra of the three components, with the average 327-MHz flux density in the vicinity of components C and D subtracted. A and D in this plot show non-thermal spectra. The spectrum of C is consistent with spectral index of ~ 0.5 between 327 MHz and 4.8 GHz. The spectral indices thus determined, however, must be treated as only tentative. Observations at other frequencies between 327 and 1400 MHz (e.g. 610 MHz) will help in clarifying the spectra and the nature of these components. The peak flux spectral index between 4.8 and 1.4 GHz ($\alpha_{1.4}^{4.8}$) for the components A, C and D was measured to be 0.0, 0.5 and 0.1 respectively while the spectral index between 1.4 and 0.327 GHz ($\alpha_{0.327}^{1.4}$) was measured to be -0.3, -0.3 and -0.5 respectively.

Could it be that the 327-MHz flux density is over-estimated and the true value is less than the value at 1428-MHz, as expected from a source of thermal emission? For this to happen, the 327-MHz flux density must be over estimated by a factor of about $\sim 2-3$, which is very unlikely. Another way the flux density can be over estimated is due to a slowly varying background emission. The average flux density in an approximately $1'$ box around this source is ≈ 0.15 Jy, comparable to the error bar of 0.1 Jy for the measured flux density. Hence, this also cannot account for an over estimated flux density. To further eliminate the possibility of a systematic flux density calibration error, we compared the flux densities of the VLA calibrator in the field located at $Dec_{J2000} = 17^h 51^m 52^s$, $RA_{J2000} = -27°24'01.33''$ and the SNR G003.7−0.2. Unfortunately, this VLA calibrator is not a good P-band calibrator and hence the VLA 327-MHz flux density is not known. However, it is listed in the Texas catalogue, and at 365 MHz, its flux density is 1.41 ± 0.09 Jy corresponding to 1.14 ± 0.09 Jy at 327 MHz (spectral index of 1.8 ± 0.7). The measured flux density from the GMRT primary beam corrected image is 1.3 ± 0.2 Jy. The flux density measured for G003.7−0.2 (see section 5.3.1) was also found to be in good agreement with the extrapolated value at 327 MHz.

We now suggest a model for the compact source C. The class of symbiotic stars is defined by the basic characteristic of an optical spectrum containing both high excitation emission lines and absorption features of a cool, late-type star (Seaquist & Taylor 1990). While most of these stars emit radiation at IR wave bands, few of these stars are also detected at radio frequencies. High frequency (GHz range) spectral index is invariably positive, ranging from 0 to 1.2 and the emission mechanism is thermal bremsstrahlung. This range of spectral indices can be explained by a simple binary model, where, the wind in the form of uniform mass loss from a cool star is ionized by a hotter companion star (Taylor & Seaquist 1984). This model predicts a lower limit of 0.6 and an upper limit of 1.3 for the spectral index, depending upon the viewing angle of the binary system, the mass loss rate from the cooler star and the ionizing photon flux from the hotter star. Some fraction of the emission, however, might be optically thin and an observed optically thick spectral index lower than 0.6 may be consistent with the binary model. The radio spectra of most of these stars, above a few GHz, turn over to a relatively flat spectral index of ~ 0.1. A radio survey of such stars in the Galaxy done by Seaquist et al. (1984) found a mean spectral index of $+0.6$ and a cut off at 1.2, in excellent agreement with the binary model.

The high frequency spectral index ($\alpha_{1.4}^{4.8}$) of component C is therefore consistent with it being such a radio loud symbiotic star. The binary-model for such objects relates the turn-over frequency and the optically thick spectral index to the physical properties, namely the mass-loss rate and the hydrogen ionizing photons flux. The present high frequency data on this source probably samples only the optically thick part of the spectrum. Continuum observations a few higher frequencies will be required to determine the true nature of this source.

About 20% of the UC H II regions mapped in the incomplete survey of Wood & Churchwell (1989b) and Kurtz et al. (1994) where of the cometary morphology. A typical example of this morphology is G034.2−0.2. van Buren et al. (1990) proposed a model of a bow shock created by a wind-blowing massive star moving supersonically through a molecular cloud. The required velocities of less than $\sim\ 10$ km sec^{-1} are comparable to the observed velocity dispersion of stars in OB associations. The gross structure seen in the radio continuum and the velocity structure in the hydrogen recombination and molecular lines is well explained by this model. Their model also make specific predictions about the OH maser spots in the leading edge of the shock as well as detectable proper motion of maser sources over a time scale of few years for the nearby UC H II region.

The higher frequency spectra of component A is flatter, typical of HII regions. The morphology of the nebula associated with the component A, as seen in the images at 1.4 and 4.8 GHz is suggestive of a cometary UC H II region. A typical UC H II region has a size of < 0.1 pc, $n_e > 10^4 \mathrm{cm}^{-3}$, and EM$> 10^7 \mathrm{pc\,cm}^{-6}$. The linear sizes of the nebula corresponding to the distances of 18.5 and 7 kpc is ~ 1.5 and ~ 5 pc respectively. Clearly, the size of the nebula in this field is much greater than the size of typical UC H II region. However, the extended emission seen towards this source could then have the same origin as the extended emission seen associated with UC H II regions in recent observations at 1.4

and 5 GHz (Kurtz et al. 1999; Kim & Koo 2001). EM for this sources, assuming $T_e = 5600$K as derived from the RRL observations, is also smaller than the typical value for UC H II region. However, the T_e estimates from the existing low resolution RRL observations may be underestimated.

The morphology in the 327-MHz image of this sources is markedly different from that at 1.4 and 4.8 GHz. The brightness contrast between the component `C` and the extended emission associated with the nebula is negligible. The structure of the nebula itself is replaced by two arcs of emission of comparable brightness. The flux density of all the three components at 327 MHz are higher than the values at higher frequencies, which is inconsistent with a purely thermal emission. The 327-MHz data is therefore suggestive of a foreground source of non-thermal emission. The spectra of `A` (Fig. 6.4) between 327 MHz and 4.8 GHz is also non-thermal with a spectral index of $\sim\ -0.4$. The spectral index, which is typical of shell-type SNRs, and the morphology seen in the 327-MHz image are consistent with the extended emission being a new SNR. High resolution observations at 233 and 610 MHz with the GMRT, along with higher resolution imaging with the VLA at higher frequencies will help in resolving the nature of the shell. A conclusive evidence of non-thermal emission could come from the detection of polarized radio emission.

6.3.2 Linear structure in the field of G356.3$-$1.5

The linear structure seen $\sim 30'$ north-east of the barrel shaped SNR G356.3$-$1.5 in the low resolution image is also clearly visible in the the high resolution image. The sub-image of this structure is shown in Fig. 6.5. The compact unresolved sources (at the ends of the linear structures) are also present in the NVSS image of this region. However, the linear structure is not detected in the NVSS image at 1420 MHz, probably due to the sensitivity and dynamic range limits (due to snapshot uv-coverage) of the NVSS in this region. Its detection in the GMRT 327-MHz image at the level of $5-7$ mJy/beam, compared to its non detection in the NVSS image, is indicative of non-thermal emission. To eliminate the possibility of this feature being an artifact of data processing or due to the presence of bad data, this data was mapped at low and high resolution. Maps were also made using a single frequency channels as well as using a number of RFI free frequency channels. The low resolution map was made using only the GMRT *Central Square* antennas at a resolution of $3-4$ arcmin which does not require 3D imaging. The high resolution map used all the available arm antennas and required 3D imaging. Multiple frequency channels were used in two ways. Five adjacent frequency channels were averaged and four of these av-

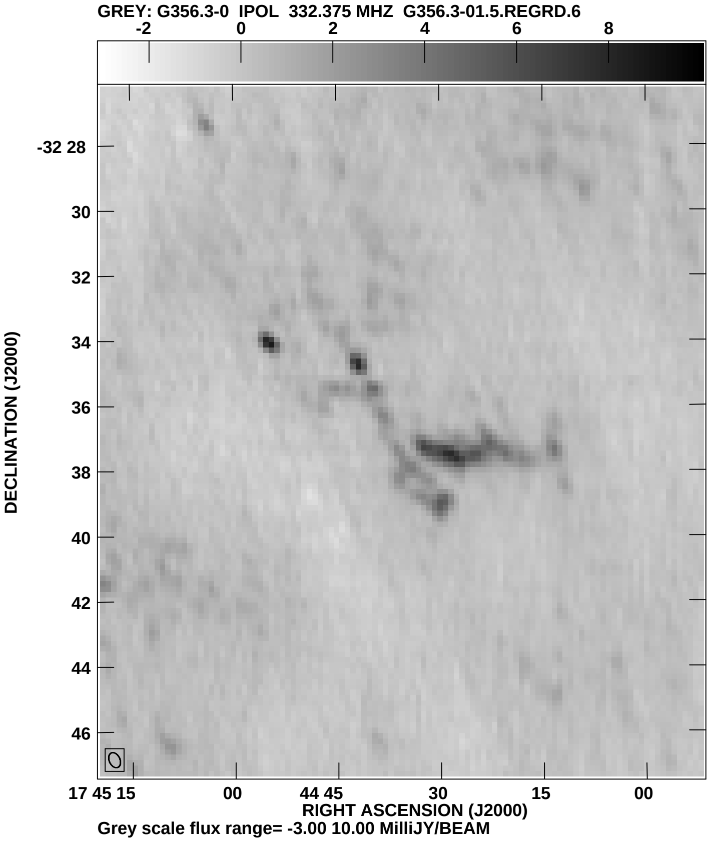

Figure 6.5: Sub-image of the linear structure seen in the full primary beam image of the region containing G356.3−1.5. This structure is seen clearly in the low resolution image as well (Fig. 4.8) and appears to be a real feature and not an artifact.

eraged channels (corresponding to twenty frequency channels at the original frequency resolution) were used for gridding the visibilities. In the second method, all twenty frequency channels were used directly for gridding. This linear structure was seen in all these images.

Marginally extended linear features similar to this structure (see also the lower resolution image in Fig. 4.8) have been detected earlier in the 843 MHz survey of the inner Galaxy (Gray 1996). One such feature, namely G357.1−0.2, was later imaged at higher resolution using the VLA at 5 GHz revealing a bizarre source with 'tubes' of highly confined emission in an even more bizarre morphology. The nature of this source, which is fairly close to the Galactic plane, is not known. The extended structure seen in this GMRT image is also suggestive of a similar source. Higher resolution continuum imaging, polarimetry and HI absorption observation towards this source will be required to get some handle on its nature.

6.4 Extended emission around Ultra Compact HII regions

6.4.1 G004.417+0.126

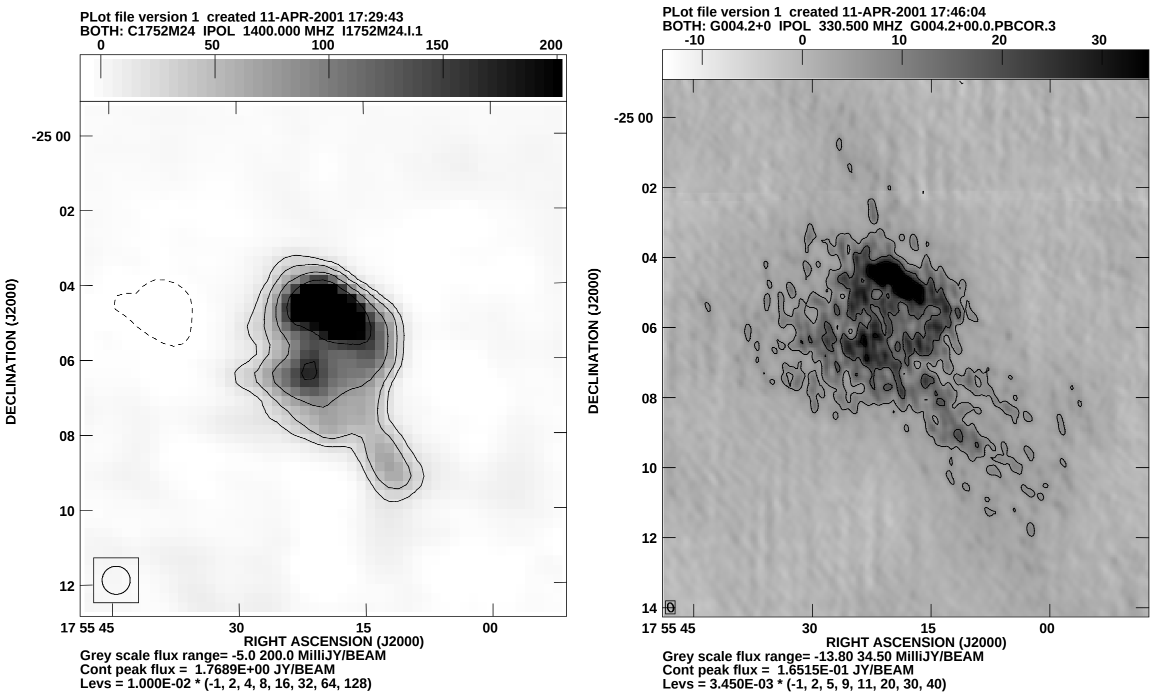

Figure 6.6: The left panel shows the NVSS image of the Ultra Compact H II region G004.4+0.1 at 1420 MHz. The RMS noise in this image is ~ 0.5 mJy and the resolution of $\sim 45 \times 45\ \mathrm{arcsec}^2$. The right panel shows the 327-MHz image. The resolution in this image is $\sim 15 \times 11\ \mathrm{arcsec}^2$ and the RMS noise of ~ 3.5 mJy.

This source, visible in the 327-MHz GMRT image as well as in the 1420-MHz NVSS image (Fig. 6.6), coincides with a an UC H II region G004.417+0.126 (Becker et al. 1994) (classified on the basis of its high frequency flux densities and IR colour selection criteria (Wood & Churchwell 1989a,b)). Images of this source at 327 MHz from the GMRT and 1420 MHz from the NVSS presented here are the first resolved images of this source. The extended emission around a compact core seen these images is similar to that detected for other UC H II regions using the VLA in D-array configuration (Kurtz et al. 1999; Kim & Koo 2001).

The peak flux densities measured at 327 and 1420 MHz, from images smoothed to the same resolution, are 0.49 and 0.51 Jy respectively. The spectral index between 327 and 1420 MHz corresponding to these values is close to zero and is consistent with this being a flat spectrum thermal source. The integrated flux densities from the 5 and 1.4 GHz Galactic plane surveys (Becker et al. 1994) however corresponds to a negative spectral index between 5 and 1.4 GHz (the 1.4 GHz flux density from their measurement is in fact underestimated due to missing flux for sources larger than 120 arcmin; inclusion of the missing flux will make the spectral index more negative). Cuts taken across the spectral index map made using the images at 327 and 1400 MHz are shown in Fig.6.7. The spectral index of the compact core is reasonably flat between 1.4 GHz and 327 MHz. Here also, away from the core, the spectral index is negative, indicative of non-thermal component of emission (neither of these images suffer from missing flux). The average spectral index measured from the resolved images at these frequencies also show a gradient from nearly zero for the core to ~ -0.3 for the nebula.

In the far infrared colour-colour plot of $\log(S_{25\mu m}/S_{12\mu m})$ vs. $\log(S_{60\mu m}/S_{12\mu m})$ (Wood & Churchwell 1989a), UC H II regions are concentrated in the upper left quadrant of the plot (around $\log(S_{25\mu m}/S_{12\mu m}) \approx 1.0$ and $\log(S_{60\mu m}/S_{12\mu m}) \approx 2.0$). The IRAS flux densities for this source are 16.07, 132.7, 1010 and 2748 Jy at 12, 25, 60 and 100μ m respectively (Becker et al. 1994). On the IR colour-colour plot, this source lies at $\log(S_{25\mu m}/S_{12\mu m}) \approx 0.9$ and $\log(S_{60\mu m}/S_{12\mu m}) \approx 1.8$, which indicates that this is an UC H II region. H85α RRL transition at $V_{LSR} = 4.1$ km sec^{-1} has also been detected towards this direction (Lockman 1989). This puts a lower limit on the linear size of a few pc corresponding to the observed angular size of ~ 4 arcmin and a distance corresponding to systemic velocity of the RRL towards this source. Again, this is large compared to the typical size for the UC H II regions (< 0.1 pc). EM of $\sim 11 \times 10^7$ pc cm^{-6} for this source, using the peak flux density at 5 GHz and assuming $T_e = 10^4$ filling the resolution element, is consistent with this source being a UC H II region (Wood & Churchwell 1989b).

Recent detection of associated extended emission around many of the so called UC H II regions (Koo et al. 1996; Kurtz et al. 1999; Kim & Koo 2001) is on a similar scale as the extended emission seen for this source. The extended emission seen in the 327 and 1400-MHz images is therefore not surprising; the advantage of high resolution provided by the GMRT simultaneously with sensitivity to large angular scales is apparent. However, it

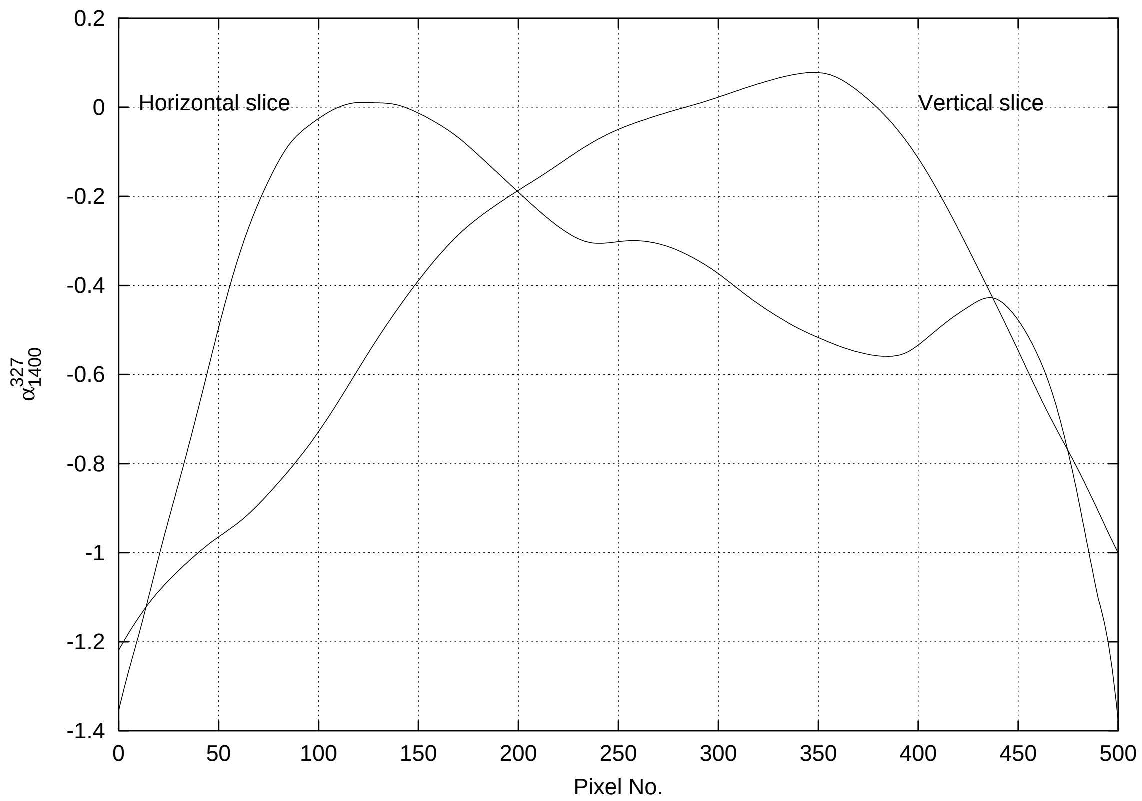

Figure 6.7: Plot of vertical and horizontal slices of the spectral index map between 327 and 1400 MHz taken across the compact core of G004.417+0.126. The compact core exhibits flat spectrum while the extended emission around the core has a steeper spectrum.

is unclear what ramifications this extended emission might have on the models that attempt to explain the morphology of UC H II regions (Kurtz 2000). Scaled versions of current models are unlikely to explain the emission at arcmin scales. Similarly, the spectral index variation across the source (from the compact core to the extended component) is harder to explain.

6.4.2 G003.349−0.076

Two UC H II regions, namely G003.349−0.076 and G003.351−0.077 (Becker et al. 1994) lie at the edge of the field containing the barrel shaped SNR G003.6−0.2. The location of these objects coincides with the northern most compact peak of emission in the subimage of this region shown in Fig. 6.8. Extended emission in the immediate vicinity of these compact sources on the scale of several arc-seconds to several arc-minutes is also

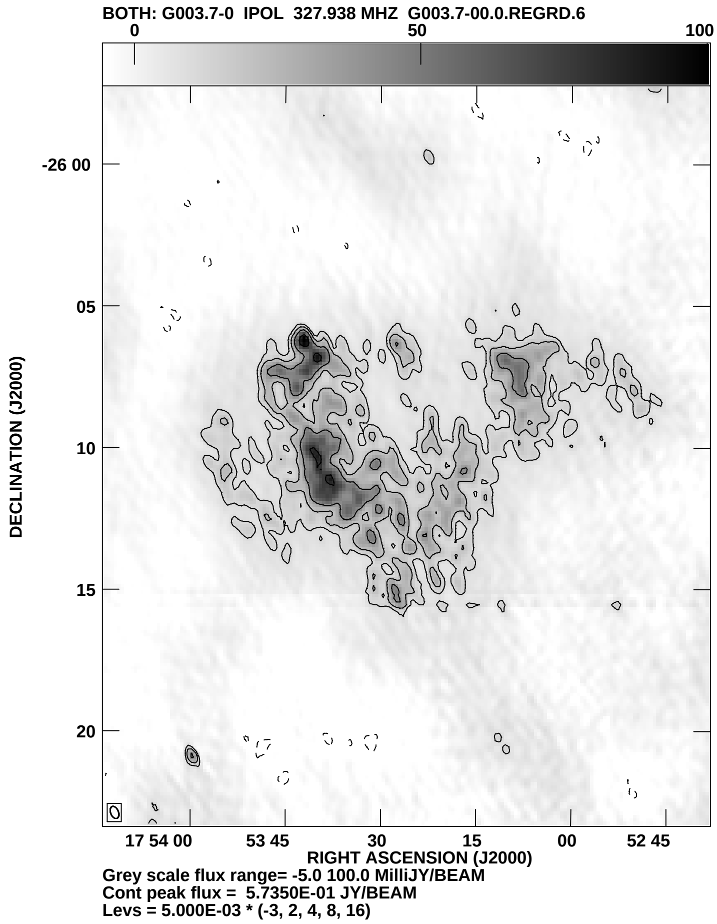

Figure 6.8: Sub-image showing extended emission around two catalogues Ultra Compact H II regions located at $\mathrm{RA}_{J2000} = 17^h53^m41^s$, $\mathrm{Dec}_{J2000} = -26°06'08''$ and $\mathrm{RA}_{J2000} = 17^h53^m41^s$, $\mathrm{Dec}_{J2000} = -26°06'04''$. The resolution in the image is $\sim 20 \times 10$ arcsec^2 and the RMS noise ~ 5 mJy/beam.

clearly visible in this image. The quality of the image for this region is, however, not very good, possibly due to primary beam attenuation as well as due to antenna tracking errors on some of the antennas due to which sources on the edge of the beams suffer from effective differential short time scale gain changes. The precise morphology of this extended emission as well as the flux density of this emission, therefore, cannot be reliably determined from this image. High resolution observations, centred on this region at a few frequencies, using the GMRT will be required to determine the nature of this extended emission.

6.5 Discussion

With the GMRT field of view of $\sim 1^\circ.4$ at 327 MHz, low frequency mapping in the Galactic plane reveal a variety of sources of compact as well extended emission. The GMRT observations of many the objects presented here, are the first high resolution observations at these low frequencies. With the *Central Square* providing reliable measurements up to $\sim 100\lambda$, these measurements are also sensitive to angular scales of up to ~ 30 arcmin. Emission at such large scales with a sub-arcsecond resolution and sensitivity of $5-20$ mJy/beam detects large and small scale structures, not detected in other earlier observations in the Galactic plane. High resolution imaging at other GMRT frequencies of the objects discussed here will provide additional information, not available from any other observation, which will help in determining the nature of these sources. In particular, thermal and non-thermal emission can be separated using the difference in the continuum spectra at these frequencies. Detailed spectral index changes within extended objects, which provides unique information about the emission mechanisms, physical parameters of the objects (e.g. H II and UC H II regions, SNRs) as well as information about the parameters of the intervening ISM, can be studied using such observations.

From the available data for G003.6−0.1, components `A` and the associate extended emission indicates that the emission is non-thermal. At higher frequencies, `C` and `D` are seen as distinct compact sources. The spectra of `C` is consistent with it being a radio loud symbiotic star. HI absorption spectra towards these three components show that `D` is farther away and probably an extragalactic background source. `A` and `C` are at similar kinematic distance and the ridge of emission seen clearly in the 5 GHz image, and marginally in the 1420 MHz image is indicative of an interaction between `C` and the extended emission. Continuum observations at 8 and possibly at 15 GHz with the VLA are needed to conclusively determine the nature of these objects. Spectral index of the emission from the shell can be measured using continuum images from the GMRT at 233 and 610 MHz. High resolution RRL observations towards G003.6−0.1 are also required to determine the source of RRL detected at 5 GHz from this direction.

The linear extended object see in the field of G356.3−1.5 is similar to that detected earlier by Gray (1996). Higher resolution observations, and if possible, measurements of polarization properties of this object are required to further ascertain the nature of this object.

327-MHz images of the UC H II regions, namely G004.4+0.1, G003.349−0.076 and G003.351−0.077, are the first images which resolve the low frequency extended emission from these fields. The morphology of G004+0.1 seen in this image is typical of UC H II regions. However, the liner size of $\sim$ 5 pc is too large compared to the size of < 0.1 pc of typical UC H II regions. Extended emission at 327 MHz in the immediate vicinity of G003.349−0.076 and G003.351−0.077 is also detected.

Extended emission around UC H II regions at angular scales of several arcmins (corresponding to linear sizes in the range of $2 - 20$ pc) have been recently detected at 5 and 1.4 GHz D-array VLA observations (Koo et al. 1996; Kim & Koo 2001). These extended components have been found to be kinematically and certainly morphologically associated with the compact components and it appears that the ionizing source of for the extended and compact components is same.

About 1000 UC H II regions have been identified so far. This gave rise to what is referred to as the "age problem" (de Pree et al. 1995, and reference therein): the number of UC H II regions estimate from the IRAS $60 - 12$ μm and $25 - 12$ μm colours, is about an order of magnitude greater than expected from other indicators of massive star formation rate based on their dynamical age (Wood & Churchwell 1989a,b). From this, it is inferred that the life of the ultra-compact phase of H II regions is $\geq\sim 10^5$ yr, larger by an order of magnitude than their sound crossing time ($\leq\sim 10^4$ yr). Most of these UC H II regions were identified from their small size (≤ 0.1 pc) and high interfered electron density ($n_e \geq 10^4$ cm^{-3}). Recently, VLA D-array imaging of an UC H II region (G005.58−0.24) revealed emission at scales ranging from 0.04 to 40 pc (Koo et al. 1996) which appeared morphologically associated with the UC H II region. It has an ultra-compact core, a compact core, an extended halo and a large diffused plateau. This prompted observations of a randomly selected sample of UC H II regions using the VLA at 3.6 cm in the D-array configuration (Kurtz et al. 1999). These observations revealed extended emission around compact cores in 12 out of 15 sources. More recently, in a survey by Kim & Koo (2001) of 16 UC H II regions using the VLA (DnC array) at 1.4 GHz, extended emission at scales of $2-12$ arcmin ($4-19$ pc) is detected in *each* one of the fields. It, therefore appears, that the previous classification of UC H II region was essentially based on high resolution observations with the VLA, which suffered from the selection effect due to the insensitivity to large scale emission and therefore revealed only the compact/ultracompact core. It now appears that the UC H II regions may be just the compact cores of larger HII regions. Evidence of this association comes from the tight correlation between the velocities of the UC H II regions, compact components and the extended envelopes (Kim & Koo 2001). The fact that the extended envelopes are detected in such a large fraction of UC H II regions in observations which *are* sensitive to large scale emission further indicates that the extended emission is associated.

The implications of a physical association of this extended emission with compact cores are far reaching. Kim & Koo (2001) estimate that most sources known as UC H II regions are likely to be associated with extended emission. Existence of extended emission at scales $\geq\sim$ few pc, ionized by the same sources, implies that the actual age of the so-called UC H II regions is $\geq\sim 10^4$ yr which could mitigate the "age problem" (de Pree et al. 1995). The IRAS colour criteria may select compact or extended H II regions, as well as UC H II regions - an idea consistent with the results of Codella et al. (1994) who found that more than half of the 445 diffuse H II regions are related to IRAS points sources which satisfy this colour criteria. No variation in the IRAS colours was also found for UC H II regions with evidence of extended emission, implying that the colour criteria is insensitive to the presence of extended emission, and a significant fraction of IRAS colour selected UC H II regions may have associated extended emission.

It therefore appears that the sequence of observations based, first on the selection of sources based on IRAS colours and then high resolution radio observations, which led to the "identification" and classification of UC H II regions is fraught with severe selection and observational biases. If most of the so-called UC H II regions have extended emission associated with them, these UC H II regions may be just compact cores, possibly composed of several compact components, of large HII regions. Observations of a larger sample of such sources with the GMRT, which provides *simultaneous* high resolution and sensitivity to large scale emission, will greatly help in settling the issue of the existence of associated large scale emission. None of the models put forth to explain the longevity of UC H II regions predicted the presence of extended emission around them. Kim & Koo (2001) have proposed a model, which is a combination of champagne flow model with the hierarchical structure of massive star-forming regions (Tenorio-Tagle 1982, and references therein). A massive star, which forms off-centre within a hot core, which in turn is embedded in a lower density molecular clump, can produce the compact component seen associated with the UC H II regions due to the hot core. The morphology of this compact component can be explained by the champagne flow, which would develop when the ionizing front breaks out of the core. The HII region inside the hot core continues of be ultracompact, while it grows to ~ 1 pc outside the core. Another champagne flow would develop when the ionization front crosses the edge of the molecular clump, which forms a more extended emission. The morphology in the radio continuum image, as well as the gradient of H76α line emission lends support to this model. However, if most of the so-called UC H II regions show associated emission, it will be difficult to explaining why so many of the UC H II regions would correspond to a situation where the star, the hot core and the molecular clump are all "carefully" arranged to give the desired observed morphology. High resolution observations, sensitive to large angular scales, of a larger sample (preferably a complete sample) of UC H II will be most desirable to make progress on this front.

The integrated spectral index for G004.417+0.126 between 5 and 1.4 GHz exhibits a negative spectral index (< -0.1). This source is well resolved at 327 and 1.4 GHz and from these images, it appears that the compact core has a flat spectrum while the extended emission has a significantly negative spectral index between these frequencies. The images at 327 MHz and 1.4 GHz for G003.349−0.076 are not reliable for the measurement of the spectral index, but there are indications that the extended emission there too has a negative spectral index. None of models for UC H II regions predict a non-thermal component. The model proposed by Kim & Koo (2001) for the extended emission, predicts a thermal spectrum for the extended emission. A larger sample of UC H II regions needs to be mapped at 327 MHz and 1.4 GHz to access if a non-thermal component is characteristic of the extended emission around UC H II or these sources are just odd cases, emission from which needs to be explained separately.

Chapter 7

Measurement of polarization leakage

Mechanical and electronic imperfections can result into polarization leakage in individual antennas of a radio interferometer. Such leakages manifest themselves as closure errors even in *co-polar* visibility measurements of unpolarized sources. Towards the very end of this dissertation, work was done to develope and test a method for the computation of polarization leakage for radio interferometric telescopes using *only* the nominally *co-polar* visibilities. This chapter describes the work done in this direction (Bhatnagar & Nityananda 2001).

7.1 Introduction

The mutual coherence function (also called the visibility function) for an unresolved and unpolarized source, measured by an interferometer array can be modeled as a product of antenna based complex gains. These complex gains can be derived from the measured visibility function using the standard algorithm, which we call `antsol`. `antsol` forms the central engine of most amplitude and phase calibration schemes used for radio interferometric data. (The earliest published reference for an algorithm for `antsol` of which we are aware is Thompson & D'Addario (1982)).

Usually antenna feeds measure the components of the incident radiation along two orthogonal polarization states by two separate feeds. The signals from the two feeds travel through essentially independent paths till the correlator. However, due to mechanical imperfections in the feed or imperfections in the electronics, the two signals can leak into each other at various points in the signal chain.

At the correlator, signals from all the antennas are multiplied with each other and the results averaged to produce the visibilities. The signals of same polarization are multiplied to produce the *co-polar* visibilities while the signals of orthogonal polarizations are multiplied to produce the *cross-polar* visibilities. The *co-polar* and *cross-polar* visibilities can be used to compute the full Stokes visibility function. Antenna based instrumental polarization and polarization leakage can be derived from the full Stokes coherence function for a source of known structure (usually an unresolved source) (Hamaker et al. 1996; Sault et al. 1996, henceforth HBS).

The correlator used for the Giant Metrewave Radio Telescope (GMRT) by default computes the *co-polar* visibilities using the *Indian mode* of the VLBA Multiplier and Accumulator (MAC) chip. Here we describe a method, which we call `leaky antsol`, for the computation of the leakages using *only* the *co-polar* visibility function for an unpolarized source. Following the notation used by HBS, we label the two orthogonal polarizations by p and q to remind us that the formulation is independent of the precise orthogonal pair of polarization states chosen.

Section 7.2 describes the motivation which led to this analysis. For orientation, Section 7.3 starts with the problem of solving for the usual complex antenna based gains and sets up an iterative scheme for the solution. The problem of *simultaneously* solving for the complex antenna gains and leakages is then posed in Section 7.3.1 and a similar iterative scheme is set up. Section 7.3.2 presents the results of the simulations done to test the scheme. Section 7.4.1 presents some results using the GMRT at 150 MHz. Also, we were fortunate to have the L-band feeds of one of the GMRT antennas converted from linear to circular polarization. We observed `3C147` in this mode where all baselines with this special antenna measured the correlation between nominally linear and circular polarization. Results of this experiment demonstrate that the leakage solutions are indeed giving information about the polarization properties of the feeds. These results and their interpretation on the Poincaré sphere are presented in section 7.4.2. Section 7.5 gives the interpretation of the leakage solutions and discusses closure errors due to polarization leakage using the Poincaré sphere.

7.2 Motivation

Rogers (1983) pointed out in the context of the VLBA, that the polarization leakage cause closure errors even in nominally *co-polar* visibilities. Massi et al. (1997) have carried out a detailed study of this effect for the telescopes of the European VLBI Network (EVN). The motivation behind this word was that the current single sideband GMRT correlator uses the so called *Indian mode* of the VLBA MAC chips to produce only the *co-polar* visibilities. Also, the planned Walsh switching has not yet been implemented at the GMRT and in any case, would not eliminate leakage generated before the switching point. Tests done using strong point source dominated fields show unaccounted closure errors at a few percent level. The motivation behind developing an algorithm to solve for gains and leakages simultaneously, using *only* the *co-polar* visibilities was to determine if the measured closure errors could be due to polarization leakage in the system. Estimates of leakage can then be used in the primary calibration to remove the effects of polarization leakage. This is where this work differs from the earlier work of HBS which is about the calibration using the full Stokes visibility function, needed for observations of polarized sources. The polarization leakage in some of the EVN antennas corrupts the *co-polar* visibilities at a level visible as a reduction in the dynamic range of the maps (Massi & Aaron 1997a,b; Massi et al. 1998). Thus such a method can also be used in imaging data from the EVN and other telescopes affected by such closure errors.

Let g^p_i represent the complex gain for the p-polarization channel of the i^{th} antenna and α^q_i represent the leakage[1] of the *q*-polarization signal into the *p*-polarization channel. The electric field measured by antenna i can then be written as

$$E^p_i = g^p_i E^p_{i,\circ} + \alpha^q_i E^q_{i,\circ} \tag{7.1}$$

where $E^p_{i,\circ}$ and $E^q_{i,\circ}$ are the responses of an *ideal* antenna to the incident radiation in the p- and q-polarization states respectively. For an unpolarized source of radiation, $\langle E^p_{i,\circ} E^{q\star}_{j,\circ} \rangle = 0$. The *co-polar* visibility for such a source, measured by an interferometer using two antennas denoted by the subscripts i and j, is given by

$$\rho^{pp}_{ij} = g^p_i g^{p\star}_j \rho^{pp}_{ij,\circ} + \alpha^q_i \alpha^{q\star}_j \rho^{qq}_{ij,\circ} + \epsilon_{ij} \tag{7.2}$$

where ϵ_{ij} is independent gaussian random baseline based noise and $\rho^{pp}_{ij,\circ} = \langle E^p_{i,\circ} E^{p\star}_{j,\circ} \rangle$ and $\rho^{qq}_{ij,\circ} = \langle E^q_{i,\circ} E^{q\star}_{j,\circ} \rangle$ are the two ideal *co-polar* visibilities. ϵ_{ij} usually represents the contribution to ρ^{pp}_{ij} which cannot be separated into antenna based quantities. ϵ_{ij} therefore is a measure of the intrinsic closure errors in the system and is usually small.

[1]Strictly speaking, the ratio α^q_i / g^p_i is the correct measure of the leakage and this is what has been plotted in Fig.7.3 below. This does not however affect the computational scheme described here.

For an unpolarized point source $\langle E^p_{i,\circ} E^{p\star}_{j,\circ}\rangle = \langle E^q_{i,\circ} E^{q\star}_{j,\circ}\rangle = \rho^{pp}_{ij,\circ} = I/2$ where I is the total flux density. Writing $X^{pp}_{ij} = \rho^{pp}_{ij}/\rho^{pp}_{ij,\circ}$ we get

$$X^{pp}_{ij} = g^p_i g^{p\star}_j + \alpha^q_i \alpha^{q\star}_j + \epsilon_{ij} \tag{7.3}$$

where ϵ_{ij} now refers to the baseline based noise in X^{pp}_{ij}.

Assuming α^q_is to be negligible, the usual `antsol` algorithm estimates g^p_is such that $\sum_{\substack{i,j\\ i\neq j}} \left| X^{pp}_{ij} - g^p_i g^{p\star}_j \right|^2$ is minimized (see section 7.3). Normally, Walsh switching (Thompson et al. 1986) is used to eliminate the polarization leakage due to cross-talk between the signal paths, such that $\alpha^q_i \alpha^{q\star}_j \ll \epsilon_{ij}$. However, α^q_is can also be finite due to mechanical imperfections in the feed or the *cross-polar* primary beam, which cannot be eliminated by Walsh switching.

In the case of significant antenna based polarization leakage (compared to $\sqrt{\epsilon_{ij}}$), the second term in Equation 7.3 involving α^q_is will combine with the closure noise ϵ_{ij}. The polarization leakage therefore manifests itself as increased closure errors (see Section 7.5 for a geometric explanation on the Poincaré sphere). This has also been pointed out by Rogers (1983) in the context of VLBA observations. However, as written in Equation 7.3, the leakages and gains are actually antenna based quantities and can be solved for, using only the *co-polar* visibilities.

7.3 Algorithm and simulation

In the absence of any polarization leakage, g_is can be estimated by minimizing

$$S = \sum_{\substack{i,j\\ i\neq j}} \left| X^{pp}_{ij} - g^p_i g^{p\star}_j \right|^2 w^{pp}_{ij} \tag{7.4}$$

with respect to g_is, where $w^{pp}_{ij} = 1/\sigma^2_{ij}$, σ_{ij} being the variance on the measurement of X^{pp}_{ij}.

In Equation 7.2, if $\rho^{pp}_{ij,\circ}$ accurately represents the source structure, X^{pp}_{ij} will have no source structure dependent terms and is purely a product of two antenna dependent complex gains. For a resolved source, $\rho^{pp}_{ij,\circ}$ can be estimated from the image of the source.

Evaluating $\frac{\partial S}{\partial g^{p\star}_i}$ and equating it to zero[2] (see Appendix D), we get

[2]Complex derivatives can be evaluated by treating g^p_i and $g^{p\star}_i$ as independent variables (Palka 1990).

$$g_i^p = \frac{\sum\limits_{\substack{j \\ j\neq i}} X_{ij}^{pp} g_j^p w_{ij}^{pp}}{\sum\limits_{\substack{j \\ j\neq i}} \left|g_j^p\right|^2 w_{ij}^{pp}} \tag{7.5}$$

This can also be derived by equating the partial derivatives of S with respect to real and imaginary parts of $g_i^{p\star}$.

Since the antenna dependent complex gains also appear on the right-hand side of Equation 7.5, it has to be solved iteratively starting with some initial guess for g_js or initializing them all to 1. Equation 7.5 can be written in the iterative form as:

$$g_i^{p,n} = g_i^{p,n-1} + \lambda \left[g_i^{p,n-1} - \frac{\sum\limits_{\substack{j \\ j\neq i}} X_{ij}^{pp} g_j^{p,n-1} w_{ij}^{pp}}{\sum\limits_{\substack{j \\ j\neq i}} \left|g_j^{p,n-1}\right|^2 w_{ij}^{pp}} \right] \tag{7.6}$$

where n is the iteration number and $0 < \lambda < 1$. Convergence would be defined by the constraint $|S_n - S_{n-1}| < \beta$ (the change in S from one iteration to another) where, β is the tolerance limit and must be related to the average value of ϵ_{ij}. Equation 7.6 forms the central engine for the classical `antsol` algorithm used for primary calibration of the visibilities and in self-calibration for imaging purposes. This algorithm was suggested by Thompson & D'Addario (1982).

7.3.1 The `leaky antsol`

In the presence of significant polarization leakage, Equation 7.3 can be used to re-write Equation 7.4 as

$$S = \sum_{\substack{i,j \\ i\neq j}} \left| X_{ij}^{pp} - (g_i^p g_j^{p^\star} + \alpha_i^q \alpha_j^{q^\star}) \right|^2 w_{ij}^{pp} \tag{7.7}$$

In this form, S is an estimator for the *true* closure noise ϵ_{ij} rather than the artificially increased closure noise $(\alpha_i^q \alpha_j^{q\star} + \epsilon_{ij})$ due to the presence of polarization leakage.

Equating the partial derivatives $\frac{\partial S}{\partial g_j^{p\star}}$, $\frac{\partial S}{\partial \alpha_j^{q\star}}$ to zero, we get

$$g_i^p = \frac{\sum\limits_{\substack{j\\ j\neq i}} X_{ij}^{pp} g_j^p w_{ij}^{pp} - \alpha_i^q \sum\limits_{\substack{j\\ j\neq i}} \alpha_j^{q\star} g_j^p w_{ij}^{pp}}{\sum\limits_{\substack{j\\ j\neq i}} \left|g_j^p\right|^2 w_{ij}^{pp}} \tag{7.8}$$

$$\alpha_i^q = \frac{\sum\limits_{\substack{j\\ j\neq i}} X_{ij}^{pp} \alpha_j^q w_{ij}^{pp} - g_i^p \sum\limits_{\substack{j\\ j\neq i}} g_j^{p\star} \alpha_j^q w_{ij}^{pp}}{\sum\limits_{\substack{j\\ j\neq i}} \left|\alpha_j^q\right|^2 w_{ij}^{pp}} \tag{7.9}$$

These non-linear equations can also be iteratively solved.

Equation 7.3, which expresses the observed visibilities on a point source unpolarized calibrator in terms of the gains and leakage coefficients of the antennas, would take the same form if written in an arbitrary orthogonal basis. It is clear that the g's and the α's will change when we change the basis, so this means that the equations cannot have a unique solution. This situation is familiar from ordinary self-calibration, when only relative phases of antennas are determinate, with one antenna acting as an arbitrary reference. For observations of unpolarized sources, we can similarly say that any feed can be chosen as a reference polarization, with zero leakage, and other feeds have gains and leakages in the basis defined by this reference. Other conventions may be more convenient, as discussed in Section 7.6 which discusses degeneracy in detail.

7.3.2 Results of the simulations

We simulated visibilities with varying fraction of polarization leakage in the antennas to test the algorithm as follows. The antenna based signal and leakage were constructed as $g_i = R_g$ and $\alpha_i = f \cdot R_\alpha$ where R_g and R_α were drawn from the same gaussian random population. The visibility from two antennas i and j was then constructed as $X_{ij} = g_i g_j^\star + \alpha_i \alpha_j^\star + \epsilon_{ij}$ for $0 \leq f < 0.1$. This is equivalent to a visibility of an unpolarized point source of unit strength with a complex antenna based gain g_i and leakage α_i of strength proportional to f. Equation 7.6 was then used to compute g_i and residual χ^2 computed as $\chi_{\rm a}^2 = \sum_{ij} \left|1 - \frac{X_{ij}}{g_i g_j^\star}\right|^2$. The computed values of g_i^p were then used to compute improved estimates for g_i^p by simultaneously solving for g_i^p and α_i^q using the iterative forms of Equations 7.8 and 7.9. The derived values of g_i^p and α_i^q matched the true values to within the tolerance limit. A new χ^2 was computed as $\chi_{\rm l}^2 = \sum_{ij} \left|1 - \frac{X_{ij}}{(g_i g_j^\star + \alpha_i \alpha_j^\star)}\right|^2$. The values of $\chi_{\rm a}^2$ and $\chi_{\rm l}^2$ as a function of f are plotted in Fig. 7.1. The two curves become distinguishable when the leakage is significantly greater than ϵ_{ij} (for f greater than $\sim$ 1%). After that, the value of χ^2_l is consistently lower than χ^2_a, where the contribution of antenna based leakage has not been removed. Also notice that χ^2_l remains constant while χ^2_a quadratically increases as a function of f. This is due to the fact that `antsol` treats the antenna based polarization leakage as closure errors resulting in an increased χ^2 with increasing fractional leakage.

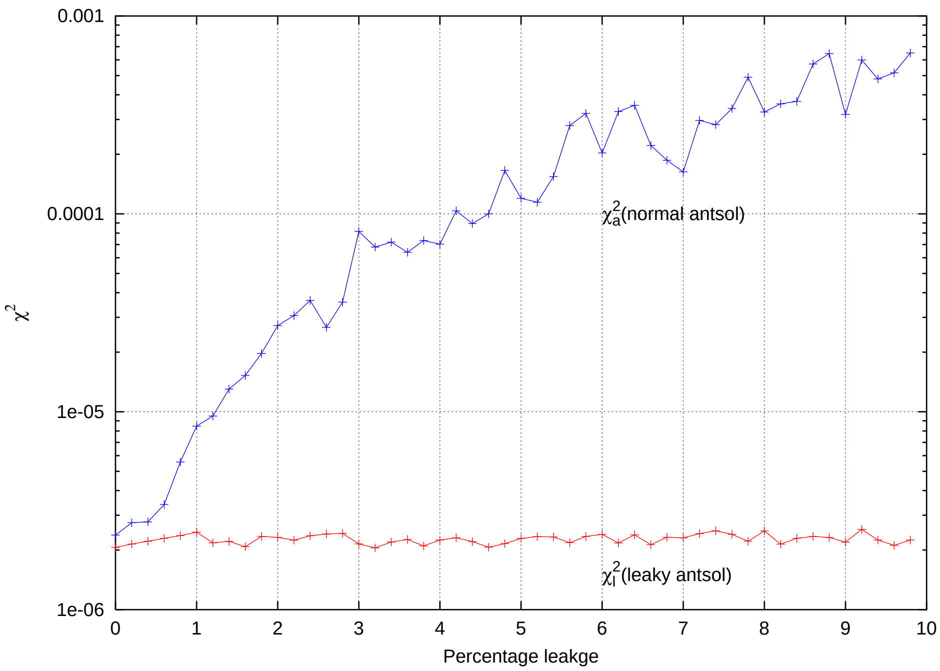

Figure 7.1: Figure showing the results of the simulations. The top curve is the value of χ^2 using the classical `antsol` (χ^2_a). The bottom curve is the value of χ^2 using the `leaky antsol` (χ^2_l) as a function of the percentage polarization leakage.

7.4 Real data

7.4.1 150 MHz data

Engineering measurements for polarization isolation at 150 MHz for the GMRT show significant polarization leakage in the system. We therefore used `leaky antsol` to calibrate the data from the Galactic plane phase calibrator `1830-36` which is known to be less than 0.2% polarized at 1.4 GHz. The percentage polarization at 150 MHz is not known, but it is expected to decrease further and it was taken to be an unpolarized point source.

Fractional polarization leakage ($|\alpha_i^q/g_i^p|$) of up to 100% was measured for most of the antennas, which is consistent with the estimated leakage measured from system engineering tests. Again, $\chi^2_{\rm a}$ and $\chi^2_{\rm l}$ were computed and the results are shown in Fig. 7.2. The 150-MHz GMRT band suffers from severe radio frequency interference (RFI). The sharp rise in the value of $\chi^2_{\rm a}$ around sample number 10 is due to one such RFI spike. This spike is present in the total power data from all antennas at this time. On an average, the χ^2 reduces by $\sim 60\%$ when leakage calibration is applied ($\chi^2_{\rm l}$). This is consistent with polarization leakage being a major source of non-closure at this frequency.

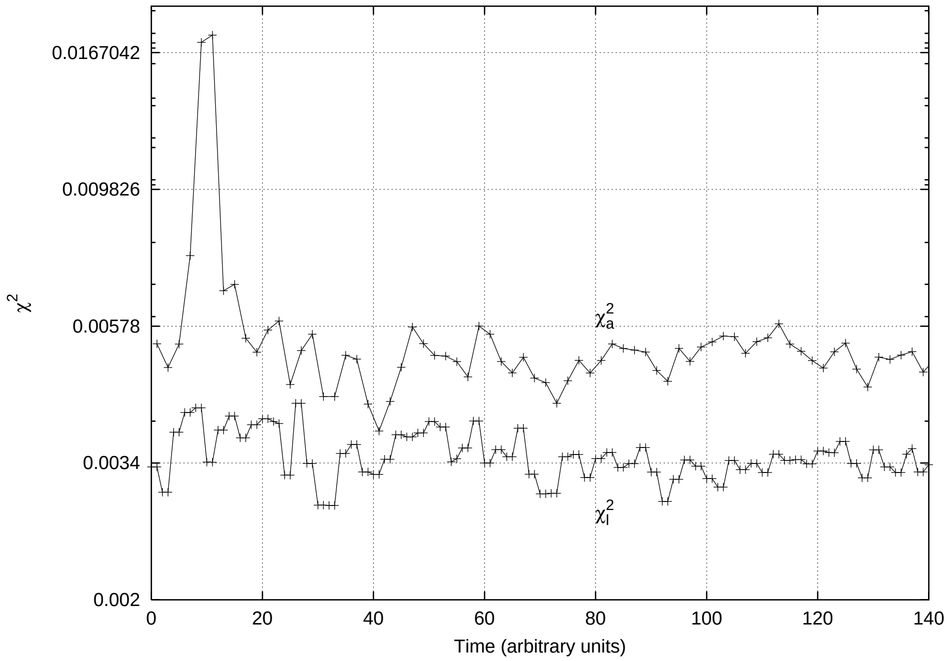

Figure 7.2: Figure showing the results using GMRT data at 150 MHz for the compact Galactic plane source `1830-36`. The top curve is the value of χ^2 using the classical `antsol` ($\chi^2_{\rm a}$). The bottom curve is the value of χ^2 using the `leaky antsol` ($\chi^2_{\rm l}$) as a function of time.

7.4.2 L-band data with circular feed

The GMRT L-band feeds are linearly polarized. For the purpose of a VLBI experiment conducted in December 2000, the L-band feed of one of the antennas was converted to a circularly polarized feed. The rest of the L-band feeds were linearly polarized and we took this opportunity to measure correlations between the circularly polarized antenna with other linearly polarized antennas using the source `3C147`. Two scans of approximately one hour long observations were done using the single side band GMRT correlator. This correlator computes only *co-polar* visibilities. With this configuration of feeds, visibilities between the circularly polarized antenna and all other linearly polarized antennas corresponds to correlation between the nominal `X-` and `R-`polarizations, labeled by `RX`, were recorded in the first scan. The polarization of the circularly polarized antenna was then flipped for the second scan to record the correlation between the nominal `X-` and `L-`polarization states, labeled by `LX`.

The VLA Calibrator Manual[3] lists the percentage polarization ($\frac{\sqrt{Q^2+U^2+V^2}}{I}$) for `3C147` at L-band $< 0.1\%$. The *cross-polar* terms in Equation 7.2, which are assumed to be zero, will therefore contribute an error of the order of 0.1%. These *cross-polar* terms will be, however, multiplied by gains of type $g_i^p \alpha_i^{q\star}$. Since g_i^p and α_i^q are both assumed to be uncorrelated between antennas, this error will manifest as random noise in Equation 7.3. Within the limits of other sources of errors, the source `3C147` can therefore be considered to be a completely unpolarized source.

Results and Interpretation

The response of an ideal circularly polarized antenna to unpolarized incident radiation can be expressed as a superposition of two linear polarization states as $E^R_{i,\circ} = E^X_{i,\circ}e^{\iota\delta} + E^Y_{i,\circ}e^{-\iota\delta}$ where, the superscripts R, X and Y denote the right circular and the two linear polarization states respectively. δ is half the phase difference between the two linear polarization states and is equal to $\pi/4$ for right-circular polarization and $-\pi/4$ for left-circular polarization. Writing the general Equation 7.1 for right-circularly polarized antenna as $E^R_i = g^R_i E^R_{i,\circ} + \alpha^L_i E^L_{i,\circ}$ and substituting for $E^R_{i,\circ}$ and $E^L_{i,\circ}$ we get

$$
\begin{aligned}
E^R_i =& g^R_i\left(E^X_{i,\circ}e^{\iota\delta} + E^Y_{i,\circ}e^{-\iota\delta}\right) + \\
& \alpha^L_i\left(E^X_{i,\circ}e^{-\iota\delta} + E^Y_{i,\circ}e^{\iota\delta}\right)
\end{aligned}
\tag{7.10}
$$

Equation 7.3 for the case of correlation between a circularly polarized and a linearly polarized antenna, with polarization leakage in both the antennas, can be written as

[3]The VLA Calibrator manual is available on the web from `http://www.aoc.nrao.edu/~gtaylor/calib.html`

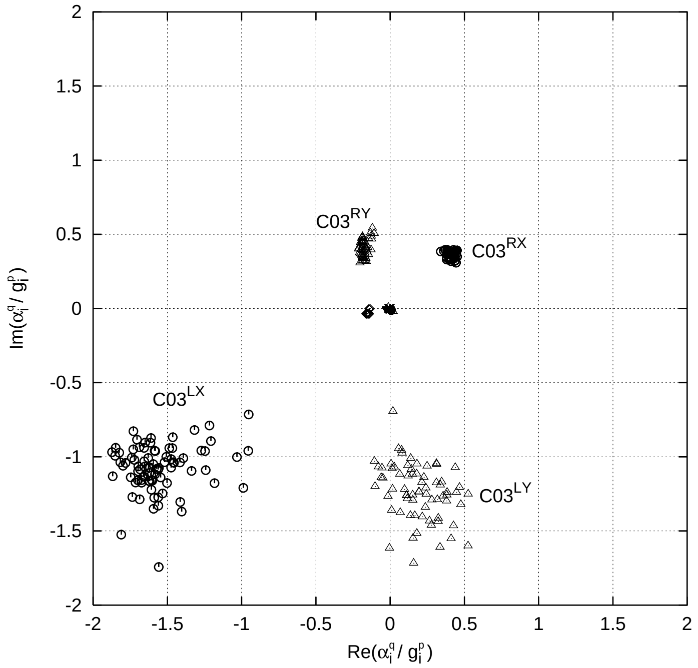

Figure 7.3: Figure showing the results using visibilities with one circularly polarized antenna and all other linearly polarized antennas at L-band. The x- and y-axis denote the real and imaginary parts of α_i^q/g_i^p respectively. g_i^p and α_i^q were solved for every integration time ($\sim 17s$). All linearly polarized antennas are close to the origin in this plot. The solutions for the circularly polarized antenna (C03) are the set of points away from the origin (shown by open circles and triangles). The two sets of points for this antenna, separated from each other by $\sim 180^\circ$ are solutions for the right- and left-circular polarization channel. The points denoted by open circles are from correlation between the right- and left-circular polarization of C03 with nominal linear X-polarization of the other antennas (labeled as $\mathrm{C03^{RX}}$ and $\mathrm{C03^{LX}}$ respectively). The points denoted by triangles are from correlation of C03 with nominal Y-polarization of the other antennas (labeled as $\mathrm{C03^{RY}}$ and $\mathrm{C03^{LY}}$).

$$\begin{aligned} X_{ij}^{RX} =& (g_i^R e^{\iota\delta} + \alpha_i^L e^{-\iota\delta}) g_j^{X\star} + \\ & (g_i^R e^{-\iota\delta} + \alpha_i^L e^{\iota\delta}) \alpha_j^{Y\star} \\ \equiv& g_i^{X'} g_j^{X\star} + \alpha_i^{Y'} \alpha_j^{Y\star} \end{aligned} \tag{7.11}$$

where $g_i^{X'} = g_i^R e^{\iota\delta} + \alpha_i^L e^{-\iota\delta}$ and $\alpha_i^{Y'} = g_i^R e^{-\iota\delta} + \alpha_i^L e^{\iota\delta}$. The `leaky antsol` solutions for the circularly polarized antenna in this case will correspond to $g_i^{X'}$ and $\alpha_i^{Y'}$.

Let $P_i = \alpha_i^Y/g_i^X$ ($P_i = \alpha_i^{Y'}/g_i^{X'}$ for the circularly polarized antenna). Then, the amplitude of P_i is a measure of the fractional polarization leakage in the antenna while the phase of P_i gives the phase difference between the signal from one of the feeds and the leaked signal from the other feed. For an ideal circularly polarized antenna, $|P_i| \approx 1$. A plot of the real and imaginary parts of this quantity for all antennas should therefore clearly show P_i for the circularly polarized antenna with an amplitude of 1 and at an angle of $\pi/2$ with respect to the nominal X-axis.

The real and imaginary parts of P_i for all antennas from this experiment are shown in Fig. 7.3. The solutions were computed for every integration cycle of ~ 17 sec and the points on this plot represent the tip of phasor P_i. The collection of points near the origin are for all the linearly polarized antennas while the collection of two sets of points away from the origin, approximately an angle of π from each other, are for the circularly polarized antenna. The solutions found by `leaky antsol` match the expected results quite well. This therefore constitutes a reasonably controlled test with real data showing that the solutions indeed provide information about the polarization leakage in the system.

This experiment however provides much more information about the polarization properties of the antenna feeds used. The collection of points in the first quadrant denoted by open circles are the values of P_i derived from the correlation between the nominal right-circularly polarized signal and the linearly polarized signals along the nominal X-axis from all other antennas. Points in the third quadrant are similarly derived using the left-circular signals. The set of points denoted by triangles in the second and fourth quadrant are derived using correlations of right- and left-circularly polarized signals with the linearly polarized signals along the nominal Y-axis from all other antennas.

A larger spread in the solutions using the left-circularly polarized signals indicates that the closure noise (from other unknown sources) in these signals is higher. The fact that the amplitude of P_i derived using the right-circularly polarized signals is ≈ 0.5 indicates that the nominal circularly polarized feed is in fact elliptically polarized with this axial ratio. The spread of $\pm 1 - 2\%$ about the origin is indicative of polarization leakage at the level of few percent in the linearly polarized antennas as well. The leakage in one of the linearly polarized antennas is significantly larger ($\approx 4\%$). Since this kind of data is routinely taken on primary calibrators during GMRT observations for synthesis imaging, `leaky antsol` provides a useful diagnostic of system health, polarization performance and numbers needed to correct the data in high accuracy work.

The following test was also carried out to check that the closure phase on a triangle involving the circular feed was indeed mainly due to polarization effects. The three baselines making up this triangle were flagged as bad baselines from the input data and a new solution found for the gains and leakages of all antennas. This solution predicted the same closure phase (to within errors) as actually observed.

7.5 Closure phase and the Poincaré sphere

In this section we use right- and left-circular polarization states as the basis. A general elliptically polarized state can be written as a superposition of two states represented by the vector $\begin{pmatrix} \cos\theta/2 \\ \sin\theta/2\, e^{\iota\phi} \end{pmatrix}$. Clearly, $\theta = \pi/2$ corresponds to linear polarization and $\theta \neq 0, \pi/2$ to elliptical polarization (see Fig. 7.4). Increasing ϕ by ζ rotates the direction of the linear state or the major axis of the ellipse by $\zeta/2$. We can chose the phase of the basis so that $\phi = 0$ corresponding to linear polarization along the x-axis. The Poincaré sphere representation of the state of polarization maps the general elliptic state to the point (θ, ϕ) on the sphere. The properties of this representation are reviewed by Ramachandran & Ramaseshan (1961). We are concerned here with one remarkable property, discovered by Pancharatnam (1956, 1975). Whenever there is constructive interference between two sources of radiation, it is natural to regard them as in phase. A remarkable property of this simple definition manifests itself when we consider 3 sources of radiation of different polarization - that if a source A is in phase with B and B in phase with C, C in general need not be in phase with A. The phase difference between A and C is known in the optics literature as the geometric or Pancharatanam phase (see also Ramaseshan & Nityananda (1986); Berry (1987)). We show that this naturally occurs in radio interferometry of an unpolarized source with three antennas of different polarizations.

Let the polarization states of the three antennas be represented by $\begin{pmatrix} g_1 \\ \alpha_1 \end{pmatrix}$, $\begin{pmatrix} g_2 \\ \alpha_2 \end{pmatrix}$, and $\begin{pmatrix} g_3 \\ \alpha_3 \end{pmatrix}$ in a circular basis. Denoting the vector $\begin{pmatrix} g_i \\ \alpha_i \end{pmatrix}$ by ψ_i, one clearly see that the visibility on the 1-2 baseline is proportional to $\psi_1^\dagger \psi_2$. Hence the closure phase around a triangle made by antennas 1, 2, and 3 is the phase of the complex number (also called the triple product) $V_{123} = (\psi_1^\dagger\psi_2)(\psi_2^\dagger\psi_3)(\psi_3^\dagger\psi_1)$. In the quantum mechanical literature, this type of quantity goes by the name of Bargmann's invariant and its connection to the geometric phase was made clear by Samuel & Bhandari (1988). With some work, one can give a general proof that the closure phase (phase of V_{123}) is equal to half the solid angle

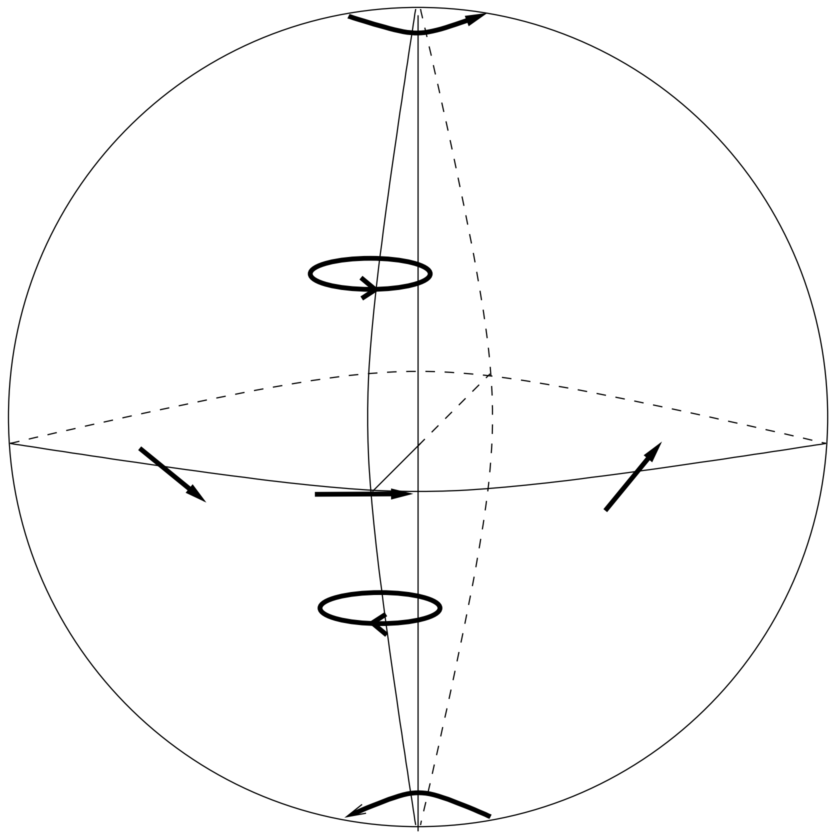

Figure 7.4: Poincaré sphere representation of the state of polarization. Poitns on north and south poles of the sphere correspond to pure right and left circular polarization. Points along the equator correspond to pure linear polarization. A linear polarization along the x-axis is represented by a point at $\theta = \pi/2$ and $\phi = 0$ while linear polarization along the y-axis is represented by a point at $\theta = \pi/2$ and $\phi = \pi/2$.

subtended at the centre of the Poincaré sphere by the points represented by ψ_1, ψ_2, and ψ_3 on the surface of the sphere. For the case where the polarization state of the three antennas are same, this phase is zero in general. However, when the polarization states of the antennas are different, this phase is non-zero.

The well known result that an arbitrary polarization state can be represented as a superposition of two orthogonal polarization states translates to representing any point on the Poincaré sphere by the superposition of two diametrically opposite states on a great circle passing through that point. For example, circular polarization can be expressed by two linear polarizations, each with intensity $1/\sqrt{2}$. In the context of the present work, the nominally circularly polarized antenna maps to a point away from the equator on the Poincaré sphere (it would be exactly on the pole if it is purely circular) while the rest of the antennas map close to the equator (they would be exactly on the equator if they are purely linear and map to a single point if they were also identical). The visibility phase due to the extra baseline based term in Equation 7.3 due to polarization mis-match is a consequence of the Pancharatanam phase mentioned above. This phase, on a triangle involving the circularly polarized antenna, will be close to the angle between the two linear antennas. For example, if $\psi_1 = \begin{pmatrix} 1 \\ \iota \end{pmatrix}$, $\psi_2 = \begin{pmatrix} 1 \\ 0 \end{pmatrix}$, and $\psi_3 = \begin{pmatrix} \cos\gamma \\ \sin\gamma \end{pmatrix}$, the phase of V_{123} will be γ. This picture can be depicted by plotting the real and imaginary parts of α_i^q/g_i^p, which is done in Fig. 7.3. The circularly polarized antenna can be clearly located in this figure as the set of point away from the origin while the linearly polarized antennas as the set of points close to the origin. The collection of points located away but almost symmetrically about the origin represents the nominal right- and left-circularly polarized feeds. Points on the equator, but significantly away from the origin represents an imperfect linearly polarized antenna. Note that the average closure phase between the nominally linear antennas is close to zero, which defines the mean reference frame in Fig. 7.3.

7.6 Non-uniqueness of solutions

We discuss the non-uniqueness of the solutions of Equation 7.3, and possible convenient conventions for choosing a specific solution. One obvious degeneracy is that multiplication of all the α's by one common phase factor independent of antenna, and all the g's, by another, in general different, common factor, does not affect the right hand side of Equation 7.3. Also, the equation was written in a specific basis, say right and left circular. But it would have had the same form when using any other orthogonal pair as basis. Hence we are free to apply this change of basis to one solution to get another solution of Equation 7.3. Under such a change, the coefficients transform according to

$$\begin{pmatrix} g' \\ \alpha' \end{pmatrix} = \begin{pmatrix} \cos\phi & e^{\iota\gamma}\sin\phi \\ -e^{-\iota\gamma}\sin\phi & \cos\phi \end{pmatrix} \begin{pmatrix} e^{\iota\zeta_1} & 0 \\ 0 & e^{\iota\zeta_2} \end{pmatrix} \begin{pmatrix} g \\ \alpha \end{pmatrix} \tag{7.12}$$

It is easy to verify that under this change, $\alpha_i'\alpha_j^{\star\prime} + g_i'g_j^{\star\prime} = \alpha_i\alpha_j^\star + g_i g_j^\star$. Clearly, since χ^2 is unchanged by these transformations, an iterative algorithm will simply pick one member of the set of possible solutions, determined by the initial conditions. Having found one such, one could apply a suitable transformation to obtain a solution satisfying some desired condition. For example, if one has nominally linear feeds, one might impose the statistical condition that there is some mean linear basis with respect to which the leakage coefficients will be as small as possible. Such a condition has the advantage that a perfect set of feeds is not described in a roundabout way as a set of leaky feeds with identical coefficients, simply because the basis chosen was different. Carrying out the minimization of $\sum |g_i|^2$ by the method of Lagrange multipliers, subject to a constant χ^2, we obtain the condition that $\sum \alpha_i^* g_i = 0$. This solution can be interpreted as requiring the leakage coefficients to be orthogonal to the gains, and is reasonable when we think about the opposite kind of situation, when the leakages are ”parallel” to the gains, i.e. identical apart from a multiplicative constant. In such a case, we would obviously change the basis to make the new leakage zero. If we have a solution which does not satisfy this orthogonality condition, we can bring it about in two steps. First, choose an overall phase for the α's so that $\sum \alpha_i^\star g_i$ is real. Then, carry out a rotation in the $g - \alpha$ plane by an angle θ satisfying $\tan\theta = \sum \alpha_i^* g_i / (\sum (g_i g_i^\star - \alpha_i \alpha_i^\star)$. This rotation has been so chosen that it makes the leakage ”orthogonal” to the gains, in the sense required above. Even after this is done, we still have the freedom to define the phase zero independently for the two orthogonal states. This is because we are only dealing with unpolarized sources. Of course, if we had a linearly polarized calibrator, the relative phase of right and left circular signals would not be arbitrary.

A more geometric view of this degeneracy is obtained when we think in terms of the Poincaré sphere representation of the states of polarization of all the feeds. The cross correlation between the outputs of two feeds, both of which receive unpolarized radiation, has a magnitude equal to the cosine of half the angle between the representative points on the sphere. Measurements of all such cross correlations with unpolarized radiation fixes the relative geometry of the points on the sphere, while leaving a two parameter degeneracy corresponding to overall rigid rotations of the sphere. This degeneracy can be lifted by the measurement of one polarized source at many parallactic angles.

Finally, we note that for the purpose of correcting the observations of unpolarized sources for the effects of non-identical feed polarization, the degeneracy is unimportant, because the correction factor is precisely the right hand side of Equation 7.3 which is unaffected by all the transformations we have discussed.

7.7 Conclusions

Rogers (1983) pointed out that non ideal feed polarizations of the individual antennas of a radio interferometer can result into closure errors in the *co-polar* visibilities. In this chapter we described and demonstrated a method to measure the polarization leakage of individual antennas using the nominally *co-polar* visibilities for an unpolarized calibrator. This method can therefore be used as a useful tool for studying the polarization purity of the antennas of radio interferometers from the observations of unpolarized calibrators. However, since only unpolarized calibrators are used, the actual solution for the leakage parameters is subject to a degeneracy. This degeneracy does not affect the correction of the visibilities and can be used to remove the closure errors due to polarization leakage. Massi et al. (1997) have shown that such polarization leakage induced closure errors in the data from the EVN is the dominant effect of instrumental polarization. For the EVN, this effect can be seen as a reduction in the dynamic range of the images. Our method can be used for such data to remove these closure errors for unpolarized sources.

The general elliptic state of the polarization of radiation can be represented by a point on the Poincaré sphere. The phase difference between three coherent sources of radiation but with different states of polarization goes by the name of Pancharatanam or geometric phase in the optics literature. We interpret the *co-polar* visibilities with polarization leakages on the Poincaré sphere and show that the polarization induced closure phase errors in radio interferometers is same as the Pancharatanam phase of optics. The antenna based leakages also map to points on the Poincaré sphere and the ambiguity in the solution can be understood as a rigid rotation of the Poincaré sphere, which leaves the leakage solutions unchanged relative to each other.

Chapter 8

Conclusions

This dissertation presented the work done towards low frequency study of a sample of new candidate Galactic Supernova remnants (SNRs). Details of the observations of this sample of new candidate SNRs, data calibration, analysis and interpretation were presented. A number of other sources are visible in the $\sim 1^\circ.4$ field of view of these observations, and the nature of some of these sources was also discussed. This work constitutes one of the first observations using the imaging capabilities of the Giant Meterwave Radio Telescope (GMRT), which is predominantly a low frequency instrument. The GMRT has only recently come to a stage where it can be used for mapping complicated fields like the ones studied in this dissertation. This required system debugging, system parameter measurements, calibration and understanding of the instrument, which in-turn led to the development of data analysis techniques and algorithms and related software. Details of instrumental calibration, debugging, related software and algorithm development were also presented. A new method for the computation of polarization leakage using *only* the *co-polar* visibilites was also described. Polarization leakage manifest themselves as closure errors in the *co-polar* visibilities and this method can be used to correct for such closure errors.

8.1 Using the Giant Meterwave Radio Telescope

The GMRT was in a state of being debugged and the hardware as well as the software was unstable during the course of this dissertation. Consequently, a large fraction of time was spent in understanding the system, debugging the hardware and software and in making astronomical observations for instrumental calibration and measurement of various system parameters.

8.1.1 Testing and debugging

Measurement of the antenna locations to an accuracy of a fraction of the wavelength (baseline calibration) as well as the measurement of the fixed delays suffered by the signals from various antennas is necessary for imaging with an aperture synthesis telescope like the GMRT. These measurements were made during the course of this work. The surveyed positions of the antennas, which were in error by > 1 m, were used to bootstrap the baseline calibration process. Visibility phase variation at 327 MHz as a function of Hour angle was used to improve upon these values to an accuracy of ~ 20 cm. Later, using 1420 MHz observations, in combination with the GPS measurements, antenna positions to an inferred accuracy of ~ 5 cm were measured. Antenna fixed delays were measured from the phase gradient across the band. Using the measured antenna positions and antenna fixed delays, software was written for off-line fringe stopping. This software was extensively used with the prototype 8-antenna correlator, which did not have the facility for fringe stopping, as well as during the early stages of the full 30-antenna correlator. Measurement of flux densities tied to standard flux scales also requires measurement of other system parameters like the primary beam attenuation, system temperature, etc. All these measurements were also made.

The digital FX type correlator of the GMRT was used for these observations for system calibration and later for scientific observations. In the early stages of the commissioning of the telescope and the correlator, data was corrupted due to problems in the hardware (servo, telemetry, antenna tracking, Local oscillators systems, etc.) as well as the software (on-line control, data acquisition system, fringe stopping and correlator control, data acquisition systems, etc.). Various tests/simulations were done to gain understanding of the working of the telescope/correlator. Several test observations were also done to identify problems and potential sources of data corruption – particularly in the correlator hardware (which often resulted in high closure errors in the data) and fringe stopping software.

8.1.2 Software development

It was clear that in these early stages of this new instrument, monitoring the data quality and the health of the system during observations was of paramount importance. Since there were many sources of data corruption and the manner in which they affect the data were varied, it was useful to develop techniques and software which can automatically identify as many of these problems, as early on in the data analysis process as possible.

Extensive software was developed for this purpose in the form of general purpose object oriented libraries, as well as in the form of programs for on-line and off-line data processing and display. In order to make application programs usable by others, a system of user interface and documentation was also developed. This software system now runs into $> 50,000$ lines of `C`, `C++` and `FORTRAN` code.

The complex visibility function, V, depends on a number of telescope parameters like the system temperature, sensitivity, antenna fixed delays, antenna positions, etc. Since the complex visibilities are a function of a multitude of parameters, and different debugging purposes require viewing V with respect to various quantities, a compact macro language was developed using which, data can be extracted from the GMRT visibility database. This was implemented in the form of a stand alone library as well as used in the application program named `xtract`. The content and the output format can be easily specified via this macro language, allowing easy access to astronomical/engineering data. This also allows easy interface to existing data display software for visualization. This was used extensively during the course of this work and is now being widely used for a variety of measurements like the system temperature, antenna sensitivity, antenna beam shapes, etc.

Equations for solving for antenna based complex gains using the complex visibility measurements for an unresolved source were derived using complex calculus. This led to a simple interpretation of the algorithm to solve for the antenna gains, which in turn led to the development of an algorithm which is robust in the presence of often large amounts of severely corrupted/bad data. This was done by (1) doing two passes to eliminate dead/bad antennas, (2) automatically eliminating out-lying points using robust averaging (where the mean value is computed by iteratively eliminating points which deviate from the mean by greater than a threshold value). This algorithm was also used to identify and flag corrupted data in a semi-automatic fashion. This algorithm, implemented in the program `rantsol`, was also extensively used and is now used by others for various measurements and for the phased array mode of operation of the GMRT (Sirothia 2000). It was also used for on-line data monitoring and for the semi-automatic identification of bad data. The output of this program was examined by another program (`badbase`) which identified consistently bad antennas and baselines in the data. This information was later used to flag data before using it for mapping. Data with high closure errors was often present on a few baselines out of a total of 435 baselines. The calibration program of `AIPS` is very sensitive to such bad data and the presence of about 10% bad baselines could result into poor solutions or sometimes no convergence at all. Automatic identification of such bad data was therefore important and a great time saver.

Signals from the two orthogonally polarized feeds can leak into each other at various point in the signal path. The planned Walsh switching of the signals from the two orthogonal feeds to minimized cross-talk has not yet been implemented for the GMRT. Besides, Walsh switching will not eliminate any leakage introduced before the switching point. Such leakage can result into closure errors even in the *co-polar* visibilities. This has been pointed out earlier by Rogers (1983) in the context of VLBA. A more detailed study of this was done by Massi et al. (1997) for European VLBI Network (EVN). Polarization leakage at a few percent level at most bands and at a much higher level at 150 MHz have been measured for the GMRT. The current GMRT correlator measures only the *co-polar* visibilities. A method was therefore developed to solve for the polarization leakage using *only* the *co-polar* visibilites for an unpolarized calibrator. The solutions, though have 3-parameter ambiguity (in the same sense as the phase ambiguity in Self-cal solutions), can be used to study the polarization properties of the individual antennas as well as to correct for the closure errors arising due to polarization leakage.

Other software developed during the course of this work includes software for time and bandpass calibration, data display, checking the consistency of the visibility database, fixing/editing data affected by problems in the system hardware/software, off-line correction of visibility phase due to antenna position offset/frequency offset, etc.

8.2 Candidate Galactic SNRs

The GMRT was finally used at 327-MHz to map a sample of seven fields selected from the surveys by Gray (1994a) and Duncan et al. (1997b) containing candidate SNRs. Most of these SNRs are large in size and their morphology is easily discernible at resolution of about an arcmin. These observations constitute the most sensitive, highest resolution observations for these and other sources which happen to be within the field of view. Partly due to system problems and ionospheric phase corruption, and partly due to the well known problem of deconvolution of extended sources, these extended sources tend to break up at higher resolution. Higher resolution images were therefore made and used only for small angular size objects.

Some of these objects are already listed in the SNR catalogue (Green 2000) based *only* on the morphological evidence from single high frequency observations. These GMRT observations establish the non-thermal nature of the emission and typical SNR morphology for six of these candidate SNRs and confirms them as Galactic SNRs. G001.4−0.0 is detected as a clear partial arc of emission, coincident with a faint arc of emission seen in the OH (1720 MHz) emission (Yusef-Zadeh et al. 1999). An OH (1720 MHz) spot has also been previously detected towards this direction and coincides with the arc seen in the radio continuum (Yusef-Zadeh et al. 1999). Recently it has been argued that the OH (1720 MHz) emission is a good tracer of the interaction between the shock front driven by the SNR blast wave and molecular clouds (Frail et al. 1994). The OH (1720 MHz) maser emission is distinguished from the OH maser emission at 1665, 1667 and 1612 MHz by the former being positionally and kinematically associated with SNRs while the later is associated with HII regions. OH (1720 MHz) emission associated with SNRs is believed to be due to the blast wave driving a shock in a denser molecular cloud. OH masers at 1665, 1667 and 1612 MHz cannot be produced under the same physical conditions and the absence of these lines in observations which detect the OH (1720 MHz) line favors this interpretation. The morphology of G001.4−0.0 in OH (1720 MHz) emission and radio continuum suggests that the arc of emission corresponds to the shock front. Absence of emission on the eastern side may be explained by the absence of such a cloud on that side. G003.8+0.3 is clearly visible as an incomplete arc of emission, embedded within a ring of thermal emission seen in the IRAS 60μm image. Its morphology is also clearly deciphered in the radio continuum image from the 11 cm 100-m Effelsberg survey (Reich et al. 1990). G004.8+6.2 is seen as an almost complete shell of emission just east of the shell-type Kepler's SNR. This SNR is also present in the field of view of a VLA observation and is also detected, although at a very low level, in the NVSS image of this region. The morphology and the measured integrated flux from the GMRT and VLA observations are in good agreement. G356.2+4.5 is a faint partial shell. This SNR is also visible in the NVSS image of this region, but the images at 327 and 1400 MHz suffer from the problem of missing flux, which did not allow the determination of the spectral index. However, the morphology is strongly in favor of this being an SNR. G356.3−1.5 is a barrel shaped SNR. The 834-MHz image of this source was severely affected by the grating response of a nearby strong source. However, the barrel morphology, with significant emission projected between the two rims, is clearly seen in the 327-MHz image. G004.2−0.0 is detected as an unresolved source. The spectra measured between 327 and 843 MHz for this source is consistent with it being a flat spectrum source. Presence of significant thermal emission in the IRAS 60μm image, however, suggests that this may not be an SNR but a flat spectrum thermal source.

8.3 Other sources in the fields

The $\sim 1^\circ.4$ beam of the GMRT at 327 MHz reveal a number of other compact, moderately resolved and as well as well resolved sources. The 1 arcmin shell type source G003.6−0.11, well resolved in the high resolution GMRT image, coincides with significant thermal emission and a H II region. A shell of emission, with three compact source superimposed is clearly visible. Resolved images of this source at 1.4 and 5 GHz were also made using older VLA observations by Gaensler (1999) and Yusef-Zadeh (data obtained from VLA achieves) respectively. Emission from the shell appears to be non-thermal while one of the compact sources is consistent with it being a symbiotic star (Seaquist & Taylor 1990). H I absorption observations towards this direction indicate that one of the compact sources and the shell are at similar distances while another compact source is a background object. Earlier, RRL emission has also been detected from this direction at ~ 5 GHz, but at a resolution which covers the entire source. Higher resolution continuum and RRL observations with the VLA are required to determine the true nature of this object.

Maps of the field containing G004.2−0.0 and G356.3−1.5 reveal extended emission, coincident with previously classified UC H II regions. Recently, such extended emission has been detected around a number of UC H II regions using the VLA in D-array configuration (Kurtz et al. 1999; Kim & Koo 2001). This extended component was not detected earlier since earlier observations were done in the B- or A-array configurations at high frequencies which were insensitive to large scale emission. The GMRT offers a unique advantage in imaging such sources in terms of providing high resolution *and* simultaneous sensitivity to emission at large scales. Such extended emission, if associated with the UC H II regions, can mitigate the “age problem” for these objects (de Pree et al. 1995, and reference therein).

A linear structure, seen in the field G356.3−1.5, is similar to other linear structures in few other observations in the Galaxy (Gray 1996). Higher resolution imaging of this feature is required to determine its physical properties.

8.4 Future directions

This work demonstrated and extensively used the imaging capabilities of the GMRT at low frequencies. The GMRT provides high resolution along with sensitivity to relatively large angular scales (~ 25 arcmin) - both of which are of crucial importance when mapping complex fields like the Galactic plane. All maps reveal a rich variety of objects in the field. For many of them, these observations constitute the first low frequency observations and reveal features not known from higher frequency observations. Sensitive high resolution observations in the Galactic plane with the GMRT is therefore expected to give rich scientific dividends. Spectral information is often a crucial ingredient for understanding the physical properties of these objects. As a future, possibly Observatory Project, a high resolution multi frequency survey of the Galactic plane with the GMRT will be of great interest.

It is clear that the role of magnetic field is as important as the kinetic energy of the relativistic electrons in explaining the emission from typical SNR. Measurements of the magnitude of the magnetic field for some of the SNRs reveal magnetic field amplification of the ambient by $2-3$ orders of magnitude. However these observations are few and far-in-between (e.g. Claussen et al. 1997; Brogan et al. 2000). High resolution images of many SNRs reveal compact sources embedded in the diffused larger scale emission from the SNR. If these objects are background sources, rotation measure (RM) measurements against these sources can provide a measure of the magnetic field for a larger sample of SNRs, which will be valuable input to the theoretical models to explain the magnetic field amplification.

Distances to many Galactic SNRs are poorly determined. Errors of a factor of 2 or more are frequently found in the quoted distance (often using the Σ-D relation (Case & Bhattacharya 1998, and references therein)). Distance estimated using the velocity structure of H I absorption profiles towards SNRs in combination with the Galactic rotation model, often provides a more reliable distance estimates. Such observations with the GMRT to determine the distance to a large sample of SNRs will be very desirable.

The 327 MHz images of the UC H II regions in the field of view of some of the images presented here reveal, somewhat unexpectedly, reasonably extended and strong emission around the compact cores. Such extended emission has also been recently detected at higher frequencies using the VLA (Kurtz et al. 1999; Kim & Koo 2001). The exact nature and the mechanism that could sustain such large scale (few pc) emission is far from clear. The GMRT images are the first low frequency images of these objects at resolutions comparable to those at higher frequencies. Such observations of a sample of UC H II, preferably at 327, 610 and possibly at 1420 MHz, which are readily doable with the GMRT in its present state, are highly desirable and will almost certainly pay rich scientific dividends in this field. In particular, the proposed model to explain the extended emission till low frequencies (see Chapter 6 and Kim & Koo (2001)) appears to have "preferred arrangement" where a massive star is formed off-centre from a hot core which is in-turn embedded in a lower density molecular cloud. If a large fraction of UC H II do show extended emission, a more refined model may be required which can relax the requirement of this preferred arrangement of the components.

Measurement of the low frequency turn-over below 100 MHz, due to free-free absorption by the wide spread extended low density warm ionized medium (ELDWIM) in the Galaxy, provides information about the continuum optical depth towards various lines of sight in the Galaxy. The path lengths and filling factors derived from the low frequency radio recombination lines (RRL), detected in almost every direction in the inner Galaxy (Roshi & Anantharamaiah 2000), suggests that the gas may be the extended low density HII envelopes surrounding higher density HII regions (Anantharamaiah 1985b, 1986). Also, the parameters of this gas, derived from RRL observations and the low frequency turn-over in the SNR spectra, are very similar, suggesting that the same gas is responsible for the RRL emission and the low frequency turn-over in SNR continuum spectra. If we assume that the properties of the ionized gas derived from these observations is typical, then we can expect to detect RRLs through stimulated emission due to the background radiation of SNRs at 330 and 1420 MHz. Such a detection will directly give the (negative) line optical depths at the two frequencies. High resolution RRL and continuum observations at low frequencies towards extended but strong SNRs will make tremendous advance in this area. All previous studies either had poor sensitivity or poor resolution (or both!) making it impossible to connect the absorption or RRL emission to known thermal sources. The GMRT and the VLA provides the required resolution at 327, 610 and 1420 MHz and are sensitive enough for these observations.

8.5 Some thoughts on the role of software for the GMRT

Mapping at low frequencies is inherently a more compute intensive job. The algorithms for eliminating the distortions due to large field of view require substantially higher computing. The yet to be developed technique for phase calibration in the presence of non-isoplanatic ionosphere is bound to further increase the requirement on computing power. These computational challenge can be handled by parallelizing the imaging and phase calibration algorithms. This can be done either on a dedicated high performance computers (work on this is already in progress in `AIPS++`) or by using a network of standalone, reasonably fast computers connected via fast data link (distributed computing). The advantage in the second approach is that it will be accessible to a larger community at a relatively cheaper price.

Deconvolution errors in the presence of extended emission, abundantly present in the Galactic plane, will be significant (Briggs 1995). Apart from generating algorithm related artifacts, the residuals are also correlated with the sources in the field indicating systematic errors in the model image (or equivalently, deconvolved image). One of the important pieces of information, not used in the deconvolution algorithms is that the extended emission has finite correlation length, which can vary across the image. Any algorithm which uses this information is likely to perform much better in terms of image fidelity. Also, most iterative deconvolution algorithms stop the iterations when the brightest component is comparable to the expected thermal noise. This stopping criterion is good for compact emission. However, for extended emission, this leaves correlated flux which is within the estimated noise level.

Field of view and the scale of radio emission at low frequencies is relatively large. Conventional deconvolution algorithms (CLEAN or MEM based), which treat each pixel in the image as an independent degree of freedom (zero correlation length), produce the well known instabilities and ”breaking up” of extended emission. A generalization of the MEM and multi-scale deconvolution algorithms using a pixel model with a finite correlation length (Pixon), would drastically reduce the number of degrees of freedom required to represent the image (Pina & Puetter 1993; Puetter & Pina 1994). Development of algorithms for the deconvolution of images made using radio interferometric telescopes is a very interesting and useful future direction of research in this field.

Mapping at low frequencies is relatively more difficult and a time consuming task. This is due to a combination of larger number of sources of data corruption and inherent difficulties in mapping at low frequencies (see Chapter 4). Refining the techniques and methodology for data calibration and analysis described in this dissertation, with the ultimate goal of developing techniques for automatic data flagging, is an interesting future direction of research, particularly in the context of low frequency instruments like the GMRT and the future instruments like the Low Frequency Array (LOFAR) and

Square Kilometre Array (SKA). Software developed during the course of this work produces information about corrupted data, at least for the calibrator scans. Development of supporting software to automatically identify systematic patters (like consistently bad baselines/channels) and transform this information into flagging tables directly readable by mapping software is highly desirable. Similarly, development of software to generate on-line flagging information based on the information of the health of various systems is required to improve the data quality. Combination of these automatic on-line and off-line flagging information will go a long way in improving the data quality and reduce the time it takes to map with such data. Work on these lines will be almost *necessary* for large scale mapping projects like multi-frequency surveys of the Galactic plane.

The software for on-line control of the telescope and the electronics is complex, requiring a large number of settings to be done for a typical observation. Complexity of this software for the GMRT at present is directly visible to the end user - something which is neither desirable nor necessary. Design and development of a integrated interface, which presents an astronomically useful view of the instrument (antenna pointing, tracking, frequency/bandwidth selection, observing schedule, etc.) will go a long way in making it easier to use the instrument as well as reduce possibility of human errors during observations.

Online data display for the GMRT is as good as missing. The data acquisition software as well as the on-line telescope control software, however, provides enough hooks from where the relevant information can be tapped and displayed online for a much improved monitoring of the system as well as the data. This again requires an integrated system of software, which can perform some on-line data processing and display. The former (on-line data processing software), to a large extent, was developed during the course of this work and is currently usable. Development of the latter (display software) is still in infancy and requires further work.

All the research and development suggested above, which ultimately also requires non-trivial software development, must be done in a well thought out manner. This usually requires participation of a number of people with varied interests and skills and at different points of time. A carefully thought-out underlying software design, for long term use and development of the software, is therefore necessary. In my opinion, a patchy ad hoc development of potentially unrelated stand-alone software, developed by people with different skills and style of coding (possibly based on old software technology and design techniques), at different times, is unlikely to be useful in the long run and will be a waste of enormous human and computing resources. Observational astronomy and related instruments have moved into a regime which is dominated by use of complex software which is not always hidden from the end user (particularly when directly using complex instruments like the GMRT). In the context of computer language design, it is said, "*The connection between the language in which we think/program and the problems and solutions we can imagine is very close. For this reason restricting language features with the intent of eliminating programmer errors is at best dangerous*"[1]. Similarly, I reckon, the connection between the problems and solutions astronomers can imagine, is closely related to their perception of the capabilities of the available data analysis software. Challenging new observations, almost by definition, require new capabilities in data analysis software and instrumentation. Aspiring and practicing observational astronomers, who like this kind of research, will therefore gain from learning new software design and development techniques. In my experience, these are not fancy tools which can be dispensed with, but actually result into stable, easy to modify and debug, and hence reliable software which in the long run, is a big time saver as well. Fluency in using/developing/modifying software gives the freedom of thought in research, which is of paramount importance in forging new areas of research – and going where few (or none) have gone before.

[1] Bjarne Stroustrup, designer of the `C++` language

Appendix A

The user interface for off-line applications

A.1 The User interface commands

The user interface of all application programs by default presents a list of keywords to which the application is sensitive. This is presented as a list of variables of an embedded interactive shell. The user can set, reset, load, save, etc. the values of these keywords using the basic shell commands in an interactive shell. In general, keywords can be assigned a list of comma-separated values. The number of values that a keyword expects can be found via the shell-command `'?'`. The value of a keyword can be set by a command of type `<KeyWord>=[<Val0>[,<Val1>[...]]]` and can be reset by omitting the values in such commands (command `<KeyWord>=`). The shell-command `help` provides the basic help about the shell itself and prints following on the screen:

```
Commands in the interactive mode:

Use <Key>=<Val1,Val2,..> to set value(s) for a keyword
Use <Key>=<RETURN> to unset value(s) for a keyword

 inp         : To see the various keywords and their values
 go          : To run the application
 gob         : To run the application in background
 cd          : Change working directory
```

```
  help        : This help
  ?           : Information on the type of the keyword
  explain     : Detailed help, optionally of keywords/task [[Key][:Task]]
  save        : Save the values, optionally in a file
  load        : Load the values, optionally from a file
  edit        : Use an editor to (un)set the values
  quit        : Quit the application

Any other input will be passed to the system shell
```

These commands form the standard set of shell-commands available from all applications. However, the user interface libraries provide mechanisms for application programmers to add application specific shell-commands as well as alter the behavior of the basic shell-commands. Hence, there may be a few extra commands which may be application dependent and will change from application to application. However, the `help` command will automatically always show all the commands available for a given application.

Following is a short description of the shell commands:

- Command `inp` displays the current setting of the keywords.
- Command `go` signifies the end of the interactive session. After this commands is issued, the values of the keywords set by the users are used by the application internally and the execution of the main program proceeds.
- Command `gob` is similar to `go` except that it will run the application in the background and print the process ID (PID) number of the background process on the screen (also see section A.2).
- Command `cd` changes the current working directory within the interactive shell.
- Command `'?'` gives some basic information about the type and the number of values the keywords expects.
- Command `explain` gives as detailed a help about the application and the keywords as the author of the application has cared to write in the help file. These help files are located in the directory specified by the environment variable `GDOC` (see section A.2).

- Command `save` saves the current setting of the keywords in a file. By default, these values are saved in a file named `./<Application Name>.def`. If a file name is supplied as an argument of this command, the values will be saved in the file. this command.

- Command `load` is the conjugate of `save` - by default it loads the settings for the keywords from the file `./<Application Name>.def`. If this file is already present when the application is started, it is loaded automatically. Alternatively, it can load settings from a file provided as an argument to the `load` command.

- Command `edit` allows user to edit the keyword values in an editor of choice specified by the environment variable `EDITOR` (see section A.2).

- Command `quit` quits the interactive session without executing the application.

All inputs to the interactive shell, which are not any of the above mentioned commands or any of the application specific commands, are passed to the underlying Operating System (OS) user shell. Hence, most of the native OS commands shall still be available from this shell. (Users however must be aware that certain OS shell commands like "`setenv`" (for `csh` users) or "`export`" (for `bash/sh` users) will seem to work, but will not have the desired effect).

As mentioned earlier, the values of the keywords can be a list of comma-separated values. The expected number of values will be reported by the shell-command `'?'` along with the type of the values, enclosed in '`[ `' and '`] `' pairs. A blank set of square brackets ("`[]`") will be printed for keywords which can accept any number of values. Some keywords may accept values of mixed types (e.g., string, floats, integers). For such keywords, the reported type will be "`UNKNOWN`".

Comma is treated as a separator in a list of values for a keyword. To suppress its interpretation as a separator, it can to be "escaped" using the backslash ('\') before the comma. For example, if the value of a keyword `key` has to be set to a string `‘‘Funny, value with a comma’’`, it can be done using

```
key=Funny\, value with a comma
```

The characters '\', '`[`', '`]`', '=', which are part of the shell-command syntax, must also be escaped similarly to be used as part of the values of the keywords.

Numeric values of keywords can be arbitrary mathematical expressions. Following functions and constants can be used in these expression:

- Functions

  sin,cos,tan,asin,acos,atan,atan2,sinh,cosh,tanh,
  exp,ln,log,flog10,sqrt,fabs,floor,ceil,rint

- Constants

  1. `PI`: value of π
  2. `C`: speed of light in meters per second.
  3. `R2D,D2R`: multiplicative constants for conversion from Radians to Deg. and vice versa
  4. `H2R,R2H`: multiplicative constants for conversion from Hours to Radians and vice versa
  5. `SOL2SID,SID2SOL`: multiplicative constants for conversion from Solar to Sidreal time and vice versa

Numbers in the expression can be in any of the following representations:

- Integer format, real (float) format
- 1.0E-1 or 1.0e-1 (=0.1)
- 1.0D-1 or 1.0d-1 (=0.1)
- 1h10m0.1s: the time format - converts the number to seconds before using it.
- $1d1'1''$: The angular format - converts to arc seconds before using it.

  ($1d1' = 3660.0''$ and $-1d1' = -3660.0''$)

A.1.1 De-referencing mechanism

The user interface system allows the application programmers to define shell symbols which are treated as constants (i.e. their values cannot be modified by the user). These symbols are referred to as the `const symbols`. Some applications may load a number of frequently used values of various keywords as `const symbols` (e.g., the list of symbols reported by the `showfmt` command of the `xtract`[1] program). However, by default, none of the `const symbols` are presented to the user and its the responsibility of application program to add extra shell-commands for viewing the list of `const symbols`.

[1]http://langur.ncra.tifr.res.in/~sanjay/Offline/xtract

Values can be transfered from one keyword or a `const symbol` to another keyword. E.g. to transfer the i^{th} value from keyword `Key1` to a keyword `Key2`, one could use `Key2 = $Key1[i]`. `Key2=$Key1` will transfer all values of `Key1` to `Key2`.

A.1.2 File name convention

Most off-line applications can perform I/O using UNIX pipes. If the input file name begins with '<', the rest of the file name is treated as a command, the output of which becomes the input of the application. For example, to supply the output of a program `tmac` as the input of the program `xtract`, the `‘‘in’’` keyword of `xtract` must be set to ‘`<tmac`”. After the shell-command `go` is issued for `xtract`, the interface of `tmac` will be started and the keywords of `tmac` can then be set in the normal fashion. When the shell-command `go` is issued again, `tmac` will begin execution, and the output of `tmac` becomes the input of `xtract`. Till this time, execution of `xtract` would remain blocked, waiting for input from `tmac`.

Similarly, if the output file name begins with the '`|`' character, the rest of the file name is treated as a command, the input of which becomes the output of the off-line program.

By convention, a blank output file name implies that the output would go to the standard output stream (usually your screen) and a blank input file name implies that the input would be read from the standard input stream (usually your keyboard).

A.2 Customization

The user interface can be customized using the following environment variables.

- `GDOC`

  `GDOC` must point to the standard directory where documents explaining the various off-line data analysis programs are kept. The `explain` command will first look for the explanation file in the local directory and then in the directory specified by this variable. The name of the explanation file is constructed by appending the suffix `‘‘.doc’’` to the application name.

- `GERR, GOUT`

  `GERR` and `GOUT` variables are used when the application is run using the `gob` command (see section A.1). The standard output of the application will be redirected to the file specified by `GOUT` while the standard error stream will be redirected to the file specified by `GERR`. By default, these variables are set to `/dev/null`.

- `GCONF`

  Some applications may load frequently used setting for some keywords. These values are loaded as constants of the interactive shell and can be stored in a configuration file. Their values can be transfered to the application keywords by referring to their value by '$' mechanism (see section A.1.1). The path of the directory containing these configuration files is specified by the environment variable `GCONF`. The configuration filename is constructed by appending the suffix "`.config`" to the application name. If `GCONF` is not defined, the application looks in the directory specified by `GDOC`. If this variable is also not defined, or the configuration file is not found, the application will look for the configuration file in the current directory.

- `EDITOR`

  `EDITOR` environment variable is used to specify the name of the text editor to be used in the `edit` command (see section A.1). The default editor is `emacs`.

- `GDEFAULTS`

  The default values of keywords can be saved in "defaults file". `GDEFAULTS` variable specifies the directory where these files are stored. Such a file can be automatically loaded by the applications upon startup. The defaults file name is constructed by appending the suffix "`.def`" to the application name.

  By default, the application will look for the defaults file in the current directory. If a keyword appears in the "`.def`" as well as in the "`.config`" file, the keyword will be treated as a shell constant. This can be used to effectively produce specialized versions of an application program by writing an appropriated "`.config`", where keywords can have fixed values, not alterable by the user (e.g., a version of `xtract` which will read input from the shared memory of the GMRT data acquisition system).

The following two variables are effective only for versions of the user interface libraries which use the GNU Readline and the History libraries.

- `GHIST`

GHIST specifies the file in which the history of the commands issued in the interactive session is saved. This file will be common to all applications. The default history file is $HOME/.g_hist.

This is also the file from which all applications will load the command history.

- MAXGHIST

  MAXGHIST should be set to the maximum number of command history entries which the user wishes to save. By default this is set to 100.

A.2.1 The help keyword

All applications are sensitive to the keyword help (not to be confused with the shell command help described in section A.1). It is never displayed in the list of keywords. To use it, it must be specified as a command-line argument. Following is the list of values that can be set for this keyword on the command-line and their effect:

- help=noprompt

  The application runs in the non-interactive mode. This is useful when the application is run from a shell script.

  When run in this mode, value of all the keywords which needs to be set must be supplied on the command-line (the order of the command-line options is not important). The keywords must be fully spelled in the command-line options (i.e., no minimum-match will be applicable).

- help=explain

  This executes the explain command of the interactive shell (see section A.1) without starting the interactive shell.

  If a keyword is supplied within brackets ('(' and ')') immediately after the explain string (e.g. help=explain(out), help will be provided for the specified keyword alone. If an application name is also included within the brackets, separated from the keyword by a colon (':') (e.g. help=explain(out:xtract), help for the named keyword of the named application will be provided. If the keyword is skipped (but not the colon), entire help of the named application will be provided.

- help=doc

This results into an empty documentation file written on the standard output, in the required format, with a list of keywords to which the application is sensitive. This is for use by authors of the applications and to encourage them to not only write the documentation, but also in a uniform format.

- `help=dbg`

  Application programmers can define hidden keywords which are normally not displayed for the user, but will be used by the application internally. These keywords can be accessed as normal keywords by setting `help` keyword to the value "`dbg`".

Appendix B

`xtract`: Usage and programming with the library

This appendix describes the design of the program `xtract` and the macro language used to extract visibility and auxiliary data from GMRT LTA database. Section A.1 is intended for ”plain” users of the program. The `xtract` macro language parser is also available as a stand-alone library, which can be used in other applications. The internal design of the library is described in section B.3 and is targeted for more enterprising users, who will find if useful to extend this program. Section B.4 describes the application programmers interface (API) of the library. Section B.5 describes the mechanism to extend the list of data/parameters which can be extracted.

B.1 The macro language

The macro language encapsulates the fact that whatever numbers we need to extract from the visibility database are either antenna based, interferometer based (or equivalently, baseline based) and/or a function of time and/or frequency within the given observing band. One may want to extract data for a list of antennas, baselines, frequency channels with selection applied in time.

The macro language syntax is a hybrid of the implicit loops of the `write` statement of `FORTRAN` (see the manual for `FORTRAN`) and the format string used by the output functions of `C` (see documentation on `printf` in the manual for `C`). Three operators are defined in the language, namely `base`, `chan` and `ant`, which loop over a list of baselines, frequency channels and antennas respectively. The implicit loops loop over the *body* of the operators. The *body* is a list of semicolon (';') separated list of *elements* enclosed in pair of curly braces ('{' and '}'). Each operator must be followed by a *body* and the *elements* of the *body* can be another operator-*body* pair. Hence, nested loops are possible.

In the `xtract` program, the list of values for the operators is supplied as a list of comma (',') separated values for the keywords `baselines`, `channels`, and `antenna` respectively. An operator for time range selection is also required, but not explicitly defined. All macros are internally the *body* of this time range operator. The time range selection can be specified via the `timestamps` keyword.

Various *elements* which the syntax recognizes are listed in Table B.1. Some of these are independent of any operator, while others need to be part of the *body* of one or more operators. The *elements* and the operators required by these *elements* are also listed in the table.

Table B.1: List of *elements* which can be part of the *body* of operators in `xtract` macros

Elements	Operators Required	Description
`ua,va,wa`	`ant` (antenna based)	(u,v,w) co-ordinates of the antennas
`u,v,w`	`base` (baseline based)	u_{ij} (=$\mathtt{ua}_i - \mathtt{ua}_j$) for the baseline ij
`re,im`	`base,chan`	Real and Imaginary parts of the visibility
`a,p`	`base,chan`	Amplitude and phase of the visibility
`cno`	`chan`	Frequency channel number
`ha,ist,lst`	none	Hour Angle, IST time stamp and LST in hrs.
`az, el`	none	Antenna Azimuth and Elevation angles in degree
`delay,phs0, dphs`	`ant`	The delay in μs applied to the antennas at the delay cards, the fringe rotation phase, and the phase ramp applied at the output of FFT

`ua,va,wa` are the co-ordinates of the antenna in the (u, v, w) co-ordinate system in units of the wavelength of the center of the observing band and `u=ua`$_1$`-ua`$_2$, where the subscripts refer to the two antennas of a baseline.

The macro to produce a table of rows with Hour Angle (HA) value in the first column followed by two columns for the real and imaginary parts of the visibility at a single frequency for all selected baselines, would be

```
fmt=base{ha;chan{re;im};\\n}
```

The special element \\n represents the actual character that will appear at the given position in the output (which is the `NEWLINE` character here). The only other special element that this syntax currently allows is \\t (TAB).

The (*u,v,w*) values for each baseline can be added to each row of the table by the following macro

```
fmt=base{ha;u;v;w;chan{re;im};\\n}
```

However note that the following macro is in error

```
fmt=ha;u;v;w;base{chan{re;im};\\n}
```

This is because the *elements* `u,v,w` are a function of the baseline and they do not appear as part of the *body* of the `base` operator. The macro parser will generate an error message pointing out the possible error in this macro.

The *elements* can also be qualified by a `C`-styled `printf` format field. Hence, for example, if the value HA needs to be written with field length of 8 characters and precision of 3 digits, the `fmt` string would become

```
fmt=base{ha%8.3f;u;v;w;chan{re;im};\\n}
```

The format for the numbers can be of type 'f','g','G','e', or 'E' (see the documentation on `printf` function of `C` language for more details).

Various output formats can be generated by changing the order of loops and *elements* in this syntax. Here are some examples. Each of these will generate a table. The values in the various columns will be as given in the explanation.

- `fmt=base{ha;u;v;w;chan{re;im};\\n}`

  Column 1 will be the Hour Angle. Columns 2,3, and 4 will have the *u,v,w* values followed by $2 \times N$ columns for real and imaginary values for the N values that the `chan` operator can take. There will be one such row in the table for each value of the `base` operator.

- `fmt=ha;lst;\\n;base{u;v;w;chan{re;im};chan{a;p};\\n}`

  This format will generate a table with rows of unequal lengths.

  Row 1 will have only HA and LST values.

  Row 2 will have u,v,w in the first 3 columns followed by real, imaginary, amplitude and phase for all channels listed in the `chan` operator. There will be one such row for every value of the `base` operator.

- `fmt=ha;base{u;v;w};\\n;base{chan{re;im}};\\n`

  This macro will generate a table of set of two rows of unequal lengths per input data record.

  First row will have the HA and u, v, w values for each selected baseline.

  Second row will have the real and imaginary values of the visibilities for all channels of the `chan` operator and for all values of the `base` operator.

B.2 Output filters

The macro language is used by the application program `xtract` to extract data from the GMRT visibility database. Most common use of `xtract` is to extract a data in the form of an ASCII table for display and/or further processing (e.g., to compute the antenna pointing errors). The output of `xtract` can be supplied to another program in two ways.

By default, `xtract` writes the output on the standard output. Hence if `xtract` is started as

```
xtract | MyProg
```

the output of `xtract` will be piped to the standard input of the program named `MyProg`. The other, probably more convenient, method of piping data is to set the `out` keyword to '`|MyProg`'.

The output will be written in ASCII format, preceded by a simple header. Apart from other fields, the header contains information about the number of rows and columns and the labels for each of the columns. This header always ends with a string "`#End`", after which the data is written. A line beginning with '`#`' is also written per LTA-scan. It is hoped that users will utilize these facilities to generate more filters to process and display data externally.

If the output file name begins with a '*', the file name is constructed after stripping the initial '*' character and the data is written in binary format (floating point numbers of size determined by the operator `sizeof(float)` of `C` or `C++`). The data itself is preceded by the ASCII header mentioned above. Hence, `out=*tst.bin` will produce a file `tst.bin`, which will contain the output in binary format and `out=*|MyProg` will pipe the binary data to `MyProg`.

For convenience of usage, a filter has been incorporated on the output stream of `xtract` which will supply the data directly to the `QDP` line plotting package. This filter can be invoked by setting `out=>QDP`. The output, in this case will be displayed as a stack of line plots using `QDP`.

A more general and usable graphical interface to the multiplot features of the freely available line plotting program `Gnuplot` has been developed by (Kudale & Bhatnagar NCRA Tech. Rep. - in prepration). The data to this software can be supplied using the piping mechanism described above. A graphical user interface then allows the user to select the available baselines/antennas and plot them interactively in a flexible manner.

B.3 Internal design

The `xtract` macros are first interpreted and then compiled in the memory. This complied code is then executed for every input data record. The details about the compilation and execution of the format string are given below.

B.3.1 Macro compilation

The process of compilation of the format string involves two steps.

First, all the loops represented by the operators in the macro are exploded into a linked list (also called the symbol table), with each node of the list corresponding to a valid *element* of the language. Each *element* is represented in the memory by a structure of the following type:

```
typedef struct StructSymbType {
  char Name[NAMELEN];
  char Fmt[FMTLEN];
  int abc[3];
  unsigned int Type;
```

```
    float (*func)(char *,float **,int);
    float *fargv[NARGV];
    int fargc;
    float *ptr;
    struct StructSymbType *next;
  } SymbType;
```

All recognized *elements* (symbols) are tabulated in the memory in a temporary table, which is a list of structure of the following type:

```
  typedef struct TT {
    char *Name;
    unsigned int Class,Type;
  } TypeTable;
```

This table is hard-coded in the file `table.h` and is used only to validate the symbols in the macro. Once validated, the `Class` and `Type` information for this table is transfered to the actual symbol table and the temporary table destroyed.

Apart from the name of the *element* and the `C` styled format string, the nodes of the symbol table also have information about the mechanism to get the numeric value associated with the *element*. This information is in the field `Type` of the structure above. Valid types for the *elements* are listed in Table B.2.

Table B.2: Table of element types in `xtract` macro language

Type	Meaning
CHARType	Represents a character to output
FTYPE	Function type: the value will be returned by a call to the function `func`
PTYPE	Pointer type: the value will be in the buffer at the location pointed to by `ptr`

The `abc` field of the *element* structure shown earlier, holds the values of the three operators (`ant`,`base`, and `chan`) applicable to the *element*.

Before an element is added to the symbol table, a check is made to ensure that all the required operators (listed in Table B.1) are active. To generate this information about the required operators, *elements* are further categorized into one of the classes listed in Table B.3.

Table B.3: Table of valid classes of the *elements* of `xtract` macro language

Class	Operators Required
IV	None
AV	`ant`
BV	`base`
CV	`chan`
BCV	`base,chan`
ABCV	`ant,base,chan`

Once the element is validated for the required active operators, a new link is created in the symbol table and filled with the `Name`, `Type` and `Class` of the *element*. By this time, the loops (represented by the list of values associated with various operators) have already been exploded (i.e., a node created in the symbol table for each value of the operator). Information about the values of the operators is transfered to the symbol table for every value of the active operators and the values of the required operators are put in the `abc` array (passive operators are assigned a value of -1). By this time, if no error has occurred, it is assured that the syntax was correct and all the *elements* in the macro were recognized.

Second step in the process of compilation is to fill in the information about the mechanism to get the numeric values of each *elements* in the list. The `Type` of the element and, if required, the values in the `abc` array are used for filling in this information.

For *elements* of type `PTYPE` , the `ptr` field is made to point to the location in the memory where the required value is to be found. This type of *element* refer to particular values in the buffer in the memory and need the offsets in the buffer which can be computed using the `abc` array. The buffer in the memory is generally the buffer in which data records from the LTA-file is read. Examples of this kind of *elements* are IST, real/imaginary values of the visibility, etc.

For *elements* of type `FTYPE`, the `func` field is filled with a pointer to a function which will be called when the value of the element is required. If the computation of the value requires some data, the pointers to this data is put in the field `fargv` and the total number of such pointer is put in the field `fargc`. These will be passed as arguments to the function when the value of the element is required. The first argument passed to the function will be the name of the element. Examples of this kind of *elements* are HA, amplitude/phase of the visibility, etc.

For *elements* of type `CHARType`, nothing needs to be done. The name of such *elements* is the character that is to be copied to the output during execution.

B.3.2 Macro execution

The process of "execution" of the compiled list of *elements* is rather simple. The program steps through the entire list of *elements* and checks the type of each element on the list. If the type is `PTYPE`, the value of memory location to which `ptr` points, is copied to the output stream using the format in the `Fmt` field of the *element*. If the type is `FTYPE`, the function specified by `func` is called with `Name`, `fargv`, and `fargc` as the arguments. The value returned by this function is then copied to the output stream using the format in the `Fmt` field of the element. If the type is `CHARType`, the first character of the `Name` field is copied to the output stream.

Following is an example of a simple routine used for execution of the compiled macros:

```
/* $Id: xtract.tex,v 1.9 2000/02/18 03:58:24 sanjay Exp sanjay $ */
#include <stdio.h>
#include <fmt.h>

int ExecuteDef(FILE *fd,SymbType *P,float *buf,int len)
{
  SymbType *i;
  int N=0;

  for (i=P;i;i=i->next)
    {
     switch(i->Type)
       {
        case PType:
         {buf[N++]= *i->ptr;break;}
        case FType:
         {buf[N++]=i->func(i->Name,i->fargv,i->fargc);break;}
```

```
          case CHARType: return N;
          default:
            fprintf(stderr,"###Error: Unknown type in ExecuteDef\n");
         }
      }
   return N;
 }
```

If the output in required is the binary format, one can write an equivalent `Execute` routine, which will ignore the `Fmt` field and `CHARType` *elements* and output the values in the binary format.

B.4 Programming with the `xtract` library

The process of compilation and execution of the `xtract` macro described above is done via a stand-alone library. This section describes the Application Programming Interface (API) of this library.

The `C/C++` interface of this library is defined in `fmt.h`, which must be included in the code and linked to `libjump.a`, in addition to all other GMRT Off-line libraries (`liboff.a, libregex.a, libkum.a`).

B.4.1 Interpretation and compilation of the format string

The `xtract` macros are interpreted via the following function call:

```
int interpret(char *fmtString, struct fftmac *fm,
              Parameters *Params, SymbType *Inst)
```

The first argument is the macro as a NULL terminated string. Second argument is the `fftmac` (Bhatnagar 1997a)[1] structure which holds the various mappings for the *LTA* database (e.g., sampler to the *MAC* mapping, etc.). This structure must be filled using services provided by the GMRT Offline Library[2] (`getFFTMac method`). The third argument is a pointer to the structure of the type `Parameters`. This structure holds the various parameters which the library uses while executing the macro. Various fields of this structure are described in Section B.4.3. The value of some of the fields of this structure are defined by

[1]http://langur.ncra.tifr.res.in/~sanjay/Offline/gstruct

[2]http://langur.ncra.tifr.res.in/~sanjay/Offline/ltaobj

the user, while others are to be extracted from the LTA database. The fourth argument is a pointer to a structure of type `SymbType`. This is the table of *elements* mentioned earlier and must be initialized to NULL before being passed to this routine. A return value of less than `EOF` (-1), indicates a syntax error in the macro.

Compilation of the macro string is done via a call to:

```
int Compile(SymbType *Inst,struct fftmac *fm,
            struct AntCoord *Tab, Parameters *Params)
```

The first argument is the symbol table returned by a call to `interpret`. It now points to the head of a linked list of nodes of type `SymbType`. The last node of this list is NULL. The second argument is the `fftmac` structure. The third argument is the table of antenna co-ordinates. This can be retrieved from the LTA database via the services provided by the GMRT Offline Library[3] (`getFFTMac method`). The fourth argument is a pointer to the `Parameters` structure. A return value of less than `EOF`(-1) indicates error in compilation of the macro. On successful compilation, it returns the size of the compiled symbol table in units of the size of the structure `SymbType`.

B.4.2 Execution of the compiled macro

If the interpretation and compilation of the macro was successful, the compiled macro can be executed via calls to a user-supplied function of signature

`int Exec(FILE *fd, SymbType *Inst, float *Buf, int ProgSize)` `fd` refers to the output file already opened for writing. `Inst` is the symbol table returned by `interpret`. In case the output data is not to be written to any file, the user can write versions of this routine which will fill the data in the buffer `Buf`. `ProgSize` is the value returned by `Compile`.

The `data` field of the `Parameters` structure (see section B.4.3) must be made to point to the buffer in which the LTA-data buffers are read. To generate a regular stream of output, corresponding to each input data record, this function must be called every time a new LTA-data record is read.

Few types of `Exec` functions are provided in the library. These include:

- `Execute`

  It writes the output data to the `fd` file descriptor. It does not use the `Buf` pointer.

[3] http://langur.ncra.tifr.res.in/~sanjay/Offline/ltaobj

- `ExecuteDef`

  This writes the output data to the buffer pointed by `Buf`. The size of the this buffer must be big enough to hold one floating point number per node of the symbol table (return value of `Compile`). This does not use the file descriptor.

- `ExecuteQDP`

  This supplies output data to the `QDP` program via a pipe opened via the `libpipe.a` library. This uses the `Buf` pointer but does not use `fd`.

To generate any other functionality, the programmers need to write their versions of this function. The recommended route for writing a new function is to modify `Execute` or `ExecuteDef` functions.

B.4.3 The `Parameters` structure

The `Parameters` structure is of the following type:

```
typedef struct StructParamType{
   int Norm;
   int *BList, *SList, *AList, *CList;
   int  NBase,  NScans, NAnt,   NChan;
   int dBNBase, dBNChan, dBNAnt;
   int dBStartChan;
   int TimeOff, ParOff,DataOff;

   float Lambda;
   float sd,cd, TUnits;
   char *data;
} Parameters;
```

Various fields and their use is as follows:

- *int Norm*

  This must be set to 1 if the visibility data is to be normalized by the geometric mean of the self correlations. Otherwise this must be set to 0.

- `int *BList, *SList, *AList, *CList`

These are pointers to the user selected list of the baseline, scan, antenna and channel numbers respectively. The list of channel numbers must be 0-relative and not the absolute channel index of the data base (which could start with number between 0 to maximum number of channels).

Typically, the user selects the baselines and antennas via the baseline/antenna names. These are supplied as strings by the user. Two functions, `MkBaselines` and `MkAntNo`, are provided to convert these stings to a list of bit fields in which the bits corresponding to the selected baselines are set to 1. Another routine `toIntList`, is provided to convert the bit fields to list of integers representing the selected baselines. These functions are available in the library `liboff.a` and are described in Appendix A of GMRT Offline Library[4].

- `int NBase, NScans, NAnt, NChan`

  These are the lengths of `BList, SList, AList` and `CList`.

- `int dBNBase, dBNChan, dBNAnt`

  These are the number of the baselines, channels and antenna in the data base.

- `int dBStartChan`

  This is the number of the first frequency channel in the data base.

- `int TimeOff, ParOff, DataOff`

  These are the offsets within the LTA-data buffer to locate the time stamp, the auxiliary parameters, and the visibility data itself. These offsets can be extracted from the *global header* of the database.

- `float sd,cd`

  These are the values of $\sin(\delta)$ and $\cos(\delta)$ where δ is the declination of the pointing center of the telescope. These are used for the calculation of the (u, v, w) coordinates during execution.

- `float TUnits`

  This is the multiplication factor used to convert the time stamp in the data to seconds of time. This is also extracted from the *global header*.

[4]http://langur.ncra.tifr.res.in/~sanjay/Offline/ltaobj

- `float Lambda`

  This the wavelength of the observing frequency in meters.

- `char *data`

  This is the pointer to the beginning of the LTA-data buffer.

B.5 Adding new *elements* to the syntax

To add a new *elements* to the `xtract` macro language, one needs to define the values of `Name`, `Class`, and `Type` of the new symbol in the table of valid *elements*. This is done by adding to the table in the file `table.h` (make sure the last element of this list is left unaltered).

One also needs to add a piece of `C`-code, which will fill the required fields of the structure `SymbType` (depending upon the `Type` of the element – the `ptr` field for `PTYPE` *elements* and the `func, fargv,` and `fargc` fields for `FTYPE` *elements*). It is the responsibility of the programmer to make sure that this code is correct in terms of getting the numeric value of the *elements*. Also, the programmer must make sure that this code is compatible with the `Type` of the *element*. Failing to do so will either generate wrong values or crash the program at the time of execution. This code is to be added in the function `Compile` in the file `Compile.c`. The application will need to be rebuilt for the new symbol to be recognized in the `fmt` syntax.

Appendix C

Antenna/baseline naming convention

C.1 Antenna naming convention

An antenna can be specified by the index of the antenna or a regular expression. A full antenna name consists of three hyphen ('-') separated fields. The first field is the antenna name, the second is the side band name and the third is the polarization name. Each of the three fields can be a regular expression. All missing fields after the last specified field are replaced by "wild card" regular expressions.

E.g., a fully qualified name for `C11`, upper side band, 175-MHz polarization channel (nominally the LL polarization) can be expressed as:

`C11-USB-175`

All central square antennas, with upper side band and 130-MHz (nominally the RR polarization) polarization channel can be expressed as:

`C.+-USB-130`

(Here '.' matches one instance of any character and the '+' operator operates on '.' zero-or-more number of times. Hence ".+" is equivalent to the '*' wild card character. This is the POSIX regular expression syntax).

All central square antennas with upper sideband and either polarization channel can be expressed as:

`C.+-USB-.+`

or simply

`C.+-USB`

Finally, all central square antennas without any selection on the side band and polarization channel can be expressed as:

`C.+-.+-.+`

or simply

`C.+`

All above examples, but with only arm antennas can be expressed by replacing "`C.+`" in the above examples by "`[EWS].+`".

C.2 Baseline naming convention

Baselines can be specified by the index of the baseline or a regular expression describing a baseline name.

A full baseline name is composed of two antenna names separated by a colon (':'). A fully qualified baseline name between the upper-side band, 175-MHz polarization signals from antennas `C11` and `C12` would be

`C11-USB-175:C12-USB-175`

Any of these fields can be regular expressions. Hence to choose all baselines with antenna `C11` upper side-band signals from either of the polarization, one would use the baseline name as:

`C11-USB-.+:.+`

If only the first field of antenna name is given, the others are taken to be the wild card characters.

If second fully qualified antenna names is missing from the baseline name, it is also replaced by wild card.

These selections will exclude all self correlations. Also, if a baseline has already got selected in a previous selection, it will be excluded from all later selections.

To select the self correlations, one must add 'A' to be beginning of the antenna names. In such a case, the name of the second antenna is redundant and therefore not required.

C.2.1 Examples

1. Baseline name to select all baselines with with `C11` = `C11`

2. Baseline name to select the self correlation of `C11` = `C11:C11` or `AC11`

3. Baseline name select the self correlation of `C11`, 130-MHz polarization channel from both side bands = `AC11-.+-130`

4. Baseline name to select *all* self correlations = `A.`

5. Baseline name to select *all* lower side-band baselines with `C11` = `C11-USB-.+:.` or `C11-USB-.+.`

6. Baseline name to select *all baselines in the database* = `.`

7. Baseline name to select *all* central square baselines with `C02-USB-175` = `C02-USB-175:C.+`

8. Baseline name to select *all* baselines of `C02-USB-175` with only arm antennas = `C02-USB-175:[EWS].+`

Appendix D

Computation of antenna based complex gains

The normalized cross-correlation function (the correlator output), measured by an interferometer using two antennas labeled by i and j, in the limit $I \ll T_i^s/\eta_i$, can be written as:

$$\rho_{ij}^{Obs} = \rho^{Obs}(u_{ij}, v_{ij}, w_{ij}) = \iint_{-\infty}^{+\infty} I(l,m)\sqrt{\frac{\eta_i \eta_j}{T_i^s T_j^s}}\; e^{2\pi\iota(u_{ij}l + v_{ij}m + w_{ij}\sqrt{1-l^2-m^2} + \phi_i - \phi_j)} \frac{dl\;dm}{\sqrt{(1-l^2-m^2)}} + \epsilon_{ij} \tag{D.1}$$

where $I(l,m)$ is the sky surface brightness, η_i is the sensitivity and T_i^s is the system temperature of the antenna i in units of Kelvin/Jy and Kelvin respectively, ϵ_{ij} is the additive noise on the baseline i-j, and ϕ_i is the antenna based phase of the signal. The rest of the symbols have the usual meaning.

In practice, however, the antenna based amplitude ($\sqrt{\eta_i/T_i^s}$) and phase (ϕ_i) are potentially time varying quantities. This could be due to changes in the ionosphere, temperature variations, ground pick up, antenna blockage, noise pick up by various electronic components, background temperature, etc. Treating the quantities under the square root in the above equation as the antenna dependent amplitude gains, these can be written as complex gains $g_i = a_i e^{-\iota\phi_i}$ where $a_i = \sqrt{\eta_i/T_i^s}$. For an unresolved source at the phase tracking center, variations in this amplitude will be indistinguishable from a variations in the ratio of η and T^s.

In terms of g_is, we can write Equation D.1 as

$$\rho_{ij}^{Obs} = g_i g_j^{\star} \rho_{ij}^{\circ} + \epsilon_{ij} \tag{D.2}$$

where

$$\rho_{ij}^{\circ} = \int_{-\infty}^{+\infty}\int_{-\infty}^{+\infty} I(l,m)\, e^{2\pi\iota(u_{ij}l+v_{ij}m+w_{ij}\sqrt{1-l^2-m^2})} \frac{dl\ dm}{\sqrt{(1-l^2-m^2)}} \tag{D.3}$$

The use of the word "antenna based gains" for g_is result in confusion for many and needs some clarifications. g_is are called complex "gains" since they multiply with the complex quantity ρ_{ij}. For an unresolved source, $|g_i|$ represents the fraction of correlated signal and $arg(g_i)$ represents the phase of the correlated part of the signal from the antenna with respect to the phase reference (usually the reference antenna). It is in this sense that it is referred to as "antenna based" gains. However, as defined here, they include T^s which in turn includes the sky background temperature. They are therefore a function of direction in the sky. However, here we assume that the angular scale over which g_is vary is larger than the antenna primary beam (isoplanatic case).

For an unresolved source at the phase tracking center, all terms in the exponent of ρ_{ij}° are exactly zero. ρ_{ij}° in this case would be proportional to the flux density of the source.

Assuming that the antenna dependent complex gains are independent, with a gaussian probability density function (this implies that the real and imaginary parts are independently gaussian random processes), one can estimate g_is by minimizing, with respect to g_is, the function S given by

$$S = \sum_{\substack{i,j\\ i\neq j}} \left|\rho_{ij}^{Obs} - g_i\ g_j^{\star}\ \rho_{ij}^{\circ}\right|^2 w_{ij} \tag{D.4}$$

where $w_{ij} = 1/\sigma_{ij}^2$, σ_{ij} being the variance on the measurement of ρ_{ij}^{Obs}

Dividing the above equation by ρ_{ij}° (the source model, which is presumed to be known – it is trivially known for an unresolved source), and writing $\rho_{ij}^{Obs}/\rho_{ij}^{\circ} = X_{ij}$, we get

$$S = \sum_{\substack{i,j\\ i\neq j}} \left|X_{ij} - g_i\ g_j^{\star}\right|^2 w_{ij} \tag{D.5}$$

If ρ_{ij}° represents the structure of the source accurately, X_{ij} will have no source dependent terms and is purely a product of the two antenna dependent complex gains.

Expanding Equation D.5, we get

$$S = \sum_{\substack{i,j \\ i \neq j}} \left[\, |X_{ij}|^2 - g_i^\star g_j X_{ij} - g_i g_j^\star X_{ij}^\star + g_i g_i^\star g_j g_j^\star \right] \, w_{ij} \tag{D.6}$$

Evaluation $\frac{\partial S}{\partial g_i^\star}$ and equating it to zero [1], we get

$$\frac{\partial S}{\partial g_i^\star} \;=\; \sum_{\substack{j \\ j \neq i}} \left[-g_j X_{ij} w_{ij} + g_i g_j g_j^\star w_{ij} \right] \;=\; 0 \tag{D.7}$$

or

$$g_i \;=\; \frac{\sum\limits_{\substack{j \\ j \neq i}} X_{ij} g_j w_{ij}}{\sum\limits_{\substack{j \\ j \neq i}} |g_j|^2 \, w_{ij}} \tag{D.8}$$

This can also be derived by equating the partial derivatives of S with respect to real and imaginary parts of g_i as shown in Section D.3.

Since the antenna dependent complex gains also appear on the right-hand side of Equation D.8, it has to be solved iteratively starting with some initial guess for g_js or initializing them all to 1.

Equation D.8 can be written in the iterative form as:

$$g_i^n \;=\; g_i^{n-1} + \alpha \left[g_i^{n-1} - \frac{\sum\limits_{\substack{j \\ j \neq i}} X_{ij} g_j^{n-1} w_{ij}}{\sum\limits_{\substack{j \\ j \neq i}} \left| g_j^{n-1} \right|^2 w_{ij}} \right] \tag{D.9}$$

where n is the iteration number and $0 < \alpha < 1$. Convergence would be defined by the constraint

$$|S_n - S_{n-1}| < \delta \tag{D.10}$$

(the change in S from one iteration to another) where δ is the tolerance limit.

[1]Complex derivatives can be evaluated by treating g_i and $g_i^\star$ as independent variables. See (Palka 1990)

D.1 Interpretation of the equation

Equation D.8 offers itself for some intuitive understanding in the following way.

X_{ij} is a product of two complex numbers, namely g_i and $g_j^\star$, which we wish to determine. X_{ij} is itself derived from the measured quantity V_{ij}^{Obs}. Numerically speaking, each term in the summation of the numerator of Equation D.8 will involve g_i (via X_{ij}) and the multiplication of X_{ij} with $g_j w_{ij}$ would give g_i an effective weight of $|g_j|^2\, w_{ij}$. Since the denominator is the sum of this effective weight, the right-hand side of Equation D.8 can be interpreted as the weighted average of g_i over all correlations with antenna i.

In the very first iteration, when $g_j = (1, 0)$, the normalization would be incorrect since the numeric value of g_j, as it appears inside X_{ij} would be different from that used in the denominator of Equation D.8. However, as the estimates of g_js improve with iterations, the equation would progressively approach a true weighted average equation. The speed of convergence will depend upon the value of α and the convergence would be defined by the constraint in Equation D.10. In the ideal case when the true value of all g_is is known, right hand side of Equation D.8 also reduces of g_i.

Estimating g_i for an antenna, by averaging over the measurements from all baselines in which it participates (for a unresolved source) makes sense since for an N element array, g_i would be present in N-1 measurements (all the $X_{ij}|_{j=1,N;j\neq i}$) and the best estimate of g_i would be the weighted average of all these measurements. Proper weight for g_i, buried in each of the products X_{ij}, can be found heuristically as follows. g_i, estimated from the measurements of a given baseline, must obviously be weighted by the signal-to-noise ratio on that baseline. This is w_{ij} in the above equations. It must also be weighted by the amplitude gain of the other antenna making the baseline, namely g_j, to account for variation in antenna sensitivities and T^s. The total weight for g_i would then be $|g_j|^2\, w_{ij}$, the sum of which appears in the denominator of Equation D.8. Knowing that ideally $X_{ij} = g_i g_j^\star$, each of the $X_{ij}|_{j=1,N}$ must be multiplied by $g_j w_{ij}$ (to apply the the above mentioned weights to g_i), before being summed for all values of j and normalized by the sum of weights to form the weighted average of g_i. One thus arrives at Equation D.8 using these heuristic arguments.

D.2 Estimation of the system temperature (T^s)

For an unresolved source of known brightness I, in the limit $T^a \ll T^s$, $\rho_{ij}^\circ = I$ and Equation D.1 can be written as

$$\rho_{ij}^{Obs} = I g_i g_j^{\star} \approx I \sqrt{\frac{\eta_i \eta_j}{T_i^s T_j^s}} \tag{D.11}$$

where $\eta_i = A_e/2k_b$, A_e is the effective area of the dish, k_b is the Boltzman's constant and

$$|g_i| = \sqrt{\frac{\eta_i}{T_i^s}} \tag{D.12}$$

Hence, knowing η_i, T_i^s can be estimated from the amplitude of the antenna dependent complex gains.

All contributions to ρ_{ij}^{Obs}, which cannot be factored into antenna dependent gains, will result in the reduction of $|g|$. η remaining constant, this will be indistinguishable from an increase in the effective system temperature. Since majority of later processing of interferometry data for mapping (primary calibration, bandpass calibration, SelfCal, etc.) is done by treating the visibility as a product of two antenna based numbers, this is the effective system temperature which will determine the noise in the final map (though, as a final step in the mapping process, baseline based calibration can possibly improve the noise in the map).

In the normal case of no significant baseline based terms (ϵ_{ij}) in X_{ij}, the system temperature as measured by the above method will be equivalent to any other determination of T_i^s.

T^s can also be determined by recording interferometric data for a strong point source with and without an independent noise source of known temperature at each antenna. In this case

$$T_i^s = T_i^n \left(\frac{g_i^{ON^2}}{g_i^{OFF^2} - g_i^{ON^2}}\right) \tag{D.13}$$

where g_i^{ON} and g_i^{OFF} are the antenna dependent gains with and without the noise source of temperature T^n. Note that η_i does not enter this equation. Also, T^n should be such that $\sqrt{T^a/(T^n + T^s)} \geq 0.1$ to ensure that the correlated signal is measured with sufficient signal-to-noise ratio. For example, for P-band, a calibrator with P-band flux density > 5 Jy must be used.

D.3 Derivation of g_i using real and imaginary parts

g_is are complex functions. One can therefore write S in terms of g_i^I and g_i^p, the real and imaginary parts of g_i and minimize with respect to g_i^I and g_i^p separately. It is shown here that the complex arithmetic achieves exactly this and the results are same as that given by complex calculus. The superscripts I and R in the following are used to represent the real and imaginary parts of complex quantities.

Expanding Equation D.5, ignoring w_{ij}s and writing it in terms of real and imaginary parts we get

$$
\begin{aligned}
\sum_{\substack{i,j \\ i\neq j}} \left| X_{ij} - g_i g_j^\star \right|^2 &= \sum_{\substack{i,j \\ i\neq j}} \left[X_{ij} - g_i g_j^\star \right] \left[X_{ij}^\star - g_i^\star g_j \right] \\
&= \sum_{\substack{i,j \\ i\neq j}} \left[\left(X_{ij}^R + \iota X_{ij}^I \right) - \left(g_i^p + \iota g_i^I \right) \left(g_j^p - \iota g_j^I \right) \right] \\
&\qquad \left[\left(X_{ij}^R - \iota X_{ij}^I \right) - \left(g_i^p - \iota g_i^I \right) \left(g_j^p + \iota g_j^I \right) \right] \\
&= \sum_{\substack{i,j \\ i\neq j}} \left[\left(X_{ij}^R - g_i^p g_j^p - g_i^I g_j^I \right) + \iota \left(X_{ij}^I + g_i^p g_j^I - g_i^I g_j^p \right) \right] \\
&\qquad \left[\left(X_{ij}^R - g_i^p g_j^p - g_i^I g_j^I \right) - \iota \left(X_{ij}^I + g_i^p g_j^I - g_i^I g_j^p \right) \right] \\
&= \sum_{\substack{i,j \\ i\neq j}} S_0 S_0^\star
\end{aligned} \tag{D.14}
$$

where

$$
S_0 = \left[X_{ij}^R - g_i^p g_j^p - g_i^I g_j^I \right] + \iota \left[X_{ij}^I + g_i^p g_j^I - g_i^I g_j^p \right] \tag{D.15}
$$

Taking partial derivative of S with respect to g_i^p and reintroducing w_{ij}, we get

$$\begin{aligned}
\frac{\partial S}{\partial g_i^p} &= \sum_{\substack{j \\ j\neq i}} \left\{ \left[-g_j^p + \iota g_j^I\right] S_0^\star - S_0 \left[g_j^p + \iota g_j^I\right] \right\} w_{ij} \\
&= -\sum_{\substack{j \\ j\neq i}} \left[S_0 g_j + g_j^\star S_0^\star\right] w_{ij} \\
&= -2\sum_{\substack{j \\ j\neq i}} Re\left(S_0 g_j w_{ij}\right) \\
&= -2\sum_{\substack{j \\ j\neq i}} \left[\left(X_{ij}^R - g_i^p g_j^p - g_i^I g_j^I\right) g_j^p + \left(X_{ij}^I + g_i^p g_j^I - g_i^I g_j^p\right) g_j^I\right] w_{ij} \\
&= -2\sum_{\substack{j \\ j\neq i}} \left[X_{ij}^R g_j^p - X_{ij}^I g_j^I - g_i^p {g_j^I}^2 - g_i^p {g_j^p}^2\right] w_{ij}
\end{aligned} \tag{D.16}$$

Therefore,

$$\frac{\partial S}{\partial g_i^p} = -2\sum_{\substack{j \\ j\neq i}} \left[Re(X_{ij} g_j^\star) - |g_j|^2 g_i^p\right] w_{ij} \tag{D.17}$$

Equating $\frac{\partial S}{\partial g_i^p}$ to zero, we get

$$g_i^p = \frac{\sum_{\substack{j \\ j\neq i}} Re(X_{ij} g_j^\star w_{ij})}{\sum_{\substack{j \\ j\neq i}} |g_j|^2 w_{ij}} \tag{D.18}$$

Similarly

$$\frac{\partial S}{\partial g_i^I} = -2\sum_{\substack{j \\ j\neq i}} \left[Im(X_{ij} g_j^\star) - |g_j|^2 g_i^I\right] w_{ij} \tag{D.19}$$

Therefore the equivalent imaginary part of Equation D.18 is

$$g_i^I = \frac{\sum_{\substack{j \\ j\neq i}} Im(X_{ij} g_j^\star w_{ij})}{\sum_{\substack{j \\ j\neq i}} |g_j|^2 w_{ij}} \tag{D.20}$$

writing $g_i = g_i^p + \iota g_i^I$ and substituting for g_i^p and g_i^I from Equation D.18 and D.20 respectively, we get

$$g_i = \frac{\sum\limits_{\substack{j \\ j\neq i}} X_{ij} g_j^\star w_{ij}}{\sum\limits_{\substack{j \\ j\neq i}} \left|g_j\right|^2 w_{ij}} \tag{D.21}$$

This is same as Equation D.8, which was arrived at by evaluating a complex derivative of Equation D.5 as $\partial S/\partial g_i^\star$, treating g_i and $g_I^\star$ as independent variables. Evaluating $\frac{\partial S}{\partial g_i} = 0$ would give the complex conjugate of Equation D.21. Hence, $\partial S/\partial g_i$ gives no independent information not present in $\partial S/\partial g_i^\star$.

Bibliography

Altenhoff, W. J., Downes, D., Pauls, T., Schraml, J., 1979. *A&AS*, 35, 23

Anantharamaiah, K. R., 1985a. *Journal of Astrophysics and Astronomy*, 6, 203

Anantharamaiah, K. R., 1985b. *Journal of Astrophysics and Astronomy*, 6, 177

Anantharamaiah, K. R., 1986. *Journal of Astrophysics and Astronomy*, 7, 131

Anderson, M. C., Rudnick, L., 1993. *ApJ*, 408, 514

Baars, J. W. M., Genzel, R., Pauliny-Toth, I. I. K., Witzel, A., 1977. *A&A*, 61, 99

Becker, R. H., White, R. L., Helfand, D. J., Zoonematkermani, S., 1994. *AJ Supp.*, 91, 347

Belfort, P., Crovisier, J., 1984. *A&A*, 136, 368

Bell, A. R., 1978a. *MNRAS*, 182, 147

Bell, A. R., 1978b. *MNRAS*, 182, 443

Berry, M. V., 1987. *J. Mod. Opt.*, 34, 1401

Bhatnagar, S., 1997a. *The* `fftmac` *Structure*. Tech. rep., National Centre for Radio Astrophysics, Pune

Bhatnagar, S., 1997b. `xtract`*: A flexible data extraction progrm for GMRT visibility databse*. Tech. rep., National Centre for Radio Astrophysics, Pune

Bhatnagar, S., 1999. *Computation Of Antenna Dependent Complex Gains*. Tech. rep., National Centre for Radio Astrophysics, Pune

Bhatnagar, S., 2000. *MNRAS*, 317, 453

Bhatnagar, S., Nityananda, R., 2001. *A&A*, 375, 344

Bhatnagar, S., Rao, A. P., 1996. *Baseline and Delay Calibration*. Tech. rep., National Centre for Radio Astrophysics, Pune

Bisnovatyi-Kogan, G. S., Lozinskaia, T. A., Silich, S. A., 1990. *ApSS*, 166, 277

Bodenheimer, P., Woosley, S. E., 1983. *ApJ*, 269, 281

Born, M., Wolf, E., 1959 [and later eds]. *Principles of Optics* (Pergamon Press, Oxford)

Bracewell, R. N., 1986 [and later eds]. *Fourier transforms and its applications* (McGraw-Hill)

Branch, D., 1998. *Ann. Rev. of A&A*, 36, 17

Briggs, D. S., 1995. *High fidelity deconvolution of moderately resolved sources*. Ph.D. thesis, The New Mexico Institute of Mining and Technology, Socorro, New Mexico, USA

Brigham, O. E., 1988 [and later eds]. *Fast Fourier transform and its applications* (Prentice-Hall International)

Brogan, C. L., Frail, D. A., Goss, W. M., Troland, T. H., 2000. *ApJ*, 537, 875

Brown, G. E., Bethe, H. A., 1994. *ApJ*, 423, 659

Case, G. L., Bhattacharya, D., 1998. *ApJ*, 504, 761

Caswell, J. L., Haynes, R. F., 1987. *A&A*, 171, 261

Caswell, J. L., Kesteven, M. J., Bedding, T. R., Turtle, A. J., 1989. *Proceedings of the Astronomical Society of Australia*, 8, 184

Caswell, J. L., Lerche, I., 1979. *MNRAS*, 187, 201

Chengalur, J. N., 2000. *Subarray Operation at the GMRT*. Tech. rep., National Centre for Radio Astrophysics, Pune

Chengalur, J. N., Bhatnagar, S., 2001. *Astronomical Calibration of the GMRT Antenna Positions*. Tech. rep., National Centre for Radio Astrophysics, Pune

Chevalier, R. A., 1982. *ApJ*, 258, 790

Chevalier, R. A., Fransson, C., 1994. *ApJ*, 420, 268

Clark, B. G., 1980. *A&A*, 89, 377

Clark, B. G., 1999. In: *ASP Conf. Ser. 180: Synthesis Imaging in Radio Astronomy II*. p. 1

Clark, D. H., Caswell, J. L., 1976. *MNRAS*, 174, 267

Clark, D. H., Caswell, J. L., Green, A. J., 1973. *Nature*, 246, 28

Clark, D. H., Caswell, J. L., Green, A. J., 1975a. *Australian Journal of Physics Astrophysical Supplement*, 1

Clark, D. H., Green, A. J., Caswell, J. L., 1975b. *Australian Journal of Physics Astrophysical Supplement*, 75

Claussen, M. J., Frail, D. A., Goss, W. M., Gaume, R. A., 1997. *ApJ*, 489, 143

Codella, C., Felli, M., Natale, V., 1994. *A&A*, 284, 233

Cornwell, T. J., Evans, K. J., 1985. *A&A*, 143, 77

Cornwell, T. J., Perley, R. A., 1992. *A&A*, 261, 353

Cornwell, T. J., Perley, R. A., 1999. In: G. B. Taylor, C. L. Carilli, R. A. Perley, (eds.) *ASP Conf. Ser. 180: Synthesis Imaging in Radio Astronomy II*

Cornwell, T. J., Uson, J. M., Haddad, N., 1992. *A&A*, 258, 583

Cornwell, T. J., Wilkinson, P. N., 1981. *MNRAS*, 196, 1067

Cowsik, R., Sarkar, S., 1984. *MNRAS*, 207, 745

Cronyn, W. M., 1972. *ApJ*, 174, 181

de Pree, C. G., Rodriguez, L. F., Goss, W. M., 1995. *Revista Mexicana de Astronomia y Astrofisica*, 31, 39

Dickel, J. R., Milne, D. K., 1976. *Australian Journal of Physics*, 29, 435

Douglas, J. N., Bash, F. N., Bozyan, F. A., Torrence, G. W., Wolfe, C., 1996. *AJ*, 111, 1945

Downes, D., Wilson, T. L., Bieging, J., Wink, J., 1980. *A&AS*, 40, 379

Dubner, G. M., Moffett, D. A., Goss, W. M., Winkler, P. F., 1993. *AJ*, 105, 2251

Dulk, G. A., Slee, O. B., 1975. *ApJ*, 199, 61

Duncan, A. R., Haynes, R. F., Jones, K. L., Stewart, R. T., 1997a. *MNRAS*, 291, 279

Duncan, A. R., Stewart, R. T., Haynes, R. F., Jones, K. L., 1997b. *MNRAS*, 287, 722

Erickson, W. C., Perley, R. A., Flatters, C., Kassim, N. E., 2001. *A&A*, 366, 1071

Fesen, R. A., Shull, J. M., Hurford, A. P., 1997. *AJ*, 113, 354

Frail, D. A., Goss, W. M., Slysh, V. I., 1994. *ApJ Lett.*, 424, L111

Frail, D. A., Kassim, N. E., Cornwell, T. J., Goss, W. M., 1995. *ApJ Lett.*, 454, L129

Frail, D. A., Mitchell, G. F., 1998. *ApJ*, 508, 690

Fürst, E., Reich, W., Reich, P., Reif, K., 1990. *A&AS*, 85, 805

Gaensler, B. M., 1998. *ApJ*, 493, 781

Gaensler, B. M., 1999. *Barrels, jets and smoke-rings: Understanding the bizarre shapes of radio supernova remnants.* Ph.D. thesis, University of Sydney, Australia

Ginzburg, V. L., Syrovatskii, S. I., 1969. *Ann. Rev. of A&A*, 7, 375

Gotthelf, E. V., Petre, R., Hwang, U., 1997. *ApJ Lett.*, 487, L175

Gotthelf, E. V., Vasisht, G., 1997. *ApJ Lett.*, 486, L133

Gotthelf, E. V., Vasisht, G., Boylan-Kolchin, M., Torii, K., 2000. *ApJ Lett.*, 542, L37

Gray, A. D., 1994a. *MNRAS*, 270, 847

Gray, A. D., 1994b. *MNRAS*, 270, 835

Gray, A. D., 1996. In: *ASP Conf. Ser. 102: The Galactic Center*. p. 443

Green, A. J., Frail, D. A., Goss, W. M., Otrupcek, R., 1997. *AJ*, 114, 2058

Green, D. A., 1984. *MNRAS*, 209, 449

Green, D. A., 1991. *PASP*, 103, 209

Green, D. A., 2000. *A Catalogue of Galactic Supernova Remnants (2000 August version)* (Mullard Radio Astronomy Observatory, Cavendish Laboratory, Cambridge, UK (available on the World-Wide-Web at "http://www.mrao.cam.ac.uk/surveys/snr/"))

Green, D. A., 2001. *in press*

Griffith, M. R., Wright, A. E., Burke, B. F., Ekers, R. D., 1994. *AJ Supp.*, 90, 179

Gull, S. F., 1973. *MNRAS*, 161, 47

Hamaker, J. P., Bregman, J. D., Sault, R. J., 1996. *A&AS*, 117, 137

Hart, L., Pedlar, A., 1976. *MNRAS*, 176, 547

Haslam, C. G. T., Klein, U., Salter, C. J., Stoffel, H., Wilson, W. E., Cleary, M. N., Cooke, D. J., Thomasson, P., 1981. *A&A*, 100, 209

Haslam, C. G. T., Salter, C. J., Stoffel, H., Wilson, W. E., 1995. In: *Astronomy Data Image Library*. p. 01

Haslam, C. G. T., Stoffel, H., Salter, C. J., Wilson, W. E., 1982. *A&AS*, 47, 1+

Haynes, R. F., Caswell, J. L., 1977. *MNRAS*, 178, 219

Heiles, C., Reach, W. T., Koo, B., 1996. *ApJ*, 466, 191

Helfand, D. J., Zoonematkermani, S., Becker, R. H., White, R. L., 1992. *AJ Supp.*, 80, 211

Högbom, J. A., 1974. *A&AS*, 15, 417

Jones, T. W., Rudnick, L., Jun, B., Borkowski, K. J., Dubner, G., Frail, D. A., Kang, H., Kassim, N. E., McCray, R., 1998. *PASP*, 110, 125

Jun, B., Jones, T. W., Norman, M. L., 1996. *ApJ Lett.*, 468, L59

Jun, B., Norman, M. L., 1996a. *ApJ*, 472, 245

Jun, B., Norman, M. L., 1996b. *ApJ*, 465, 800

Kaspi, V. M., 1998. *Advances in Space Research*, 21, 167

Kassim, N. E., 1989. *ApJ*, 347, 915

Kassim, N. E., Weiler, K. W., 1990. *ApJ*, 360, 184

Kassim, N. E., Weiler, K. W., Erickson, W. C., Wilson, T. L., 1989a. *ApJ*, 338, 152

Kassim, N. E., Weiler, K. W., Erickson, W. C., Wilson, T. L., 1989b. *ApJ*, 338, 152

Katz-Stone, D., Rudnick, L., 1995. In: *American Astronomical Society Meeting*. vol. 187, p. 10001

Katz-Stone, D. M., Kassim, N. E., Lazio, T. J. W., O'Donnell, R., 2000a. *ApJ*, 529, 453

Katz-Stone, D. M., Kassim, N. E., Lazio, T. J. W., O'Donnell, R., 2000b. *ApJ*, 529, 453

Kerr, F. J., Lynden-Bell, D., 1986. *MNRAS*, 221, 1023

Kesteven, M. J., Caswell, J. L., 1987. *A&A*, 183, 118

Kim, K., Koo, B., 2001. *ApJ*, 549, 979

Koo, B., Kim, K., Lee, H., Yun, M., Ho, P. T. P., 1996. *ApJ*, 456, 662+

Kuchar, T. A., Clark, F. O., 1997. *ApJ*, 488, 224

Kudale, S. S., Bhatnagar, S., NCRA Tech. Rep. - in prepration. *A Tcl/Tk based GUI for Gnuplot/multiplot*. Tech. rep., National Centre for Radio Astrophysics, Pune

Kulkarni, A. S., 1997. *Report on GPS measurements at GMRT*. Tech. rep., IIGM, Colaba, Mumbai

Kurtz, S., Churchwell, E., Wood, D. O. S., 1994. *AJ Supp.*, 91, 659

Kurtz, S. E., 2000. In: *Revista Mexicana de Astronomia y Astrofisica Conference Series*. vol. 9, pp. 169–176

Kurtz, S. E., Watson, A. M., Hofner, P., Otte, B., 1999. *ApJ*, 514, 232

LaRosa, T. N., Kassim, N. E., Lazio, T. J. W., Hyman, S. D., 2000. *AJ*, 119, 207

Liszt, H. S., 1992. *AJ Supp.*, 82, 495

Lockett, P., Gauthier, E., Elitzur, M., 1999. *ApJ*, 511, 235

Lockman, F. J., 1980. In: *ASSL Vol. 80: Radio Recombination Lines*. pp. 185–204

Lockman, F. J., 1989. *AJ Supp.*, 71, 469

Manchester, R. N., Durdin, J. M., 1983. In: *IAU Symp. 101: Supernova Remnants and their X-ray Emission*. vol. 101, pp. 421–427

Massi, M., Aaron, S., 1997a. *EVN Tech. Memo*, N75

Massi, M., Aaron, S., 1997b. *EVN Tech. Memo*, N77

Massi, M., Rioja, M., Gabuzda, D., Leppaenen, K., Sanghera, H., Ruf, K., Moscadelli, L., 1997. *A&A*, 318, L32

Massi, M., Ruf, K., Orfei, A., 1998. *EVN Tech. Memo*, N85

Mathur, N. C., 1969. *Radio Science*, 4, 235

Matsui, Y., Long, K. S., Dickel, J. R., Greisen, E. W., 1984. *ApJ*, 287, 295

McKee, C. F., Williams, J. P., 1997. *ApJ*, 476, 144

Mereghetti, S., Sidoli, L., Israel, G. L., 1998. *A&A*, 331, L77

Moffet, A. T., 1975. *Star and Stellar Systems*, vol. 9 (Chicago: University of Chicago Press)

Palka, B. P., 1990. *Complex Functional Analysis* (Springer-Verlag)

Pancharatnam, S., 1956. *S. Proc. Indian Aad. Sci.*, A44, 247

Pancharatnam, S., 1975. *Collected Works of S. Pancharatnam* (Oxford Univ. Press)

Pearson, T. J., Readhead, A. C. S., 1984. *Ann. Rev. of A&A*, 22, 97

Perley, R., Crane, P., 1986. *NRAO Newsletter*, 27, 9

Pina, R. K., Puetter, R. C., 1993. *PASP*, 105, 630

Praveen Kumar, A., 2000. In: J. N. Chengalur, Y. Gupta, K. S. Dwarakanath, (eds.) *SERC School on the GMRT*

Praveen Kumar, A., Srinivas, M., 1996. *Signal Flow Analysis of the GMRT Receiver System.* Tech. rep., National Centre for Radio Astrophysics, Pune

Predehl, P., Schmitt, J. H. M. M., 1995. *A&A*, 293, 889

Puetter, R. C., Pina, R. K., 1994

Ramachandran, G. N., Ramaseshan, S., 1961. *Handbuch der Physik*, vol. 25, part 1 (Springer, Berlin)

Ramaseshan, S., Nityananda, R., 1986. *Current Science*, 55, 1125

Reach, W. T., Rho, J., 1998. *ApJ Lett.*, 507, L93

Reach, W. T., Rho, J., 1999. *ApJ*, 511, 836

Reich, W., Fuerst, E., Reich, P., Reif, K., 1990. *A&AS*, 85, 633

Reynolds, S. P., 1988. In: G. L. Vecshuur, K. I. Kellermann, (eds.) *Galactic and Extragalactic Radio Astronomy* (Springer-Verlag). pp. 439–479

Reynolds, S. P., Chevalier, R. A., 1984. *ApJ*, 278, 630

Reynolds, S. P., Ellison, D. C., 1992. *ApJ Lett.*, 399, L75

Reynoso, E. M., Goss, W. M., 1999. *AJ*, 118, 926

Rho, J., Petre, R., 1998. *ApJ Lett.*, 503, L167

Rogers, A. E. E., 1983. *VLB Array Memo No. 253*

Roshi, D. A., Anantharamaiah, K. R., 2000. *ApJ*, 535, 231

Rozyczka, M., Tenorio-Tagle, G., Franco, J., Bodenheimer, P., 1993. *MNRAS*, 261, 674

Salter, C. J., Brown, R. L., 1988. In: G. L. Vecshuur, K. I. Kellermann, (eds.) *Galactic and Extragalactic Radio Astronomy* (Springer-Verlag). pp. 1–34

Samuel, J., Bhandari, R., 1988. *Physical Review Letters*, 60, 2339

Sankar, G., 2000. In: J. N. Chengalur, Y. Gupta, K. S. Dwarakanath, (eds.) *SERC School on the GMRT*

Sankrit, R., Hester, J. J., 1997. *ApJ*, 491, 796

Sault, R. J., Hamaker, J. P., Bregman, J. D., 1996. *A&AS*, 117, 149

Schwab, F. R., 1984. *AJ*, 89, 1076

Seaquist, E. R., Taylor, A. R., 1990. *ApJ*, 349, 313

Seaquist, E. R., Taylor, A. R., Button, S., 1984. *ApJ*, 284, 202

Sedov, L. I., 1959. *Similarity and Dimensional Methods in Mechanics* (Similarity and Dimensional Methods in Mechanics, New York: Academic Press, 1959)

Shaver, P. A., 1969. *MNRAS*, 142, 273

Shaver, P. A., Radhakrishnan, V., Anantharamaiah, K. R., Retallack, D. S., Wamsteker, W., Danks, A. C., 1982. *A&A*, 106, 105

Singh, R. K., 2000. In: J. N. Chengalur, Y. Gupta, K. S. Dwarakanath, (eds.) *SERC School on the GMRT*

Sirothia, S. K., 2000. *NCRA-IUCAA Gratudate School Project Report*

Subrahmanya, C. R., 1989. In: J. E. Baldwin, W. Shouguan, (eds.) *URSI/IAU Symp. on Radio Astronomical Seeing*. p. 198

Subrahmanyan, R., 1992a. *MNRAS*, 254, 291

Subrahmanyan, R., 1992b. *MNRAS*, 254, 719

Subrahmanyan, R., Goss, W. M., 1995. *MNRAS*, 275, 755

Swarup, G., Ananthakrishnan, S., Kapahi, V. K., Rao, A. P., Subrahmanya, C. R., Kulkarni, V. K., 1991. *CURRENT SCIENCE V.60, NO.2/JAN25, P. 95, 1991*, 60, 95

Tatke, V. M., 1998. *A Digital Spetral Correlator for GMRT*. Master's thesis, Indian Institue of Science, Bangalore, India

Taylor, A. R., Seaquist, E. R., 1984. *ApJ*, 286, 263

Taylor, J. H., Cordes, J. M., 1993. *ApJ*, 411, 674

Taylor, J. H., Manchester, R. N., Lyne, A. G., 1993. *AJ Supp.*, 88, 529

Tenorio-Tagle, G., 1982. In: *ASSL Vol. 93: Regions of Recent Star Formation*. pp. 1–13

Thompson, A. R., D'Addario, L. R., 1982. *Radio Science*, 17, 357

Thompson, A. R., Moran, J. M., Swenson, G. W., J., 1986. *Interferometry and Synthesis in Radio Astronomy* (John Wiley & Sons, Inc.)

Trimble, V., 1982. *Reviews of Modern Physics*, 54, 1183

Trushkin, S. A., 1998. *Bull. Special Astrophys. Obs., 46, 62-96 (1998)*, 46, 62

Trushkin, S. A., 1999. *A&A*, 352, L103

Turner, B. E., 1982. *ApJ Lett.*, 255, L33

van Buren, D., Mac Low, M., Wood, D. O. S., Churchwell, E., 1990. *ApJ*, 353, 570

van der Laan, H., 1962. *MNRAS*, 124, 179

van Dishoeck, E. F., Jansen, D. J., Phillips, T. G., 1993. *A&A*, 279, 541

Vasisht, G., Gotthelf, E. V., 1997. *ApJ Lett.*, 486, L129

Vasisht, G., Gotthelf, E. V., Torii, K., Gaensler, B. M., 2000. *ApJ Lett.*, 542, L49

Wallace, B. J., Landecker, T. L., Taylor, A. R., Pineault, S., 1997. *A&A*, 317, 212

Wardle, M., Yusef-Zadeh, F., Geballe, T. R., 1999. In: *ASP Conf. Ser. 186: The Central Parsecs of the Galaxy*. p. 432

Weiler, K. W., Sramek, R. A., 1988. *Ann. Rev. of A&A*, 26, 295

Weiler, K. W., Sramek, R. A., Panagia, N., van der Hulst, J. M., Salvati, M., 1986. *ApJ*, 301, 790

Whiteoak, J. B., Gardner, F. F., 1968. *ApJ*, 154, 807

Whiteoak, J. B. Z., Green, A. J., 1996. *A&AS*, 118, 329

Willingale, R., West, R. G., Pye, J. P., Stewart, G. C., 1996. *MNRAS*, 278, 749

Wilson, T. L., Jaeger, B., 1987. *A&A*, 184, 291

Wink, J. E., Altenhoff, W. J., Mezger, P. G., 1982. *A&A*, 108, 227

Wink, J. E., Wilson, T. L., Bieging, J. H., 1983. *A&A*, 127, 211

Woltjer, L., 1972. *Ann. Rev. of A&A*, 10, 129

Wood, D. O. S., Churchwell, E., 1989a. *ApJ*, 340, 265

Wood, D. O. S., Churchwell, E., 1989b. *AJ Supp.*, 69, 831

Woosley, S. E., Weaver, T. A., 1986. *Ann. Rev. of A&A*, 24, 205

Yusef-Zadeh, F., Goss, W. M., Roberts, D. A., Robinson, B., Frail, D. A., 1999. *ApJ*, 527, 172